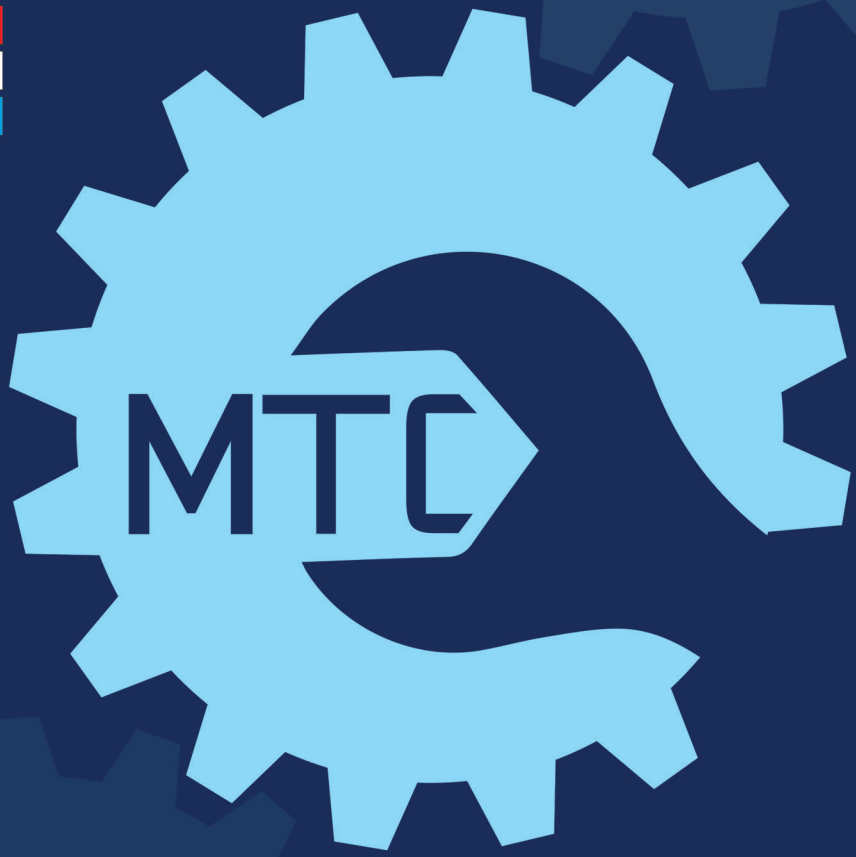
ISSN 0042-8469
e-ISSN 2217-4753
UDC 623 + 355/359

Vol. 74, Issue 4
2026





SCIENTIFIC JOURNAL OF THE MINISTRY OF DEFENCE AND THE SERBIAN ARMED FORCES

MILITARY TECHNICAL COURIER

www.vtg.mod.gov.rs

MILITARY TECHNICAL COURIER
4 2026

ISSN 0042-8469
e-ISSN 2217-4753
UDC 623 + 355/359

Vol. 74, Issue 4

2026

NAUČNI ČASOPIS MINISTARSTVA ODBRANE REPUBLIKE SRBIJE

VOJNOTEHNIČKI GLASNIK

vtg.mo.upr.srb

www.vtg.mod.gov.rs

C O N T E N T S / S A D R Ž A J

ORIGINAL SCIENTIFIC PAPERS / ORIGINALNI NAUČNI RADOVI

Poonam Goyal, Naresh Sharma

Fixed point approximation generalized (α, ψ) − contraction mappings for fixed-point analysis in Branciari multiplicative b-quasi metric spaces

Aproksimacija fiksnih tačaka pomoću generalizovanih (α , ψ) - kontraktivnih preslikavanja za analizu fiksnih tačaka u Branciari multiplikativnim b-kvazi-metričkim prostorima 807-837

Vasanthi Shanmuganathan, James Viyagappan

Symmetric matrix generation using third order recurrence relations

Generisanje simetrične matrice korišćenjem rekurentnih relacija trećeg reda 838-855

Do Duc Trung, Sanjib Biswas, Nguyen Xuan Truong, Darko I Božanić

An integrated multi-criteria decision analysis framework for comparing inland port transport capabilities in maritime logistics

Integrisani okvir za višekriterijumsku analizu odlučivanja za poređenje transportnih kapaciteta unutrašnjih luka u pomorskoj logistici 856-884

Ba Ngoc Dang, Martin Macko, František Racek, Viet Dung Bui Bui, Anh Quang Mai

The effect of elastic components on the firing stability of automatic weapons mounted on combat vehicles

Uticaj elastičnih elemenata na stabilnost gađanja automatskog naoružanja postavljenog na borbena vozila 885-912

Van Dung Nguyen, Van Bien Vo, Minh Phu Nguyen, Xuan Long Vu

Analyzing the belt feed dynamics of gas-operated machine guns

Analiza dinamike dovoda redenika kod mitraljeza sa gasnim sistemom 913-939

Sonia Adjroud, Djenba Samir, Khedidja Abdelhamid, Amireche Hamza

Functional hierarchy using GIS: Diagnosis and traffic regulation solutions in Batna City (Northeastern Algeria)

Funkcionalna hijerarhija primenom GIS-a: dijagnostika i rešenja za regulaciju saobraćaja u gradu Batna (severoistočni Alžir)..... 940-963

Habib Hebali, Fatima Zohra Djidar, Abdelhak Derras

Influence of visco-Pasternak foundation parameters on the bending and vibrational behavior of thick isotropic plates

Uticaj parametara viskoelastične Pasternakove osnove na savijanje i vibraciono ponašanje debelih izotropnih ploča 964-993

Fatma Zohra Halfaya, Mahmoud Bensaibi

AHP-based seismic vulnerability index for critical urban water and sanitation infrastructure

Indeks seizmičke ranjivosti kritične urbane vodovodne i kanalizacione infrastrukture zasnovan na metodi AHP 994-1014

Aboubakeur Boukhelkhal, Amina Djoudi, Yacine Hadj Aissa,

Amar Benguit, Cherifi Rima Hibat Errahmane

Performance of sustainable self-compacting

repair mortar including metakaolin and glass fibers

Performanse samozbijajućeg maltera za

reparaciju sa metakaolinom i staklenim vlaknima..... 1015-1039

Benamar Balegh, Mohammed Fatehi, Hamid Sellaf, Adda Hadj Mostefa, Mohamed Elamine Dahamni , Lyacine Bennacer

Treatment and improvement of clay soils by adding waste rubber in arid regions

Tretiranje i poboljšavanje glinovitih tla

dodavanjem otpadne gume u sušnim područjima 1040-1058

Dmitry Nebratenko, Linfan Wang

Properties of modified bitumen based on SBS-polymers of various topologies

Svojstva modifikovanog bitumena na bazi SBS-polimera različitih topologija 1059-1073

REVIEW PAPERS / PREGLEDNI RADOVI

Dejan Bajić, Slavica Prvulović, Eleonora Desnica, Mića Đurđev,

Ljiljana Radovanović, Branislava Radišić

Comparative analysis of the traditional and

modern taper tap manufacturing processes

Uporedna analiza tradicionalnog i savremenog

tehnološkog postupka izrade instrumentacionog trna..... 1074-1086

CALL FOR PAPERS AND INSTRUCTIONS FOR

AUTHORS / POZIV I UPUTSTVO AUTORIMA 1087-1097

Fixed point approximation generalized $(\alpha, \psi)-$ contraction mappings for fixed-point analysis in Branciari multiplicative b-quasi-metric spaces

Poonam Goyal[a], *Naresh* Sharma[b]

[a] Research Scholar, G D Goenka University, Gurugram, India
e-mail: goyalpoonam2311@gmail.com,
ORCID iD: https://orcid.org/0009-0004-9876-3299

[b] G D Goenka University, Gurugram, India
e-mail: naresh.sharma2006@gmail.com, **corresponding author**,
ORCID iD: https://orcid.org/0000-0001-8398-927X

https://doi.org/10.5937/vojtehg74-59915

FIELD: mathematics
ARTICLE TYPE: original scientific paper

Abstract:

Introduction/purpose: In this paper, we introduce a new class of Branciari-type multiplicative structures, termed b-quasi-metric spaces. This framework extends and unifies several existing concepts, including Branciari metric spaces, quasi-metric spaces, and b-metric spaces. By broadening these foundational structures, we aim to establish a more general setting for the analysis of fixed-point phenomena.

Methods: Within the proposed b-quasi-metric framework, we formulate a generalized class of $(\alpha, \psi)-$ contraction mappings. We then analyze these mappings using fixed point techniques adapted to the newly defined space. The study includes the identification of sufficient conditions guaranteeing the validity of the contraction principle and the development of tools for verifying these conditions.

Results: We establish key properties of the proposed $(\alpha, \psi)-$ contraction mappings, including the existence and uniqueness of fixed points under appropriate hypotheses. These results substantially generalize several earlier fixed point theorems formulated in Branciari, quasi-metric, and b-metric settings. Additionally, illustrative examples are provided to confirm the correctness and applicability of the theoretical findings.

Conclusion: The introduction of b-quasi-metric spaces and the associated class of $(\alpha, \psi)-$ contractions yields a unified and comprehensive extension of previous fixed point results. The examples and applications to specific integral equations further demonstrate the practical relevance of the framework, offering a solid foundation for future theoretical developments and applications.

Key words: fixed points, multiplicative metric space, Branciari multiplicative b- quasi-metric space, generalized multiplicative $(\alpha, \psi)-$contraction mappings.

Introduction

Fixed point (F_p) theory stands as a foundational and adaptable branch within the domain of mathematics, boasting extensive implications spanning numerous disciplines. Its central focus revolves around the notion of F_{ps}, which refer to solutions to equations or mappings that retain their identity even when subjected to specific transformations. This theory furnishes a potent framework for comprehending the presence, singularity and stability of solutions across a broad spectrum of mathematical and real-world scenarios. The origins of F_p theory can be traced back to the early 20th century, marked by influential contributions from luminaries in mathematics, including Banach, Brouwer, and Kakutani. Since its inception, this field has matured into a thriving domain replete with diverse applications in both pure and applied mathematics (Czerwik, 1993) , as well as within a multitude of scientific and engineering domains. In its essence, F_p theory seeks to address fundamental questions such as the determination of the existence of solutions, the assessment of their uniqueness and the development of methodologies for computation or approximation. These inquiries hold profound implications across a wide spectrum of fields, encompassing areas such as real analysis, functional analysis, topology, optimization, control theory, computer science, among others. The ubiquity of F_p theory within the realm of mathematics, along with its wide-ranging relevance in diverse disciplines, underscores its paramount importance. Be it in the examination of dynamical system behavior, the formulation of numerical algorithms, the modeling of economic equilibria, or the design of efficient computational processes in the domain of computer science, F_p theory emerges as an invaluable instrument for gaining insight into the multifaceted intricacies of the world around us. This introductory overview offers but a glimpse into the rich and complex tapestry of F_p theory. As we delve deeper into this captivating field, we will uncover its pivotal concepts, theorem foundations, and the profound ramifications that it holds not just within mathematics but also extending far beyond its boundaries. The foundational concept of contraction mapping, first introduced by Banach (1922) holds immense significance within the domain of F_p theory. Subse-

quently, researchers have extended and enriched the Banach contraction principle. In 2014, Lin and fellow researchers (Lin et al., 2014) introduced the notion of rectangular quasi-metric spaces and provided empirical evidence of an F_p theorem that applies to Meir-Keeler contractive mappings within this specific spatial framework.

Ozavsar & Cevikel (2012) investigated multiplicative metric mappings and examined certain topological characteristics of the corresponding multiplicative metric space. During their discussions, they made an interesting observation: the collection of positive real numbers, denoted as $\mathbb{R}^+$, forms a complete multiplicative metric spaces when equipped with the multiplicative absolute value function. Furthermore, they established the notion of contraction mappings in the framework of multiplicative calculus and offered proofs for specific F_p theorems applicable to these mappings in complete multiplicative metric spaces. Karapinar & Lakzian (2014) introduced the concept of (α, ψ)-contractive mappings in the context of rectangular quasi-metric spaces. They subsequently proved F_p theorems for these mappings. George et al. (2015) extended this concept by introducing rectangular $\boldsymbol{b}-$metric spaces, which encompassed metric spaces and Branciari spaces. This development piqued the interest of many researchers, leading to investigations into a wide range of F_p theorems within these spaces. Alharbi et al. (2018) defined (α)-contractive mappings and provided proofs for F_p theorems tailored specifically to rectangular metric spaces. More recently, Bodaghi et al. (2023) & Abagaro et al. (2022) introduced the concept of ψ-contraction and investigated F_p properties related to ψ-contraction mappings in complete rectangular quasi-metric spaces. Their research confirmed the existence and uniqueness of F_{ps} within this context. Building on the groundwork laid by Ozavsar & Cevikel (2017), as well as the contributions of well-known authors (cf. Abagaro et al., 2022), the primary objective of this paper is to establish F_p properties for multiplicative generalized (α, ψ)-contraction mappings in the framework of Branciari multiplicative $\boldsymbol{b}-$quasi-metric spaces.

The set Ψ consists of functions $\psi : \mathbb{R}^+ \to \mathbb{R}^+$ that are continuous, non-decreasing, and satisfy the following conditions:

1. The infinite product $\prod_{k=1}^{\infty} \psi_k(\nu)^{s_k}$ converges for all $\nu > 0$.
2. $\psi(\nu)^k < \nu$ for all $\nu > 0$ and for all integers k.
3. $\psi(1) = 1$ if and only if $\nu = 1$.

Here, ψ^k represents the kth iteration of the function ψ, and $s \in [1, \infty)$. In order to better comprehend multiplicative metric spaces, b-metric spaces, Branciari spaces, and Branciari b-metric spaces, readers are advised to refer to Branciari et al. (2000), Aydi et al. (2012), and Karapınar (2014). It is important to emphasize that all metric spaces belong to the Branciari metric spaces class, and every Branciari metric space can be viewed as a Branciari b-metric space with coefficient $s = 1$. Branciari metric spaces are necessarily rectangular b-metric spaces, but the opposite may not always be true. To illustrate, Lin et al. (2014) demonstrated that not all Branciari b-metric spaces can be classified as Branciari metric spaces (cf. George et al., 2015). In order to understand the significance of Branciari quasi-metric spaces, readers are advised to refer to Samet et al. (2012). To illustrate that any Branciari metric space is also a Branciari quasi-metric space, but the converse is not always the case, Lin et al. (2014) provided an example to demonstrate that not every Branciari quasi-metric space on a set Θ can be considered a Branciari metric space on the same set Θ (cf. Lakzian & Samet, 2012; Lin et al, 2014; Alma-halebi et al., 2014).

Definition 1. *Consider a non-empty set Θ, a mapping $\Gamma : \Theta \to \Theta$ of Θ, and a function $\alpha : \Theta \times \Theta \to \mathbb{R}^+$. Then the mapping Γ is considered as α-admissible if, for any $\varsigma,\ \omega \in \Theta$,*

$$\alpha(\varsigma,\ \omega) \in [1, \infty) \ \textit{implies} \ \alpha(\Gamma\varsigma, \Gamma\omega) \in [1, \infty)$$

Definition 2. *Suppose we have a multiplicative rectangular quasi-metric spaces denoted as $(\Theta, \eth)$, a sequence $\{\varsigma_\jmath\}$ in Θ, and an element $\varsigma \in \Theta$. In this context, it holds that*

1. *The sequence $\{\varsigma_\jmath\}$ is said to converge to the point $\varsigma \in \Theta$ if, as the limit as $\jmath$ approaches infinity, both $\eth(\varsigma_\jmath, x)$ and $\eth(\varsigma, \varsigma_\jmath)$ become 1. This convergence is symbolized by $\lim_{\jmath\to\infty} \varsigma_\jmath = \varsigma$ or $\varsigma_\jmath \to \varsigma$ as $\jmath \to \infty$.*
2. *The sequence $\{\varsigma_\jmath\}$ is Cauchy in $(\Theta, \eth)$ if*

$$\lim_{\jmath\to\infty} \eth\left(\varsigma_\jmath, \varsigma_{\jmath+\iota}\right) = 1 = \lim_{\jmath\to\infty} \eth\left(\varsigma_{\jmath+\iota}, \varsigma_\jmath\right)$$

   for every $\iota > 0$.
3. *In the case where Cauchy sequence within Θ converges to a particular point $\varsigma \in \Theta$, the space is considered to be a complete Branciar quasi-metric space.*

Main results

The major objective of this section is threefold. First, to explain the concept of Br_{mult} $\boldsymbol{b}$-quasi-metric spaces, second, to define generalized (α, ψ) multiplicative contraction mappings, and finally, to investigate the F_p results for these mappings within the context of Br_{mult} $\boldsymbol{b}-$quasi-metric spaces.

To begin, we will introduce the concept of a Br_{mult} $\boldsymbol{b}-$ quasi-metric space as follows:

Definition 3. *Consider* $\Theta \neq \emptyset$ *(a non-empty set) and* $s \geq 1$. *Suppose that the function* $\eth$ *defined from* $\Theta \times \Theta$ *to* $\mathbb{R}+$ *satisfies the subsequent conditions:*

1. $\eth(\varsigma,\ \omega) = 1$ *iff* $\varsigma = \omega$*;*
2. $\eth(\varsigma,\ \omega) \leq (\eth(\varsigma, \eta_1).\eth(\eta_1, \eta_2).\eth(\eta_2,\ \omega))^s$ *(Br_{mult} inequality)*

for every $\varsigma,\ \omega \in \Theta$ *and all distinct points* $\eta_1,\ \eta_2 \in \Theta \backslash \{\varsigma,\ \omega\}$.

In such case, we refer to $\eth$ *as a* Br_{mult} $\boldsymbol{b}-$ *quasi-met defined on the set* Θ*, and we denote the pair* $(\Theta, \eth)$ *as a* Br_{mult} $\boldsymbol{b}-$ *quasi-metric space.*

In the section that follows, we provide an illustration of a Br_{mult} $\boldsymbol{b}-$ quasi-metric space.

Example 1. Consider the set Θ defined as the union of $\mathcal{O}_1$ and $\mathcal{O}_2$, where $\mathcal{O}_1 = \{0.50, 0.33, 0.25, 0.20\}$ and $\mathcal{O}_2 = [1, 2]$. Let us define the generalized metric $\eth$ on Θ in the following manner:

$$\eth(0.50, 0.33) = \eth(0.25, 0.20) = 0.3; \eth(0.33, 0.50) = \eth(0.20, 0.25)$$

$$= \eth(0.33, 0.25) = 0.1;$$
$$\eth(0.50, 0.25) = \eth(0.33, 0.20) = 0.6; \eth(0.25, 0.50) = \eth(0.20, 0.33) = 0.4;$$
$$\eth(0.50, 0.20) = 1.05; \eth(0.20, 0.50) = \eth(0.25, 0.33) = 0.5;$$
$$\eth(0.50, 0.50) = \eth(0.33, 0.33) = \eth(0.25, 0.25) = \eth(0.20, 0.20) = 1;$$
and $\eth(\varsigma,\ \omega) = \left|\frac{\varsigma}{\omega}\right|$ if $\varsigma,\ \omega \in \mathcal{O}_2$ or $\varsigma \in \mathcal{O}_1,\ \omega \in \mathcal{O}_2$ or $\varsigma \in \mathcal{O}_2,\ \omega \in \mathcal{O}_1$.

Here, we have $(\Theta, \eth)$ forming a Br_{mult} $\boldsymbol{b}-$ quasi-metric space, and the coefficient is $s = 1.5$, which exceeds 1. Meeting condition (1) in Definition

Gojal P. et al., Fixed point approx. gen. contract. mappings for fixed-point anal. in Branciari multiplicative b-quasi-metric spaces, pp.807–837

3 is relatively straightforward. Let us now use an example that proves that condition (2) in Definition (3) is also satisfied:

Case (a)

Given that $\varsigma,\ \omega \in \mathcal{O}_1$, we have

$\eth(\varsigma,\ \omega) = \eth\,(0.5, 0.33) = 0.3 \leq [\eth\,(0.5, \eta_1) \times \eth(\eta_1, \eta_2) \times \eth\,(\eta_2, 0.33)]^s$
when $\eta_1, \eta_2 \in \{0.25, 0.20\}$.

$\eth(\varsigma,\ \omega) = \eth\,(0.33, 0.50) = 0.1 \leq [\eth\,(0.33, \eta_1) \times \eth(\eta_1, \eta_2) \times \eth\,(\eta_2, 0.50)]^s$
when $\eta_1, \eta_2 \in \{0.25, 0.20\}$.

$\eth(\varsigma,\ \omega) = \eth\,(0.33, 0.25) = 0.1 \leq [\eth\,(0.33, \eta_1) \times \eth(\eta_1, \eta_2) \times \eth\,(\eta_2, 0.25)]^s$
when $\eta_1,\ \eta_2 \in \{0.50, 0.20\}$.

$\eth(\varsigma,\ \omega) = \eth\,(0.25, 0.33) = 0.5 \leq [\eth\,(0.25, \eta_1) \times \eth(\eta_1, \eta_2) \times \eth\,(\eta_2, 0.33)]^s$
when $\eta_1, \eta_2 \in \{0.50, 0.20\}$.

$\eth(\varsigma,\ \omega) = \eth\,(0.25, 0.20) = 0.3 \leq [\eth\,(0.25, \eta_1) \times \eth(\eta_1, \eta_2) \times \eth\,(\eta_2, 0.25)]^s$
when $\eta_1, \eta_2 \in \{0.50, 0.33\}$.

$\eth(\varsigma,\ \omega) = \eth\,(0.20, 0.25) = 0.1 \leq [\eth\,(0.20, \eta_1) \times \eth(\eta_1, \eta_2) \times \eth\,(\eta_2, 0.25)]^s$
when $\eta_1, \eta_2 \in \{0.50, 0.33\}$.

$\eth(\varsigma,\ \omega) = \eth\,(0.50, 0.25) = 0.6 \leq [\eth\,(0.50, \eta_1) \times \eth(\eta_1, \eta_2) \times \eth\,(\eta_2, 0.25)]^s$
when $\eta_1, \eta_2 \in \{0.33, 0.20\}$.

$\eth(\varsigma,\ \omega) = \eth\,(0.25, 0.50) = 0.4 \leq [\eth\,(0.25, \eta_1) \times \eth(\eta_1, \eta_2) \times \eth\,(\eta_2, 0.50)]^s$
when $\eta_1, \eta_2 \in \{0.33, 0.20\}$.

$\eth(\varsigma,\ \omega) = \eth\,(0.50, 0.20) = 1.05 \leq [\eth\,(0.50, \eta_1) \times \eth(\eta_1, \eta_2) \times \eth\,(\eta_2, 0.20)]^s$
when $\eta_1, \eta_2 \in \{0.33, 0.25\}$.

$\eth(\varsigma,\ \omega) = \eth\,(0.20, 0.50) = 0.5 \leq [\eth\,(0.20, \eta_1) \times \eth(\eta_1, \eta_2) \times \eth\,(\eta_2, 0.50)]^s$
when $\eta_1, \eta_2 \in \{0.33, 0.25\}$.

$\eth(\varsigma,\ \omega) = \eth\,(0.33, 0.20) = 0.6 \leq [\eth\,(0.33, \eta_1) \times \eth(\eta_1, \eta_2) \times \eth\,(\eta_2, 0.20)]^s$
when $\eta_1, \eta_2 \in \{0.50, 0.25\}$.

$\eth(\varsigma,\ \omega) = \eth\,(0.20, 0.33) = 0.4 \leq [\eth\,(0.20, \eta_1) \times \eth(\eta_1, \eta_2) \times \eth\,(\eta_2, 0.33)]^s$
when $\eta_1, \eta_2 \in \{0.50, 0.25\}$.

$\eth(\varsigma,\ \omega) = \eth\,(0.20, 0.33) = 0.4 \leq [\eth\,(0.20, \eta_1) \times \eth(\eta_1, \eta_2) \times \eth\,(\eta_2, 0.33)]^s$
when $u\eta_1, \eta_2 \in \{0.50, 0.25\}$.

Case (b)

If $\varsigma,\ \omega \in \mathcal{O}_2$ or $\varsigma \in \mathcal{O}_1,\ \omega \in \mathcal{O}_2$ or $\varsigma \in \mathcal{O}_2,\ \omega \in \mathcal{O}_1$, then

$\eth(\varsigma,\ \omega) = \left|\frac{\varsigma}{\omega}\right| \leq \left\{\left|\frac{\varsigma}{\eta_1}\right| \times \left|\frac{\eta_1}{\eta_2}\right| \times \left|\frac{\eta_2}{\omega}\right|\right\}^s$ for every distinct points $\eta_1,\ \eta_2 \in \Theta\backslash\{\varsigma,\ \omega\}$.

However, it is important to note that $(\Theta, \eth)$ do not satisfy the criteria for being a metric space, a rectangular quasi-metric space or a Branciari metric space. This is due to the failure of the triangle inequality, symmetry, and Br_{mult} inequality, which can be demonstrated as follows:

$$\eth(0.50, 0.25) = 0.6 \nleq 0.4 = \eth(0.50, 0.33) \times \eth(0.33, 0.25) = 0.3 \times 0.1,$$
$$\eth(0.50, 0.25) = 0.6 \neq 0.4 = \eth(0.25, 0.50), \text{ and}$$
$$\eth(0.50, 0.20) = 1.05 \nleq 0.7 = \eth(0.50, 0.33) \times \eth(0.33, 0.25) \times \eth(0.25, 0.20).$$

Next, we will provide the definitions for the convergence of a sequence in Br_{mult} $\boldsymbol{b}-$ quasi-metric spaces and the completeness of such spaces.

Definition 4. *Suppose we have a Br_{mult} $\boldsymbol{b}-$ quasi-metric space $(\Theta, \eth)$ and consider a sequence $\{\varsigma_\jmath\}$ in Θ along with an element $\varsigma \in \Theta$. Then, the following holds:*

(i) $\{\varsigma_\jmath\}$ is said to be convergent to Θ if $\lim_{\jmath\to\infty} \eth(\varsigma_\jmath, \varsigma) = 1 = \lim_{\jmath\to\infty} \eth(\varsigma, \varsigma_\jmath)$ that is $\lim_{\jmath\to\infty} \varsigma_\jmath = \varsigma$ or $\varsigma_\jmath \to \varsigma$ as $\jmath \to \infty$.

(ii) Sequence $\{\varsigma_\jmath\}$ is referred to be the Cauchy sequence in $(\Theta, \eth)$ if

$$\lim_{\jmath\to\infty} \eth(\varsigma_\jmath, \varsigma_{\jmath+\iota}) = 1 = \lim_{\jmath\to\infty} \eth(\varsigma_{\jmath+\iota}, \varsigma_\jmath)$$

for every $\iota > 0$.

(iii) If every Cauchy sequence in Θ converges to some $\varsigma \in \Theta$ then $(\Theta, \eth)$ is called a complete Br_{mult} $\boldsymbol{b}$- quasi-metric space.

Remark 1. Let $(\Theta, \eth)$ be a Br_{mult} $\boldsymbol{b}-$ quasi-metric space. For $\varsigma \in \Theta$, the open ball with center $Theta$ and radius $r > 0$ is defined by

$$B_r(\varsigma, r) = \{\omega \in \Theta : \sup\{\eth(\varsigma,\ \omega), \eth(\omega, \varsigma)\} < r\}.$$

In a broader context, it is worth noting that an open ball within a Branciari metric space may not necessarily qualify as an open set. Similarly, a Br_{mult} $\boldsymbol{b}-$ quasi-metric space may lack continuity. The convergence of a

sequence in a Branciari multiplicative $\boldsymbol{b}$- quasi-metric space does not necessarily imply that it is a Cauchy sequence. Additionally, such a space may not adhere to the Hausdorff property, which implies that the uniqueness of limits cannot be assured.

To exemplify these ideas, here is an example in accordance with Remark 1.

Example 2. Consider $\Theta = \mathcal{O}_1 \cup \mathcal{O}_2$, where $\mathcal{O}_1 = \left\{1 - \frac{1}{\eta},\ \alpha \in \mathbb{N}\right\}$, and $\mathcal{O}_2 = \{1, 3\}$. Let a function $\eth$ define from $\Theta \times \Theta$ to $\mathbb{R}^+$ such that

$$\eth(\varsigma,\ \omega) = \begin{cases} 1 & \text{if } \varsigma = \omega \\ 4.5 & \text{if } \varsigma,\ \omega \in \mathcal{O}_1 \\ 1 + \frac{1}{\jmath} & \text{if } \varsigma \in \mathcal{O}_1,\ \omega \in \mathcal{O}_2 \\ 1 + \frac{1}{\jmath+1} & \text{if } \varsigma \in \mathcal{O}_2,\ \omega \in \mathcal{O}_1 \\ 2 & \text{if } \varsigma,\ \omega \in \mathcal{O}_2. \end{cases}$$

where $\jmath \in \mathcal{O}_1$

The function $\eth$ is a Br_{mult} $\boldsymbol{b}$- quasi-metric space with a coefficient of $s = 2$. However, $\eth$ does not meet the criteria to be considered either a Branciari quasi-met or a Branciari $\boldsymbol{b}$-metric space, due to the following factors:

$\eth(0.50, 0.33) = 4.5 \nleq 2.75 = \eth(0.50, 0) \times \eth(0, 3) \times \eth(3, 0.33)$ and
$\eth(0.33, 0) = 0.33 \neq 0.25 = \eth(0, 0.33)$.

It is also evident that

$$\lim_{\jmath\to\infty} \eth\left(1 + \frac{1}{2\jmath}, 0\right) = \lim_{\jmath\to\infty}(1 + \frac{1}{\jmath}) = 1 = \lim_{\jmath\to\infty} \eth\left(0, 1 + \frac{1}{2\jmath}\right) = \lim_{\jmath\to\infty}(1 + \frac{1}{\jmath+1})$$

and

$$\lim_{\jmath\to\infty} \eth\left(1 + \frac{1}{2\jmath}, 3\right) = \lim_{\jmath\to\infty}(1 + \frac{1}{\jmath}) = 1 = \lim_{\jmath\to\infty} \eth\left(3, 1 + \frac{1}{2\jmath}\right) = \lim_{\jmath\to\infty}(1 + \frac{1}{\jmath+1}),$$

In other words, the sequence $\left\{1 + \frac{1}{2\jmath}\right\}$ has two distinct limits, namely, 1 and 4. Moreover, the sequence $\left\{\frac{1}{2\jmath}\right\}$ demonstrates Br_{mult} quasi-$\boldsymbol{b}$-

convergence but does not meet the requirements for being a Br_{mult} quasi-$\boldsymbol{b}$-Cauchy sequence. This is because:

$$\lim_{\jmath\to\infty} \eth\left(\varsigma_\jmath, \varsigma_{\jmath+p}\right) = \lim_{\jmath\to\infty} \eth\left(1+\frac{1}{2\jmath}, 1+\frac{1}{2\jmath+p}\right) = 4.5$$

and

$$\lim_{\jmath\to\infty} \eth\left(\varsigma_{\jmath+p}, \varsigma_\jmath\right) = \lim_{\jmath\to\infty} \eth\left(1+\frac{1}{2\jmath+p}, 1+\frac{1}{2\jmath}\right) = 4.5.$$

Next, we will establish the definition of an multiplicatibe $(\alpha,\psi)-$contraction mapping within the framework of a Br_{mult} $\boldsymbol{b}-$quasi-metric space.

Definition 5. *Consider a Br_{mult} $\boldsymbol{b}-$quasi-metric space $(\Theta,\eth)$ and a given mapping $\Gamma:\Theta\longrightarrow\Theta$. We classify Γ as a generalized $(\alpha,\psi)-$ contraction mapping under the condition of two functions: $\alpha:\Theta\times\Theta\to\mathbb{R}^+$ and $\psi\in\Psi$. This classification holds when the following conditions are met:*

$$(\eth(\Gamma\varsigma,\Gamma\omega))^{\alpha(\varsigma,\ \omega)} \leq \psi(\Xi(\varsigma,\ \omega)) \ \ \forall\ \ \varsigma,\ \omega\in\Theta, \tag{1}$$

where

$$\Xi(\varsigma,\omega) = \sup\Big\{\ (\eth(\varsigma,\Gamma\varsigma)\cdot\eth(\varsigma,\Gamma\omega))^{\left(1+\eth(\varsigma,\Gamma\omega)+\eth(\omega,\Gamma\varsigma)\right)^{-1}}, \eth(\varsigma,\Gamma\varsigma), \eth(\varsigma,\omega), \eth(\omega,\Gamma\omega)\Big\}.$$

We now introduce and illustrate the subsequent F_p theorem.

Theorem 1. Consider a complete Br_{mult} $\boldsymbol{b}-$quasi-metric space $(\Theta,\eth)$ and a generalized $(\alpha,\psi)-$ contraction mapping $\Gamma:\Theta\to\Theta$. Take into account the subsequent assumption:

1. Γ is a mapping that satisfies the α-admissibility condition;
2. $\exists\ \ \varsigma_0\ \in\ \Theta$ such that $\alpha\left(\varsigma_0,\Gamma\varsigma_0\right)\ \in\ [1,\infty), \alpha\left(\Gamma\varsigma_0,\varsigma_0\right)\ \in\ [1,\infty), \alpha\left(\varsigma_0,\Gamma^2\varsigma_0\right)\in[1,\infty)$, and $\alpha\left(\Gamma^2\varsigma_0,\varsigma_0\right)\in[1,\infty)$;
3. mapping Γ is continuous.

In this case, mapping Γ has a F_p.

Proof. As indicated in condition (2) mentioned earlier, $\exists\ \varsigma_0$ in Θ such that $\alpha(\varsigma_0,\Gamma\varsigma_0)\in[1,\infty)$ and $\alpha(\Gamma\varsigma_0,\varsigma_0)\in[1,\infty)$. Now, we establish a sequence

Gojal P. et al., Fixed point approx. gen. contract. mappings for fixed-point anal. in Branciari multiplicative b-quasi-metric spaces, pp.807–837

$\{\varsigma_n\}$ in Θ by defining $\varsigma_{\jmath+1} = \Gamma\varsigma_n = \Gamma^{\jmath+1}\varsigma_0$ for every $\jmath \geq 0$. Let us assume that $\varsigma_{\jmath_0} = \varsigma_{\jmath_0+1}$ for some $\jmath_0 \geq 0$. Given that $\Gamma\varsigma_{\jmath_0} = \varsigma_{\jmath_0+1}$, it follows that the point $\eta_1 = \varsigma_{\jmath_0}$ serves as a F_p for Γ. Consequently, this concludes the proof. It should be noted that we are working under the assumption that $\varsigma_n \neq \varsigma_{\jmath+1}$ for every $\jmath \in \mathbb{N} \cup \{0\}$.

As Γ is a mapping that satisfies the α-admissibility condition, it follows that

$$\alpha(\varsigma_0, \varsigma_1) = \alpha(\varsigma_0, \Gamma\varsigma_0) \in [1, \infty) \Rightarrow \alpha(\Gamma\varsigma_0, \Gamma\varsigma_1) = \alpha(\varsigma_1, \varsigma_2) \in [1, \infty).$$

By employing the given expression, we can deduce that

$$\alpha(\varsigma_\jmath, \varsigma_{\jmath+1}) \in [1, \infty), \ \forall\, \jmath = 0,\ 1, \ldots, \tag{2}$$

and $\alpha(\varsigma_1, \varsigma_0) = \alpha(\Gamma\varsigma_0, \varsigma_0) \in [1, \infty) \Rightarrow \alpha(\Gamma\varsigma_1, \Gamma\varsigma_0) = \alpha(\varsigma_2, \varsigma_1) \in [1, \infty)$. Again, by employing the given expression, we can deduce that

$$\alpha(\varsigma_{\jmath+1}, \varsigma_\jmath) \in [1, \infty), \quad \forall\, \jmath = 0,\ 1, \ldots \tag{3}$$

Using a similar approach, we ascertain that $\alpha(\varsigma_0, \varsigma_2) = \alpha\left(\varsigma_0, \Gamma^2\varsigma_0\right) \in [1, \infty)$. This further implies that

$$\alpha(\Gamma\varsigma_0, \Gamma\varsigma_2) = \alpha(\varsigma_1, \varsigma_3) \in [1, \infty).$$

Through a series of recursive steps, it becomes evident that

$$\alpha(\varsigma_\jmath, \varsigma_{\jmath+2}) \in [1, \infty), \quad \forall\, \jmath = 0,\ 1, \ldots \tag{4}$$

In a comparable manner, we can readily conclude that

$$\alpha(\varsigma_{\jmath+2}, \varsigma_\jmath) \in [1, \infty), \quad \forall\, \jmath = 0,\ 1, \ldots \tag{5}$$

Step 1: we illustrate that

$$\eth(\varsigma_\jmath, \varsigma_{\jmath+1}) \to 1 \text{ as } \jmath \to \infty, \text{ and } \eth(\varsigma_{\jmath+1}, \varsigma_\jmath) \to 1 \text{ as } \jmath \to \infty,$$

also

$$\eth(\varsigma_\jmath, \varsigma_{\jmath+2}) \to 1 \text{ as } \jmath \to \infty, \text{ and } \eth(\varsigma_{\jmath+2}, \varsigma_\jmath) \to 1 \text{ as } \jmath \to \infty.$$

With respect to equation (1), we have

$$\eth(\varsigma_\jmath, \varsigma_{\jmath+1}) = \eth(\Gamma\varsigma_{\jmath-1}, \Gamma\varsigma_\jmath)$$

which results in

$$\begin{aligned}\eth\left(\varsigma_{\jmath},\varsigma_{\jmath+1}\right) &\leq \left(\eth\left(\Gamma\varsigma_{\jmath-1},\Gamma\varsigma_{\jmath}\right)\right)^{\alpha(\varsigma_{\jmath-1},\varsigma_{\jmath})} \\ &\leq \psi\left(\Xi\left(\varsigma_{\jmath-1},\varsigma_{\jmath}\right)\right), \quad \forall\, \jmath \geq 1, \end{aligned} \tag{6}$$

where

$$\Xi(\varsigma_{\jmath-1},\varsigma_{\jmath}) = \sup\Bigg\{ \left(\eth(\varsigma_{\jmath-1},\Gamma\varsigma_{\jmath-1})\,\eth(\varsigma_{\jmath-1},\Gamma\varsigma_{\jmath})\right)^{(1+\eth(\varsigma_{\jmath-1},\Gamma\varsigma_{\jmath})+\eth(\varsigma_{\jmath},\Gamma\varsigma_{\jmath-1}))^{-1}},$$

$$\eth(\varsigma_{\jmath-1},\Gamma\varsigma_{\jmath-1}),\ \eth(\varsigma_{\jmath-1},\varsigma_{\jmath}),\ \eth(\varsigma_{\jmath},\Gamma\varsigma_{\jmath})\Bigg\}$$

which results in

$$\Xi\left(\varsigma_{\jmath-1},\varsigma_{\jmath}\right) = \sup\Bigg\{\left(\eth\left(\varsigma_{\jmath-1},\varsigma_{\jmath}\right).\eth\left(\varsigma_{\jmath-1},\varsigma_{\jmath+1}\right)\right)^{\left(1+\eth\left(\varsigma_{\jmath-1},\varsigma_{\jmath+1}\right)+\eth\left(\varsigma_{\jmath},\varsigma_{\jmath}\right)\right)^{-1}},$$

$$\eth\left(\varsigma_{\jmath-1},\varsigma_{\jmath}\right),\eth\left(\varsigma_{\jmath-1},\varsigma_{\jmath}\right),\eth\left(\varsigma_{\jmath},\varsigma_{\jmath+1}.\right)\Bigg\}$$

Therefore, we obtain

$$\Xi\left(\varsigma_{\jmath-1},\varsigma_{\jmath}\right) = \max\Big\{\eth\left(\varsigma_{\jmath-1},\varsigma_{\jmath}\right),\eth\left(\varsigma_{\jmath},\varsigma_{\jmath+1}\right)\Big\}.$$

If $\Xi\left(\varsigma_{\jmath-1},\varsigma_{\jmath}\right) = \eth\left(\varsigma_{\jmath},\varsigma_{\jmath+1}\right)$.

Subsequently, based on (6), we obtain

$$\eth\left(\varsigma_{\jmath},\varsigma_{\jmath+1}\right) \leq \psi\left(\eth\left(\varsigma_{\jmath},\varsigma_{\jmath+1}\right)\right) \leq \left(\psi\left(\eth\left(\varsigma_{\jmath},\varsigma_{\jmath+1}\right)\right)\right)^{s} \leq \eth\left(\varsigma_{\jmath},\varsigma_{\jmath+1}\right),$$

which conflicts with the earlier assertion. Hence, $\Xi\left(\varsigma_{\jmath-1},\varsigma_{\jmath}\right)$ is equal to $\eth\left(\varsigma_{\jmath-1},\varsigma_{\jmath}\right)$. Let

$$e_{\jmath} = \eth\left(\varsigma_{\jmath},\varsigma_{\jmath+1}\right), l_{\jmath} = \eth\left(\varsigma_{\jmath+1},\varsigma_{\jmath}\right), e_{\jmath}^{*} = \eth\left(\varsigma_{\jmath},\varsigma_{\jmath+2}\right)$$

and $l_{\jmath}^{*} = \eth\left(\varsigma_{\jmath+2},\varsigma_{\jmath}\right)$ for every $\jmath \geq 0$. Utilizing (6), we obtain

$$\begin{aligned} e_{\jmath} = \eth\left(\varsigma_{\jmath},\varsigma_{\jmath+1}\right) &= \eth\left(\Gamma\varsigma_{\jmath-1},\Gamma\varsigma_{\jmath}\right) \leq \psi\left(\eth\left(\varsigma_{\jmath-1},\varsigma_{\jmath}\right)\right) \\ &= \psi\left(\eth\left(\Gamma\varsigma_{\jmath-2},\Gamma\varsigma_{\jmath-1}\right)\right) \\ &\leq \psi^{2}\left(\eth\left(\varsigma_{\jmath-2},\varsigma_{\jmath-1}\right)\right) \end{aligned}$$

Gojal P. et al., Fixed point approx. gen. contract. mappings for fixed-point anal. in Branciari multiplicative b-quasi-metric spaces, pp.807–837

$$\vdots$$

$$\leq \psi^{\jmath}\left(\eth\left(\varsigma_0,\varsigma_1\right)\right)=\psi^{\jmath}\left(e_0\right)\longrightarrow 1 \text{ as } \jmath\longrightarrow\infty. \tag{7}$$

Furthermore,

$$\begin{aligned} l_{\jmath}=\eth\left(\varsigma_{\jmath+1},\varsigma_{\jmath}\right)&=\eth\left(\Gamma\varsigma_{\jmath},\Gamma\varsigma_{\jmath-1}\right)\\ &\leq\left(\eth\left(\Gamma\varsigma_{\jmath},\Gamma\varsigma_{\jmath-1}\right)\right)^{\alpha(\varsigma_{\jmath},\varsigma_{\jmath-1})}\\ &\leq\psi\left(\Xi\left(\varsigma_{\jmath},\varsigma_{\jmath-1}\right)\right), \end{aligned} \tag{8}$$

$\forall\ \jmath\in[1,\infty)$ wherein

$$\Xi(\varsigma_{\jmath},\varsigma_{\jmath-1})=\sup\left\{\begin{matrix}\left(\eth(\varsigma_{\jmath},\Gamma\varsigma_{\jmath})\,\eth(\varsigma_{\jmath},\Gamma\varsigma_{\jmath-1})\right)^{\left(1+\eth(\varsigma_{\jmath},\Gamma\varsigma_{\jmath-1})+\eth(\varsigma_{\jmath-1},\Gamma\varsigma_{\jmath})\right)^{-1}},\\ \eth(\varsigma_{\jmath},\Gamma\varsigma_{\jmath}),\quad \eth(\varsigma_{\jmath},\varsigma_{\jmath-1}),\quad \eth(\varsigma_{\jmath-1},\Gamma\varsigma_{\jmath-1})\end{matrix}\right\}.$$

As a result,

$$=\sup\left\{\begin{matrix}\left(\eth\left(\varsigma_{\jmath},\varsigma_{\jmath+1}\right).\eth\left(\varsigma_{\jmath},\varsigma_{\jmath}\right)\right)^{\left(1+\eth\left(\varsigma_{\jmath},\varsigma_{\jmath}\right)+\eth\left(\varsigma_{\jmath-1},\varsigma_{\jmath+1}\right)\right)^{-1}},\\ \eth\left(\varsigma_{\jmath},\varsigma_{\jmath+1}\right),\eth\left(\varsigma_{\jmath},\varsigma_{\jmath-1}\right),\eth\left(\varsigma_{\jmath-1},\varsigma_{\jmath}\right)\end{matrix}\right\}$$

$$\Xi\left(\varsigma_{\jmath},\varsigma_{\jmath-1}\right)=\sup\left\{\eth\left(\varsigma_{\jmath},\varsigma_{\jmath-1}\right),\eth\left(\varsigma_{\jmath},\varsigma_{\jmath+1}\right),\eth\left(\varsigma_{\jmath-1},\varsigma_{\jmath}\right)\right\}.$$

We analyze three distinct cases.

Case (c) Provided that $\Xi\left(\varsigma_{\jmath},\varsigma_{\jmath-1}\right)=\eth\left(\varsigma_{\jmath-1},\varsigma_{\jmath}\right)$, according to (8), we obtain

$$\begin{aligned}\eth\left(\varsigma_{\jmath+1},\varsigma_{\jmath}\right)&\leq\psi\left(\eth\left(\varsigma_{\jmath-1},\varsigma_{\jmath}\right)\right)\\ &\leq\psi^{\jmath}\left(\eth\left(\varsigma_0,\varsigma_1\right)\right)=\psi^{\jmath}\left(e_0\right)\longrightarrow 1\quad \text{as } \jmath\longrightarrow\infty.\end{aligned}$$

Case (d) Provided that $\Xi\left(\varsigma_{\jmath},\varsigma_{\jmath-1}\right)$ is same as $\eth\left(\varsigma_{\jmath},\varsigma_{\jmath+1}\right)$, based on equation (8), we have

$$\begin{aligned}\eth\left(\varsigma_{\jmath+1},\varsigma_{\jmath}\right)&\leq\psi\left(\eth\left(\varsigma_{\jmath},\varsigma_{\jmath+1}\right)\right)\\ &\leq\psi^{\jmath}\left(\eth\left(\varsigma_0,\varsigma_1\right)\right)=\psi^{\jmath}\left(e_0\right)\longrightarrow 1\quad \text{as } \jmath\longrightarrow\infty.\end{aligned}$$

Case (e) Provided that $\Xi(\varsigma_\jmath, \varsigma_{\jmath-1})$ is same as $\eth(\varsigma_\jmath, \varsigma_{\jmath-1})$, following the equation (8), we have

$$\begin{aligned} l_\jmath &= \eth(\varsigma_{\jmath+1}, \varsigma_\jmath) \\ &= \eth(\Gamma\varsigma_\jmath, \Gamma\varsigma_{\jmath-1}) \leq \psi(\eth(\varsigma_\jmath, \varsigma_{\jmath-1})) \\ &= \psi(\eth(\Gamma\varsigma_{\jmath-1}, \Gamma\varsigma_{\jmath-2})) \\ &\leq \psi^2(\eth(\varsigma_{\jmath-1}, \varsigma_{\jmath-2})) \\ &\vdots \\ &\leq \psi^\jmath(\eth(\varsigma_1, \varsigma_0)) = \psi^\jmath(l_0) \longrightarrow 0 \quad \text{as } \jmath \longrightarrow \infty. \end{aligned}$$

Combining all the above-mentioned cases, we obtain

$$l_\jmath = \eth(\varsigma_{\jmath+1}, \varsigma_\jmath) \longrightarrow 1 \quad \text{as } \jmath \longrightarrow \infty. \tag{9}$$

Using equations (7) and (9), we can infer that

$$\eth(\varsigma_\jmath, \varsigma_{\jmath+1}) \to 1, \text{ as } \jmath \to \infty \text{ and } \eth(\varsigma_{\jmath+1}, \varsigma_\jmath) \to 1 \text{ as } \jmath \to \infty. \tag{10}$$

Now, to prove that $\lim_{\jmath\to\infty} \eth(\varsigma_\jmath, \varsigma_{\jmath+2}) = 1 = \lim_{\jmath\to\infty} \eth(\varsigma_{\jmath+2}, \varsigma_\jmath)$.

$$\begin{aligned} e^*_\jmath &= \eth(\varsigma_\jmath, \varsigma_{\jmath+2}) = \eth(\Gamma\varsigma_{\jmath-1}, \Gamma\varsigma_{\jmath+1}) \\ &\leq (\eth(\Gamma\varsigma_{\jmath-1}, \Gamma\varsigma_{\jmath+1}))^{\alpha(\varsigma_{\jmath-1}, \varsigma_{\jmath+1})} \\ &\leq \psi(\Xi(\varsigma_{\jmath-1}, \varsigma_{\jmath+1})), \quad \forall\, \jmath \geq 1 \end{aligned} \tag{11}$$

wherein

$$\Xi(\varsigma_{\jmath-1}, \varsigma_{\jmath+1})$$

$$= \sup \left\{ \begin{matrix} (\eth(\varsigma_{\jmath-1}, \Gamma\varsigma_{\jmath-1})\, \eth(\varsigma_{\jmath-1}, \Gamma\varsigma_{\jmath+1})^{\left(1+\eth(\varsigma_{\jmath-1}, \Gamma\varsigma_{\jmath+1})+\eth(\varsigma_{\jmath+1}, \Gamma\varsigma_{\jmath-1})\right)^{-1}}, \\ \eth(\varsigma_{\jmath-1}, \Gamma\varsigma_{\jmath-1}), \quad \eth(\varsigma_{\jmath-1}, \varsigma_{\jmath+1}), \quad \eth(\varsigma_{\jmath+1}, \Gamma\varsigma_{\jmath+1}) \end{matrix} \right\}.$$

As a result,

$$\Xi(\varsigma_{\jmath-1}, \varsigma_{\jmath+1}) = \sup \left\{ \begin{matrix} (\eth(\varsigma_{\jmath-1}, \varsigma_\jmath)\, \eth(\varsigma_{\jmath-1}, \varsigma_{\jmath+2}))^{(1+\eth(\varsigma_{\jmath-1}, \varsigma_{\jmath+2})+\eth(\varsigma_{\jmath+1}, \varsigma_\jmath))^{-1}}, \\ \eth(\varsigma_{\jmath-1}, \varsigma_\jmath), \quad \eth(\varsigma_{\jmath-1}, \varsigma_{\jmath+1}), \quad \eth(\varsigma_{\jmath+1}, \varsigma_{\jmath+2}) \end{matrix} \right\}.$$

Therefore, we have

$$\Xi(\varsigma_{\jmath-1}, \varsigma_{\jmath+1}) = \sup \left\{ \eth(\varsigma_{\jmath-1}, \varsigma_{\jmath+1}), \eth(\varsigma_{\jmath-1}, \varsigma_\jmath), \eth(\varsigma_{\jmath+1}, \varsigma_{\jmath+2}) \right\}.$$

We analyze three distinct cases:

Case (f) If $\Xi(\varsigma_\jmath, \varsigma_{\jmath-1}) = \eth(\varsigma_{\jmath-1}, \varsigma_{\jmath+1})$, with the use of (11), we obtain

$$\begin{aligned}\eth(\varsigma_\jmath, \varsigma_{\jmath+2}) &\leq \psi(\eth(\varsigma_{\jmath-1}, \varsigma_{\jmath+1})) \\ &\leq \psi^{\jmath-1}(\eth(\varsigma_0, \varsigma_2)) = \psi^{\jmath-1}(e_0^*) \longrightarrow 1 \quad \text{as } \jmath \longrightarrow \infty.\end{aligned}$$

Case (g) If $\Xi(\varsigma_{\jmath-1}, \varsigma_{\jmath+1}) = \eth(\varsigma_{\jmath-1}, \varsigma_\jmath)$, with the use of (11), we obtain

$$\begin{aligned}\eth(\varsigma_\jmath, \varsigma_{\jmath+2}) &\leq \psi(\eth(\varsigma_{\jmath-1}, \varsigma_\jmath)) \\ &\leq \psi^{\jmath-1}(\eth(\varsigma_0, \varsigma_1)) = \psi^{\jmath-1}(e_0) \longrightarrow 0 \quad \text{as } \jmath \longrightarrow \infty.\end{aligned}$$

Case (h) If $\Xi(\varsigma_{\jmath-1}, \varsigma_{\jmath+1}) = \eth(\varsigma_{\jmath+1}, \varsigma_{\jmath+2})$, based on equation (11), we have

$$\begin{aligned}\eth(\varsigma_\jmath, \varsigma_{\jmath+2}) &\leq \psi(\eth(\varsigma_{\jmath+1}, \varsigma_{\jmath+2})) \\ &\leq \psi^{\jmath+1}(\eth(\varsigma_0, \varsigma_1)) \\ &= \psi^{\jmath+1}(e_0) \longrightarrow 1 \text{ as } \jmath \longrightarrow \infty.\end{aligned}$$

Aggregation of all the aforementioned cases results in

$$e_\jmath^* = \eth(\varsigma_\jmath, \varsigma_{\jmath+2}) \longrightarrow 1 \quad \text{as } \jmath \longrightarrow \infty \tag{12}$$

$$\begin{aligned}\eth(\varsigma_{\jmath+2}, \varsigma_\jmath) &= \eth(\Gamma\varsigma_{\jmath+1}, \Gamma\varsigma_{\jmath-1}) \\ &\leq (\eth(\Gamma\varsigma_{\jmath+1}, \Gamma\varsigma_{\jmath-1}))^{\alpha(\varsigma_{\jmath+1}, \varsigma_{\jmath-1})} \\ &\leq \psi(\Xi(\varsigma_{\jmath+1}, \varsigma_{\jmath-1})), \quad \forall\, \jmath \in [1, \infty)\end{aligned} \tag{13}$$

wherein

$$\Xi(\varsigma_{\jmath+1}, \varsigma_{\jmath-1})$$

$$= \sup \left\{ \begin{array}{l} (\eth(\varsigma_{\jmath+1}, \Gamma\varsigma_{\jmath+1}) . \eth(\varsigma_{\jmath+1}, \Gamma\varsigma_{\jmath-1}))^{(1 + \eth(\varsigma_{\jmath+1}, \Gamma\varsigma_{\jmath-1}) + \eth(\varsigma_{\jmath-1}, \Gamma\varsigma_{\jmath+1}))^{-1}}, \\ \eth(\varsigma_{\jmath+1}, \Gamma\varsigma_{\jmath+1}), \eth(\varsigma_{\jmath+1}, \varsigma_{\jmath-1}), \eth(\varsigma_{\jmath-1}, \Gamma\varsigma_{\jmath-1}) \end{array} \right\}.$$

$$= \sup \left\{ \begin{array}{l} (\eth(\varsigma_{\jmath+1}, \varsigma_{\jmath+2}) . \eth(\varsigma_{\jmath+1}, \varsigma_\jmath))^{(1 + \eth(\varsigma_{\jmath+1}, \varsigma_\jmath) + \eth(\varsigma_{\jmath-1}, \varsigma_{\jmath+2}))^{-1}}, \\ \eth(\varsigma_{\jmath+1}, \varsigma_{\jmath-1}), \eth(\varsigma_{\jmath+1}, \varsigma_{\jmath-1}), \eth(\varsigma_{\jmath+1}, \varsigma_{\jmath+2}, \eth(\varsigma_{\jmath-1}, \varsigma_\jmath) \end{array} \right\}$$

Now, we analyze three distinct cases:

Case (i) Given that $\Xi(\varsigma_{\jmath+1}, \varsigma_{\jmath-1}) = \eth(\varsigma_{\jmath+1}, \varsigma_{\jmath-1})$, then by (13), we get

$$\begin{aligned}\eth(\varsigma_{\jmath+2}, \varsigma_{\jmath}) &\leq \psi(\eth(\varsigma_{\jmath+1}, \varsigma_{\jmath-1})) \\ &\leq \psi^{\jmath+1}(\eth(\varsigma_2, \varsigma_0)) \\ &= \psi^{\jmath+1}(l_0^*) \longrightarrow 1 \quad \text{as } \jmath \longrightarrow \infty.\end{aligned}$$

Case (j) Given that $\Xi(\varsigma_{\jmath+1}, \varsigma_{\jmath-1}) = \eth(\varsigma_{\jmath+1}, \varsigma_{\jmath+2})$, by using equation (13), we have

$$\begin{aligned}\eth(\varsigma_{\jmath+2}, \varsigma_{\jmath}) &\leq \psi(\eth(\varsigma_{\jmath+1}, \varsigma_{\jmath+2})) \\ &\leq \psi^{\jmath+1}(\eth(\varsigma_0, \varsigma_1)) \\ &= \psi^{\jmath+1}(e_0) \longrightarrow 1 \quad \text{as } \jmath \longrightarrow \infty.\end{aligned}$$

Case (k) Provided that $\Xi(\varsigma_{\jmath+1}, \varsigma_{\jmath-1}) = \eth(\varsigma_{\jmath-1}, \varsigma_{\jmath})$, by employing equation (13), we have $\eth(\varsigma_{\jmath+2}, \varsigma_{\jmath}) \leq \psi(\eth(\varsigma_{\jmath-1}, \varsigma_{\jmath}))$ and hence

$$\eth(\varsigma_{\jmath+2}, \varsigma_{\jmath}) \leq \psi^{\jmath-1}(\eth(\varsigma_0, \varsigma_1)). \tag{14}$$

It results that $\eth(\varsigma_{\jmath+2}, \varsigma_{\jmath}) = \psi^{\jmath-1}(e_0) \longrightarrow 0 \quad \text{as } \jmath \longrightarrow \infty$. Based on equation (12) and equation (14), we infer that

$$\lim_{\jmath\to\infty} \eth(\varsigma_{\jmath}, \varsigma_{\jmath+2}) = 1 = \lim_{\jmath\to\infty} \eth(\varsigma_{\jmath+2}, \varsigma_{\jmath}).$$

Step 2: We will establish that $\{\varsigma_{\jmath}\}$ qualifies as a Br_{mult} $\boldsymbol{b}$- quasi-Cauchy sequence, signifying that

$$\lim_{\jmath\to\infty} \eth(\varsigma_{\jmath}, \varsigma_{\jmath+\iota}) = 1 = \lim_{\jmath\to\infty} \eth(\varsigma_{\jmath+\iota}, \varsigma_{\jmath}) \quad \forall\ \iota \in \mathbb{N}.$$

Case (l) Assume that, for certain natural numbers $\jmath$ and h, where $h > \jmath$, we find that $\varsigma_{\jmath} = \varsigma_h$, as indicated by equation (10).

$$\begin{aligned}\eth(\varsigma_{\jmath}, \varsigma_{\jmath+1}) &= \eth(\varsigma_{\jmath}, \Gamma\varsigma_{\jmath}) \\ &= \eth(\varsigma_h, \Gamma\varsigma_h) \\ &= \eth(\varsigma_h, \varsigma_{h+1}) \\ &\leq \psi^{h-\jmath}(\eth(\varsigma_{\jmath}, \varsigma_{\jmath+1}))\end{aligned}$$

$$\leq (\psi(\eth(\varsigma_{\jmath}, \varsigma_{\jmath+1})))$$
$$< (\eth(\varsigma_{\jmath}, \varsigma_{\jmath+1}))^{s}.$$

This statement conflicts with the previous results.

Case (m) Let us assume that there exist natural numbers $\jmath$ and h such that $\jmath > h$. We observe that $\varsigma_{\jmath} = \varsigma_{h}$ based on equation (10).

$$\begin{aligned}\eth(\varsigma_{h+1}, \varsigma_{h}) &= \eth(\Gamma\varsigma_{h}, \varsigma_{h}) = \eth(\Gamma\varsigma_{\jmath}, \varsigma_{\jmath}) = \eth(\varsigma_{\jmath+1}, \varsigma_{\jmath}) \\ &\leq \psi^{\jmath-h}(\eth(\varsigma_{h+1}, \varsigma_{h}))^{s} \\ &\leq \psi(\eth(\varsigma_{h+1}, \varsigma_{h})) < \eth(\varsigma_{h+1}, \varsigma_{h})\end{aligned}$$

This inconsistency implies that, considering both Case (a) and Case (b), it is clear that $\varsigma_{\jmath}$ is not equal to ς_{h} for h is not equal to $\jmath$. Now, let us move on to the cases of $\iota = 1$ and $\iota = 2$, which we have successfully proved. Next, we will discuss the case where $\iota \geq 3$, and we will do so arbitrarily by distinguishing between four distinct cases:

Case (n) Assume that $\iota = 2h$ ($h \geq 2$). Now, by employing the Br_{mult} inequality, we have $\eth(\varsigma_{\jmath}, \varsigma_{\jmath+2h}) \leq (\eth(\varsigma_{\jmath}, \varsigma_{\jmath+2}) \times \eth(\varsigma_{\jmath+2}, \varsigma_{\jmath+3}) \times \eth(\varsigma_{\jmath+3}, \varsigma_{\jmath+2h}))^{s}$. It further results that

$$\begin{aligned}\eth(\varsigma_{\jmath}, \varsigma_{\jmath+2h}) \leq{}& (\eth(\varsigma_{\jmath}, \varsigma_{\jmath+2}))^{s} \times (\eth(\varsigma_{\jmath+2}, \varsigma_{\jmath+3}))^{s} \times (\eth(\varsigma_{\jmath+3}, \varsigma_{\jmath+4}) \\ &\times \eth(\varsigma_{\jmath+4}, \varsigma_{\jmath+5}) \times \eth(\varsigma_{\jmath+5}, \varsigma_{\jmath+2h}))^{s^2} \\ ={}& (\eth(\varsigma_{\jmath}, \varsigma_{\jmath+2}))^{s} \times (\eth(\varsigma_{\jmath+2}, \varsigma_{\jmath+3}))^{s} \times (\eth(\varsigma_{\jmath+3}, \varsigma_{\jmath+4}))^{s^2} \\ &\times (\eth(\varsigma_{\jmath+4}, \varsigma_{\jmath+5}))^{s^2} \times (\eth(\varsigma_{\jmath+5}, \varsigma_{\jmath+2h}))^{s^2}.\end{aligned}$$

Inductively, we have

$$\begin{aligned}\eth(\varsigma_{\jmath}, \varsigma_{\jmath+2h}) \leq{}& (\eth(\varsigma_{\jmath}, \varsigma_{\jmath+2}))^{s} \times (\eth(\varsigma_{\jmath+2}, \varsigma_{\jmath+3}))^{s^3} \times (\eth(\varsigma_{\jmath+3}, \varsigma_{\jmath+4}))^{s^4}, \\ &\times (\eth(\varsigma_{\jmath+4}, \varsigma_{\jmath+5}))^{s^5} \times \cdots \times (\eth(\varsigma_{\jmath+2h-1}, \varsigma_{\jmath+2h}))^{s^{2h}},\end{aligned} \tag{15}$$

which results in

$$\begin{aligned}\eth(\varsigma_{\jmath}, \varsigma_{\jmath+2h}) ={}& (\eth(\varsigma_{\jmath}, \varsigma_{\jmath+2}))^{s} \times \prod_{k=\jmath+2}^{\jmath+2h-1} (\eth(\varsigma_{k}, \varsigma_{k+1}))^{s^{k-\jmath+1}} \\ \leq{}& (\eth(\varsigma_{\jmath}, \varsigma_{\jmath+2}))^{s} \times \prod_{k=\jmath+2}^{\jmath+2h-1} (\psi^{k}(e_0))^{s^{k}}\end{aligned}$$

$$\leq (\eth(\varsigma_\jmath, \varsigma_{\jmath+2}))^s \times \sum_{k=\jmath+2}^{\infty} (\psi^k(e_0))^{s^k}.$$

Now, by referring to equation (14),

$$\lim_{\jmath\to\infty} \eth(\varsigma_\jmath, \varsigma_{\jmath+2}) = 1 \text{ and } \prod_{k=\jmath+2}^{\infty} (\psi^k(e_0))^{s^k} \longrightarrow 1 \text{ as } \jmath \longrightarrow \infty.$$

Consequently, $\lim_{\jmath,h\to\infty} \eth(\varsigma_\jmath, \varsigma_{\jmath+2h}) = 1$.

Case (o) Consider ι as $2h+1$ ($h \geq 1$). By utilizing the Br_{mult} inequality, we have

$$\begin{aligned}\eth(\varsigma_\jmath, \varsigma_{\jmath+2h+1}) \leq & (\eth(\varsigma_\jmath, \varsigma_{\jmath+1}) \times \eth(\varsigma_{\jmath+1}, \varsigma_{\jmath+2}) \times \eth(\varsigma_{\jmath+2}, \varsigma_{\jmath+2h+1}))^s \\ & \leq (\eth(\varsigma_\jmath, \varsigma_{\jmath+1}))^s \times (\eth(\varsigma_{\jmath+1}, \varsigma_{\jmath+2}))^s \\ & \times (\eth(\varsigma_{\jmath+2}, \varsigma_{\jmath+3}) \times \eth(\varsigma_{\jmath+3}, \varsigma_{\jmath+4}) \times \eth(\varsigma_{\jmath+4}, \varsigma_{\jmath+2h+1}))^{s^2}.\end{aligned}$$

As a result, we have

$$\begin{aligned}\eth(\varsigma_\jmath, \varsigma_{\jmath+2h+1}) = & (\eth(\varsigma_\jmath, \varsigma_{\jmath+1}))^s \times (\eth(\varsigma_{\jmath+1}, \varsigma_{\jmath+2}))^s \times (\eth(\varsigma_{\jmath+2}, \varsigma_{\jmath+3}))^{s^2} \\ & \times (\eth(\varsigma_{\jmath+3}, \varsigma_{\jmath+4}))^{s^2} \times (\eth(\varsigma_{\jmath+4}, \varsigma_{\jmath+2h+1}))^{s^2}\end{aligned} \tag{16}$$

With the same approach, we have

$$\begin{aligned}\eth(\varsigma_\jmath, \varsigma_{\jmath+2h+1}) \leq & (\eth(\varsigma_\jmath, \varsigma_{\jmath+1}))^s \times (\eth(\varsigma_{\jmath+1}, \varsigma_{\jmath+2}))^{s^2} \times (\eth(\varsigma_{\jmath+2}, \varsigma_{\jmath+3}))^{s^3} \\ & \times (\eth(\varsigma_{\jmath+3}, \varsigma_{\jmath+4}))^{s^4} \times \cdots \times (\eth(\varsigma_{\jmath+2h}, \varsigma_{\jmath+2h+1}))^{s^{2h+1}}.\end{aligned} \tag{17}$$

Therefore, we have

$$\eth(\varsigma_\jmath, \varsigma_{\jmath+2h+1}) = \prod_{k=\jmath}^{\jmath+2h} (\eth(\varsigma_k, \varsigma_{k+1}))^{s^{k-\jmath+1}} = \prod_{k=\jmath}^{\jmath+2h} (\psi^k(e_0))^{s^{k-\jmath+1}},$$

which results in

$$\begin{aligned}\eth(\varsigma_\jmath, \varsigma_{\jmath+2h+1}) \leq & \prod_{k=\jmath}^{\jmath+2h} (\psi^k(e_0))^{s^k} \\ & \leq \prod_{k=\jmath}^{\infty} (\psi^k(e_0))^{s^k} \longrightarrow 1 \quad \text{as } \jmath \longrightarrow \infty.\end{aligned}$$

Gojal P. et al., Fixed point approx. gen. contract. mappings for fixed-point anal. in Branciari multiplicative b-quasi-metric spaces, pp.807–837

As a result, we have $\lim_{\jmath,h\to\infty} \eth\left(\varsigma_\jmath, \varsigma_{\jmath+2h+1}\right) = 1$.

Case (p) Consider $\iota = 2h$, where $h > 2$. Applying the Br_{mult} inequality, we have

$$\begin{aligned}
\eth\left(\varsigma_{\jmath+2h}, \varsigma_\jmath\right) \leq & \left(\eth\left(\varsigma_{\jmath+2h}, \varsigma_{\jmath+2h-2}\right) \times \eth\left(\varsigma_{\jmath+2h-2}, \varsigma_{\jmath+2h-3}\right) \times \eth\left(\varsigma_{\jmath+2h-3}, \varsigma_\jmath\right)\right)^s \\
\leq & \left(\eth\left(\varsigma_{\jmath+2h}, \varsigma_{\jmath+2h-2}\right)\right)^s \times \left(\eth\left(\varsigma_{\jmath+2h-2}, \varsigma_{\jmath+2h-3}\right)\right)^s \\
& \times \left(\eth\left(\varsigma_{\jmath+2h-3}, \varsigma_{\jmath+2h-4}\right) \times \eth\left(\varsigma_{\jmath+2h-4}, \varsigma_{\jmath+2h-5}\right) \times \eth\left(\varsigma_{\jmath+2h-5}, \varsigma_\jmath\right)\right)^{s^2} \\
= & \left(\eth\left(\varsigma_{\jmath+2h}, \varsigma_{\jmath+2h-2}\right)\right)^s \times \left(\eth\left(\varsigma_{\jmath+2h-2}, \varsigma_{\jmath+2h-3}\right)\right)^s \qquad (18) \\
& \times \left(\eth\left(\varsigma_{\jmath+2h-3}, \varsigma_{\jmath+2h-4}\right)\right)^{s^2} \times \left(\eth\left(\varsigma_{\jmath+2h-4}, \varsigma_{\jmath+2h-5}\right)\right)^{s^2} \\
& \times \left(\eth\left(\varsigma_{\jmath+2h-5}, \varsigma_\jmath\right)\right)^{s^2}.
\end{aligned}$$

Inductively, we have

$$\begin{aligned}
\eth\left(\varsigma_{\jmath+2h}, \varsigma_\jmath\right) \leq & \left(\eth\left(\varsigma_{\jmath+2h}, \varsigma_{\jmath+2h-2}\right)\right)^s \times \left(\eth\left(\varsigma_{\jmath+2h-2}, \varsigma_{\jmath+2h-3}\right)\right)^{s^{\jmath+2h-2}} \\
& \times \left(\eth\left(\varsigma_{\jmath+2h-3}, \varsigma_{\jmath+2h-4}\right)\right)^{s^{\jmath+2h-3}} \times \left(\eth\left(\varsigma_{\jmath+2h-4}, \varsigma_{\jmath+2h-5}\right)\right)^{s^{\jmath+2h-4}} \\
& \times \cdots \times \left(\eth\left(\varsigma_{\jmath-1}, \varsigma_\jmath\right)\right)^{s^{\jmath-1}}.
\end{aligned}$$

Therefore, we have

$$\begin{aligned}
\eth\left(\varsigma_{\jmath+2h}, \varsigma_\jmath\right) &= \left(\eth\left(\varsigma_{\jmath+2h}, \varsigma_{\jmath+2h-2}\right)\right)^s \times \prod_{k=\jmath-1}^{\jmath+2h-1} \left(\eth\left(\varsigma_k, \varsigma_{k+1}\right)\right)^{s^k} \\
&\leq \left(\eth\left(\varsigma_{\jmath+2h}, \varsigma_{\jmath+2h-2}\right)\right)^s \times \prod_{k=\jmath-1}^{\jmath+2h-1} \left(\psi^k\left(l_0^*\right)\right)^{s^k}.
\end{aligned}$$

It results that

$$\eth\left(\varsigma_{\jmath+2h}, \varsigma_\jmath\right) \leq \left(\eth\left(\varsigma_{\jmath+2h}, \varsigma_{\jmath+2h-2}\right)\right)^s \times \prod_{k=\jmath-1}^{\infty} \left(\psi^k\left(l_0^*\right)\right)^{s^k}.$$

As $\lim_{m,\jmath\to\infty} \eth\left(\varsigma_{\jmath+2h}, \varsigma_{\jmath+2h-2}\right) = 1$ and $\prod_{k=\jmath-1}^{\infty} \left(\psi^k\left(l_0^*\right)\right)^{s^k} \longrightarrow 1$ as $\jmath \longrightarrow \infty$, we have

$$\eth\left(\varsigma_{\jmath+2h}, \varsigma_\jmath\right) \longrightarrow 1,\ h,\ j \to \infty\ .$$

Case (q) Consider $\iota = 2h+1$, $h \geq 1$. Now, by using Br_{mult} inequality, we get

$$\eth\left(\varsigma_{\jmath+2h+1}, \varsigma_\jmath\right) \leq \left(\eth\left(\varsigma_{\jmath+2h+1}, \varsigma_{\jmath+2h}\right) \times \eth\left(\varsigma_{\jmath+2h}, \varsigma_{\jmath+2h-1}\right) \times \eth\left(\varsigma_{\jmath+2h-1}, \varsigma_\jmath\right)\right)^s$$

$$\begin{aligned}\leq&(\eth(\varsigma_{\jmath+2h+1},\varsigma_{\jmath+2h}))^{s}\times(\eth(\varsigma_{\jmath+2h},\varsigma_{\jmath+2h-1}))^{s}\\&\times(\eth(\varsigma_{\jmath+2h-1},\varsigma_{\jmath+2h-2})\times\eth(\varsigma_{\jmath+2h-2},\varsigma_{\jmath+2h-3})\\&\times\eth(\varsigma_{\jmath+2h-3},\varsigma_{\jmath}))^{s^{2}}.\end{aligned}\tag{19}$$

Therefore, we have

$$\begin{aligned}\eth(\varsigma_{\jmath+2h+1},\varsigma_{\jmath})=&(\eth(\varsigma_{\jmath+2h+1},\varsigma_{\jmath+2h}))^{s}\times(\eth(\varsigma_{\jmath+2h},\varsigma_{\jmath+2h-1}))^{s}\\&\times(\eth(\varsigma_{\jmath+2h-1},\varsigma_{\jmath+2h-2}))^{s^{2}}\times(\eth(\varsigma_{\jmath+2h-2},\varsigma_{\jmath+2h-3}))^{s^{2}}\\&\times(\eth(\varsigma_{\jmath+2h-3},\varsigma_{\jmath}))^{s^{2}}.\end{aligned}\tag{20}$$

Inductively, we have

$$\begin{aligned}\eth(\varsigma_{\jmath+2h+1},\varsigma_{\jmath})\leq&(\eth(\varsigma_{\jmath+2h+1},\varsigma_{\jmath+2h}))^{s^{\jmath+2h+1}}\times(\eth(\varsigma_{\jmath+2h},\varsigma_{\jmath+2h-1}))^{s^{\jmath+2h}}\\&\times(\eth(\varsigma_{\jmath+2h-1},\varsigma_{\jmath+2h-2}))^{s^{\jmath+2h-1}}\times(\eth(\varsigma_{\jmath+2h-2},\varsigma_{\jmath+2h-3}))^{s^{\jmath+2h-2}}\\&\times\cdots\times(\eth(\varsigma_{\jmath+1},\varsigma_{\jmath}))^{s^{\jmath+1}}\end{aligned}$$

and hence

$$\eth(\varsigma_{\jmath+2h+1},\varsigma_{\jmath})=\prod_{k=\jmath+1}^{\jmath+2h}(\eth(\varsigma_{k+1},\varsigma_{k}))^{s^{k}}=\prod_{k=\jmath+1}^{\jmath+2h}(\psi^{k}(l_{0}))^{s^{k-\jmath+1}}.$$

Consecutively, we have

$$\eth(\varsigma_{\jmath+2h+1},\varsigma_{\jmath})\leq\prod_{k=\jmath+1}^{\jmath+2h}(\psi^{k}(l_{0}))^{s^{k}}\longrightarrow 1\ \text{ as } n\longrightarrow\infty.$$

Therefore, we can deduce that as $\jmath$ and h tend towards infinity, whereas the limiting value of $\eth(\varsigma_{\jmath+2h+1},\varsigma_{\jmath})$ is 1. Additionally, by considering the cases (a) to (d), we can conclude that as $\jmath$ approaches infinity, the limits of $\eth(\varsigma_{\jmath},\varsigma_{\jmath+\iota})$ and $\eth(\varsigma_{\jmath+\iota},\varsigma_{\jmath})$ are both equal to 1 for every value of ι greater than or equal to 3. Consequently, it can be inferred that the sequence $\{\varsigma_{\jmath}\}$ is a Br_{mult} $\boldsymbol{b}$- quasi-Cauchy within the metric spaces $(\Theta,\eth)$. Since Θ is a complete Br_{mult} $\boldsymbol{b}-$ quasi-metric space, $\exists\ \eta_{1}$ in Θ such that

$$\lim_{\jmath\to\infty}\varsigma_{\jmath}=\eta_{1},\ \text{i.e.,}\ \lim_{\jmath\to\infty}\eth(\varsigma_{\jmath},\eta_{1})=1=\lim_{\jmath\to\infty}\eth(\eta_{1},\varsigma_{\jmath}).\tag{21}$$

Following that, we establish that η_{1} acts a F_{p} under the mapping of Γ. As Γ exhibits continuity, we can infer from equation (21) that $\eta_{1}=$

$\lim_{\jmath\to\infty}\varsigma_{\jmath+1}=\lim_{\jmath\to\infty}\Gamma\left(\varsigma_{\jmath}\right)=\Xi\left(\lim_{\jmath\to\infty}\varsigma_{\jmath}\right)=\eta_1$, which gives $\eta_1=\Gamma\eta_1$. Therefore, we can conclude that η_1 is indeed a F_p when the mapping Γ is applied. Now, we introduce the following F_p theorem by omitting the condition for continuity in the mapping Γ from Theorem 1.

Theorem 2. *Consider a complete* Br_{mult} $\boldsymbol{b}-$*quasi-metric space denoted as* $(\Theta,\eth)$ *and let* $\Gamma:\Theta\longrightarrow\Theta$ *be a generalized mapping with multiplicative* $(\alpha,\psi)-$*contraction properties. Assume that:*

1. Γ *is a mapping that satisfies the* α*-admissibility condition;*
2. *there is an existence of* $\varsigma_0\in\Theta$ *in a way that* $\alpha\left(\varsigma_0,\Gamma\varsigma_0\right)\in[1,\infty),\alpha\left(\Gamma\varsigma_0,\varsigma_0\right)\in[1,\infty),\alpha\left(\varsigma_0,\Gamma^2\varsigma_0\right)\in[1,\infty)$*, as well as* $\alpha\left(\Gamma^2\varsigma_0,\varsigma_0\right)\in[1,\infty)$;
3. *As* $\varsigma_{\jmath}$ *represents a sequence within* Θ *in such a way that* $\alpha\left(\varsigma_{\jmath},\varsigma_{\jmath+1}\right)\in[1,\infty)\ \forall\ \jmath\geq0$*, and as* $\jmath$ *approaches infinity,* $\varsigma_{\jmath}\longrightarrow\varsigma\in\Theta$*, then* $\alpha\left(\varsigma_{\jmath},\varsigma\right)\in[1,\infty)\ \forall\ \jmath\geq0$.

Under these conditions, a F_p *exists for the operator* Γ.

Proof. After considering the proofs of Theorem 1, we have established that the sequence $\{\varsigma_{\jmath}\}$, which is defined by the recurrence relation $\varsigma_{\jmath+1}=\Gamma\varsigma_{\jmath}$ for every $\jmath\geq0$, exhibits Br_{mult} quasi-$\boldsymbol{b}$-convergence towards a point η_1 within the space Θ. Our aim now is to demonstrate that Γ possesses a F_p. Utilizing the Br_{mult} inequality within the context of Br_{mult} $\boldsymbol{b}-$ quasi-metric spaces, the properties of ψ, and condition (iii), we can state the following:

$$\begin{aligned}\eth(\eta_1,\Gamma\eta_1)&\leq\left(\eth\left(\eta_1,\varsigma_{\jmath}\right)\right)^s\times\left(\eth\left(\varsigma_{\jmath},\varsigma_{\jmath+1}\right)\right)^s\times\left(\eth\left(\varsigma_{\jmath+1},\Gamma\eta_1\right)\right)^s\\&=\left(\eth\left(\eta_1,\varsigma_{\jmath}\right)\right)^s\times\left(\eth\left(\varsigma_{\jmath},\varsigma_{\jmath+1}\right)\right)^s\times\left(\eth\left(\Gamma\varsigma_{\jmath},\Gamma\eta_1\right)\right)^s\\&\leq\left(\eth\left(\eta_1,\varsigma_{\jmath}\right)\right)^s\times\left(\eth\left(\varsigma_{\jmath},\varsigma_{\jmath+1}\right)\right)^s\times\left(\eth\left(\Gamma\varsigma_{\jmath},\Gamma\eta_1\right)\right)^{s\alpha(\varsigma_{\jmath},\eta_1)}\\&\leq\left(\eth\left(\eta_1,\varsigma_{\jmath}\right)\right)^s\times\left(\eth\left(\varsigma_{\jmath},\varsigma_{\jmath+1}\right)\right)^s\times\left(\psi(\Xi\left(\Gamma\varsigma_{\jmath},\Gamma\eta_1\right))\right)^s\end{aligned}\tag{22}$$

where

$$\Xi\left(\varsigma_{\jmath},\eta_1\right)=\sup\left\{\begin{matrix}\left(\eth\left(\varsigma_{\jmath},\Gamma\varsigma_{\jmath}\right).\eth\left(\varsigma_{\jmath},\Gamma\eta_1\right)\right)\left(1+\eth\left(\varsigma_{\jmath},\Gamma\eta_1\right)+\eth\left(\eta_1,\Gamma\varsigma_{\jmath}\right)\right)^{-1},\\\eth\left(\varsigma_{\jmath},\Gamma\varsigma_{\jmath}\right),\eth\left(\varsigma_{\jmath},\eta_1\right),\eth\left(\eta_1,\Gamma\eta_1\right)\end{matrix}\right\}$$

and hence, we have

$$\Xi\left(\varsigma_{\jmath},\eta_{1}\right)=\sup\left\{\begin{array}{l}\left(\eth\left(\varsigma_{\jmath},\varsigma_{\jmath+1}\right).\eth\left(\varsigma_{\jmath},\Gamma\eta_{1}\right)\right)^{\left(1+\eth\left(\varsigma_{\jmath},\Gamma\eta_{1}\right)+\eth\left(\eta_{1},\varsigma_{\jmath+1}\right)\right)^{-1}},\\ \eth\left(\varsigma_{\jmath},\varsigma_{\jmath+1}\right),\eth\left(\varsigma_{\jmath},\eta_{1}\right),\eth\left(\eta_{1},\Gamma\eta_{1}\right)\end{array}\right\}$$

which results in

$$\Xi\left(\varsigma_{\jmath},\eta_{1}\right)=\sup\left\{\eth\left(\varsigma_{\jmath},\eta_{1}\right),\eth(\varsigma_{\jmath},\varsigma_{\jmath+1}),\eth\left(\eta_{1},\Gamma\eta_{1}\right)\right\}.$$

We analyze some distinct cases, which can be described as follows:

Case (r) Given that $\Xi\left(\varsigma_{\jmath},\eta_{1}\right)$ is the same as $\eth\left(\varsigma_{\jmath},\eta_{1}\right)$, then by (22), we get

$$\begin{aligned}\eth(\eta_{1},\Gamma\eta_{1})&\leq\left(\eth\left(\eta_{1},\varsigma_{\jmath}\right)\right)^{s}\times\left(\eth\left(\varsigma_{\jmath},\varsigma_{\jmath+1}\right)\right)^{s}\times\left(\psi\left(\eth\left(\varsigma_{\jmath},\eta_{1}\right)\right)\right)^{s}\\&<\left(\eth\left(\eta_{1},\varsigma_{\jmath}\right)\right)^{s}\times\left(\eth\left(\varsigma_{\jmath},\varsigma_{\jmath+1}\right)\right)^{s}\times\eth\left(\varsigma_{\jmath},\eta_{1}\right).\end{aligned}$$

By allowing $\jmath$ to approach infinity in the preceding inequality, considering equations (10) and (21), we obtain the following:

$$\eth(\eta_{1},\Gamma\eta_{1})\leq 1.$$

Case (s) Given that $\Xi\left(\varsigma_{\jmath},\eta_{1}\right)$ and $\eth\left(\varsigma_{\jmath},\varsigma_{\jmath+1}\right)$ are the same, then by (16), we get

$$\begin{aligned}\eth(\eta_{1},\Gamma\eta_{1})&\leq\left(\eth\left(\eta_{1},\varsigma_{\jmath}\right)\right)^{s}\times\left(\eth\left(\varsigma_{\jmath},\varsigma_{\jmath+1}\right)\right)^{s}\times\left(\psi\left(\eth\left(\varsigma_{\jmath},\varsigma_{\jmath+1}\right)\right)\right)^{s}\\&<\left(\eth\left(\eta_{1},\varsigma_{\jmath}\right)\right)^{s}\times\left(\eth\left(\varsigma_{\jmath},\varsigma_{\jmath+1}\right)\right)^{s}\times\eth\left(\varsigma_{\jmath},\varsigma_{\jmath+1}\right).\end{aligned}$$

By allowing $\jmath\longrightarrow\infty$ in the preceding inequality, considering equations (10) and (15), we obtain the following:

$$\eth(\eta_{1},\Gamma\eta_{1})\leq 1$$

Case (t) Let $\Xi\left(\varsigma_{\jmath},\eta_{1}\right)$ and $\eth(\eta_{1},\Gamma\eta_{1})$ be same, then by (16), we get

$$\begin{aligned}\eth(\eta_{1},\Gamma\eta_{1})&\leq\left(\eth\left(\eta_{1},\varsigma_{\jmath}\right)\right)^{s}\times\left(\eth\left(\varsigma_{\jmath},\varsigma_{\jmath+1}\right)\right)^{s}\times\left(\psi(\eth(\eta_{1},\Gamma\eta_{1}))\right)^{s}\\&<\left(\eth\left(\eta_{1},\varsigma_{\jmath}\right)\right)^{s}\times\left(\eth\left(\varsigma_{\jmath},\varsigma_{\jmath+1}\right)\right)^{s}\times\left(\eth(\eta_{1},\Gamma\eta_{1})\right)^{s}.\end{aligned}$$

As we let $\jmath\longrightarrow\infty$ in the inequality mentioned above, and taking into account equations (10) and (15), we arrive at the trivial statement that $0\leq 0$,

Gojal P. et al., Fixed point approx. gen. contract. mappings for fixed-point anal. in Branciari multiplicative b-quasi-metric spaces, pp.807–837

which is universally true. Obviously, $\eth(\eta_1, \Gamma\eta_1)$ is greater than or equal to 0, and by examining the aforementioned cases, we can derive the following:

$$\eth(\eta_1, \Gamma\eta_1) = 1. \tag{23}$$

Also,

$$\begin{aligned}\eth(\Gamma\eta_1, \eta_1) &\leq (\eth(\Gamma\eta_1, \varsigma_\jmath))^s \times (\eth(\varsigma_\jmath, \varsigma_{\jmath+1}))^s \times (\psi(\eth(\varsigma_{\jmath+1}, \eta_1)))^s \\ &= (\eth(\Gamma\eta_1, \Gamma\varsigma_{\jmath-1}))^s \times (\eth(\varsigma_\jmath, \varsigma_{\jmath+1}))^s \times (\psi(\eth(\varsigma_{\jmath+1}, \eta_1)))^s\end{aligned}$$

which results in

$$\begin{aligned}\eth(\Gamma\eta_1, \eta_1) &\leq (\eth(\Gamma\eta_1, \Gamma\varsigma_{\jmath-1}))^{s\alpha(\eta_1, \varsigma_{\jmath-1})} \times (\eth(\varsigma_\jmath, \varsigma_{\jmath+1}))^s \times (\eth(\varsigma_{\jmath+1}, \eta_1))^s \\ &\leq (\psi(\Xi(\eta_1, \varsigma_{\jmath-1})))^s \times (\eth(\varsigma_\jmath, \varsigma_{\jmath+1}))^s \times (\eth(\varsigma_{\jmath+1}, \eta_1))^s. \end{aligned} \tag{24}$$

where

$$\Xi(\eta_1, \varsigma_{\jmath-1}) = \sup\Big\{(\eth(\eta_1, \Gamma\eta_1)\eth(\eta_1, \Gamma\varsigma_{\jmath-1}))^{(1+\eth(\eta_1, \Gamma\varsigma_{\jmath-1})+\eth(\varsigma_{\jmath-1}, \Gamma\eta_1))^{-1}},$$
$$\eth(\eta_1, \Gamma\eta_1), \eth(\eta_1, \varsigma_{\jmath-1}), \eth(\varsigma_{\jmath-1}, \Gamma\varsigma_{\jmath-1})\Big\}$$

and hence,

$$\Xi(\eta_1, \varsigma_{\jmath-1}) = \sup\Big\{(\eth(\eta_1, \Gamma\eta_1)\eth(\eta_1, \varsigma_{\jmath-1}))^{(1+\eth(\eta_1, \varsigma_\jmath)+\eth(\varsigma_{\jmath-1}, \Gamma\eta_1))^{-1}},$$
$$\eth(\eta_1, \Gamma\eta_1), \eth(\eta_1, \varsigma_{\jmath-1}), \eth(\varsigma_{\jmath-1}, \Gamma\varsigma_{\jmath-1})\Big\}.$$

Consequently,

$$\Xi(\eta_1, \varsigma_{\jmath-1}) = \sup\Big\{\eth(\eta_1, \varsigma_{\jmath-1}), \eth(\varsigma_\jmath, \varsigma_{\jmath+1}), \eth(\eta_1, \Gamma\eta_1)\Big\}.$$

As a result, we analyze the following distinct cases:

Case (u) Given that $\Xi(\eta_1, \varsigma_{\jmath-1})$ and $\eth(\eta_1, \varsigma_{\jmath-1})$ are the same, then by (24), we get $\eth(\Gamma\eta_1, \eta_1) \leq (\psi(\eth(\eta_1, \varsigma_{\jmath-1})))^s \times (\eth(\varsigma_\jmath, \varsigma_{\jmath+1}))^s \times (\eth(\varsigma_{\jmath+1}, \eta_1))^s$, which further results in

$$\eth(\Gamma\eta_1, \eta_1) < \eth(\eta_1, \varsigma_{\jmath-1}) \times (\eth(\varsigma_\jmath, \varsigma_{\jmath+1}))^s \times (\eth(\varsigma_{\jmath+1}, \eta_1))^s.$$

By letting $\jmath$ approach infinity in the previous equation, and making use of equations (10) and (15), we can deduce that $\eth(\Gamma\eta_1, \eta_1) \leq 1$.

Case (v) Let it be given that $\Xi(\eta_1, \varsigma_{\jmath-1}) = \eth(\varsigma_\jmath, \varsigma_{\jmath+1})$, then by (18), we get

$$\begin{aligned}\eth(\Gamma\eta_1, \eta_1) &\leq (\psi(\eth(\varsigma_\jmath, \varsigma_{\jmath+1})))^s \times (\eth(\varsigma_\jmath, \varsigma_{\jmath+1}))^s \times (\eth(\varsigma_{\jmath+1}, \eta_1))^s \\ &< (\eth(\varsigma_\jmath, \varsigma_{\jmath+1})) \times (\eth(\varsigma_\jmath, \varsigma_{\jmath+1}))^s \times (\eth(\varsigma_{\jmath+1}, \eta_1))^s.\end{aligned}$$

By allowing the value of $\jmath \longrightarrow \infty$ in the inequality mentioned earlier and considering equations (10) and (21), we have $\eth(\Gamma\eta_1, \eta_1) \leq 1$.

Case (w) If $\Xi(\eta_1, \varsigma_{\jmath-1}) = \eth(\eta_1, \Gamma\eta_1)$, then by (18), we get

$$\begin{aligned}\eth(\Gamma\eta_1, \eta_1) &\leq (\psi(\eth(\eta_1, \Gamma\eta_1)))^s \times (\eth(\varsigma_\jmath, \varsigma_{\jmath+1}))^s \times (\eth(\varsigma_{\jmath+1}, \eta_1))^s \\ &< \eth(\eta_1, \Gamma\eta_1) \times (\eth(\varsigma_\jmath, \varsigma_{\jmath+1}))^s \times (\eth(\varsigma_{\jmath+1}, \eta_1))^s\end{aligned}$$

By allowing the value of $\jmath \longrightarrow \infty$ in the inequality mentioned earlier and considering equations (10), (21) and (23) we have $\eth(\Gamma\eta_1, \eta_1) \leq 1$. It is evident that $\eth(\eta_1, \Gamma\eta_1) \in [1, \infty)$, and we can deduce from the analysis of cases (i) to (iii) that

$$\eth(\Gamma\eta_1, \eta_1) = 1. \tag{25}$$

By considering equations (23) and (25), we can conclude that $\eth(\eta_1, \Gamma\eta_1) = 1 = \eth(\Gamma\eta_1, \eta_1)$, which implies that $\Gamma\eta_1 = \eta_1$. This means that η_1 remains unchanged under the action of Γ i.e. η_1 is a F_p.

To ensure that there is only one F_p for Γ, we will examine the following criterion.

Property U for every ς and ω belonging to the set of F_{ps} of Γ, denoted as $\mathrm{Fix}(\Gamma)$, holds that $\alpha(\varsigma, \omega) \in [1, \infty)$ and $\alpha(\omega, \varsigma) \in [1, \infty)$.

Theorem 3. *If we add condition (U) to the assumptions made in Theorem 1 (or Theorem 2), we can guarantee the uniqueness of the F_p of Γ.*

Proof. We establish that $\mathrm{Fix}(\Gamma)$ is not an empty set by employing proof of Theorem 1 and Theorem 2 respectively. Let us assume that $\eta_1 \neq \eta_2$ are

two F_{ps} of Γ. Then Condition (U) implies that

$$\alpha(\Gamma\eta_1, \Gamma\eta_2) = \alpha(\eta_1, \eta_2) \in [1, \infty) \text{ and } \alpha(\Gamma\eta_2, \Gamma\eta_1) = \alpha(\eta_2, \eta_1) \in [1, \infty).$$

Consequently, due to the multiplicative $\alpha-$admissibility property of mapping Γ and the aforementioned inequality, we can deduce that

$$\begin{aligned}\eth(\eta_1, \eta_2) &\leq (\eth(\eta_1, \eta_2))^{\alpha(\eta_1, \eta_2)} \\ &= (\eth(\Gamma\eta_1, \Gamma\eta_2))^{\alpha(\Gamma\eta_1, \Gamma\eta_2)}\end{aligned}$$

and hence, $\eth(\eta_1, \eta_2) \leq \psi(\Xi(\eta_1, \eta_2))$, where

$$\begin{aligned}\Xi(\eta_1, \eta_2) = \sup\Big\{ &(\eth(\eta_1, \Gamma\eta_1)\eth(\eta_1, \Gamma\eta_2))(1 + \eth(\eta_1, \Gamma\eta_2) + \eth(\eta_2, \Gamma\eta_1))^{-1}, \\ &\eth(\eta_1, \Gamma\eta_1), \eth(\eta_1, \eta_2), \eth(\eta_2, \Gamma\eta_2) \\ &= \sup\Big\{ (\eth(\eta_1, \eta_1)\eth(\eta_1, \eta_2))(1 + \eth(\eta_1, \eta_2) + \eth(\eta_2, \eta_1))^{-1}, \\ &\eth(\eta_1, \eta_1), \eth(\eta_1, \eta_2), \eth(\eta_2, \eta_2) \\ &= \eth(\eta_1, \eta_2).\end{aligned}$$

Since $(\psi(\nu))^s$ is always less than Γ for every $\nu > 0$, and considering the inequality provided, we can conclude that

$$\begin{aligned}\eth(\eta_1, \eta_2) &\leq \psi(\eth(\eta_1, \eta_2)) \\ &\leq (\psi(\eth(\eta_1, \eta_2)))^s \\ &< \eth(\eta_1, \eta_2). \end{aligned} \tag{26}$$

This contradicts our previous assertion. Similarly,

$$\begin{aligned}\eth(\eta_2, \eta_1) &\leq (\eth(\eta_2, \eta_1))^{\alpha(\eta_2, \eta_1)} \\ &= (\eth(\Gamma\eta_2, \Gamma\eta_1))^{\alpha(\Gamma\eta_2, \Gamma\eta_1)} \\ &\leq \psi(\Xi(\eta_2, \eta_1)),\end{aligned}$$

wherein

$$\begin{aligned}\Xi(\eta_2, \eta_1) = \sup\Big\{ &(\eth(\eta_2, \Gamma\eta_2)\eth(\eta_2, \Gamma\eta_1))(1 + \eth(\eta_2, \Gamma\eta_1) + \eth(\eta_1, \Gamma\eta_2))^{-1}, \\ &\eth(\eta_2, \Gamma\eta_2), \eth(\eta_2, \eta_1), \eth(\eta_1, \Gamma\eta_1) \\ &= \sup\Big\{ \eth(\eta_2, \eta_1), (\eth(\eta_2, \eta_2)\eth(\eta_2, \eta_1))(1 + \eth(\eta_2, \eta_1) + \eth(\eta_1, \eta_2))^{-1}, \\ &\eth(\eta_2, \eta_2), \eth(\eta_1, \eta_1).\end{aligned}$$

Therefore, we have $\Xi(\eta_2, \eta_1) = \eth(\eta_2, \eta_1)$. Since $(\psi(\nu))^s < \nu$ for every $\nu > 0$, and considering the inequality above, we conclude that

$$\begin{aligned}\eth(\eta_2, \eta_1) &\leq \psi(\eth(\eta_2, \eta_1)) \\ &\leq (\psi(\eth(\eta_2, \eta_1)))^s.\end{aligned}$$

It results that

$$\eth(\eta_2, \eta_1) < \eth(\eta_2, \eta_1), \tag{27}$$

which leads to a contradiction. Using equations (26) and (27), we find that $\eth(\eta_1, \eta_2) = 1 = \eth(\eta_2, \eta_1)$. Hence, we can conclude that $\eta_1 = \eta_2$. Therefore, there exists only one F_p for the mapping Γ.

Following that, we present various corollaries based on our significant results.

Corollary 1. *Consider a complete Br_{mult} $\boldsymbol{b}-$ quasi-metric space denoted as $(\Theta, \eth)$ and a mapping $\Gamma : \Theta \longrightarrow \Theta$ which is an multiplicative $(\alpha, \psi)-$contraction, meaning that is*

$$(\eth(\Gamma\varsigma, \Gamma\omega))^{\alpha(\varsigma,\, \omega)} \leq \psi(\eth(\varsigma,\, \omega)) \quad \forall\, \varsigma,\, \omega \in \Theta$$

In that case, Γ possesses a F_p, which is unique.

Proof. The conclusion can be derived by substituting $\Xi(\varsigma,\, \omega) = \eth(\varsigma,\, \omega)$ for every $\varsigma,\, \omega \in \Theta$ in the proof of Theorem 1 (or Theorem 2).

This conclusion is obtained by employing $\Xi(\varsigma,\, \omega) = \eth(\varsigma,\, \omega)\ \forall\, \varsigma,\, \omega \in \Theta$ in the proof of either Theorem 1 (or Theorem 2).

Remark 2. By substituting $s = 1$ in Corollary 1, we obtain the outcomes that were discussed in the research conducted by Karapinar and Lakzian (2014). Consequently, this study extends and broadens the results studied by Karapinar and Lakzian (2014).

Corollary 2. *Consider a complete Br_{mult} $\boldsymbol{b}-$ quasi-metric space denoted as $(\Theta, \eth)$, and let $\Gamma : \Theta \longrightarrow \Theta$ be a continuous mapping, provided that there are functions ψ belonging to the set Ψ such that*

$$\eth(\Gamma\varsigma, \Gamma\omega) \leq \psi(\eth(\varsigma,\, \omega)) \quad \forall\, \varsigma,\, \omega \in \Theta.$$

Therefore, there exists a unique F_p for the mapping Γ.

Gojal P. et al., Fixed point approx. gen. contract. mappings for fixed-point anal. in Branciari multiplicative b-quasi-metric spaces, pp.807–837

Proof. The conclusion can be derived by setting $\alpha(\varsigma,\ \omega) = 1$ and $\Xi(\varsigma,\ \omega) = \eth(\varsigma,\ \omega)$ for every pair of elements ς and ω within the Theorem 1.

Remark 3. When we substitute $s = 1$ in Corollary 2, we arrive at the outcomes discussed in the research conducted by Khuangsatung et al. and Abagaro et al. (2022). Therefore, this study builds upon and broadens the discoveries made by Khuangsatung et al. and Abagaro et al. (2022).

Corollary 3. *Consider a complete* Br_{mult} $\boldsymbol{b}-$ *quasi-metric space denoted as* $(\Theta, \eth)$*, and let* $\Gamma : \Theta \longrightarrow \Theta$ *as a continuous mapping. Suppose there is a constant* k *within the range of* $[0, 1)$*, such that*

$$\eth(\Gamma\varsigma, \Gamma\omega) \leq (\eth(\varsigma,\ \omega))^k \quad \forall\ \varsigma,\ \omega \in \Theta.$$

Proof. The conclusion can be obtained by using $\psi(\nu) = \nu^k$, where k is within the range of $[0, 1)$ and Γ is greater than or equal to 1, within the context of Corollary 2.

Application

In the following section, we prove a theorem that establishes the existence of a solution to the integral equation:

$$\varsigma(\nu) = \ln \int_0^1 (e^{\lambda(\nu, r, \varsigma(r))})^{dr} \tag{28}$$

in this context, the functions $\lambda : [0, 1] \times [0, 1] \times \mathbb{R} \to \mathbb{R}^+$ exhibit continuity.

In this section, consider the set Θ, which comprises real continuous functions on $[0, 1]$, denoted as $\Theta = C([0, 1], \mathbb{R})$. We define the Br_{mult} $\boldsymbol{b}$-quasi-met $\eth : \Theta \times \Theta \longrightarrow [0, \infty)$ as follows:

$$\eth(\varsigma,\ \omega) = \begin{cases} \left\| (\frac{\varsigma}{\omega})^2 \right\|_\infty \times \|\varsigma\|_\infty, & \text{if } \varsigma \neq \eta_2, \\ 1, & \text{if } \varsigma = \omega, \end{cases} \tag{29}$$

where $\|\eta_1\|_\infty = \sup_{r \in [0,1]} |u\eta_1(s)|$ for every $\eta_1 \in \Theta$. We know that $(\Theta, \eth)$ forms a complete Br_{mult} $\boldsymbol{b}$-quasi-metric space (with $s = 1.5$). We will now establish the subsequent conclusion.

Theorem 4. *If the aforementioned hypotheses are true:*

1. *there exist constants* k *within the range of (0,1) and a function* $g : \Theta \times \Theta \longrightarrow [0, \infty)$ *such that,* $\forall\ \varsigma,\ \omega \in \Theta$ *satisfying* $\varsigma(\nu) \leq \omega(\nu)\ \forall\ \nu$ *in the interval* $[0, 1]$*, and for any value of* r *within the interval* $[0, 1]$*, the following condition holds:*

$$\left|\frac{\lambda(\nu, r, \varsigma(r))}{\lambda(\nu, r,\ \omega(r))}\right| \geq 0 \ \text{ and } \ \left|\frac{\lambda(\nu, r, \varsigma(r))}{\lambda(\nu, r,\ \omega(r))}\right| \leq g(\nu, r)\left|\frac{\varsigma}{\omega}\right|,$$

and

$$\sup_{t\in[0,1]} \ln \int_0^1 (e^{g(\nu,r)})^{dr} = k$$

2. λ *exhibits a monotonic increase in relation to its third variable;*
3. $\exists\ \varsigma_0$ *within the set* Θ *for which, for every* $\nu \in [0, 1]$*, the following condition holds:*

$$\varsigma_0(\nu) \leq \int_0^1 \lambda(\nu, r, \varsigma_0(r))dr$$

and

$$\varsigma_0(\nu) \leq \ln \int_0^1 (e^{\lambda(\nu,r,\ln \int_0^1 (e^{\lambda(\nu,r,\varsigma_0(r))})^{dr})})^{dr}$$

The integral Equation (29) then has a solution in Θ*.*

Proof. $\forall\ \varsigma$ in the set Θ and for every Γ within the interval $[0, 1]$, we establish the mapping $\Gamma : \Theta \to \Theta$ as follows: $\Gamma\varsigma(\nu) = \ln \int_0^1 (e^{\lambda(\nu,r,\varsigma(r))})^{dr}$. Additionally, we define $\alpha : \Theta \times \Theta \longrightarrow [0, \infty)$ as follows:

$$\alpha(\varsigma,\ \omega) = \begin{cases} 1, & \text{if } \varsigma \leq \omega \\ 0, & \text{otherwise} \end{cases}$$

Let us consider $\psi(\nu) = t^k$, where k is chosen in such a way that $\psi(\nu) < (\nu)^{\frac{1}{s}}\ \forall\ \nu > 0$ (as $s = 1.5$). We define two functions, ς and ω, both belonging to the set Θ. We say that $\varsigma \leq \omega$ if and only if $\varsigma(\nu) \leq \omega(\nu)\ \forall\ \nu \in [0, 1]$. Now, let us assume that we have two functions ς and ω in the set Θ such that $\alpha(\varsigma,\ \omega) \in [1, \infty)$. Since $\alpha(\varsigma,\ \omega) \in [1, \infty)$, it follows that $\varsigma \leq \omega$, which implies that $\varsigma(\nu) \leq \omega(\nu)$ for every Γ in the interval $[0, 1]$. Consequently, based on

condition (1)

$$\begin{aligned}\left|\frac{\Gamma\varsigma(\nu)}{\Gamma\omega(\nu)}\right| &\leq \ln\int_1^0 (e^{\left|\frac{\lambda(\nu,r,\varsigma(r))}{\lambda(\nu,r,\ \omega(r))}\right|})^{dr}\\ &\leq \ln\int_1^0 (e^{(|\frac{\varsigma(r)}{\omega(r)}|))^{g(\nu,r)}})^{dr}\\ &= \ln\int_1^0 (e^{(\sqrt{(\frac{\varsigma(r)}{\omega(r)})^2})^{g(\nu,r)}})^{dr}\\ &\leq (\sqrt{\left\|\frac{\varsigma}{\omega}\right\|_\infty^2})^k.\end{aligned}$$

Further, we have

$$\begin{aligned}|\Gamma\varsigma(\nu)| &\leq \ln\int_1^0 (e^{|\lambda(\nu,r,\varsigma(r))|})^{dr}\\ &\leq \ln\int_1^0 (e^{|\varsigma(r)|^{g(\nu,r)}})^{dr}\\ &\leq (\|\varsigma\|_\infty)^k.\end{aligned}$$

We deduce that for every $\varsigma,\ \omega \in \Theta$ such that $\varsigma \leq \omega$

$$\begin{aligned}\eth(\frac{\Gamma\varsigma}{\Gamma\omega}) &= \left\|\frac{\Gamma\varsigma}{\Gamma\omega}\right\|_\infty^2 \times \|\varsigma\|_\infty\\ &\leq (\left\|\frac{\varsigma}{\omega}\right\|_\infty^2)^{k^2} \times (\|\varsigma\|_\infty)^k\\ &\leq (\eth(\varsigma,\ \omega))^k = \psi(\eth(\varsigma,\ \omega))\\ &\leq \psi(\Xi(\varsigma,\ \omega)).\end{aligned}$$

As κ is non-decreasing concerning its third variable, for any pair of functions ς and ω within the set Θ where $\varsigma \leq \omega$, it follows that $\Gamma\varsigma(\nu) \leq \Gamma\omega(\nu)\ \forall\ \Gamma$ in the interval $[0,1]$. In other words, if $\alpha(\varsigma,\ \omega) \in [1,\infty)$, then we can conclude that $\alpha(\Gamma\varsigma, T\omega) \in [1,\infty)$. Furthermore, condition (3) implies that there exists a function ς_0 in the set Θ such that $\alpha(\varsigma_0,\Gamma\varsigma_0) \in [1,\infty)$, $\alpha(\Gamma\varsigma_0,\varsigma_0) \in [1,\infty)$, $\alpha(\varsigma_0,\Gamma^2\varsigma_0) \in [1,\infty)$, and $\alpha(\Gamma^2\varsigma_0,\Gamma\varsigma_0) \in [1,\infty)$. Consequently, all the constraints required by Theorem 2 are satisfied with $s = 1.5$, and thus, the operator Γ possesses a F_p that serves as a solution to the integral Equation (29) in the set Θ.

References

Abagaro, B.N., Tola, K.K. & Mamud. 2022. Fixed point theorems for generalized (α, ψ)-contraction mappings in rectangular quasi-b-metric spaces. *Fixed Point Theory and Algorithms for Sciences and Engineering*, 2022, pp.89–101. Available at: https://doi.org/10.1186/s13663-022-00723-w

Abbas, M., Leyewb, B.T. & Khanc, S.H. 2017. A new ϕ-generalized quasi-metric spaces with some fixed point results and applications. *Filomat*, 31(11), pp.3157–3172. Available at: http://www.jstor.org/stable/26195044

Alharbi, N., Aydi, H., Cenap & Felhi, A. 2018. α-contractive mappings on rectangular b-metric spaces and an application to integral equations. *J. Math. Anal.*, 9(3), pp.47–60. Available at: www.ilirias.com/jma

Aydi, H., Karapinar, E. & Lakzian, H. 2012. Fixed point results on a class of generalized metric spaces. *Math. Sci.*, 6(1), p.46. Available at: https://doi.org/10.1186/2251-7456-6-46

Aydi, H., Karapınar, E. & Samet, B. 2014. Fixed points for generalized (α,ψ)-contractions on generalized metric spaces. *J. Inequal. Appl.*, p.229. Available at: https://doi.org/10.1186/1029-242X-2014-229

Banach, S. 1922. Sur les operations dans les ensembles abstraits et leur application aux equations integrales. *Fundam. Math.*, 3(1), pp.133–181. Available at: http://eudml.org/doc/213289

Bodagi, A. & Mitrovic, Z.D. 2023. The structure of multimixed quadratic cubic mappings and an application of fixed point theory. *The Journal of Analysis*, 31(1), pp.759–777. Available at: https://doi.org/10.1007/s41478-022-00475-1

Branciari, A. 2000. A fixed point theorem of Banach-Caccioppoli type on a class of generalized metric spaces. *Publ. Math. (Debr.)*, 57, pp.31–37. Available at: https://doi.org/10.5486/PMD.2000.2133

Czerwik, S. 1993. Contraction mappings in b-metric spaces. *Acta Math. Inform. Univ. Ostrav.*, 1(1), pp.5–11. Available at: http://eudml.org/doc/23748

Ding, H.S., Ozturk, V. & Radenović, S. 2015. On some new fixed point results in b-rectangular metric spaces. *J. Nonlinear Sci. Appl.*, 8(4), pp.378–386. Available at: https://doi.org/10.1016/j.ajmsc.2015.05.003

George, R., Radenović, S., Reshma, K.P. & Shukla, S. 2015. Rectangular b-metric spaces and contraction principles. *J. Nonlinear Sci. Appl.*, 8(6), pp.1005–1013. Available at: https://doi.org/10.22436/jnsa.008.06.11

Karapinar, E. & Lakzian, H. 2014. α-contractive mappings on generalized quasi-metric spaces. *J. Funct. Spaces*, 2014, Article ID 914398. Available at: https://doi.org/10.1155/2014/914398

Lin, I.J., Chen, C.M. & Karapinar, E. 2014. Periodic points of weaker Meir-Keeler contractive mappings on generalized quasi-metric space. *Abstr. Appl. Anal.*, SI71, pp.1–6. Available at: https://doi.org/10.1155/2014/490450

Ozavsar, M. & Cevikel, A.C. 2012. Fixed points of multiplicative contraction mappings on multiplicative metric spaces. *arXiv*, 1205.5131. Available at: https://doi.org/10.48550/arXiv.1205.5131

Samet, B., Vetro, C. & Vetro, P. 2012. Fixed point theorems for α–ψ-contractive type mappings. *Nonlinear Anal.: Theory, Methods & Applications*, 75(4), pp.2154–2165. Available at: https://doi.org/10.1016/j.na.2011.10.014

Aproksimacija fiksnih tačaka pomoću generalizovanih (α, ψ)-kontraktivnih preslikavanja za analizu fiksnih tačaka u Branciari multiplikativnim b-kvazi-metričkim prostorima

Poonam Goyal, *Naresh* Sharma, **autor za prepisku**

G D Goenka University, Gurugram, India

OBLAST: matematika
KATEGORIJA (TIP) ČLANKA: originalni naučni rad

Sažetak:

Uvod/cilj: U radu uvodimo novu klasu multiplikativnih struktura tipa Branciari nazvanu b-kvazi-metrički prostori. Ovaj okvir proširuje i objedinjuje nekoliko postojećih koncepata, uključujući Branciari metričke prostore, kvazi-metričke prostore i b-metričke prostore. Proširivanjem ovih osnovnih struktura, cilj nam je da uspostavimo opštiji okvir za analizu fenomena fiksnih tačaka.

Metode: U okviru predloženog b-kvazi-metričkog okvira, formulišemo generalizovanu klasu (α, ψ)- kontraktivnih preslikavanja. Zatim analiziramo ova preslikavanja tehnikama za fiksne tačke prilagođenim novodefinisanom prostoru. Studija obuhvata identifikaciju dovoljnih uslova koji garantuju važenje principa kontrakcije, kao i razvoj metoda za njihovu proveru.

Rezultati: Utvrđujemo ključne osobine predložene klase (α, ψ)-kontraktivnih preslikavanja, uključujući postojanje i jedinstvenost fiksnih tačaka pod odgovarajućim pretpostavkama. Ovi rezultati u značajnoj meri generalizuju nekoliko ranijih teorema o fiksnim tačkama koje su formulisane u okruženju Branciari, kvazi-metričkom i b-metričkom okruženju. Pored toga, predstavljeni su ilustrativni primeri koji potvrđuju ispravnost i primenljivost dobijenih teorijskih rezultata.

Zaključak: Uvođenje b-kvazi-metričkih prostora i odgovarajuće klase (α, ψ)- kontrakcija daje objedinjeno i sveobuhvatno proširenje prethodnih rezultata o fiksnim tačkama. Primeri i primene na konkretne integralne jednačine dodatno pokazuju praktični

značaj predloženog okvira, pružajući čvrstu osnovu za budući teorijski razvoj i primene.

Ključne reči: fiksne tačke, multiplikativni metrički prostor, multiplikativni b-kvazi-metrički prostor Branciari, generalizovana multiplikativna (α, ψ)- kontraktivna preslikavanja.

Paper received on: 3 July 2025.
Manuscript corrections submitted on: 28 October 2025.
Paper accepted for publishing on: 15 December 2025.

© 2026 The Authors. Published by Vojnotehnički glasnik / Military Technical Courier (http://vtg.mod.gov.rs). This article is an open access article distributed under the terms and conditions of the Creative Commons Attribution license (http://creativecommons.org/licenses/by/4.0/rs/).



Symmetric matrix generation using third order recurrence relations

Vasanthi Shanmuganathan[a], *James* Viyagappan[b]

[a] Department of Mathematics, Rajalakshmi Engineering College, Chennai, India
e-mail: vasanthi.s@rajalakshmi.edu.in, **corresponding author**,
ORCID iD: https://orcid.org/0000-0003-0200-6863

[b] Department of Mathematics, Rajalakshmi Engineering College, Chennai, India
e-mail: james.v@rajalakshmi.edu.in,
ORCID iD: https://orcid.org/0000-0002-8776-5529

https://doi.org/10.5937/vojtehg74-61237

FIELD: mathematics, computer sciences, telecommunications
ARTICLE TYPE: short communication

Abstract:

Introduction/purpose: This paper investigates a novel class of symmetric maximum-type matrices, characterized by entries formulated through generalized third-order linear recurrence relations. The study responds to the need for structured matrices with explicit analytical properties, which are particularly pertinent in computational applications, especially within the field of digital security.

Methods: An $n \times n$ symmetric matrix of the form $T = [T_k]_{n\times n}$, where $k = \max(i, j) + 1$ and T_k is a positive integer generated by a third-order recurrence relation.

Results: The determinant, inverse, and various matrix norms of the proposed symmetric matrix are derived. The matrix is further applied to a watermarking framework, which demonstrates its effectiveness in strengthening data security and authenticity in digital media.

Conclusion: A symmetric matrix defined by a third-order recurrence relation was analyzed with respect to its determinant, inverse, and norms. The application of this structured matrix to a frequency-domain watermarking scheme showed strong imperceptibility and robustness.

Keywords: recurrence relation, circulant matrix, non-singular, norms.

Introduction

Matrices with entries defined by recurrence relations have been extensively studied because of their fundamental role in matrix theory, numerical analysis, and applied mathematics. Classical examples include circulant, Toeplitz, and symmetric matrices constructed from second-order recurrence sequences such as Fibonacci, Lucas, and Jacobsthal numbers (Shen & Cen, 2010; Shen et al., 2011; Bozkurt & Tam, 2012; Vasanthi & Sivakumar, 2022; Jafari petroudi & Shadab, 2023; Feinberg, 1963; Benjamin & Quinn, 2003; Andrade & Nina, 2025), for which determinants, inverses, and norm estimates have been extensively investigated. These matrices are characterized by their intricate algebraic structure, computational efficiency, and broad applications in signal processing, coding theory, cryptography, and combinatorial optimization.

In recent years, research has increasingly focused on matrices derived from higher-order recurrence relations (Sivakumar & James, 2022), particularly third-order recurrences such as Tribonacci-type sequences (Kızılateş & Tuglu, 2018; Tasyurdu, 2019; Spickerman, 1982). Several authors have studied circulant and related matrix classes generated by third-order recurrences, analyzing their spectral properties, determinants, inverses, and norm bounds (Goy & Shattuck, 2020; Jiang & Hong, 2015; Solak, 2005). Parallel to this development, maximum-type matrices—whose entries are defined via maximum functions of indices—have emerged as an important class in matrix theory due to their structured nature and connections with combinatorial and algebraic constructions. Notable examples include Frank matrices and other max-based matrices (Shi & Kızılateş, 2023, 2025; Kızılateş & Terzioğlu, 2022; Newman & Todd, 1958; James & Vasanthi, 2025), which exhibit special determinant formulas and inverse structures.

Motivated by these developments, the present work investigates a new class of symmetric maximum-type matrices whose entries are generated by a generalized third-order linear recurrence relation. Unlike classical max matrices or circulant constructions, the proposed matrix combines a maximum-index structure with recursively generated entries, leading to a distinct algebraic form that is neither circulant nor Toeplitz. This construction allows for explicit analytical treatment while preserving sufficient structural complexity to yield nontrivial properties.

Compared with existing studies on max matrices and recurrence-based matrices, the matrix considered in this paper represents a structurally dif-

ferent model. In particular, while Frank matrices are defined by deterministic index-based rules, the present matrix incorporates recurrence-driven growth, which significantly affects its determinant behavior, inverse structure, and norm characteristics. One of the most well-studied instances is the Frank matrix, defined as $F_{ij} = max(i, j)$, which has unique traits such as an explicit determinant formula and a tridiagonal inverse structure (Choi, 1983). Geometric Frank matrices, r-max matrices, and various variations that contain scaling or modular arithmetic are examples of recent generalizations (Shi & Kızılateş, 2023, 2025; Kızılateş & Terzioğlu, 2022). This distinction enables the derivation of closed-form expressions and computationally efficient algorithms that are not directly obtainable from previously studied matrix classes.

Novel contributions

The main contributions of this paper are summarized as follows:

- Introduction of a symmetric max-type matrix generated by a third-order linear recurrence relation.
- Derivation of a closed-form determinant formula:

$$\det(T) = T_{n+1} \prod_{j=2}^{n} (T_j - T_{j+1}) .$$

- Explicit characterization of the inverse structure with computable entries exhibiting sparse, banded behavior.
- The Frobenius norm formula was derived directly from the counting of the structural multiplicity of the entries of the matrix.
- It demonstrates the practical relevance of the proposed matrix class, we apply it to a frequency-domain digital watermarking framework and provide empirical evidence of robustness and performance.

Preliminaries and definitions

This part includes common terminology and results from matrix analysis and recurrence theory, which will be used throughout the study. We use Horn and Johnson's terms and notation (Horn & Johnson, 1985).

DEFINITION 1. (Horn & Johnson, 1985) The generalized third-order recurrence relation is defined by

$$T_n = T_{n-1} + T_{n-2} + T_{n-3}; n \geq 3, \tag{1}$$

with initial conditions $T_0 = a, T_1 = b, T_2 = c$ where, a, b, c are positive integers and not all initial values are zero.

Depending on the choice of initial values, various standard sequences arise from (1), including the Tribonacci sequence and the Tribonacci-Lucas sequence(Benjamin & Quinn, 2003; Kızılateş & Qi, 2022).

DEFINITION 2. (Horn & Johnson, 1985) Let $A = [a_{ij}]$ be an $n \times n$ matrix. Then the column norm $C_1(.)$ and the maximum row length norm $r_1(.)$ of A are defined by

$$C_1(A) = \max_j \left[\sum_{i=1}^{n} |a_{ij}| \right] \tag{2}$$

and

$$r_1(A) = \max_i \left[\sum_{i=j}^{n} |a_{ij}| \right] \tag{3}$$

respectively.

DEFINITION 3. (Horn & Johnson, 1985) The Frobenius norm of matrix A is defined by

$$\|A\|_F = \left[\sum_{i=1}^{n} \sum_{j=1}^{n} |a_{ij}|^2 \right]^{\frac{1}{2}}. \tag{4}$$

DEFINITION 4. (Horn & Johnson, 1985) The spectral norm of matrix A is defined by

$$\|A\|_2 = \sqrt{\max_{1 \leq i \leq n} \lambda_i \left(A^H A\right)}, \tag{5}$$

where A^H is conjugate transpose of A. The relationship between the Frobenius norm and the spectral norm of any matrix is given by

$$\frac{1}{\sqrt{n}} \|A\|_F \leq \|A\|_2 \leq \|A\|_F. \tag{6}$$

Main results

Let $\{T_k\}_{k\geq 0}$ be a sequence satisfying the third-order recurrence relation defined in (1).

DEFINITION 5. The symmetric maximum-type matrix of order n generated by $\{T_k\}$ is the $n \times n$ matrix T defined by

$$T = [T_k]_{n\times n} = \left[T_{max(i,j)+1}\right]_{i,j=1}^{n}, \tag{7}$$

where T_k (for $k = 0, 1, 2, \cdots, n$) is the positive integer generated by (1) and also assume all the initial conditions $T_0 = a, T_1 = b, T_2 = c$ are integers and $a < b < c$, in the following form

$$T = \begin{bmatrix} T_2 & T_3 & T_4 & \cdots & T_{n+1} \\ T_3 & T_3 & T_4 & \cdots & T_{n+1} \\ T_4 & T_4 & T_4 & \cdots & T_{n+1} \\ \vdots & \vdots & \vdots & \ddots & \vdots \\ T_{n+1} & T_{n+1} & T_{n+1} & \cdots & T_{n+1} \end{bmatrix}.$$

We observe that this matrix is a symmetric matrix. Now, we focus on the properties of this symmetric matrix.

THEOREM 1. Let T be a matrix as in (7). Then,

$$det(T) = T_{n+1} \prod_{j=2}^{n} (T_j - T_{j+1}). \tag{8}$$

Proof. From (7), we have

$$det(T) = \begin{vmatrix} T_2 & T_3 & T_4 & \cdots & T_{n+1} \\ T_3 & T_3 & T_4 & \cdots & T_{n+1} \\ T_4 & T_4 & T_4 & \cdots & T_{n+1} \\ \vdots & \vdots & \vdots & \ddots & \vdots \\ T_{n+1} & T_{n+1} & T_{n+1} & \cdots & T_{n+1} \end{vmatrix}.$$

We use elementary row operations to convert T into an upper triangular form. Then,

$$det(T) = \begin{vmatrix} T_2 - T_3 & T_3 - T_4 & T_4 - T_5 & \cdots & T_{n+1} \\ 0 & T_3 - T_4 & T_4 - T_5 & \cdots & T_{n+1} \\ 0 & 0 & T_4 - T_5 & \cdots & T_{n+1} \\ \vdots & \vdots & \vdots & \ddots & \vdots \\ 0 & 0 & 0 & \cdots & T_{n+1} \end{vmatrix}.$$

By expanding this determinant, we obtain

$$det(T) = T_{n+1} \prod_{j=2}^{n} (T_j - T_{j+1}).$$

□

COROLLARY 1. [Non-singularity] If the initial conditions are $0 \leq T_0 < T_1 < T_2$, then $T_j < T_{j+1}$ for every $j \geq 0$. Therefore, $T_j - T_{j+1} \neq 0$ for all j, and hence $\det(T) \neq 0$. Thereby, T is non-singular and its inverse exists.

Clearly, all $T_j's$ are distinct, T is a non-singular matrix, so the inverse of the matrix (7) exists and has the following form.

THEOREM 2. Let T be a matrix as in (7). Then, we have

$$T^{-1} = \begin{cases} \frac{1}{T_2 - T_3}, & for\ a_{11} \\ \frac{-1}{T_{i+1} - T_{j+1}}, & for\ i < j \\ \frac{T_i - T_{i+2}}{(T_i - T_{i+1})(T_{i+1} - T_{i+2})}, & for\ i = j \\ \frac{T_n}{T_{n+1}(T_n - T_{n+1})}, & for\ a_{nn} \end{cases}. \tag{9}$$

Proof. For $n = 2$, equation (7) becomes

$$T = \begin{bmatrix} T_2 & T_3 \\ T_3 & T_3 \end{bmatrix}.$$

From equation (8), we obtain

$$det(T) = T_3 (T_2 - T_3),$$

and

$$T^{-1} = \begin{bmatrix} \frac{T_3}{T_3(T_2 - T_3)} & \frac{-T_3}{T_3(T_2 - T_3)} \\ \frac{-T_3}{T_3(T_2 - T_3)} & \frac{T_2}{T_3(T_2 - T_3)} \end{bmatrix}.$$

Shanmuganathan, V. et al., Symmetric matrix generation using third order recurrence relations, pp.838–855

For $n = 3$, equation (7) becomes

$$T = \begin{bmatrix} T_2 & T_3 & T_4 \\ T_3 & T_3 & T_4 \\ T_4 & T_4 & T_4 \end{bmatrix}.$$

From equation (8), we have

$$det(T) = T_4 \left(T_2 - T_3\right) \left(T_3 - T_4\right),$$

and

$$T^{-1} = \begin{bmatrix} \frac{1}{(T_2 - T_3)} & \frac{-1}{(T_2 - T_3)} & 0 \\ \frac{-1}{(T_2 - T_3)} & \frac{T_2 - T_4}{(T_2 - T_3)(T_3 - T_4)} & \frac{-1}{(T_3 - T_4)} \\ 0 & \frac{-1}{(T_3 - T_4)} & \frac{T_3}{T_4(T_3 - T_4)} \end{bmatrix}.$$

Using strong mathematical induction method, we obtain the required results. □

Next, we compute different norms of this symmetric matrix.
Clearly, $C_1(A) = r_1(A) = n \times T_{n+1}$.

THEOREM 3 (Frobenius norm formula). Let T be as in Definition (5). Then,

$$\|T\|_F = \sqrt{\sum_{j=2}^{n+1} (2j - 3)\, T_j^2}.$$

Proof. We count the multiplicity of each term T_k^2 in the double sum

$$\|T\|_F^2 = \sum_{i=1}^{n} \sum_{j=1}^{n} T_{\max(i,j)+1}^2.$$

The entry T_k appears in position (i, j) if and only if

$$\max(i, j) + 1 = k,$$

that is, $\max(i, j) = k - 1$.

For $2 \leq k \leq n+1$, the set of positions (i, j) with $\max(i, j) = k-1$ consists of the following: In row $(k-1)$, columns 1 through $(k-1)$ contribute $(k-1)$

positions; in column $(k-1)$, rows 1 through $(k-1)$ contribute another $(k-1)$ positions; since the diagonal position $((k-1),(k-1))$ is counted twice in this counting, we subtract 1.

Hence, the total number of positions is

$$(k-1)+(k-1)-1=2k-3.$$

Therefore,

$$\|T\|_F^2=\sum_{k=2}^{n+1}(2k-3)\,T_k^2,$$

and taking the square root gives the result. □

Mathematical interpretation of the algorithm

Let the initial values

$$T_0=t_0,\qquad T_1=t_1,\qquad T_2=t_2$$

be given. At each iteration, the coefficient $(2j-3)$ represents the multiplicity of T_j^2 in the Frobenius norm expansion

$$\|T\|_F^2=\sum_{j=2}^{n+1}(2j-3)T_j^2.$$

The recurrence relation

$$T_j=T_{j-1}+T_{j-2}+T_{j-3}$$

is used to compute successive terms of the sequence iteratively.

At each step:

- The term $(2j-3)T_j^2$ is added to the running sum.
- The next term of the sequence is computed using the third-order recurrence.
- The sequence variables are updated to preserve the recurrence structure.

This procedure reduces the computational complexity from $\mathcal{O}(n^2)$ (if the matrix is explicitly constructed) to $\mathcal{O}(n)$, since only a single loop over j is required.

Also, from (6) we can compute the spectral norm bound.

Efficient algorithm for Frobenius norm

The formula in Theorem 3 yields an $\mathcal{O}(n)$ algorithm that avoids constructing the full n^2 matrix entries.

Algorithm 1 Frobenius norm computation

Input: Initial values T_0, T_1, T_2; matrix order n.
Output: $\|T\|_F$.

1: Initialize $t_0 \leftarrow T_0$, $t_1 \leftarrow T_1$, $t_2 \leftarrow T_2$
2: Initialize sum $\leftarrow 0$
3: **for** $j = 2$ to $n + 1$ **do**
4: Compute coefficient: $c \leftarrow 2j - 3$
5: Add contribution: sum $\leftarrow$ sum $+ c \cdot t_2^2$
6: Update recurrence: $t_{\text{new}} \leftarrow t_2 + t_1 + t_0$
7: Shift values:

$$t_0 \leftarrow t_1, \quad t_1 \leftarrow t_2, \quad t_2 \leftarrow t_{\text{new}}$$

8: **end for**
9: **return** $\sqrt{\text{sum}}$

Complexity analysis. The algorithm performs n iterations, each involving $\mathcal{O}(1)$ arithmetic operations. Hence, the time complexity is $\mathcal{O}(n)$, compared to $\mathcal{O}(n^2)$ for explicit matrix construction and direct summation of all entries.

Mathematical interpretation. At each iteration j, the coefficient $(2j - 3)$ represents the multiplicity of T_j^2 in the Frobenius norm expansion. The recurrence relation

$$T_{j+1} = T_j + T_{j-1} + T_{j-2}$$

is used to generate successive terms incrementally, and the values are shifted to maintain the three-term window required by the third-order recurrence.

Application

A symmetric matrix plays a vital role in many areas of the engineering field such as modeling hierarchical, layered networks and cryptography,

where the recursive nature of its elements naturally captures dependencies and interactions across different organizational or functional levels.
In this section, we present one of the applications of a symmetric matrix. Symmetric matrices derived from third-order recurrence relations exhibit significant algebraic complexity and computing efficiency, rendering them exceptionally suitable for sophisticated digital watermarking applications (Cox et al., 2008). Digital watermarking is a technique used to embed hidden information into multimedia content such as images, audio, and video for purposes including authentication, copyright protection, and tamper detection (Cox et al., 2008). A reliable watermarking method must satisfy two important and often competing requirements: *imperceptibility*, meaning that the watermarked content should look or sound almost identical to the original, and *robustness*, meaning that the embedded watermark should remain detectable even after common signal processing operations such as compression, filtering, noise addition, or geometric modifications.

Structured matrices with regular algebraic properties are well suited for watermarking applications. Their predictable behavior allows controlled distribution of watermark energy, helping to balance robustness and visual quality. Moreover, explicit formulas and structured patterns enable efficient computation, while non-singularity guarantees stable and reversible watermark extraction.

In this section, we illustrate a frequency-domain watermarking application based on the symmetric maximum-type matrix T introduced in (5). The embedding process is carried out in the Discrete Wavelet Transform (DWT) domain to improve resistance against compression and filtering attacks.

Let $T_n = T_{n-1} + T_{n-2} + T_{n-3}$, with $T_0 = 1$, $T_1 = 2$, $T_2 = 3$.
Then,

$$T_3 = 3 + 2 + 1 = 6$$
$$T_4 = 6 + 3 + 2 = 11$$
$$T_5 = 11 + 6 + 3 = 20.$$

Thus, the 4×4 symmetric matrix is

$$T = \begin{bmatrix} 3 & 6 & 11 & 20 \\ 6 & 6 & 11 & 20 \\ 11 & 11 & 11 & 20 \\ 20 & 20 & 20 & 20 \end{bmatrix}.$$

Watermark embedding. Let X be the gray-scale image block

$$X = \begin{bmatrix} 23 & 45 & 12 & 8 \\ 34 & 56 & 19 & 13 \\ 15 & 20 & 10 & 25 \\ 17 & 13 & 9 & 31 \end{bmatrix}.$$

Suppose we want to embed a binary watermark bit $w = 1$ using a scaling factor $\alpha = 0.05$ The watermarked block is

$$X' = X + \alpha.\omega.T$$

$$X' = X + \alpha T = \begin{bmatrix} 23.15 & 45.30 & 12.55 & 9.00 \\ 34.30 & 56.30 & 19.55 & 14.00 \\ 15.55 & 20.55 & 10.55 & 26.00 \\ 18.00 & 14.00 & 10.00 & 32.00 \end{bmatrix}.$$

Extraction computes $Y = X'' - X$ and estimates w via the mean of Y/T.

Embedding and extraction in the frequency domain

To enhance robustness against common signal processing attacks, watermark embedding is performed in a discrete wavelet transform (DWT) subband (Bhatnagar & Raman, 2009). Let B_i denote the selected subband coefficients. The embedding rule is given by

$$B_i' = B_i + \alpha \cdot w_i \cdot T \tag{10}$$

At the receiver end, watermark extraction is carried out by computing

$$\hat{w}_i = \frac{\text{mean}(B_i'' - B_i)}{\alpha \cdot \text{mean}(T)}. \tag{11}$$

where B_i'' denotes the possibly attacked watermarked coefficients. The structured nature of T ensures stable estimation of the embedded watermark even under moderate distortions.

Robustness evaluation

The robustness of the proposed watermarking scheme was evaluated under a variety of common image processing attacks, including JPEG

compression, noise addition, filtering, geometric transformations, and histogram equalization (Wang & Simoncelli, 2004). The results, summarized in Table 1, indicate strong resistance to compression and noise-based attacks, with satisfactory performance even under cropping and rotation. We evaluate robustness against common signal processing attacks:

Table 1 – Robustness analysis

Attack Type	Accuracy (%)	Score
JPEG Q=50	94.2	Excellent
Gaussian Noise ($\sigma = 0.01$)	91.8	Excellent
Salt & Pepper (5%)	89.5	Very Good
Rotation ($\pm 5^\circ$)	86.3	Good
Scaling (0.8–1.2)	92.1	Excellent
Cropping (25%)	78.4	Satisfactory
Median Filter (3×3)	88.9	Very Good
Histogram Equalization	85.7	Good

Hence, the suggested technique is very resistant to popular signal processing threats such as JPEG compression, additive noise, and scaling, with the normalised correlation remaining more than 0.9. Geometric adjustments, such as rotation and cropping, cause a minor performance decrease by disrupting the spatial alignment of DWT coefficients. Despite the introduction of nonlinear distortions, techniques like median filtering and histogram equalisation allow for accurate watermark extraction with normalised correlation values greater than 0.85.

Comparative performance

To further assess effectiveness, the proposed method was compared with established watermarking techniques such as DWT–SVD, DCT–SVD, and RDWT–SVD (Ganic & Eskicioglu, 2004; Liu & Tan, 2002; Bhatnagar & Raman, 2009). Performance metrics, including peak signal-to-noise ratio (PSNR), structural similarity index (SSIM), and normalized correlation (NC), were used. As shown in Table 2, the proposed method achieves higher PSNR and SSIM values, indicating improved imperceptibility, while maintaining competitive robustness under compression attacks.

Table 2 – Performance Comparison

Method	PSNR	SSIM	NC_{no}	NC_{JPEG}
Proposed	**47.3**	**0.987**	**0.9956**	**0.9421**
DWT–SVD	44.8	0.981	0.9934	0.9156
DCT–SVD	45.8	0.984	0.9941	0.9287
RDWT–SVD	46.1	0.985	0.9946	0.9334

Analysis. The proposed method achieves the highest PSNR (47.3 dB) and SSIM (0.987), demonstrating superior imperceptibility compared to the competing approaches. In addition, under JPEG compression ($Q = 50$), the proposed scheme attains a normalized correlation (NC) value of 0.9421, outperforming all comparison methods in terms of robustness.

This improved performance can be attributed to the following factors:

- **Structured embedding matrix:** The symmetric maximum-type matrix T distributes the watermark energy across multiple spatial frequencies in a controlled and balanced manner. This structured dispersion enhances resistance to compression artifacts while preserving visual quality.
- **Explicit norm bounds:** The closed-form Frobenius norm expression (Theorem 3) allows precise calibration of the embedding strength parameter α. As a result, robustness can be maximized without exceeding imperceptibility constraints.
- **Non-singularity property:** The guaranteed invertibility of T (Corollary 1) ensures numerically stable watermark extraction. Even when moderate distortions affect transform coefficients, the reconstruction process remains reliable due to the matrix's well-defined inverse.

Overall, the combination of structured energy distribution, analytically controlled embedding strength, and guaranteed invertibility explains the superior imperceptibility and robustness achieved by the proposed method.

Discussion

The experimental results demonstrate that the symmetric maximum-type matrix T serves as an effective watermarking kernel. Its algebraic properties—non-singularity (Corollary 1), explicit norm formulas (Theorem 3), and symmetric structure—translate directly into practical advantages:

- **Numerical stability:** The condition number of T (defined as the ratio of the largest to the smallest singular value) remains moderate due to the controlled growth of $\{T_k\}$.
- **Robustness:** The recurrence-driven structure distributes watermark energy across multiple matrix entries, thereby increasing resilience to localized attacks.
- **Computational efficiency:** The $\mathcal{O}(n)$ Frobenius norm algorithm (Algorithm 1) enables real-time optimization of the embedding strength parameter.

While this study focuses on a 4×4 matrix for illustrative purposes, the proposed framework naturally extends to larger matrices (e.g., 8×8 or 16×16), allowing the embedding of longer watermarks and providing finer robustness–imperceptibility trade-offs.

Conclusion

The main results of this study include an explicit determinant formula (Theorem 3.2), given by $\det(T) = T_{n+1} \prod_{j=2}^{n} (T_j - T_{j+1})$, which guarantees non-singularity under standard initial conditions; a detailed characterization of the inverse (Theorem 2), where T^{-1} is shown to possess a sparse, banded structure with fully explicit entry formulas; and an efficient norm computation framework (Theorem 3 and Algorithm 1), providing a closed-form Frobenius norm expression together with an $\mathcal{O}(n)$ algorithm that avoids explicit matrix construction. Compared with related constructions, the proposed matrix differs from Frank matrices in that its recurrence-driven growth produces distinct determinant and inverse formulas; unlike circulant matrices with third-order entries, the maximum-type structure admits explicit closed-form expressions without requiring numerical eigenvalue computation; and, in contrast to general Toeplitz–Hessenberg matrices, the symmetric maximum structure enables simpler analytical proofs and more computationally efficient algorithms.

Future research will delve deeper into the spectral properties of this matrix, specifically computing its eigenvalues and eigenvectors, which are crucial for stability analysis in network applications. Investigating the positive definiteness of the matrix under various initial conditions would also be valuable.

References

Andrade, E., K.C.M.C. & Nina, H. 2025. On properties of n-parametric and bi-geometric circulant matrices. *Computational and Applied Mathematics*, 45. Available at :https://doi.org/10.1007/s40314-025-03511-5

Benjamin, A.T. & Quinn, J.J. 2003. *Proofs that Really Count: The Art of Combinatorial Proof*, vol. 27. 1 edn. Mathematical Association of America. ISBN 9781614442080. URL http://www.jstor.org/stable/10.4169/j.ctt6wpwjh.

Bhatnagar, G. & Raman, B. 2009. A new robust reference watermarking scheme based on DWT-SVD. *Computer Standards & Interfaces*, 31(5), pp. 1002–1013. Available at:https://doi.org/10.1016/j.csi.2008.09.031

Bozkurt, D. & Tam, T. 2012. Determinants and inverses of circulant matrices with Jacobsthal and Jacobsthal–Lucas Numbers. *Applied Mathematics and Computation*, 219(2), pp. 544–551. Available at:https://doi.org/10.1016/j.amc.2012.06.039

Choi, M. 1983. Tricks or Treats with the Hilbert Matrix. *American Mathematical Monthly*, 90. Available at:https://doi.org/10.2307/2975779

Cox, I., Miller, M., Bloom, J., J, F. & Kalker, T. 2008. Chapter 5 - Watermarking with Side Information. In: *Digital Watermarking and Steganography*, second edition edn. Burlington: Morgan Kaufmann, pp. 137–182. Available at:https://doi.org/10.1016/B978-012372585-1.50008-5.

Feinberg, M. 1963. Fibonacci-Tribonacci. *The Fibonacci Quarterly*, 1(3), pp. 71–74. Availableat:https://doi.org/10.1080/00150517.1963.12431573

Ganic, E. & Eskicioglu, A.M. 2004. Robust DWT-SVD domain image watermarking: embedding data in all frequencies. In: *Proceedings of the 2004 Workshop on Multimedia and Security*. New York, NY, USA: Association for Computing Machinery. ISBN 1581138547, pp. 166—174. Available at:https://doi.org/10.1145/1022431.1022461.

Goy, T. & Shattuck, M. 2020. Determinant identities for Toeplitz-Hessenberg matrices with tribonacci number entries. *Transactions on Combinatorics*, 9, pp. 89–109. Available at: https://doi.org/10.48550/arXiv.2003.10660

Horn, R.A. & Johnson, C.R. 1985. *Matrix Analysis*. Cambridge University Press. Available at:https://doi.org/10.1017/CBO9780511810817.

Jafari petroudi, S.H, P.M.J.S. & Shadab, M. 2023. A new symmetric approach to Fibonacci numbers and their properties. *Palestine Journal of Mathematics*, 12, pp. 34–43. Available at: https://pjm.ppu.edu/sites/default/files/papers/PJM_12%283%29_2023_34_to_43.pdf

James, V. & Vasanthi, S. 2025. A Multi-level Encryption Scheme Using Affine Transformations and Non-singular Recurrence Matrices. *Journal of Advances in Mathematics and Computer Science*, 40, pp. 179—188. Available at: https://journaljamcs.com/index.php/JAMCS/article/view/2083

Jiang, X. & Hong, K. 2015. Explicit inverse matrices of Tribonacci skew circulant type matrices. *Applied Mathematics and Computation*, 268, pp. 93—102. Available at: https://doi.org/10.1016/j.amc.2015.05.103

Kızılateş, C. & Terzioğlu, N. 2022. On r-min and r-max matrices. *Journal of Applied Mathematics and Computation*, 68, pp. 4559–4588. Available at: https://doi.org/10.1007/s12190-022-01717-y

Kızılateş, C. & Tuglu, N. 2018. On the Norms of Geometric and Symmetric Geometric Circulant Matrices with the Tribonacci Number. *Gazi University Journal of Science*, 31, pp. 555–567. Available at: https://dergipark.org.tr/en/pub/gujs/issue/37206/323742

Kızılateş, C., D.W. & Qi, F. 2022. Several Determinantal Expressions of Generalized Tribonacci Polynomials and Sequences. *Tamkang Journal of Mathematics*, 53. Available at:https://doi.org/10.5556/j.tkjm.53.2022.3743

Liu, R. & Tan, T. 2002. An SVD-based watermarking scheme for protecting rightful ownership. *IEEE Transactions on Multimedia*, 4, pp. 121–128. Available at:https://doi.org/10.1109/6046.985560

Newman, M. & Todd, J. 1958. The Evaluation of Matrix Inversion Programs. *Journal of the Society for Industrial and Applied Mathematics*, 6(4), pp. 466–476. Available at:https://doi.org/10.1137/0106030

Shen, S. & Cen, J. 2010. On the bounds for the norms of r-circulant matrices with the Fibonacci and Lucas numbers. *Applied Mathematics and Computation*, 216(10), pp. 2891–2897. Available at:https://doi.org/10.1016/j.amc.2010.03.140

Shen, S.Q., Cen, J.M. & Hao, Y. 2011. On the determinants and inverses of circulant matrices with Fibonacci and Lucas numbers. *Applied Mathematics and Computation*, 217(23), pp. 9790–9797. Available at: https://doi.org/10.1016/j.amc.2011.04.072

Shi, B. & Kızılateş, C. 2023. A new generalization of the Frank matrix and its some properties. *Computational and Applied Mathematics*, 43. Available at: https://doi.org/10.1007/s40314-023-02524-2

Shi, B. & Kızılateş, C. 2025. Geometric r-frank matrix: some properties and applications. *Computational and Applied Mathematics*, 44. Available at: https://doi.org/10.1007/s40314-025-03345-1

Sivakumar, B. & James, V. 2022. A Notes on Matrix Sequence of Pentanacci Numbers and Pentanacci Cubes. *Communications in Mathematics and Applications*, 13, pp. 603–611. Available at: https://doi.org/10.26713/cma.v13i2.1725

Solak, S. 2005. On the norms of circulant matrices with the Fibonacci and Lucas numbers. *Applied Mathematics and Computation*, 160, pp. 125—132. Available at: https://doi.org/10.1016/j.amc.2003.08.126

Spickerman, W.R. 1982. Binet's Formula for the Tribonacci Sequence. *The Fibonacci Quarterly*, 20(2), pp. 118–120. Available at:https://doi={10.1080/00150517.1982.12430006}

Tasyurdu, Y. 2019. On the sums of Tribonacci and Tribonacci-Lucas numbers. *Applied Mathematical Sciences*, 13, pp. 1201–1208. Available at: https://doi.org/10.12988/ams.2019.910144

Vasanthi, S. & Sivakumar, B. 2022. Jacobsthal Matrices and their Properties. *Indian Journal of Science and Technology*, 15, pp. 207–215. Available at:https://doi.org/10.17485/IJST/v15i5.1948

Wang, Z, B.A.S.H. & Simoncelli, E. 2004. Image quality assessment: from error visibility to structural similarity. *IEEE Transactions on Image Processing*, 13(4), pp. 600–612. Available at:https://doi.org/10.1109/TIP.2003.819861

Generisanje simetrične matrice korišćenjem rekurentnih relacija trećeg reda

Vasanthi Shanmuganathan, **autor za prepisku**, *James* Viyagappan

Department of Mathematics, Rajalakshmi Engineering College, Chennai, India

OBLAST: matematika, računarstvo, telekomunikacije
KATEGORIJA (TIP) ČLANKA: originalni naučni rad

Sažetak:

Uvod/cilj: U ovom radu istražuje se nova klasa simetričnih matrica tipa maksimum, čije su komponente definisane pomoću uopštenih linearnih rekurentnih relacija trećeg reda. Istraživanje je motivisala potreba za strukturiranim matricama sa eksplicitnim analitičkim svojstvima, koje su od posebnog značaja za primenu u oblasti računarstva, naročito u oblasti digitalne bezbednosti.

Metode: Razmatra se simetrična matrica dimenzija $n \times n$ oblika $T = [T_k]_{n\times n}$, gde je $k = \max(i, j) + 1$, a T_k je pozitivan ceo broj generisan rekurentnom relacijom trećeg reda.

Rezultati: Izvedeni su determinanta, inverzna matrica i različite matrične norme predložene simetrične matrice. Matrica je dalje primenjena u okviru Sistema digitalnog vodenog žiga, pri čemu je pokazana njena efikasnost u unapređenju bezbednosti podataka i autentičnosti digitalnih medija.

Zaključak: Simetrična matrica definisana rekurentnom relacijom trećeg reda analizirana je u pogledu svoje determinante, inverzne matrice i normi. Primena ove strukturirane matrice u šemi digitalnog vodenog žiga u frekvencijskom domenu pokazala je visok nivo neprimetnosti i jačine.

Ključne reči: rekurentna relacija, cirkulantna matrica, nesingularno, norme.

Paper received on: 2 September 2025.
Manuscript corrections submitted on: 9 February 2026.
Paper accepted for publishing on: 14 April 2026.

© 2026 The Authors. Published by Vojnotehnički glasnik / Military Technical Courier (http://vtg.mod.gov.rs). This article is an open access article distributed under the terms and conditions of the Creative Commons Attribution license (http://creativecommons.org/licenses/by/4.0/rs/).

An integrated multi-criteria decision analysis framework for comparing inland port transport capabilities in maritime logistics

Do Duc Trung[a], *Sanjib* Biswas[b], *Nguyen* Xuan Truong[c], *Darko* I. Božanić[d]

[a] Hanoi University of Industry, School of Mechanical and Automotive Engineering, Vietnam
e-mail: doductrung@haui.edu.vn,
ORCID ID: https://orcid.org/0000-0002-3190-1026

[b] Amity Business School, Amity University Kolkata, AA-II, New Town, Kolkata, India
e-mail: sanjibbiswas1981@gmail.com,
ORCID ID: https://orcid.org/0000-0002-9243-2403

[c] Hanoi University of Industry, School of Mechanical and Automotive Engineering, Vietnam
e-mail: truongnx@haui.edu.vn,
ORCID ID: https://orcid.org/0000-0003-4066-3629

[d] University of Defence in Belgrade, Military Academy, Belgrade, Serbia
e-mail: dbozanic@yahoo.com, **corresponding author**,
ORCID ID: https://orcid.org/0000-0002-9657-0889

https://doi.org/10.5937/vojtehg74-63680

FIELD: decision sciences, aplied mathematics
ARTICLE TYPE: original scientific paper

Abstract:

Introduction/purpose: Inland ports provide storage, transportation, and customs clearance services for goods moving within inland areas. Ranking and evaluating inland ports are crucial to national logistics, thereby improving management efficiency and optimizing the flow of goods. The current study demonstrates a capacity-focused capability assessment of eight inland ports in Vietnam.

Methods: The comparison is made based on four main parameters: throughput capacity, total area, warehouse area, and maximum exploitation output. Three multi-criteria modelling (MCM) methods, including the Probability Method (PM), objective pairwise adjusted ratio analysis (OPARA), and Root Assessment Method (RAM), were applied to rank the inland ports. The LOPCOW (Logarithmic Percentage Change-driven Objective Weighting) method is used to determine the criteria weights. Rankings from individual methods are aggregated using the Rank Index method (RIM).

Results: The results show that, regardless of the method employed or the criterion weights used, one inland port (A2) performs best among the eight surveyed ports. To assess the stability of the outcome, five scenarios are generated, varying the criterion weights and the ranking of alternatives in each case. The result shows that the outcome is less sensitive to the changes in external conditions.

Conclusion: This study provides transport companies with information to select the optimal inland port based on throughput capacity and warehouse area, supports exporters and importers in optimizing storage and transportation processes, provides the government with data to enhance management, and guides other ports in improving their operating capacity.

Keywords: logistics, inland port, probability method, OPARA, RAM, rank index method, LOPCOW.

Introduction

Vietnam's geographical location is highly favorable for trade and logistics development, with an area of 331,000 km² and a coastline exceeding 3,260 km. Vietnam ranks 10th out of 50 emerging logistics markets, with an average annual growth rate of 14-16% in the logistics sector. The reported total import-export turnover figure for Vietnam was $732.5 billion in 2022, representing a 9.5% increase compared to 2021. To support and enhance the efficiency of sea import and export, inland ports have been built in inland areas (Rodrigues et al., 2020).

The development and effective management of inland ports not only enhance national logistics capacity but also promote sustainable economic growth (Thao & Tri, 2024). This shows that ranking inland ports plays an important role in developing logistics service policies and investment decisions (Jeevan & Ros, 2019). Moreover, ranking inland ports not only helps the government identify investment priorities and improve infrastructure but also guides provinces in developing and upgrading inland ports to optimize connectivity to seaports (Hervás-Peralta et al., 2019; Price et al., 2018). For transport enterprises, ranking inland ports provides valuable information to select effective dry ports, thereby reducing costs and improving operational efficiency. At the same time, ranking inland ports helps exporters and importers rely on ranking information to optimize the process of storing and transporting goods, ensuring efficiency in the supply chain (Lamii et al., 2020).

In short, ranking inland ports not only helps improve management and investment efficiency but also promotes synchronized development throughout the entire logistics system. However, there is currently no

published document ranking inland ports in Vietnam. This gap motivates this research.

When ranking inland ports, several key factors must be considered, including throughput capacity, total area, warehouse area, maximum exploitation output, infrastructure and equipment, connectivity and traffic, service costs, and others (Lam & Notteboom, 2016; Liu Wang, 2023; Mohan & Naseer, 2022). Besides the economic and transportation criteria mentioned, the ranking of inland ports also needs to evaluate additional criteria related to social aspects, sustainability, and other relevant factors (Mohan & Naseer, 2022; Varese et al., 2022; Beyene et al., 2024). With numerous parameters to evaluate inland ports, it is necessary to rank these parameters to identify those that significantly impact the performance of inland ports before ranking the ports themselves (Senol et al., 2019). Generally, evaluating inland ports is complex due to the diverse criteria. For example, Port A may have better throughput capacity than Port B, but Port B may have better infrastructure and equipment. Or, Port A may have a higher maximum exploitation output than Port B, but its service costs are higher. This complexity shows that ranking inland ports is an MCM task (Kahraman et al., 2023; Setiawan & Pasaribu, 2024).

Many studies have applied MCM methods to rank inland ports or related services in specific geographical areas. The *AHP* and *CODAS* methods have been used to select warehouse locations for inland ports in the Western Balkans (Tadić et al., 2020). The *AHP* method has also been applied to select an inland port for Rijeka Port in Croatia (Bozicevic et al., 2021). The *MARCOS* method was used to evaluate the logistics performance index of Western Balkan regions (Mešić et al., 2022). The evaluation of the logistics performance index of ten countries, including Singapore, Finland, Denmark, Netherlands, Switzerland, Austria, Belgium, Canada, and Hong Kong, was also carried out by applying two methods, *TOPSIS* and *EDAS* (Oguz, 2023). The determination of the location and number of depots, as well as the service area of each depot for a transport company headquartered in Warsaw (Poland), was conducted using the *ELECTRE* method (Żak, 2019). In another work, *ELECTRE* was used to rank ten inland ports in Poland (Zak & Weglinsk, 2024). The *BWM* method was used to rank the challenges of using drones in post operations (Çıkmak et al., 2023). The selection of locations for organizing freight villages (another type of dry port) in Istanbul (Turkey) was done by using the *PROMETHEE* method (Yildirim& Onder, 2014). In other research, *the PROMETHEE method was used to select locations for inland port construction* in Thailand (Komchornrit, 2017).

Thus, it can be seen that the ranking of inland ports by location and capacity using *MCM* methods has been carried out in many countries and territories. Ranking inland ports in Vietnam will contribute valuable resources to this research direction. In this paper, an integrated MCDM framework using three newly developed methods—Probability, OPARA, and RAM—is applied to rank inland ports. These three MCM methods, such as PM, OPARA, and RAM, are all newly discovered methods. PM first appeared in January 2023 (Zheng et al., 2021), the *OPARA* method first appeared in June 2024 (Keshavarz-Ghorabaee et al., 2024), and the *RAM* method first appeared in September 2023 (Sotoudeh-Anvari, 2023). PM offers a fundamental advantage of considering "simultaneous optimization of multiple indices," unlike the conventional additive approach followed in MCM methods. PM works on the concept of favourable ("higher is better") and unfavourable ("lower is better") probabilities. The advantages of the OPARA method are: a) free from the selection of normalization techniques to avoid any possible information loss; b) use of the concept of pairwise adjusted ratios considering the entire decision matrix for all alternatives. In effect, the potential local superiority of any alternative with respect to its performance values is subject to the influence of the criteria; c) use of adjustment parameters to take into account the effect of range and linearity of the criteria while allowing the decision-maker flexibility make adjustments even with objective data. As a result, the OPARA method helps to circumvent the negative influence of non-linear data and potential bias, making the analysis more equitable. The benefits of using RAM are: a) avoidance of the compensatory effect of superior performance on cost criteria on the inferior performance at profit criteria; b) use of the effect of cost criteria as index and that of profit criteria as radicand. This allows putting a reward for the superior performance on profit-type criteria while penalizing cost-type criteria; c) ability to provide stable and reliable results even with no presence of cost criteria and/or with a large-sized decision matrix.

While the *RAM* method has been applied in some instances, such as determining the optimal solution for mushroom cultivation (Do et al., 2025), selecting fireproof materials (Trung, 2024), and ranking universities (Do, 2024), the two methods, Probability and OPARA, do not appear to have garnered the attention of scientists. Despite efforts, no documents applying the Probability and *OPARA* methods have been found. The absence of studies applying the Probability and *OPARA* methods, as well as the novelty of all three methods, creates an incentive to use them simultaneously in a study. Using all three new methods (Probability, *OPARA*, and *RAM*) to rank inland ports in Vietnam further enhances the

novelty and uniqueness of this research. The extant literature shows that the use of multiple MCM helps to rank the alternatives from multiple perspectives comprehensively (ÇalikoğluŁuczak, 2024). Therefore, to achieve objective ranking results, each ranking should be performed by at least two different methods (Genç et al., 2024).

To derive the weights of the criteria, this paper employs the LOPCOW method (Ecer & Pamucar, 2022). The LOPCOW method provides several unique advantages, such as: a) use of statistical concepts and logarithmic operators for rational distribution of criteria weights; b) aptness to deal with negative and zero appraisal values of the alternatives in the decision matrix; c) suitability to provide reliable and stable results with a large decision matrix (Biswas et al., 2022a). LOPCOW has been a widely used approach since its inception, applied in various complex problems (Sumanto et al., 2024; Dhruva et al., 2024; Biswas et al., 2022b; Ulutaş et al., 2024; Biswas & Joshi, 2023; Simic et al., 2023; Rong et al., 2024; Biswas & Mukhopadhyaya, 2022; Biswas et al., 2023). While several scholars have employed the LOPCOW method in multiple contexts, there is no instance of its use in conjunction with the PM, OPARA, and RAM methods. This provides another motivation for using LOPCOW in conjunction with the integrated framework presented in this paper. To aggregate the rankings of various MCDM models, we employ a simple approach, such as RIM (Yang et al., 2019). The current study addresses two primary research questions:

RQ1. How can the transport capabilities of the inland ports be scientifically compared to support maritime logistics?

RQ2. How can a reliable and robust hybrid MCDM framework be developed for inland port capability assessment in a real-world maritime logistics context?

The present work offers several contributions to the growing strand of literature, such as:

a) It offers a multi-criteria-based assessment of the capabilities of inland ports, considering capacity aspects in the context of Vietnam.
b) The present study widens the scope of applications of PM, OPARA, and RAM.
c) A novel integrated framework of multiple MCDM models with different philosophies is developed.

In what follows is the description of the organization of the remainder of this paper. Section 2 outlines the theoretical basis and computational steps of various methods used by the current study. Section 3 elaborates on the case study. In Section 4, the application of the LOPCOW-PM-OPARA-RAM framework is exemplified through the ranking of eight inland

ports in Vietnam. Section 5 draws various inferences from the findings and showcases research implications, limitations, and some future scopes for further extension work. Finally, Section 6 concludes with remarks.

Methods

The probability method

What follows are the computational steps of the PM to facilitate the ranking of the alternatives (Zheng et al., 2021).

Step 1: Construct a decision matrix (DM). Let, x_{ij} be the value of option A_i for criterion C_j where $i = 1,2,..,m$ and $j = 1,2,\ldots,n$. Let w_j be the weight of the j^{th} criterion. Then DM can be represented as

$$X = \begin{bmatrix} x_{11} & x_{12} & \ldots & x_{1n} \\ x_{21} & x_{22} & \ldots & x_{2n} \\ \ldots & \ldots & \ldots & \ldots \\ x_{m1} & x_{m2} & \ldots & x_{mn} \end{bmatrix}_{m \times n} \quad (1)$$

Step 2: For the benefit criteria, denoted as type *B* criteria, the probability of achieving a favorable outcome in decision-making is calculated according to Eq. (2).

$$P_{ij} \infty x_{ij}, P_{ij} = \alpha_j x_{ij}; i = 1,2,...,m; \; j = 1,2,...,n \quad (2)$$

Here, α_j is the normalization coefficient of the j^{th} benefit criterion, and it is calculated according to Eq. (3).

$$\alpha_j = \frac{1}{\sum_{i=1}^{m} x_{ij}} \quad (3)$$

Step 3: For the cost criteria, denoted as type *C* criteria, the probability of achieving a favorable outcome in decision-making is calculated according to Eq. (4).

$$P_{ij} \infty (x_{j\max} + x_{j\min} - x_{ij}), P_{ij} = \beta_j (x_{j\max} + x_{j\min} - x_{ij}) \quad (4)$$

Here, βj is the normalization coefficient of the j^{th} cost criterion, and it is calculated according to Eq. (5).

$$\beta_j = \frac{1}{m\left(x_{j\max} + x_{j\min} - \frac{\sum_{i=1}^{m} x_{ij}}{m} \right)} \tag{5}$$

Step 4: Calculate the overall favorable probability of option *i* subject to the weights of the criteria as given by Eq. (6). The alternative ranked first is the one with the highest overall favorable probability.

$$P_i = \prod_{j=1}^{n} (P_{ij})^{w_j} \tag{6}$$

The OPARA method

Use the *OPARA* method to determine the ranking of options in the following sequence (Keshavarz-Ghorabaee et al., 2024):

Step 1: Follow step 1 of the Probability method.

Step 2: Derive the range-based pairwise adjusted ratio, aka *RPAR,* between option *k* and option *l* according to Eq. (7).

$$RPAR_{kl} = \sum_{j \in B} w_j \left(\frac{x_{kj}}{x_{lj}} \right)^{\rho_j} + \sum_{j \in C} w_j \left(\frac{x_{lj}}{x_{kj}} \right)^{\rho_j}, k, l \in \{1, 2, .., n\} \tag{7}$$

In Eq. (7), ρ_j is the adjustment coefficient in *RPAR*, which is calculated according to Eq. (8).

$$\rho_j = \begin{cases} \dfrac{(\alpha - 1)\max(x_{ij}) + \min(x_{ij})}{\alpha(\max(x_{ij}))}; \text{ If } \dfrac{\max(x_{ij}) - \min(x_{ij})}{\max(x_{ij}) + \min(x_{ij})} > \beta \\ 1, \text{ Otherwise} \end{cases} \tag{8}$$

In Eq. (8), the values of the two quantities α and β are chosen to be 5 and 0.8, respectively (Keshavarz-Ghorabaee et al., 2024).

Step 3: Determine the linearity-based pairwise adjusted ratio (*LPAR*) between option *k* and option *l* according to Eq. (9).

$$LPAR_{kl} = \sum_{j \in B} w_j \left(\frac{x_{kj}}{x_{lj}} \right)^{\tau_j} + \sum_{j \in C} w_j \left(\frac{x_{lj}}{x_{kj}} \right)^{\tau_j}, k, l \in \{1, 2, .., n\} \tag{9}$$

The value of the quantity τ_j in Eq. (9) is determined by the user. When a criterion has a linear nature, τ_j is equal to 1. To increase *LPAR*, choose τ_j greater than 1; conversely, to decrease *LPAR*, choose τ_j less than 1.

Step 4: Calculate the aggregated pairwise adjusted ratios ($APAR_{kl}$) according to Eq. (10).

$$APAR_{kl} = \omega RPAR_{kl} + (1-\omega) LPAR_{kl} \tag{10}$$

In Eq. (10), $\omega \in [0,1]$ and is usually chosen to be 0.5.

Step 5: Calculate the scores of the options according to Eq. (11). The option with the highest score is ranked first, and vice versa.

$$S_i = \frac{1}{n}\left(\sum_{l=1}^{n}\left(\frac{APAR_{il}}{\sum_{k=1}^{n} APAR_{kl}}\right)\right) \tag{11}$$

The RAM method

The computational steps are as follows (Sotoudeh-Anvari, 2023):

Step 1: Same as the Probability method.

Step 2: Normalize the data according to Eq. (12).

$$r_{ij} = \frac{x_{ij}}{\sum_{i=1}^{m} x_{ij}} \tag{12}$$

Step 3: Computation of the normalized values according to Eq. (13).

$$y_{ij} = w_j r_{ij} \tag{13}$$

Step 4: Obtain the total normalized scores according to Eq. (14) and (15).

$$S_{+i} = \sum_{j=1}^{n} y_{+ij};\ j \in B \tag{14}$$

$$S_{-i} = \sum_{j=1}^{n} y_{-ij};\ j \in C \tag{15}$$

Step 5: Derive the final appraisal score of each option utilizing Eq. (16). The options are ranked in descending order of their final appraisal scores.

$$R_i = \sqrt[2+S_{-i}]{2+S_{+i}} \tag{16}$$

The LOPCOW method

The procedural steps (Ecer & Pamucar, 2022) are described below briefly:

Step 1. Similar to Step 1 of the Probability method.

Step 2. Do the normalization of the elements of the decision matrix.

By adopting the linear max-min normalization approach, we obtain the elements of the normalized decision matrix (NDM) as demonstrated below.

$$r_{ij} = \begin{cases} \dfrac{x_{ij} - x_{j\min}}{x_{j\max} - x_{j\min}}; \; j \in B \\ \dfrac{x_{j\max} - x_{ij}}{x_{j\max} - x_{j\min}}; \; j \in C \end{cases} \tag{17}$$

Step 3. For each criterion, obtain the percentage value.

The percentage values subject to various criteria effects are obtained by using Eq. (18) as follows.

$$\xi_j = \left| \ln \left(\frac{\sqrt{\dfrac{\sum_{i=1}^{m} r_{ij}^2}{m}}}{\sigma} \right) .100 \right| \tag{18}$$

σ is the standard deviation of the normalized performance values of the alternatives for each criterion. In effect, step 3 rationalizes the variations in the performance values in the decision matrix to obtain the criteria weights in the next step.

Step 4. Obtain the criteria weights by using percentage values.

The percentage values (obtained at step 3) are used to compute the weight for the j^{th} criterion according to Eq. (19) as follows.

$$w_j = \frac{\xi_j}{\sum_{j=1}^{n} \xi_j}; \; w_j > 0, \sum w_j = 1 \tag{19}$$

The Rank Index Method (RIM)

RIM is used to aggregate the results obtained by using various MCDM models (Yang et al., 2019). The method has been used in various situations for aggregation purpose (Kumar et al., 2021; Wakeel et al., 2021; Mahajan et al., 2024). The computational steps are described as follows.

Step 1. Formulate the rank frequency matrix (RFM).

Given that there are m alternatives, the values of the elements of RFM $RF = (\gamma_{ik})_{m \times m}$ are obtained by using Eq. (20).

$$\gamma_{ik} = \sum_{t=1}^{t} \varphi_{ik}^{(t)} \tag{20}$$

$\varphi_{ik}^{(t)}$ denotes the rank state variable for the i^{th} alternative for a specific rank position k for the t^{th} model ($i = 1, 2...m; \; k = 1, 2...m; \; t = 1, 2...t$).

Step 2. Find out the membership degrees of the alternatives.

The membership degree for any particular i^{th} alternative at a specific rank position k is obtained by using Eq. (21).

$$\psi_{ik} = \frac{\xi_{ik}}{t}; \; \sum_{k=1}^{m} \psi_{ik} = 1 \tag{21}$$

Step 3. Deduce the final rank index score (RIS).

RIS for the i^{th} alternative is computed as

$$RIS_i = \sum_{k=1}^{m} k\psi_{ik} \tag{22}$$

The alternative, having at least RIS, is ranked first.

Practical case study

In this section, we briefly describe the case study. Table 1 summarizes the data on eight inland ports in Vietnam (Source: Ministry of Industry and Trade of Vietnam). These eight inland ports are denoted by

options A1-A8. Four criteria are used to evaluate each option: throughput capacity (C1), total area (C2), warehouse area (C3), and maximum exploitable output per month (C4). All these criteria are of type B. The selection of criteria follows the guidelines of the Vietnamese Ministry of Industry and Trade.

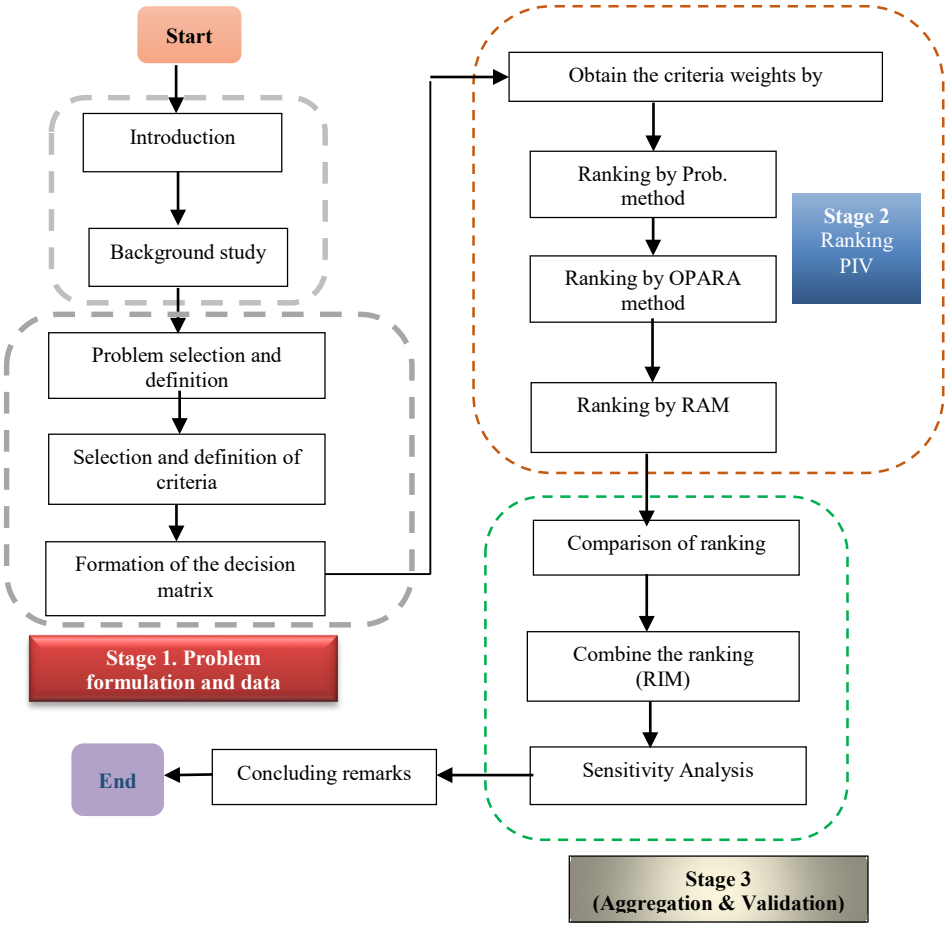


Figure 1 - Research framework

The study examines capacity-based metrics to support the development of operational capability and policy relevance in Vietnam. Critical criteria, including throughput capacity and storage space, are vital for evaluating an inland port's capability to provide maritime operations. These metrics are recorded by the Vietnamese Ministry of Industry and

Trade, guaranteeing data consistency. The study focuses on competence benchmarking rather than comprehensive sustainability evaluations, using capacity measures as preliminary tools for infrastructure design and investment prioritization. The scope may broaden in the future to include operational, environmental, and social factors. Figure 1 shows the flowchart of the research methodology.

Table 1 - Data of inland ports in Vietnam (Source: Ministry of Industry and Trade of Vietnam)

Port Name	Alt.	Throughput Capacity (TEU/year)	Total Area (ha)	Warehouse Area (m²)	Maximum Exploitable Output (TEU/month)
		C1	C2	C3	C4
Phúc Lộc	A1	100000	10	50000	200
Móng Cái	A2	200000	15	110000	8000
Tân cảng Hà Nam	A3	50000	9.4	11000	350
Tân cảng Quế Võ	A4	105000	10	30000	4500
Hải Linh	A5	65000	5	20000	300
Tân cảng Hải Phòng	A6	120000	15	79000	2000
Đình Vũ	A7	150000	24.5	55000	600
Long Biên	A8	135000	12	50000	1500

Criteria description

What follows is a short description of the criteria used in this case study.

C1- Throughput Capacity (TEU/year): This is an indicator of a dry port's ability to handle cargo in a year. In other words, it shows how much cargo the dry port can receive, process, and dispatch within a specific period. The unit of C1 is TEU (Twenty-foot Equivalent Unit) per year.

C2- Total Area (ha): This is the total land area that the dry port occupies, including the cargo handling area, warehouse, office, and other auxiliary facilities. The unit of C2 is a hectare (ha), which is a unit of land area equivalent to 10,000 square meters.

C3 - Warehouse Area (m^2): This is the area specifically designated for cargo storage, including both outdoor and indoor warehouses. The unit of C3 is square meter (m^2).

C4 - Maximum Exploitable Output (TEU/month): This is the maximum amount of cargo that a dry port can handle in a month, based on its current capacity and ideal working conditions. The unit of C4 is TEU per month.

It is observed that option A2 has the highest values for three criteria: C1, C3, and C4, compared to the other options. However, the highest value for criterion C2 belongs to option A7. This means that by only observing the data in Table 1, it is not possible to determine which inland port is the best. To select the best inland port, all four parameters must be considered simultaneously, meaning a decision must be made by weighing all four criteria for each option. This task will be carried out by applying the three methods: Probability, *OPARA*, and *RAM* in this study.

Results

The essential task when ranking options using the Probability, *OPARA*, and *RAM* methods is to determine the weights for the criteria. First, we show the calculation of criteria weights using the LOPCOW method. Using Eqs. (17)-(19), the criteria weights are calculated (Table 2).

Table 2 - Calculation of criteria weights (LOPCOW)

Items	C1	C2	C3	C4
Sum of Square	2.2389	1.8372	2.0248	1.3881
Mean Square	0.2799	0.2297	0.2531	0.1735
Standard Deviation	0.3179	0.2971	0.3258	0.3529
Percentage Values	50.9135	47.7969	43.4379	16.5714
Criteria Weights	0.3208	0.3011	0.2737	0.1044

Table 2 indicates that throughput capacity (C1) and total area (C2) are assigned the greatest weights, signifying their predominant role in distinguishing inland ports. The maximum exploitable output (C4) is assigned the lowest weight because of its lower variability among options. This distribution indicates that LOPCOW objectively highlights factors with greater discriminative power, thereby enhancing the legitimacy of the weighing procedure.

Now, we use the calculated weights to rank inland ports using three MCDM methods following a step-by-step approach. Table 3 summarizes the findings, including appraisal scores and ranks.

The OPARA methodology employs parameters (α, β, γ) that correspond with its foundational framework to support theoretical coherence and outcome comparability. α and β regulate the sensitivity of range-based adjustments, whereas γ mediates the compromise between range-based and linearity-based ratios. The investigation used parameter values suggested by OPARA developers, which have been empirically shown to optimize stability and discriminatory power. This constrains subjectivity and prevents overfitting to an individual case study.

Table 3 - Ranking of alternatives using various methods

Method	PM		OPARA		RAM	
Alternative	Pi	Rank	Si	Rank	Ri	Rank
A1	0.0864	6	0.7339	6	1.4490	6
A2	0.2224	1	2.0146	1	1.4954	1
A3	0.0476	8	0.4228	7	1.4335	7
A4	0.1056	5	1.0262	4	1.4538	5
A5	0.0496	7	0.4073	8	1.4328	8
A6	0.1492	2	1.1907	3	1.4669	3
A7	0.1484	3	1.2230	2	1.4717	2
A8	0.1240	4	0.9814	5	1.4579	4

Table 3 shows robust agreement among the three MCDM methodologies. Inland port A2 is continuously ranked #1 across all methodologies, whilst A3 and A5 constantly hold lower rankings. Minor rank fluctuations among intermediate options indicate methodological discrepancies rather than volatility. This convergence reinforces the resilience of the integrated architecture and substantiates the use of various ranking methodologies.

We proceed to examine the consistency among the rankings of alternatives provided by various methods. By applying Spearman's rank correlation test (Table 4), we observe that PM, OPARA, and RAM are highly correlated with each other. It suggests that these methods are in harmony and, hence, an integrated MCDM framework is possible to rank the alternatives. However, all these methods provide different ranges of appraisal scores for the alternatives (Figure 2).

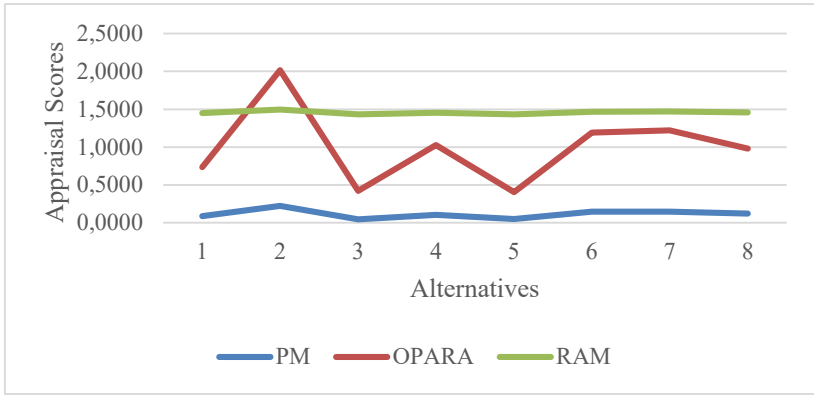


Figure 2 - Distribution of appraisal scores of alternatives (provided by various methods)

Table 4 presents significantly high Spearman correlation coefficients (>0.9), highlighting robust concordance among PM, OPARA, and RAM. The statistical consistency validates that the techniques, despite varying computational philosophies, identify consistent performance patterns, thereby enhancing trust in the resultant rankings.

Table 4 - Association among ranking of PM, OPARA and RAM

Coefficient	Method	PM	OPARA	RAM
Spearman's rho	PM	1		
Spearman's rho	OPARA	.929**	1	
Spearman's rho	RAM	.952**	.976**	1

** Correlation is significant at the 0.01 level (2-tailed).

Figure 2 illustrates that although the ranges of evaluation scores vary among techniques, the relative ranking of alternatives stays consistent. RAM demonstrates score compression, indicative of its conservative and non-compensatory characteristics, while OPARA offers enhanced score dispersion. These discrepancies underscore methodological consistency.

Next, the ranking results provided by PM, OPARA, and RAM are aggregated by using the procedural steps of RIM. Using Eq. (20), we obtain the RFM, and then, by applying Eq. (21) and Eq. (22), the membership degrees and RIS are found to arrive at the final ranking of the alternatives (Table 5). A2 retains its position as the premier inland port, succeeded by A7 and A6. The aggregate verifies that dominance is independent of the strategy employed and that the integrated approach reduces bias inherent in separate models.

Table 5 - Final ranking of the alternatives (RIM)

Alternatives	Rank positions								Score	Final Rank
	1	2	3	4	5	6	7	8		
A1	0.00	0.00	0.00	0.00	0.00	1.00	0.00	0.00	6.00	6
A2	1.00	0.00	0.00	0.00	0.00	0.00	0.00	0.00	1.00	1
A3	0.00	0.00	0.00	0.00	0.00	0.00	0.67	0.33	7.33	7
A4	0.00	0.00	0.00	0.33	0.67	0.00	0.00	0.00	4.67	5
A5	0.00	0.00	0.00	0.00	0.00	0.00	0.33	0.67	7.67	8
A6	0.00	0.33	0.67	0.00	0.00	0.00	0.00	0.00	2.67	3
A7	0.00	0.67	0.33	0.00	0.00	0.00	0.00	0.00	2.33	2
A8	0.00	0.00	0.00	0.67	0.33	0.00	0.00	0.00	4.33	4

Table 6 exhibits the correlation among the aggregated ranking (provided by RIM) and the MCDM methods like PM, OPARA, and RAM. It is evident that all methods maintain a high correlation with the aggregated ranking.

Table 6 - Correlation among various methods and final ranking

Coefficient	Method	PM	OPARA	RAM
Spearman's rho	RIM	.952**	.976**	1.000**

*** Correlation is significant at the 0.01 level (2-tailed).*

Comparison of MCDM methods

There are several MCDM methods. These MCDM methods have different underlying conditions to arrive at the appraisal scores of the alternatives for ranking them (Komatina, 2025; Chakraborty & Saha, 2024). Therefore, it is essential to compare the results of various MCDM methods to examine the reliability of a specific model (Wardany & Zahedi, 2024; Pramanik et al., 2021; Biswas et al., 2025). In this work, we compare the ranking results of PM, OPARA, and RAM methods with other models like CRADIS, MABAC, ARAS, and SAW by applying Spearman's rank correlation test (Table 7). The values of Spearman's rho coefficient suggest that all methods are consistent with each other. Figure 3 shows the distribution of the ranking of the alternatives provided by various methods. It is evident that there is no significant variation in the ranking.

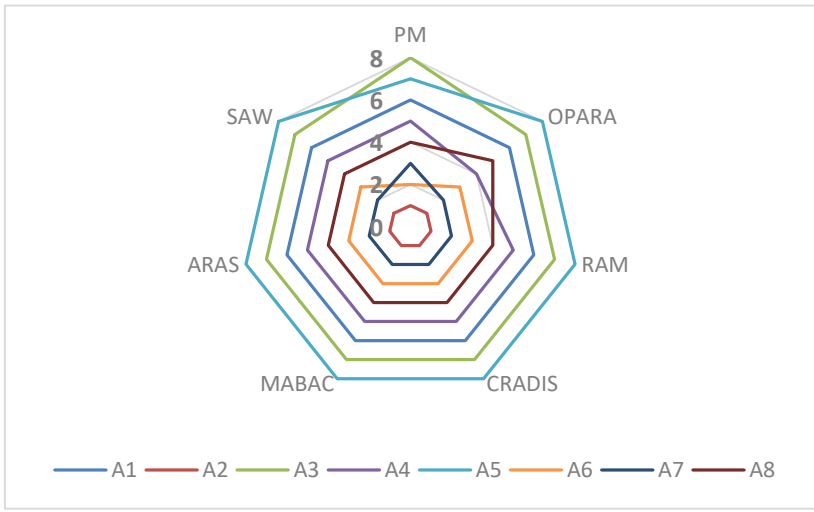


Figure 3 - Distribution of ranking of alternatives (provided by various methods)

Table 7 - Association among the ranking of various methods

Coefficient	Method	CRADIS	MABAC	ARAS	SAW
Spearman's rho	PM	.952**	.952**	.952**	.952**
Spearman's rho	OPARA	.976**	.976**	.976**	.976**
Spearman's rho	RAM	1.000**	1.000**	1.000**	1.000**

*** Correlation is significant at the 0.01 level (2-tailed).*

Sensitivity analysis

MCDM models are susceptible to changes in the external conditions, which arise due to the inclusion/exclusion of criteria and alternatives, changes in criteria weights, variations in the aggregation parameters, alterations in normalizations, and others (Więckowski & Sałabun, 2025; Stević et al., 2024; Biswas et al., 2025a). To ascertain the stability of the final outcome, sensitivity analysis is carried out (Görçün et al., 2023; Özekenc, 2025; Mishra et al., 2025). Accordingly, in this paper to ensure that the evaluation results of the inland ports are objective, the weights of the criteria have been determined in five different scenarios. In the first scenario (*S1*), the weights of the criteria are chosen to be equal, i.e., 0.25. In the remaining four scenarios (from *S2* to *S5*), the weight of one criterion is chosen to be twice the weight of the other criteria. For example, in scenario *S2*, w_1 is chosen to be 0.4, while the values of w_2, w_3, and w_4 are all 0.2. For for scenario *S3*, w_2 is chosen to be 0.4, while the values of w_2, w_3, and w_4 are all 0.2, etc. The values of the weights in the scenarios are summarized in Table 8.

Table 8 - Different scenarios for the weights of the criteria

Scenario	w_1	w_2	w_3	w_4
S1	0.25	0.25	0.25	0.25
S2	0.4	0.2	0.2	0.2
S3	0.2	0.4	0.2	0.2
S4	0.2	0.2	0.4	0.2
S5	0.2	0.2	0.2	0.4

Applying the procedural steps of the MCDM methods described in Section 2, the inland ports have been ranked using different methods in various scenarios. The data has been summarized in Table 9.

It has been found that, across all five scenarios surveyed and using all three MCDM methods, the ranking of the inland ports does not change significantly. Notably, in all surveyed cases, A2 is ranked 1st, A1 is ranked 6th, and A3 and A5 alternate between 7th and 8th. For other options, the

change in ranking is also not significant. To comprehensively evaluate changes in the options across different ranking methods and scenarios, the Spearman's rank correlation coefficient was used. This coefficient is calculated according to Eq. (23) (Thien & Son, 2024; Aazagreyir et al., 2024), where Ri denotes the difference in the ranking of option i across different methods/scenarios.

$$\rho = 1 - \frac{6R_i^2}{m(m^2 - 1)} \tag{23}$$

Because it is limited by the framework of the data table, the notation of the combination of weighting scenarios with *MCDM* methods is done as follows. For example, in scenario *S1*, *S1-P*, *S1-O,* and *S1-R* represent the ranking results of alternatives using Probability, *OPARA,* and *RAM* methods; in scenario *S2*, *S2-P*, *S2-O* and *S2-R* also represent the ranking results of alternatives using Probability, *OPARA* and *RAM* methods; etc. The value of the Spearman coefficient has been calculated and summarized in Table 10.

Table 9 - Ranking of inland ports

Scenario	Method	*A1*	*A2*	*A3*	*A4*	*A5*	*A6*	*A7*	*A8*
S1	Probability	6	1	8	3	7	2	5	4
	OPARA	6	1	7	2	8	3	4	5
	RAM	6	1	7	4	8	2	3	5
S2	Probability	6	1	8	5	7	2	3	4
	OPARA	6	1	8	2	7	3	4	5
	RAM	6	1	8	4	7	3	2	5
S3	Probability	6	1	7	5	8	2	3	4
	OPARA	6	1	7	2	8	4	3	5
	RAM	6	1	7	4	8	3	2	5
S4	Probability	6	1	8	5	7	2	3	4
	OPARA	6	1	8	3	7	2	4	5
	RAM	6	1	8	4	7	2	3	5
S5	Probability	6	1	7	2	8	3	5	4
	OPARA	6	1	7	2	8	3	5	4
	RAM	6	1	7	2	8	3	4	5

It is observed that the Spearman correlation coefficients between the methods/scenarios are all very high, with the smallest being 0.81. This indicates that the rankings of the options show very little difference when ranked by different methods/scenarios (Keshavarz et al., 2016). Additionally,

many Spearman correlation coefficient values are very close to 1, and there are even values where the Spearman correlation coefficient is 1 (between *S1-O* and *S5-R*, between *S2-P* and *S4-P*, and between *S5-P* and *S5-O*), further demonstrating a very high level of consistency in the rankings of the options when ranked by different methods in different scenarios.

Table 10 - Spearman rank correlation test among ranking under experimental cases

	S1-P	S1-O	S1-R	S2-P	S2-O	S2-R	S3-P	S3-O	S3-R	S4-P	S4-O	S4-R	S5-P	S5-O	S5-R
S1-P	1	0.93	0.9	0.9	0.95	0.86	0.88	0.86	0.83	0.9	0.98	0.93	0.95	0.95	0.93
S1-O		1	0.93	0.83	0.98	0.88	0.86	0.98	0.9	0.83	0.95	0.9	0.98	0.98	1
S1-R			1	0.95	0.9	0.95	0.98	0.9	0.98	0.95	0.95	0.98	0.88	0.88	0.93
S2-P				1	0.86	0.95	0.98	0.81	0.93	1	0.93	0.98	0.81	0.81	0.83
S2-O					1	0.9	0.83	0.95	0.88	0.86	0.98	0.93	0.95	0.95	0.98
S2-R						1	0.93	0.9	0.98	0.95	0.93	0.98	0.81	0.81	0.88
S3-P							1	0.83	0.95	0.98	0.9	0.95	0.83	0.83	0.86
S3-O								1	0.93	0.81	0.9	0.88	0.93	0.93	0.98
S3-R									1	0.93	0.9	0.95	0.83	0.83	0.9
S4-P										1	0.93	0.98	0.81	0.81	0.83
S4-O											1	0.98	0.93	0.93	0.95
S4-R												1	0.86	0.86	0.9
S5-P													1	1	0.98
S5-O														1	0.98
S5-R															1

(all coefficients are statistically significant at 0.05 level, two-tailed)

Discussion

The above results show that confirming A2 is the best option is an assertion that ensures very high accuracy. This conclusion creates an opportunity for transportation businesses to have a basis for choosing inland ports for their purposes. Furthermore, the ranking results of inland ports in Table 3 also help managers make appropriate policies for exploiting the potential of high-ranking ports and taking measures to upgrade existing dry ports. This ranking also helps inland ports themselves see their true capacity to have appropriate upgrading solutions, creating a healthy competitive environment among inland ports.

The persistent top ranking of inland port A2 across all methodologies and weighting scenarios is currently seen as indicative of its structural capacity superiority, particularly in throughput, warehousing space, and

maximum exploitable output. This suggests that the competitiveness of inland ports in Vietnam is primarily driven by scalable handling capacity rather than land availability alone, while ports with greater total acreage (e.g., A7) do not always achieve superior overall performance.

The strong correlation among PM, OPARA, and RAM rankings indicates latent performance uniformity across mid-ranked ports, suggesting that small capacity improvements—rather than extensive expansion—could substantially modify their relative standings. The observed stability in rankings during sensitivity analysis indicates infrastructure-driven resilience, suggesting that policy decisions derived from the proposed framework are unlikely to be influenced by mild fluctuations in preferences.

The RAM framework demonstrates a non-compensatory, conservative evaluation of alternatives, designed to minimize excessive score fluctuations. It imposes penalties for cost performance while incentivizing superior benefit performance, using benefit-oriented criteria that yield narrower score distributions. This approach improves decision reliability by reducing dominance stemming from negligible performance disparities. Significantly, RAM reliably preserves rank ordering, which is essential for comparative decision-making.

Research implications

The present research offers a number of significant implications.

a) First, the current work provides a capacity-focused capability analysis of inland ports. Maritime logistics is an important area for supply chain and logistics decision-makers. To strategize an effective logistics delivery chain in the country, while connecting the global market, inland ports play critical roles. In this regard, the present work demonstrates a novel decision-making framework.
b) Secondly, from the point of view of an emerging economy like Vietnam, the current study is a crucial one for strategic decision-making and policy formulation, resource mobilization, and infrastructure development while deciding the investment requirements directed towards enhancing the most promising ports.
c) Thirdly, the current work sheds light on an important aspect of the assessment of overall operational efficiency of inland port-based logistics operations. The findings of this work contribute notably to enhancing supply chain and logistics performance.
d) Fourthly, the framework used in the ongoing work contributes to the development of competitive benchmarking for performance

assessment of inland ports, which stimulates the ports to adopt best practices and invest in improvements.

e) Fifthly, the present research provides a novel integrated MCDM framework with objective information that may act as a robust technique to solve various other complex issues of logistics and supply chain management and, eventually, can be applied to several other real-life issues.

Limitation and future scope

While the current work offers numerous benefits and implications for strategic and operational decision-making and data analysis, the ongoing work is limited to crisp information only. Furthermore, a limited set of criteria undermines the generalizability of the results. The analysis is confined to capacity-based criteria, which, although objective, fail to encompass operational efficiency, service quality, or sustainability aspects. Secondly, the study relies on precise quantitative data, limiting its ability to capture the uncertainty and ambiguity inherent in real-world logistics systems. Third, the absence of expert opinion limits stakeholder-driven preference modeling.

There are a number of scopes for further extensions in the near future.

a) First, the present work is limited to a few criteria only. Future work may consider a more general approach by considering strategic, operational, social, and sustainability aspects. This in turn helps to develop a comprehensive framework for assessing the efficiency and effectiveness of inland ports.

b) Second, future work may extend the scope of the present model for assessment of multi-modal maritime logistics.

c) Third, technology and analytics play a critical role in shaping the performance of logistics. The ongoing work has not considered the technological capability analysis of inland ports and its impact on operational efficiency and capacity. Future work may address this aspect.

d) Fourth, the current work provides a comparative analysis of capacities. However, a further extension may attempt to optimize inland port efficiency based on capacity parameters.

e) Fifth, in this present work, we have not considered experts' opinions. A future work may be conceptualized to synthesize experts' opinions and operational performance together to develop a multi-faceted framework.

f) Sixth, in this paper we have used a crisp information-based MCDM framework of very recently developed methods that can be extended with fuzzy and rough numbers for uncertain modelling purposes.
g) Future work may also concentrate on developing a hybrid machine learning- and MCDM-based approach (e.g., Tešić, 2025) for uncertainty prediction and optimization.
h) Future work may investigate the causal relationships among various factors influencing inland port performance in maritime logistics by utilizing the frameworks such as DEMATEL in an uncertain environment (e.g., Appasamy, 2026).
i) The current study uses a standalone normalization approach, which may not accurately reflect the true differentiation among the alternatives in dynamic, changing situations. Scholars (e.g., Biswas et al., 2026) have argued for using multiple normalizations to effectively represent the initial decision matrix. This highlights a new scope for further extension of our work.

Conclusion

This study presents a novel multi-criteria decision-making (MCDM) framework for evaluating and ranking the transport capabilities of inland ports in Vietnam, marking a significant advancement in the field of logistics and transportation management. By employing three distinct MCDM methods—Probability, OPARA, and RAM along with RIM and LOPCOW, the ranking of eight inland ports in Vietnam is carried out for the first time in this study. This is also the first research to use all three methods, Probability, *OPARA,* and *RAM* simultaneously in one study. Notably, this is also the first study to use the Probability and *OPARA* methods since they were proposed until now. Although there are many novelties mentioned in this study, the findings reveal that one inland port (A2) consistently ranks as the top performer, highlighting its superior capabilities in terms of throughput capacity, total area, warehouse area, and maximum exploitable output. The present work shows a capacity-focused capability analysis of inland ports that helps decision-makers with benchmarking the best performances.

References

Aazagreyir, P, Appiahene, P., Appiah, O. & Boateng, S. 2024. Comparative analysis of fuzzy multi-criteria decision-making methods for quality of service-based web service selection, *IAES International Journal of Artificial Intelligence*, 13(2), pp.1408-1419. Available at: https://doi.org/10.11591/ijai.v13.i2.pp1408-1419

Appasamy, S. 2026. A Study on DEMATEL Approach Under Uncertainty Environments. *Spectrum of Operational Research*, 3(1), pp. 29-39. Available at: https://doi.org/10.31181/sor31202628

Beyene, Z.T., Nadeem, S. P., Jaleta, M E., & Kreie, A. 2024. Research Trends in Inland portSustainability: A Bibliometric Analysis. *Sustainability, 16(1)*, art.number: 263. Available at: https://doi.org/10.3390/su16010263

Biswas, S., & Joshi, N. 2023. A Performance based Ranking of Initial Public Offerings (IPOs) in India. *Journal of Decision Analytics and Intelligent Computing*, 3(1), pp.15–32. Available at: https://doi.org/10.31181/10023022023b

Biswas, S., Bandyopadhyay, G., & Mukhopadhyaya, J.N. 2022a. A multi-criteria based analytic framework for exploring the impact of Covid-19 on firm performance in emerging market. *Decision Analytics Journal*, *5*, art.number: 100143. Available at: https://doi.org/10.1016/j.dajour.2022.100143

Biswas, S., Bandyopadhyay, G., Pamucar, D., & Sanyal, A. 2022b. A decision making framework for comparing sales and operational performance of firms in emerging market. *International Journal of Knowledge-based and Intelligent Engineering Systems*, *26*(3), 229-248. Available at: https://doi.org/10.3233/KES-221601

Biswas, S., Biswas, B., & Mitra, K. 2025. A Novel Group Decision Making Model to Compare Online Shopping Platforms. *Spectrum of Decision Making and Applications*, *2*(1), pp.1-27. Available at: https://doi.org/10.31181/sdmap2120259

Biswas, S., Mitra, K., & Biswas, B., 2025a. Barriers to adapt quantum cryptography technology in digital supply chains: a q rung Orthopair fuzzy model. *Yugoslav Journal of Operations Research*, pp. 1-26. https://doi.org/10.2298/YJOR240819019B

Biswas, S., Datta, D., & Kar, S. 2023. Energy Efficiency and Environmental Sustainability: A Multi-Criteria based Comparison of BRICS and G7 Countries. In book: Emerging Technology and Management Trends in Environment and Sustainability. Available at: https://doi.org/10.4324/9781003356233-11

Bozicevic, J., Lovric, I., Bartulovic, D., Steiner, S., Roso, V. & Skrinjar, J. P. 2021. Determining Optimal Inland portLocation for Seaport Rijeka Using AHP Decision-Making Methodology, *Sustainability*, 13(11), art.number: 6471. Available at: https://doi.org/10.3390/su13116471

Çalikoğlu, C., & Łuczak, A. 2024. Multidimensional Assessment of SDI and HDI using TOPSIS and Bilinear Ordering. *International Journal of Economic Sciences*, *13*(2), pp. 116-128. Available at: https://doi.org/10.52950/ES.2024.13.2.007

Chakraborty, S., & Saha, A. 2024. Selection of forklift unit for transport handling using integrated MCDM under neutrosophic environment. *Facta Universitatis, Series: Mechanical Engineering, 22*(2), pp.235-256. Available at: https://doi.org/10.22190/FUME220620039C

Çıkmak, S., Kırbaç, G., & Kesici, B. 2023. Analyzing the Challenges to Adoption of Drones in the Logistics Sector Using the Best-Worst Method. *Business and Economics Research Journal*, 14(2), pp.227-242. Available at: http://dx.doi.org/10.20409/berj.2023.413

Dhruva, S., Krishankumar, R., Zavadskas, E.K., Ravichandran, K.S., & Gandomi, A.H. 2024. Selection of suitable cloud vendors for health centre: a personalized decision framework with frematean fuzzy set, LOPCOW, and CoCoSo. *Informatica*, *35*(1), pp.65-98. Available at: https://doi.org/10.15388/23-INFOR537

Do, D.T. 2024. Assessing the Impact of Criterion Weights on the Ranking of the Top Ten Universities in Vietnam. *Engineering, Technology & Applied Science Research, 14(4), pp.14899-14903*. Available at: *https://doi.org/10.48084/etasr.7607*

Do, D.T., Duong, V.D., Nguyen, C.B. & Duong, T.T.T. 2025. Using the root assessment method to choose the optimal solution for mushroom cultivation**.** *Yugoslav Journal of Operations Research*, 35(2), pp.271-281. Available at: https://doi.org/10.2298/YJOR240115007T

Ecer, F. & Pamucar, D. 2022. A novel LOPCOW-DOBI multi-criteria sustainability performance assessment methodology: An application in developing country banking sector. *Omega*, *112*, 102690. Available at: https://doi.org/10.1016/j.omega.2022.102690

Genç, E., Keleş, M.K. & Özdağoğlu, A. 2024. A hybrid MCDM model for personnel selection based on a novel Gray AHP, Gray MOORA and Gray MAUT methods in terms of business management: An application in the tourism sector. *Journal of Decision Analytics and Intelligent Computing*, *4*(1), pp.263–284. Available at: https://doi.org/10.31181/jdaic10024122024g

Görçün, Ö. F., Pamucar, D., & Biswas, S. 2023. The blockchain technology selection in the logistics industry using a novel MCDM framework based on Fermatean fuzzy sets and Dombi aggregation. *Information Sciences*, *635*, pp.345-374. Available at: https://doi.org/10.1016/j.ins.2023.03.113

Hervás-Peralta, M., Poveda-Reyes, S., Molero, G. D., Santarremigia, F. E & Pastor-Ferrando, J. P. 2019. Improving the Performance of Dry and Maritime Ports by Increasing Knowledge about the Most Relevant Functionalities of the Terminal Operating System (TOS), *Sustainability 11*, 1648. Available at: https://doi.org/10.3390/su11061648

Jeevan, J & Ros, V. 2019. Exploring seaport - inland portsdyadic integration to meet the increase in container vessels size. *Jeevan and Roso Journal of Shipping and Trade*, 4(8), pp.1-18. Available at: https://doi.org/10.1186/s41072-019-0047-4

Kahraman, C., Oztaysi, S.C.B. & Ona, S.C. 2023. Decomposed Fuzzy Sets and Their Usage in Multi-Attribute Decision Making: A Novel Decomposed Fuzzy

TOPSIS Method, *Mathematics, 11*, 3867, Available at: https://doi.org/10.20944/preprints202306.1398.v1

Keshavarz Ghorabaee, M., Zavadskas, E.K., Amiri, M. & Antucheviciene, J. 2016. Evaluation by an area-based method of ranking interval type-2 fuzzy sets (EAMRIT-2F) for multi-criteria group decision-making. *Transformations in Business & Economics*, 15(3), pp.76-95. ISSN 1648 - 4460

Keshavarz-Ghorabaee, M., Rastegar, A., Amiri, M., Zavadskas, E.K. & Antucheviciene, J. 2024. Multi-Criteria Personnel Evaluation and Selection Using an Objective Pairwise Adjusted Ratio Analysis (OPARA). *Economic Computation and Economic Cybernetics Studies and Research*, 58(2), pp.23-45. Available at: https://doi.org/10.24818/18423264/58.2.24.02

Komatina, N. 2025. A Novel BWM-RADAR Approach for Multi-Attribute Selection of Equipment in the Automotive Industry. *Spectrum of Mechanical Engineering and Operational Research*, 2(1), pp. 104-120. Available at: https://doi.org/10.31181/smeor21202531

Komchornrit, K. 2017. The Selection of Inland portLocation by a Hybrid CFA-MACBETH-PROMETHEE Method: A Case Study of Southern Thailand. *The Asian Journal of Shipping and Logistics*, 33(3), pp.141-153. Available at: http://dx.doi.org/10.1016/j.ajsl.2017.09.004

Kumar, R., Dubey, R., Singh, S., Singh, S., Prakash, C., Nirsanametla, Y., ... & Chudy, R. 2021. Multiple-criteria decision-making and sensitivity analysis for selection of materials for knee implant femoral component. *Materials*, 14(8), 2084. Available at: https://doi.org/10.3390/ma14082084

Lam, N. C. & Notteboom, T. 2016. A Multi-Criteria Approach to Inland portLocation in Developing Economies with Application to Vietnam. *The Asian Journal of Shipping and Logistics*, 32(1), pp.23-32. Available at: http://dx.doi.org/10.1016/j.ajsl.2016.03.003

Lamii, N., Bentaleb, F., Fri, M., Douaioui, K., Mabrouki, C & Semma, E.A. 2020. Systematic Review of Literature on Inland portConcept Evolution. *Transactions on Maritime Science.* 9(2), pp.248-270. Available at: https://doi.org/10.7225/toms.v09.n02.009

Liu, T. & Wang, H. 2023. Evaluating the Service Capacity of Port-Centric IntermodalTransshipment Hub. *Journal of Marine Science and Engineering*, *11*, 1403. Available at: https://doi.org/10.3390/jmse11071403

Mahajan, A., Singh, I., & Arora, N. 2024. An integrated multi-criteria decision-making framework for the selection of sustainable biodegradable polymer for food packaging applications. *Environment, Development and Sustainability*, 26(4), pp.8399-8420. Available at: https://doi.org/10.1007/s10668-023-03052-z

Mešić, A., Miškić, S., Stević, Z., & Mastilo, Z. 2022. Hybrid MCDM solutions for evaluation of the logistics performance index of the western BALKAN COUNTRIES. *Economics*, 10(1), pp.13-34. Available at: https://doi.org/10.2478/eoik-2022-0004

Mishra, A. R., Rani, P., Pamucar, D., Alshamrani, A. M., & Alrasheedi, A. F. 2025. Intuitionistic fuzzy macont method for logistics 4.0 based circular economy interested regions assessment in the agri-food sector. *Facta Universitatis, Series:*

Mechanical Engineering, *23*(3), pp. 407-432. https://doi.org/10.22190/FUME241001052M

Mohan, V.G. & Nasee, M.A. 2022. Prioritisation of Inland portLocations Using MCDM Methods: A Case of Cochin Port. Journal of The Institution of Engineers (India): Series A, 103, pp.841–856. Available at: https://doi.org/10.1007/s40030-022-00648-y

Mohan, V.G. & Naseer M.A. 2022. Inland portLocation Factor Determination using Delphi in Peninsular Region. *Transactions on Maritime Science*, 11(1), pp.169-184. Available at: https://doi.org/10.7225/toms.v11.n01.w05

Oguz, S. 2023, Valuation of customs, infrastructure and logistics services with multi-criteria decision-making methods: a comparative analysis for the top 10 countries in the logistics performance index. *Journal of Management, Marketing and Logistics (JMML)*, 10(4), pp.167-178. Available at: http://doi.org/10.17261/Pressacademia.2023.1837

Özekenci, E. K. 2025. A Multi-Criteria Framework for Economic Decision Support in Urban Sustainability: Comparative Insights from European Cities. *International Journal of Economic Sciences*, *14*(1), pp.162-181. Available at: https://doi.org/10.31181/ijes1412025188

Pramanik, P.K.D., Biswas, S., Pal, S., Marinković, D., & Choudhury, P. 2021. A comparative analysis of multi-criteria decision-making methods for resource selection in mobile crowd computing. *Symmetry*, *13*(9), 1713. Available at: https://doi.org/10.3390/sym13091713

Price, C.C., Zhu, J. & Hillier, F.S. 2018. Multi-Criteria Decision Making in Maritime Studies and Logistics: Applications and Cases. *International Series in Operations Research & Management Science*, 260. Available at: http://doi.org/10.1007/978-3-319-62338-2

Rodrigues, T.A., Mota, C.M.M & Santos, I.M. 2020. Determining inland portcriteria that support decision making. *Research in Transportation Economics*, 88, 100994. Available at: https://doi.org/10.1016/j.retrec.2020.100994

Rong, Y., Yu, L., Liu, Y., Simic, V., & Garg, H. 2024. The FMEA model based on LOPCOW-ARAS methods with interval-valued Fermatean fuzzy information for risk assessment of R&D projects in industrial robot offline programming systems. *Computational and Applied Mathematics*, *43*(25). Available at: https://doi.org/10.1007/s40314-023-02532-2

Senol, M.B., Adem, A., & Dagdeviren, M. 2019. A fuzzy MCDM approach to determine the most influential logistic factors. *Politeknik Dergisi*, 22(3), pp.793-800. Available at: https://doi.org/10.2339/politeknik.586041

Setiawan, G. D. & Pasaribu, A.F.O. 2024. Implementasi Kombinasi LOPCOW dan Operational Competitiveness Rating Analysis Dalam Rekomendasi Tempat Wisata Indoor. *Jurnal Sistem dan Teknologi Informasi Indonesia*, 9(2), pp.109-120, Available at: https://doi.org/10.32528/justindo.v9i2.1914

Simic, V., Dabic-Miletic, S., Tirkolaee, E. B., Stević, Ž., Ala, A., & Amirteimoori, A. 2023. Neutrosophic LOPCOW-ARAS model for prioritizing industry 4.0-based material handling technologies in smart and sustainable

warehouse management systems. *Applied Soft Computing*, *143*, 110400. Available at: https://doi.org/10.1016/j.asoc.2023.110400

Sotoudeh-Anvari, A. 2023. Root Assessment Method (RAM): A novel multi-criteria decision making method and its applications in sustainability challenges. *Journal of Cleaner Production*, 423, 138695. Available at: https://doi.org/10.1016/j.jclepro.2023.138695

Stević, Ž., Baydaş, M., Kavacık, M., Ayhan, E., & Marinković, D. 2024. Selection of data conversion technique via sensitivity-performance matching: Ranking of small E-vans with PROBID method. *Facta Universitatis, Series: Mechanical Engineering,* *22*(4), pp.643-671. Available at: https://doi.org/10.22190/FUME240305023S

Sumanto, S., Radiyah, U., Supriyatna, A., Pujiastuti, L., Yani, A., & Marita, L. S. 2024. Accurate and Objective Lecturer Appraisal System: Implementation of the LOPCOW Method. *Komputasi: Jurnal Ilmiah Ilmu Komputer dan Matematika*, *21*(2), pp.105-113. Available at: https://doi.org/10.33751/komputasi.v21i2.10188

Tadić, S., Krstić, M., Roso, V. & Brnja, N. 2020. Inland portTerminal Location Selection by Applying the Hybrid Grey MCDM Model, *Sustainability*, 12(17), 6983. Available at: https://doi.org/10.3390/su12176983

Tešić, D. (2025). A Machine Learning and Multi-Criteria Decision-Making Framework for Student Grade Prediction. *Smart Multi-Criteria Analytics and Reasoning Technologies*, *1*(1), 22-32. https://doi.org/10.65069/smart1120253

Thien, N.V. & Son, N.H. 2024. Material Selection for PMEDM Process, *International Journal of Mechanical Engineering and Robotics Research*, 13(3), pp.315-324. Available at: https://doi.org/10.18178/ijmerr.13.3.315-324

Trung, D.D. 2024. Using RAM method for optimal selection of flame retardant nanocomposite material fabrication solution. *EPJ Applied Metamaterials*. 11(4). Available at: https://doi.org/10.1051/epjam/2024005

Ulutaş, A., Topal, A., Görçün, Ö. F., & Ecer, F. 2024. Evaluation of third-party logistics service providers for car manufacturing firms using a novel integrated grey LOPCOW-PSI-MACONT model. *Expert Systems with Applications*, *241*, 122680. https://doi.org/10.1016/j.eswa.2023.122680

Varese, E., Bux, C., Amicarelli, V. & Lombardi, M. 2022. Assessing Dry Ports' Environmental Sustainability, *Environments,* *9*(9). Available at: https://doi.org/10.3390/environments9090117

Wakeel, S., Bingol, S., Bashir, M. N., & Ahmad, S. 2021. Selection of sustainable material for the manufacturing of complex automotive products using a new hybrid Goal Programming Model for Best Worst Method–Proximity Indexed Value method. *Proceedings of the Institution of Mechanical Engineers, Part L: Journal of Materials: Design and Applications*, 235(2), pp.385-399. Available at: https://doi.org/10.1177/1464420720966347

Wardany, R., & Zahedi. 2024. A Study Comparative of PSI, PSI-TOPSIS, and PSI-MABAC Methods in Analyzing the Financial Performance of State-Owned Enterprises Companies Listed on the Indonesia Stock Exchange.

Yugoslav Journal of Operations Research, 35(2), pp.313-330. Available at: https://doi.org/10.2298/YJOR240115017W

Więckowski, J., & Sałabun, W. 2025. Comparative Sensitivity Analysis in Composite Material Selection: Evaluating OAT and COMSAM Methods in Multi-criteria Decision-making. *Spectrum of Mechanical Engineering and Operational Research*, *2*(1), pp.1-12. Available at: https://doi.org/10.31181/smeor21202524

Yang, W. C., Chon, S. H., Choe, C. M., & Un-Ha, K. 2019. Materials selection method combined with different MADM methods. *Journal of Artificial Intelligence*, 1(2), pp.89-99. Available at: https://doi.org/10.32604/jai.2019.07885

Yildirim, B.F. & Onder, E. 2014. Evaluating Potential Freight Villages in Istanbul Using Multi Criteria Decision Making Techniques, *Journal of Logistics Management*, 3(1), pp.1-10. Available at: http://dx.doi.org/10.5923/j.logistics.20140301.01

Zak, J. & Weglinsk. 2024. The selection of the logistics center location based on MCDM/A methodology. *Transportation Research Procedia*, 3, pp.555 – 564. Available at: http://doi.org/10.1016/j.trpro.2014.10.034

Żak, J. 2019. The Application of Multiple Criteria Decision Making/Aiding Methodology in the Evaluation and Redesign of Logistics Systems. *Decision Making in Manufacturing and Services*, 13(1-2), pp.53-71. Available at: https://doi.org/10.7494/dmms.2019.13.1-2.3328

Zheng, M., Teng, H. & Wang, Y. 2021. A simple approach for multi-criteria decision-making on basis of probability theory. *Engineering Structures and Technologies*, 13(1), pp.26-30. Available at: https://doi.org/10.3846/est.2021.18404

Integrisani okvir za višekriterijumsku analizu odlučivanja za poređenje transportnih kapaciteta unutrašnjih luka u pomorskoj logistici

Do Duc Trung[a], *Sanjib* Biswas[b], *Nguyen* Xuan Truong[a], *Darko* I. Božanić[c], **autor za prepisku**

[a] Hanoi University of Industry, School of Mechanical and Automotive Engineering, Vietnam

[b] Amity Business School, Amity University Kolkata, AA-II, New Town, Kolkata, India

[c] Univerzitet odbrane u Beogradu, Vojna akademija, Beograd, Srbija

OBLAST: nauke o odlučivanju, primenjena matematika
KATEGORIJA (TIP) ČLANKA: originalni naučni rad

Sažetak:

Uvod/cilj: Unutrašnje luke pružaju usluge skladištenja, transporta i carinjenja robe koja se kreće na kopnu. Rangiranje i evaluacija unutrašnjih luka od ključnog su značaja za nacionalnu logistiku, jer unapređuju efikasnost upravljanja i optimizuju tok robe. Ovaj rad predstavlja procenu sposobnosti orijentisanu na kapacitete osam unutrašnjih luka u Vijetnamu.

Metode: Poređenje se vrši na osnovu četiri glavna parametra: kapaciteta pretovara, ukupne površine, površine skladišta i maksimalnog eksploatacionog učinka. Tri metode višekriterijumskog modeliranja (eng. MCM), uključujući Metodu verovatnoće (eng. PM), objektivnu analizu parno prilagođenih odnosa (eng. OPARA) i Metodu procene korena (eng. RAM), primenjene su za rangiranje unutrašnjih luka. Metoda LOPCOW (eng. Logarithmic Percentage Change-driven Objective Weighting) koristi se za određivanje težina kriterijuma. Rangiranja dobijena pojedinačnim metodama objedinjuju se primenom metode indeksa ranga (RIM).

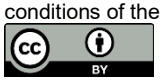
Rezultati: Rezultati pokazuju da, bez obzira na primenjeni metod ili težine kriterijuma, od osam posmatranih unutrašnja luka jedna luka (A2) ostvaruje najbolji rezultat. Radi procene stabilnosti rezultata, formirano je pet scenarija u kojima se menjaju težine kriterijuma i rangiranje alternativa. Rezultati pokazuju da je ishod manje osetljiv na promene spoljašnjih uslova.

Zaključak: Ova studija pruža transportnim kompanijama informacije za izbor optimalne unutrašnje luke na osnovu kapaciteta pretovara i površine skladišta, podržava izvoznike i uvoznike u optimizaciji procesa skladištenja i transporta, pruža državnim organima podatke za unapređenje upravljanja i usmerava druge luke ka poboljšanju svojih operativnih kapaciteta.

Ključne reči: logistika, unutrašnja luka, metoda verovatnoće, OPARA, RAM, metoda indeksa ranga, LOPCOW.

Paper received on: 23 December 2025.
Manuscript corrections submitted on: 29 January 2026.
Paper accepted for publishing on: 23 February 2026.

© 2026 The Authors. Published by Vojnotehnički glasnik / Military Technical Courier (www.vtg.mod.gov.rs).This article is an open access article distributed under the terms and conditions of the Creative Commons Attribution license (http://creativecommons.org/licenses/by/4.0/rs/



The effect of elastic components on the firing stability of automatic weapons mounted on combat vehicles

Ba Ngoc Dang[a], *Martin* Macko[b], *Frantisek* Racek[c]
Viet Dung Bui[d], *Quang* A. Mai[e]

[a] University of Defence, Faculty of Military Technology, Department of Weapons and Ammunition, Brno, Czech Republic
e-mail: bangoc.dang@unob.cz, **corresponding author**,
ORCID iD: https://orcid.org/0009-0006-0481-4572

[b] University of Defence, Faculty of Military Technology, Department of Weapons and Ammunition, Brno, Czech Republic
e-mail: martin.macko@unob.cz,
ORCID iD: https://orcid.org/0000-0002-3896-0803

[c] University of Defence, Faculty of Military Technology, Department of Weapons and Ammunition, Brno, Czech Republic
e-mail: frantisek.racek@unob.cz,
ORCID iD: https://orcid.org/0000-0003-4985-2557

[d] Tran Dai Nghia University, Faculty of Ammunition, Department of Explosives and Ballistics, Hochiminh, Socialist Republic of Vietnam
e-mail: vietdungpt90@gmail.com,
ORCID iD: https://orcid.org/0009-0004-9752-9054

[e] Tran Dai Nghia University, Faculty of Ammunition, Department of Explosives and Ballistics, Hochiminh, Socialist Republic of Vietnam
e-mail: quangvhp2008@gmail.com,
ORCID iD: https://orcid.org/0009-0008-4648-0560

https://doi.org/10.5937/vojtehg74-63124

FIELD: mathematics, mechanical engineering
ARTICLE TYPE: original scientific paper

Abstract:

Introduction/purpose: Investigating the factors affecting the vibration of an automatic weapon system mounted on a combat vehicle is essential and provides an important scientific basis for improving firing stability, accuracy, and target destruction capability. For multi-barrel automatic weapons, internal deviations within the weapon may cause the automatic mechanisms of the individual barrels to operate asynchronously, one of the main reasons being discrepancies in the elastic elements of each barrel. The phase difference between the barrels leads to instability in both elevation and traverse angles, thereby reducing firing accuracy.

Methods: The system's differential equations were solved numerically in Maple to investigate how different return-spring stiffness values induce

phase shifts between the two barrels, and the results were validated experimentally.

Results: The simulation results indicate a considerable influence of the elastic element's stiffness on the azimuthal oscillation of the system. High speed camera FASTCAM SA1.1 measurements performed on a dual-barrel 37 mm gun in automatic firing mode show a high degree of correlation between the theoretical model and the experimental results. The vibration characteristics of the system in both the firing plane and the horizontal plane closely match the actual behavior, with an error of less than 8.6%.

Conclusion: The dynamic model enables the optimization of structural parameters of the weapon system. The obtained results provide an important basis for proposing solutions to increase the rate of fire and improve firing stability for weapon systems mounted on vehicles, unmanned ground platforms, and combat robots.

Key words: dual-barrel automatic weapon, firing stability, recoil spring, combat vehicle.

Introduction

The research, design, and development of multi-barrel weapon systems with high firepower and elevated target-kill probability have been a major focus of investment in countries with advanced defense industries, and numerous systems following this development direction have already been produced. At present, multi-barrel weapons play a critical role in protecting national strategic spaces and providing readiness to intercept any unexpected hostile attacks against key targets in both national defense and security domains. Compared with single-barrel systems, multi-barrel weapons offer several outstanding advantages, such as significantly higher rates of fire, greater destructive power, and higher target-kill probability.

Given these advantages, it is evident that research on modeling and dynamic analysis of multi-barrel weapon systems mounted on combat vehicles, calculating structural parameters, and proposing solutions to enhance system stability has been systematically and comprehensively conducted worldwide. However, as these studies belong to the military domain, not all of them are publicly available, and access is limited due to security constraints.

Several notable studies on the dynamic modeling of weapon systems mounted on combat vehicles include: Van Bien et al. (2021) developed a dynamic model for evaluating the oscillations of the BM-21 multiple rocket launcher mounted on a wheeled combat vehicle, in which the system consists of eight degrees of freedom. The computed oscillations in both

the firing plane and the horizontal plane serve as the foundation for assessing firing stability and determining the optimal rate of fire. Aparow et al. (2015) investigated a wheeled armored vehicle model comprising 17 degrees of freedom: 7 for vehicle motion, 7 for the control module, and 3 for the steering unit and turret. Vehicle stability was evaluated through yaw angle, sideslip angle, lateral acceleration, and vehicle displacement. The vibration model of a light machine gun mounted on a UAZ-469 combat vehicle was presented by Nguyen et al. (2021), in which vibration-reduction solutions using passive absorbers were proposed. Borkowski et al. (2007) developed a mathematical model to determine the dynamic loads acting on a combat vehicle during firing, taking into account terrain effects and vehicle speed. The establishment of mathematical models describing weapon–vehicle systems is also presented in studies by Dziopa et al. (2016), Balla (2011), and Sun et al. (2009). These studies, however, only considered dynamics in the vertical (firing) plane and did not address vibrations in the horizontal plane. Consequently, factors directly influencing the weapon's operating process during firing, particularly the internal characteristics of automatic weapons, have not yet been adequately examined.

In practice, during firing, the barrels of multi-barrel automatic weapons operating on the short-recoil principle always exhibit phase deviation due to internal factors such as variations in the oil-flow clearance between the throttling ring and throttling rod, changes in the stiffness of the return spring, wear of components in the feed and firing mechanisms, and differences in ignition characteristics between the barrels. These factors lead to discrepancies in recoil stroke length among the barrels during firing. Consequently, the loads acting on each barrel differ either in magnitude at the same instant or in timing for the same load value. This results in a yawing moment that destabilizes the weapon in both elevation and azimuth, thereby reducing firing accuracy and lowering the probability of target kill.

Several studies have addressed the factors affecting vibration and stability of weapon systems. Balla et al. (2018) conducted vibration measurements on a gun mounted on a tracked vehicle; their results showed turret vibrations at multiple frequencies caused by parameters such as the vehicle-body damping coefficient, stiffness, and backlash in the elevation drive gear train, all of which significantly influence firing accuracy. Dynamic characteristics of automatic weapons equipped with floating mechanisms, as well as the effects of firing platform ground conditions and gunner input on firing stability, have also been reported (Thai et al., 2017; Lu & Zhou, 2019). Stiavnicky et al. (2013) analyzed

factors affecting weapon operation and system vibration, including projectile–barrel interaction during firing, impulsive loads as the projectile exits the barrel, and structural elements attached to the weapon as well as mounting conditions used to evaluate stability. Truong et al. (2021) identified several structural parameters of automatic weapon mounts, such as mass and length, that significantly influence weapon vibration.

For automatic weapons operating on the short-recoil principle, once the projectile leaves the barrel, the gas-pressure impulse drives the barrel rearward, compressing the return spring. At the end of the recoil stroke, the spring pushes the barrel forward to its initial position. Therefore, the stiffness of the return spring has a substantial impact on the functioning of the automatic mechanism, affecting the cyclic rate, firing accuracy, and the overall stability of the system. Macko et al. (2021) established a dynamic computational model for a short-recoil automatic mechanism to determine the motion laws of its components, supported by experiments validating the theoretical model. Doan et al. (2023) formulated differential equations of motion and investigated the vibration characteristics of the twin-barrel 37 mm K65 anti-aircraft gun, considering in particular the influence of insufficient oil in the recoil brake on system oscillations. Experimental results demonstrated good agreement with the theoretical model. However, these studies have not yet addressed the influence of certain components of the automatic mechanism or internal factors inherent to the automatic firing cycle that contribute to weapon-system vibration.



Figure1 - Overview of the 37 mm K65 model dual-barrel machine gun

The purpose of this paper is not only to refine and formulate a comprehensive mathematical model describing the full vibration behavior of the coupled system consisting of a twin-barrel automatic weapon and its combat vehicle, but also to determine the governing effects of the stiffness of the elastic element (the return spring) on the operating process

of an automatic weapon based on the short-recoil principle. This is achieved through an assessment of the stability of the elevation and traverse mechanisms and, consequently, the overall stability of the weapon system. The findings provide an essential foundation for proposing solutions to optimize the rate of fire and enhance the stability of both the weapon mechanism and the vehicle-mounted system. In this study, the two barrels are considered as independent bodies in terms of mass and applied loads, moving along the longitudinal axis of the weapon.

The theoretical calculations and experimental validations are performed on the dual-barrel 37 mm K65 anti-aircraft gun (Figure 1).

Mathematical model

Vibration model of dual-barrel automatic weapon mounted on combat vehicle

To evaluate the effect of recoil spring stiffness on the vibrations of the weapon system and the combat vehicle, it is necessary to establish a system of differential equations that describe the vibrations of the entire system. Several assumptions have been presented by Doan et al. (2023); this paper further elaborates and clarifies these assumptions as follows:

- The weapon, when fired, is placed on an elastic ground substrate. During firing, the four vehicle outriggers are fixed with four metal stakes, ensuring that the jacks remain in contact with the ground throughout the firing process. Since the deformation of the jacks is smaller than the deformation of the ground substrate, the elastic deformations of the jacks and the vehicle body can be equivalently represented by the position of the ground where the jacks make contact. Therefore, the connection between the jacks and the ground can be modeled using elements with stiffness k_i and damping coefficients c_i.

- The vibrations of the elevation and traversing mechanisms are caused by the elastic deformation elements, which induce vibrations in the system. It is assumed that the connection between the components of the elevation and traversing mechanisms has no clearance. In this case, their deformations are replaced by linear springs with stiffness coefficients c_{ek} and c_{eq}, respectively.

- The connections between the links and mechanisms are assumed to be non-deformable during operation and without any clearance.

During firing, the system is stabilized by four outriggers, with the elevation angle φ and the traversing rotation angle α.

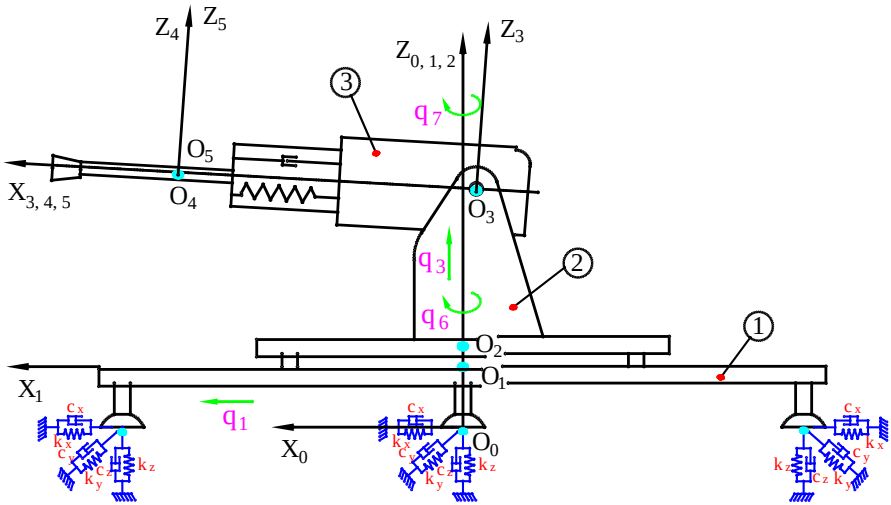


Figure 2 - Model of dual-barrel gun (side view)

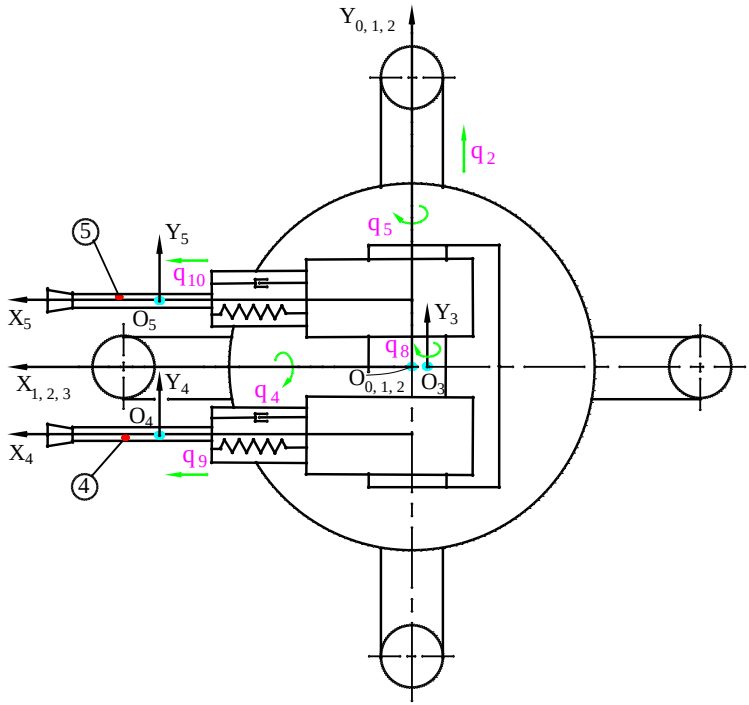


Figure 3 - Model of dual-barrel gun (overhead view)

The mechanical system consists of 5 bodies (Figures 2 and 3). Body 1: The combat vehicle with mass m_1. Due to the deformation of the outriggers being smaller than that of the ground substrate, the elastic deformations of the jacks and the vehicle body are effectively concentrated at the point where the jacks make contact with the ground. During firing, due to the phase shift between the two barrels, the vehicle body with mass m_1 will rotate around the axes O_1X_1, O_1Y_1, O_1Z_1 and translate along the axes O_1X_1, O_1Y_1, O_1Z_1.

Body 2: The gun platform with mass m_2, which connects the elevation and traversing mechanisms. The gun platform can rotate around the center of the vehicle body. Body 3: The gun mount (or elevation mechanism) with mass m_3, which can rotate around the trunnion axis (the shaft that connects the two trunnions on both sides of the gun cradle, enabling the gun to elevate during firing). Body 4: The recoil mechanism and the components moving with the recoil mechanism of the left barrel with mass m_4. Body 5: The recoil mechanism and the components moving with the recoil mechanism of the right barrel with mass m_5. In addition to these 5 bodies, the automatic mechanism is also involved in the system. Since bodies 4 and 5 are the base links transmitting motion to the working links, each link has a reduced mass m_i', transmission ratio K_i, and an efficiency η_i. As bodies 4 and 5 move along their travel paths, they sequentially engage and disengage with the working links. Therefore, the reduced mass of bodies 4 and 5 also changes during operation.

$$m_4 = (m_{recoiling\ mass} + \sum_{i=1}^{n} \frac{K_i^{\,2}}{\eta_i} m'_i) \frac{dq_9}{dt} \tag{1}$$

$$m_5 = (m_{recoiling\ mass} + \sum_{i=1}^{n} \frac{K_i^{\,2}}{\eta_i} m'_i) \frac{dq_{10}}{dt} \tag{2}$$

To investigate the dynamics of the mechanical system, each body is considered within a coordinate system with the origin at the center of mass of each body (Figure 3). The coordinate system $O_0X_0Y_0Z_0$ fixed to the ground where the weapon is mounted has its origin at the projection of the vehicle's center of mass onto the ground. The generalized coordinates are as follows:

q_1 - translation of body 1 along the O_1X_1 axis; q_2 – translation of body 1 along the O_1Y_1 axis; q_3 - translation of body 1 along the O_1Z_1 axis; q_4 – rotation of body 1 around the O_1X_1 axis; q_5 – rotation of body 1 around the O_1Y_1 axis; q_6 – rotation of body 1 around the O_1Z_1 axis; q_7 – rotation of body 2 around the O_2Z_2 axis; q_8 – rotation of body 3 around the O_3Y_3 axis; q_9 – translation of the center of mass of body 4 along the barrel axis of the

left barrel (along the O_4Z_4 axis); q_{10} – translation of the center of mass of body 5 along the barrel axis of the right barrel (along the O_5Z_5 axis); q_i – the working links of the automatic mechanism of the two barrels, which are related to the displacement of the base link with mass m_i'.

Thus, the generalized coordinate vector for the system is $q_r = [q_1, q_2, q_3, q_4, q_5, q_6, q_7, q_8, q_9, q_{10}, q_i]^T$.

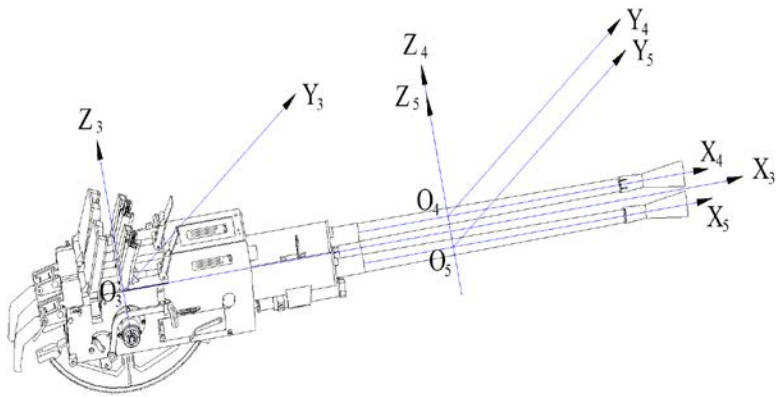


Figure 4 - Left barrel and right barrel

The mechanical system is subject to holonomic constraints, which are considered as non-holonomic, holding the system with 10 degrees of freedom. To formulate the system of differential equations for a multi-body system, several studies have employed the Lagrangian formulation (Doan et al., 2023; Bien et al., 2023; Balla et al., 2021; Konečný et al., 2021; Nguyen et al., 2023). To accurately describe the vibrations of the system, the potential-energy function Π and the dissipation function D of the elastic and viscous-damping elements are added to the equations of motion, specifically:

$$\frac{\mathrm{d}}{\mathrm{d}t}\left(\frac{\partial T}{\partial \dot{q}}\right)-\frac{\partial T}{\partial q}=-\frac{\partial \Pi}{\partial q}-\frac{\partial D}{\partial \dot{q}}+Q \tag{3}$$

where: T - is the kinetic energy of the system, Π - is the potential energy function of the force elements with potential; D - is the dissipation function of the damping forces in the system; Q - is the generalized force vector of external forces with no potential and no damping acting on the system; q and $\dot{q}$ are the generalized coordinate and velocity vectors of the system, respectively.

The kinetic-energy function T and the generalized force Q were presented by Doan et al. (2023).

The Kinetic-energy T of the mechanical system:

$$T_k = \frac{1}{2}\sum_{k=1}^{5}\left(\dot{R}_k^T M_k \dot{R}_k + \overline{\omega}_k^T A_0^k I_k A_0^{kT} \overline{\omega}_k\right) \quad (4)$$

Where: R_k is the center of mass vector of body *k* in the fixed coordinate system O_0; M_k is the mass matrix of body *k*; $\overline{\omega}_k$ is the angular velocity vector of the body *k* represented in the fixed coordinate O_0; A_0^k is the transfer matrix from system O_k to system O_0; A_0^{kT} is the inverse matrix of the matrix A_0^k; I_k is the matrix of the inertia tensor of the body *k* to the axis system O_k.

The generalized force Q_j is determined as follows:

Virtual work of generalized force F_k and torque M_k are calculated:

$$\delta WF_k = \sum_{k=1}^{5}\sum_{j=1}^{10} F_k^T \frac{\partial R_k}{\partial q_j} = \sum_{j=1}^{10}\left[\sum_{k=1}^{5} F_k^T \frac{\partial R_k}{\partial q_j}\right]\delta q_j \quad (5)$$

$$\delta WM_k = \sum_{k=1}^{5}\sum_{j=1}^{10} M_k^T \frac{\partial \theta_k}{\partial q_j} = \sum_{j=1}^{10}\left[\sum_{k=1}^{5} M_k^T \frac{\partial \theta_k}{\partial q_j}\right]\delta q_j \quad (6)$$

where: δWF_k is the virtual work produced by the force F_k; δWM_k is the virtual work produced by the moment M_k.

When the link is recognized as the ideal constraint and neglect friction, at this case the potential work of the constraint force (or constraint reaction force) is zero:

$$Q_j = \sum_{k=1}^{5} F_k^T \frac{\partial R_k}{\partial q_j} \quad (7)$$

$$Q_j = \sum_{k=1}^{5} M_k^T \frac{\partial \theta_k}{\partial q_j} \quad (8)$$

The potential energy of the system includes the gravitational potential energy referenced to the O_0 coordinate system and the potential energy of the elastic elements:

$$\Pi_\Sigma = \Pi_G + \Pi_{CT} + \Pi_{CS} + \Pi_{CGT} + \Pi_{CGP} + \Pi_{ek} + \Pi_{eq} \quad (9)$$

where: Π_G is the gravitational potential energy of the bodies; Π_{CT}, Π_{CS}, Π_{CGT}, Π_{CGP} are the potential energies of the front, rear, left, and right support points, respectively; Π_{ek} and Π_{eq} are the potential energies of the elevation and traverse mechanisms, respectively.

- Gravitational potential energy of the bodies

For gravitational forces acting at the centers of mass of the five bodies, it is calculated as follows:

$$\prod_G = \sum_{i=1}^{5} m_i.g.r_i[z] \tag{10}$$

- Potential energy of the front and rear supports

$$\Pi_{CT} = \Pi_{CS} = \frac{1}{2} K_1.\zeta^2 \tag{11}$$

Stiffness matrix K_1 for the front and rear supports:

$$K_1 = \begin{pmatrix} K_{1x} & 0 & 0 \\ 0 & K_{1y} & 0 \\ 0 & 0 & K_{1z} \end{pmatrix}$$

where: K_{1x}, K_{1y}, K_{1z} is the stiffness coefficient of the ground supporting the front and rear points along the respective *X, Y* and *Z* directions; ζ are the displacements of the front, rear, left, and right supports.

- Potential energy of the left and right supports

$$\Pi_{CGT} = \Pi_{CGP} = \frac{1}{2} K_2.\zeta^2 \tag{12}$$

For the left and right supports, the stiffness matrix K_2:

$$K_2 = \begin{pmatrix} K_{2x} & 0 & 0 \\ 0 & K_{2y} & 0 \\ 0 & 0 & K_{2z} \end{pmatrix}$$

where: K_{2x}, K_{2y}, K_{2z} represents the stiffness coefficients of the surface supporting the left and right points along the *X, Y,* and *Z* directions.

- Potential energy of the traverse mechanism

$$\Pi_{eq} = \frac{1}{2} K_{eq} . \zeta_{eq}^2 = \frac{1}{2} c_{eq} . q_7^2(t) \tag{13}$$

where: K_{eq} - stiffness matrix element of the traverse mechanism; ζ_{eq} - angular displacement of the traverse mechanism.

$$K_{eq} = \begin{pmatrix} 0 & 0 & 0 \\ 0 & c_{eq} & 0 \\ 0 & 0 & 0 \end{pmatrix}; \quad \zeta_{eq} = \begin{pmatrix} 0 \\ q_7(t) \\ 0 \end{pmatrix}$$

- Potential energy of the elevation mechanism

$$\Pi_{ek} = \frac{1}{2} K_{ek} . \zeta_{ek}^2 = \frac{1}{2} c_{ek} . q_8^2(t) \tag{14}$$

where: K_{ek} - stiffness matrix element of the elevation mechanism; ζ_{ek} - angular displacement of the elevation mechanism.

$$K_{ek} = \begin{pmatrix} 0 & 0 & 0 \\ 0 & c_{ek} & 0 \\ 0 & 0 & 0 \end{pmatrix}; \quad \zeta_{ek} = \begin{pmatrix} 0 \\ q_8(t) \\ 0 \end{pmatrix}$$

The mechanical system includes four actuator legs, which are the components that generate dissipative forces. The value of the dissipation function corresponding to these elements is calculated using Rayleigh's formula as follows (Safko et al., 2002):

$$D_i = \frac{1}{2} \sum_i c_i \dot{q}_i^2 \tag{15}$$

where: $\dot{q}_i$ - The rate of change of the vector representing the system element; c_i – The damping coefficient matrix of the ground is determined:

$$c_i = \begin{pmatrix} c_{ix} & 0 & 0 \\ 0 & c_{iy} & 0 \\ 0 & 0 & c_{iz} \end{pmatrix} \tag{16}$$

where: c_{ix}, c_{iy}, c_{iz} are the ground viscous damping coefficients of the four support legs in the *X*, *Y*, and *Z* directions, respectively.

Substituting the values from formulas (4), (7), (8), (9), and (15) into the system of differential equations of the mechanical system (3), we obtained a system of second-order differential equations with variables being the second-time derivatives of the generalized coordinates, describing the vibrations of the system during firing. The quadratic equation system (*EQS*) is as follows:

$$EQS = \{eq_1, eq_2, ..., eq_{10}\} \tag{17}$$

Assuming that the ground effect is modeled as a viscoelastic system, it is equivalent to an elastic element with stiffness k_i and a damper with damping coefficient c_i (Doan et al., 2023). Depending on the motion directions and the types of ground, the values of k_i and c_i will differ. Let k_x, k_y, k_z and c_x, c_y, c_z represent the stiffness and damping coefficients of the ground in the *X, Y,* and *Z* directions, respectively. Doan et al. (2023) determined the elastic parameters of the ground $k_x, k_y, k_z, c_x, c_y, c_z$ and the elastic parameters of the elevation and traversing mechanisms c_{ek}, c_{eq} shown in Table 1.

Table 1 - The parameters of elasticity and viscous resistance

Parameter	Symbol	Value
Coefficient elastic of the background in the X-direction	k_x	(250 ÷ 350) N/m
Coefficient elastic of the background in the Y-direction	k_y	(250 ÷ 350) N/m
Coefficient elastic of the background in the Z-direction	k_z	(450 ÷ 520) N/m
Drag coefficient viscous of the background in the X-direction	c_x	(1 ÷ 1.5) Ns/m
Drag coefficient viscous of the background in the Y-direction	c_y	(1 ÷ 1.5) Ns/m
Drag coefficient viscous of the background in the Z-direction	c_z	(2 ÷ 3) Ns/m
Stiffness of elevating mechanisms	c_{ek}	1.03×10^4 Nm/rad
Stiffness of traversing mechanisms	c_{eq}	2.8×10^3 Nm/rad

Investigate the effect of the recoil spring stiffness

The structure of the automatic mechanism components is illustrated in Figure 5, in which the gun barrel (5) serves as the base link that transmits motion to the working components to execute the next firing cycle. The recoil spring (6) directly affects both the recoil stroke and the return stroke of the gun barrel.

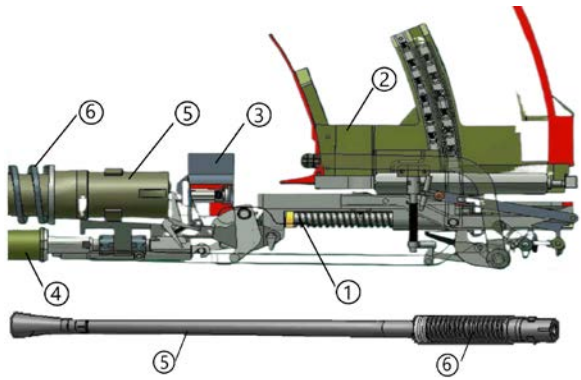


Figure 5 - Components of the automatic mechanism
1 – ejection mechanism; 2 – ammunition feed mechanism; 3 – breech block;
4 – recoil buffer; 5 – gun barrel; 6 – recoil spring

To evaluate the operational accuracy of the automatic mechanism, attention must be paid to the firing rate of the weapon and the recoil distance of the recoiling mass. In particular, the recoil stroke must remain within a permissible range to ensure the proper functioning of the individual components. Deviations in recoil length can cause oscillatory motion in the system, resulting in barrel misalignment, which in turn leads to a change in the projectile's exit direction from the barrel. By solving the automatic mechanism model, the recoil resistance force R_{hl} of both gun barrels can be determined. The value of R_{hl} for the right barrel is varied, while the left barrel's value is held constant. Based on this, the vibration behavior of the weapon system is obtained, and the time difference in the firing moments of the two barrels is identified. According to Macko et al. (2021), the recoil resistance force R_{hl} is defined as follows:

$$R_{hl} = \Phi_{HL} + \Pi + R_F - Q_0 \sin\varphi \tag{12}$$

where: $\Phi_{HL} = f(a_x)\, V^2$ - the hydraulic recoil resistance force generated by the recoil buffer; $f(a_x)$ - a function characterizing the dependence of the hydraulic resistance force in the recoil buffer on the main flow orifice area a_x, V - the velocity of the recoiling mass; $\Pi = \Pi_0 + c_{dl}\, X$ - the restoring

force of the recuperator spring (in spring-type recuperator systems), Π_0 - the initial preload force of the spring, c_{dl} - the stiffness of the recuperator spring, X - the displacement of the spring (the recoil travel); $R_F = Q_0(f\cos\varphi + \nu)$ - the resultant friction force, Q_0 - the weight of the recoiling mass, f – the coefficient of friction between the gun cradle and the recoiling mass, φ - the elevation angle of the barrel, ν - the friction coefficient between the recoiling mass and the sealing components.

It is observed that variations in the stiffness of the return spring affect the recoil stroke length of the barrel, causing the two gun barrels to operate out of phase. As a result, a moment is generated that leads to a deviation in the azimuth direction. To investigate the influence of the return spring, other parameters of the gun are kept constant while varying the stiffness of the return spring. The results are presented in Table 2. The simulation is carried out at a elevation angle of 0° and an traversing rotation angle of 0°.

Table 2 - Results of the investigation on the influence of return spring stiffness

c_{dl} (N/m)	25500	22500	19500
x_n (mm)	165.49	168.35	179.35
T_{db} (rounds per minute)	169	163	156

where: T_{db} - firing rate of the gun; x_n - maximum recoil distance of the recoiling mass.

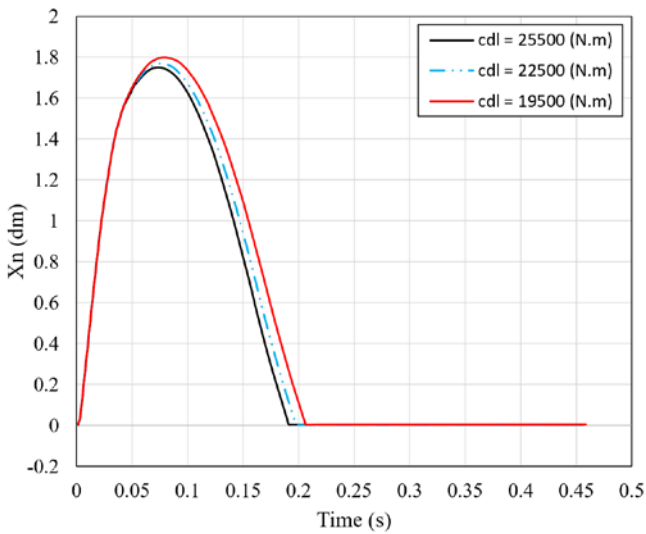


Figure 6 - Graph of the retreat length when the spring stiffness changes

Macko et al. (2021) developed a dynamic model of an automatic weapon operating on the short-recoil principle and solved the dynamic problem of a dual-barrel 37 mm gun by combining the system of differential equations governing the automatic firing mechanism with the internal ballistics equations. The solution was obtained using the Runge–Kutta method implemented in MATLAB. The results of the study determined the recoil stroke x_n and the recoil velocity v_n of the recoiling mass.

Figure 6 and Figure 7 show the results of the displacement and velocity graphs at the end of the push phase of the gun each time the spring stiffness parameter, c_{dl} is changed.

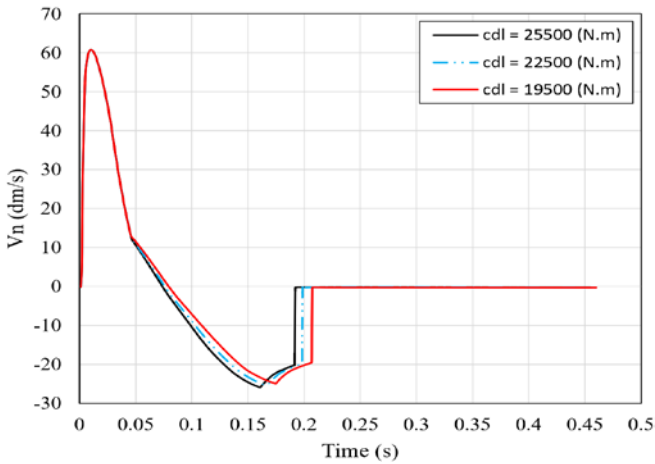


Figure 7 - Graph of the velocity of the recoiling parts when the stiffness of the spring pushes up changes

As c_{dl} increases, the firing speed increases while the displacement of the block decreases.

The maximum velocity of the block when moving backward does not change significantly. However, the velocity during the push phase increases, and the firing cycle becomes narrower, with the firing speed increasing. Conversely, when c_{dl} is reduced, the firing speed decreases rapidly, and the displacement of the block increases. The maximum velocity of the block during the push phase decreases, as shown by the outermost curves on the block velocity graph (see Figure 7).

When changing the spring stiffness c_{dl}, we also observe the change in the firing force applied to the frame, as shown in Figure 8. When c_{dl} is decreased, the firing force applied to the frame decreases accordingly.

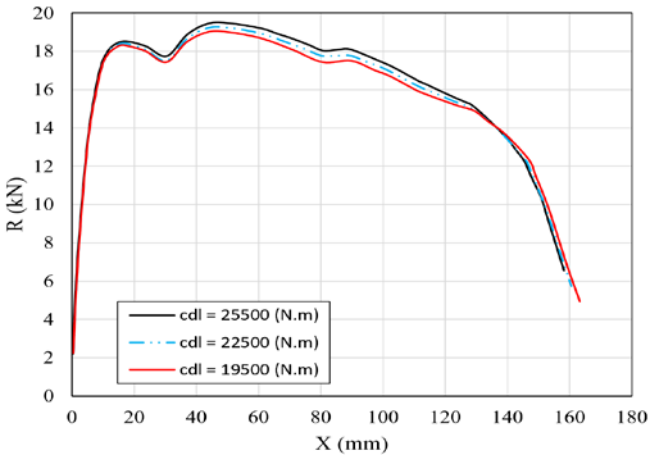


Figure 8 - The graph of the recoil force as the spring stiffness (c_{dl}) changes

With the force applied to the frame as described above, solving the vibration problem by keeping the force applied to the left barrel constant and varying the force applied to the right barrel according to the changes in spring stiffness as mentioned, we can determine the vibration laws of the traversing rotation angle $q_7(t)$ and the elevation angle $q_8(t)$ as shown in Figure 9 and Figure 10.

For the left barrel with c_{dl} = 25500 N/m and the right barrel with c_{dl} = 22500 N/m the maximum vibration of five shots when turning to the right is 50 mrad (approximately 2.86°), and when turning to the left, it is 30 mrad (approximately 1.72°), see Figure 9. The maximum vibration of 5 shots when turning upward is 4 mrad (approximately 0.229°), and when turning downward is 2.6 mrad (approximately 0.149°), see Figure 10.

Similarly, for the left barrel with c_{dl} = 25500 N/m and the right barrel with c_{dl} = 19500 N/m the maximum vibration of 5 shots when turning to the right is 55 mrad (approximately 3.15°), and when turning to the left, it is 35 mrad (approximately 2°), see Figure 9. The maximum vibration of 5 shots when turning upward is 5 mrad (approximately 0.286°), and when turning downward is 3.4 mrad (approximately 0.19°), see Figure 10.

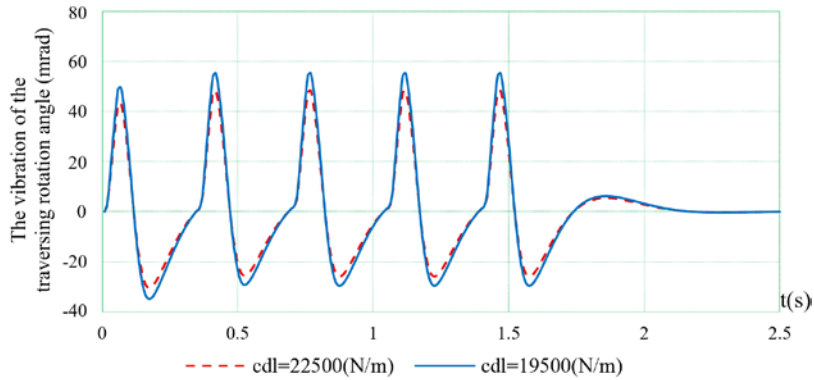


Figure 9 - The vibration of the traversing rotation angle as the spring stiffness changes

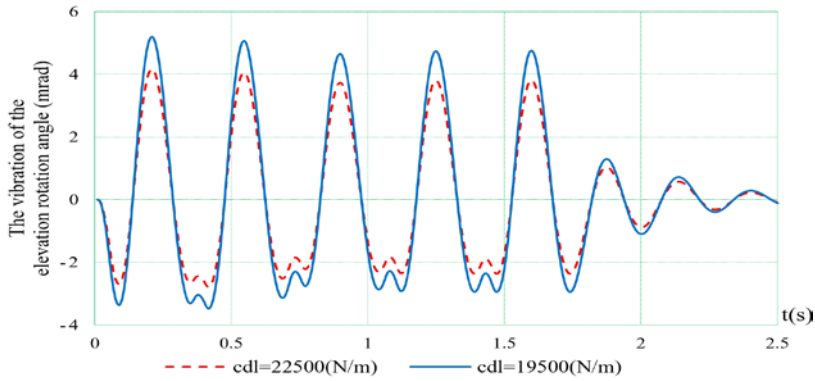


Figure 10 - The vibration of the elevation rotation angle as the spring stiffness changes

In the ideal case where both barrels fire simultaneously, meaning the left and right barrels have the same spring stiffness with c_{dl} = 25500 N/m, the vibration laws of the traversing rotation angle and the elevation angle are shown in Figure 11 and Figure 12. When both barrels fire simultaneously, the vibration of the traversing rotation angle has a very small vibration period, with the maximum vibration for 5 shots being 10 mrad (approximately 0.57°) when turning to the right and 8 mrad (approximately 0.46°) when turning to the left, see Figure 11. The vibration of the elevation angle when both barrels fire simultaneously has the largest amplitude of 3.5 mrad (approximately 0.2°) during both upward and downward vibrations, see Figure 12.

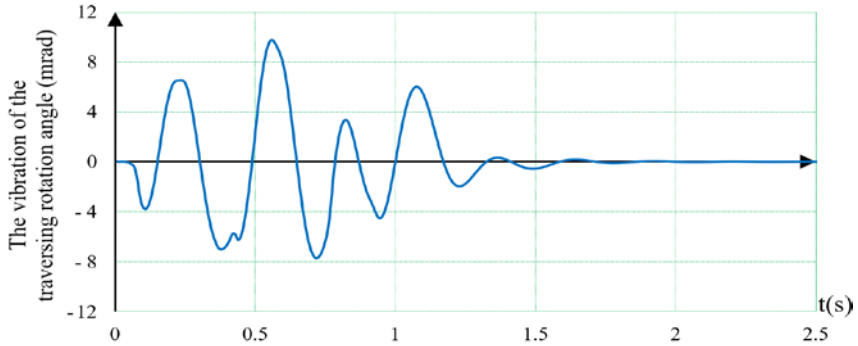


Figure 11 - The vibration of the traversing rotation angle when both barrels fire simultaneously

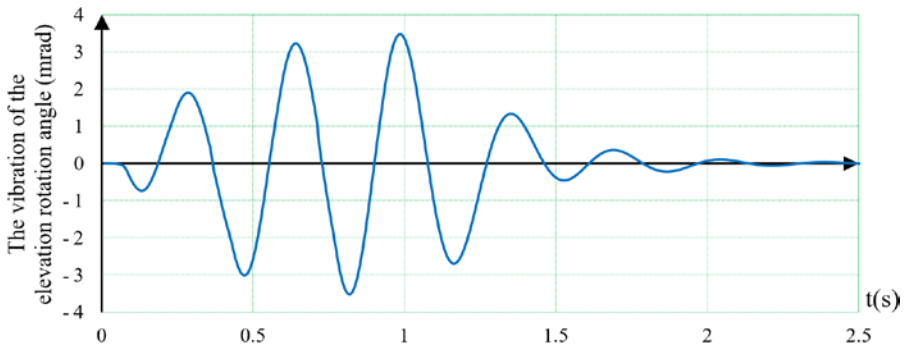


Figure 12 - The vibration of the elevation angle when both barrels fire simultaneously

A comparison of the oscillation plots in Figure 10 and Figure 12 indicates that the elevation oscillation amplitude does not change significantly.

The above computational results and analyses demonstrate that variations in the return spring stiffness cause discrepancies in the recoil stroke of the two barrels, leading to significant deviations in the weapon's aiming direction during firing. This is a primary factor that reduces the firing accuracy of the weapon system.

The experiment

The paper reports experimental measurements on the 37 mm dual-barrel K65 gun to assess the reliability of the established model and then compared the theoretical calculation results with the experimental data. The authors tested the initial spring lengths of the recoil blocks on the left and right sides. The results showed that after a period of operation, there

was a deviation in the initial length, with the recoil block on the right side measuring 539 mm and the block on the left side measuring 578 mm. Therefore, under experimental conditions where the structural factors of both recoil blocks are assumed to be identical and the recoil oil damping in both blocks is the same, a phase shift exists between the left and right barrels due to the spring stiffness. At this point, the left and right barrels of the automatic firing mode do not operate simultaneously, and the forces applied to the two barrels are different.

To measure the motion law of the recoil block and the vibration law of the gun, a high-speed camera SA1.1 was used. The high-speed camera is employed to capture the movement of the recoil block and analyze the dynamic behavior of the gun during firing.



Figure 13 - The FASTCAM SA1.1 model 675K - C1

Technical Specifications of the High-Speed Camera:

- Maximum Recording Speed: 67500 fps;
- Data Memory: 8GB, equivalent to 5457 images at 64x16 pixels and 5400 images at 1024x1024 pixels;
- Sensor: 12-bit DAC;
- Trigger Mode: A mode that ensures reliable activation of the system to capture high-speed images, with available trigger modes in the system (Stats, Center, and End trigger modes);
- Control Computer: SONY VAIO used for installing the PFV software and storing information and captured image files. TEMA software is installed on the SONY VAIO computer to analyze the measurement results (Vo et al., 2021; Tien et al., 2022**;** Nguyen et al., 2024; Vo et al., 2025).

For the high-speed camera, considering the assumed weapon motion velocity, the weapon dimensions, and the required image quality, a recording frequency of 5400 frames per second was selected, providing a resolution of 1024 × 1024 pixels.

The layout diagram of the testing equipment is shown in Figure 14. In this setup, high-speed camera number 2 was used to measure horizontal

vibration and high-speed camera number 3 was used to measure displacement and vibration of the gun. According to (Bien et al., 2021**;** Balla et al., 2011), the measured vibrations serve as the basis for evaluating the stability and firing accuracy of the weapon system.

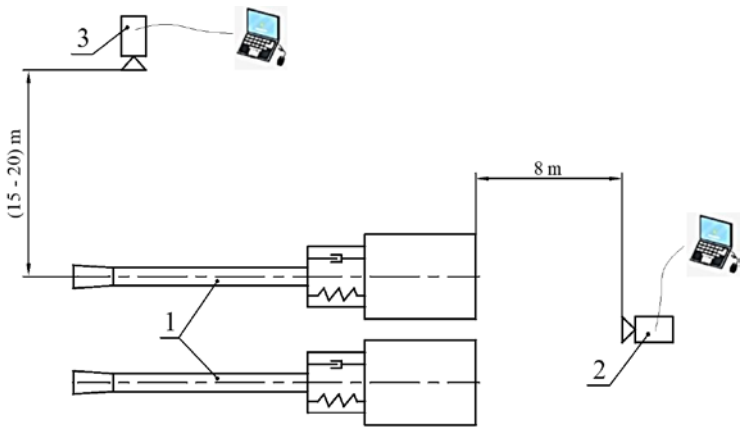


Figure 14 - Experimental setup diagram
1 – 37 mm dual - barrel gun; 2 – high speed camera 2 to measure horizontal vibration; 3 – high speed camera 3 to measure displacement and vibration of the gun

The accelerometers 8766A250BB IEPE, manufactured by KISTLER (Germany), are used to measure the acceleration components along the direction of gravitational acceleration at the sensor mounting locations. The technical specifications of the accelerometer are as follows: measurement range ±250 g; sensitivity 20 mV/g; operating temperature -54°C to +120°C; resolution (1 ÷ 0.01) mg; linearity ±0.5% FS; supply voltage (3.3 ÷ 5) V; frequency response (0.5 ÷ 10.000) Hz.

These sensors are employed to determine the axial acceleration acting on the gun barrel and the vibration characteristics of the gun mount in three directions. Based on the axial acceleration profile of the barrel, the timing of cartridge feeding, ignition, and other operating phases of each barrel can be identified. The system includes: two single-axis accelerometers mounted on the muzzle of the right barrel to measure axial acceleration and lateral vibration, and one tri-axial accelerometer mounted on the muzzle of the left barrel (Figure 15 and Figure 16).

The experiment was conducted under weather conditions with an outdoor temperature of 25°C and an air humidity of 75%. The gun was set to fire in the mode with an elevation angle and traversing rotation angle of 0°. A lifting device was positioned at the rear, camera 2 was aligned with the barrel axis to enable observation of the lateral vibration of the gun

(Figure 17). Camera 3 was positioned perpendicular to the barrel motion to record axial displacement and vibrations in the XOZ plane (Figure 18).

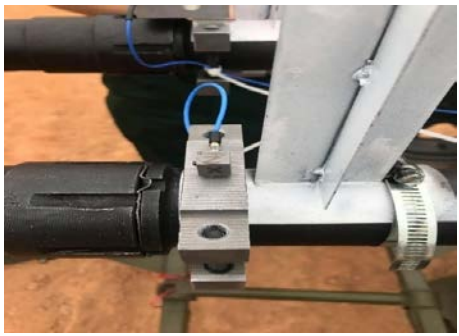


Figure 15 - Fixture and tri-axial accelerometer mounted on the muzzle of the left barrel



Figure 16 - Fixture and single-axis accelerometer mounted on the right barrel



Figure 17 - Position of camera 2



Figure 18 - Position of camera 3

TEMA software is a motion analysis tool that processes and analyzes images captured by high-speed cameras and outputs the analysis results in the form of graphs. The firing results obtained from the accelerometers, the high-speed camera, and the specialized software TEMA allow us to determine the displacement laws of the recoil block (Figure 19, Figure 20) and the vibration of the gun (Figure 21, Figure 22). The experimental results are compared with theoretical calculations based on selecting survey points at the muzzle, which coincide with the measurement points during the firing process.

The experimental results show that the motion laws of the left and right barrels are consistent with the theoretical calculations. Both theoretical and experimental results indicate a discrepancy in the recoil velocity during the recoil phase between the left and right barrels (Figure

19 and Figure 20), with the right barrel having a higher recoil velocity than the left barrel. Specifically, in the first shot, the maximum recoil velocity of the right barrel is 2.85 m/s, and the left barrel is 2.63 m/s. In contrast, according to theoretical calculations, the maximum recoil velocity of the right barrel is 2.67 m/s, and the left barrel is 2.45 m/s. The relative errors are 6.31% and 6.84%, respectively. In the second shot, the maximum recoil velocity of the right barrel is 2.86 m/s, and the left barrel is 2.65 m/s. In contrast, according to theoretical calculations, the maximum recoil velocity of the right barrel is 2.67 m/s, and the left barrel is 2.45 m/s. The relative errors are 6.64% and 7.54%, respectively. The theoretical firing cycle duration for the right barrel is 0.344 s, compared to the experimental measurement of 0.354 s, corresponding to a relative error of 2.8%. Similarly, the firing cycle error for the left barrel is 2.6%.



Figure 19 - Velocity-time curve of the right barrel

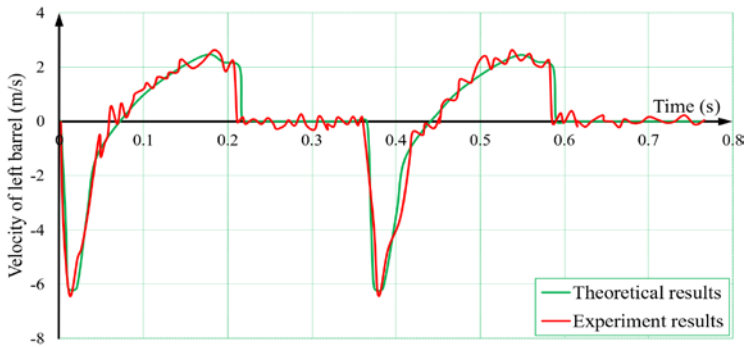


Figure 20 - Velocity-time curve of the left barrel

The vibration law of the gun is relatively accurate and aligns with reality (Figure 21 and Figure 22). The experimental results of the gun's vibration in the vertical plane for two shots at an elevation and traversing rotation angle of 0° (Figure 21) show the following: In the first shot, the maximum amplitude is 8.526 cm at 0.096 s, and the vibration in the

opposite direction has a maximum amplitude of 3.189 cm at 0.228 s. Meanwhile, the experimental results show an amplitude of 7.938 cm at 0.106 s, and in the opposite direction, the amplitude is 3.478 cm at 0.239 s. The maximum time deviation is small, and the amplitude of the upward vibration shows a deviation of 0.588 cm, with a relative error of 6.89%, while the downward vibration has a deviation of 0.289 cm, with a relative error of 8.30%. Similarly, the deviation in the second shot was determined at the points corresponding to the maximum amplitude, with a relative error of 8.51% for the upward vibration and 6.43% for the downward vibration.

Moreover, the misalignment of the two barrels causes a moment of rotation, leading to the gun's horizontal vibration. To assess the accuracy of the model and investigate further, a comparison was made between the theoretical and experimental results of the gun's horizontal vibration (Figure 22). The experimental results, with three shots at an elevation and traversing rotation angle of 0°, show that the horizontal vibration has a maximum amplitude of 5.845 cm to the left and 3.119 cm to the right. The theoretical results for horizontal vibration follow a pattern that is relatively close to the experimental results, with the left vibration having an amplitude of 6.323 cm and the right vibration having an amplitude of 3.412 cm. The amplitude error between theory and experiment is 7.55% for the left vibration and 8.58% for the right vibration. The discrepancy in the results can be attributed to the actual movement of the gun during live firing, where the gun's support legs may shift, and other factors may influence the results. The data in Figure 21 and Figure 22 also show that the time points at which the maximum amplitudes are reached have very little deviation. The vibration law proves that the proposed model is reasonable and relatively close to the experimental results.

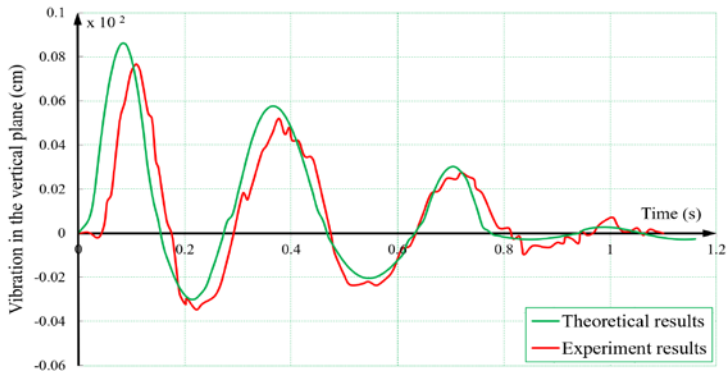


Figure 21 - The vibration in the vertical plane

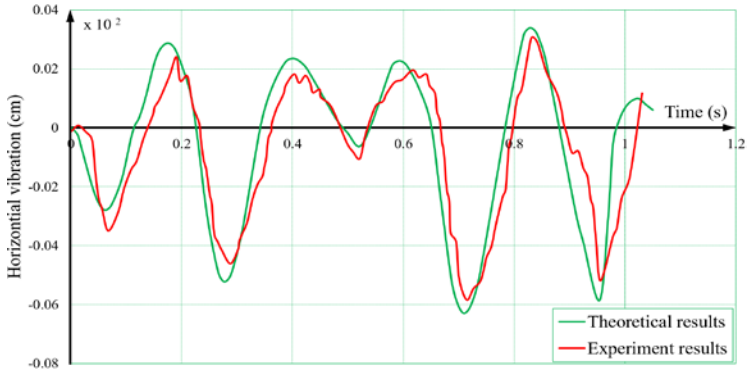


Figure 22 - The horizontal vibration

Conclusion

The paper presents a method for evaluating the firing stability of a dual-barrel automatic weapon on a combat vehicle by investigating the impact of the stiffness of elastic components on the operation of the automatic system. The experimental results were measured using modern, reliable equipment. The experimental method ensures accuracy and safety. Some of the causes of the error can be attributed to the use of assumptions to simplify the theoretical calculation model. Additionally, the phase shift between the two barrels in reality can be due to uneven wear among various components of the gun.

The change in recoil spring stiffness c_{dl} significantly affects the firing cycle of the gun. To increase the firing rate, c_{dl} needs to be increased, but attention must also be paid to the change in the gun's return velocity. The larger the difference in spring stiffness between the two barrels, the greater the vibration of the system, which leads to a decrease in shooting accuracy and a reduced probability of hitting the target.

The obtained results can be applied to the study of changes in the structural parameters of the 37 mm K65 dual-barrel automatic gun, contributing to the improvement of the firing rate, stability, and shooting accuracy. The survey model and research method can be applied to other types of automatic weapons mounted on unmanned vehicles.

References

Aparow, V. R., Hudha, K., Ahmad, M. M. H. M., & Abdullah, S. 2015. Study on the dynamic performance of armored vehicle in lateral direction due to firing impact. *Advances in Military Technology*, 10(2), 5-20 [online]. Available at: https://www.aimt.cz/index.php/aimt/article/download/1076/209. [Accessed: 30 November 2025].

Balla, J. 2011. Dynamics of Mounted Automatic Cannon on Track Vehicle. *International Journal of Mathematical Model and Methods in Applied Sciences*, 5(3), 2011: 423-432 [online]. Available at: https://www.researchgate.net/profile/Jiri-Balla/publication/271749765_Dynamics_of_mounted_automatic_cannon_on_track_vehicle/links/54d0af1c0cf298d65667e77e/Dynamics-of-mounted-automatic-cannon-on-track-vehicle.pdf. [Accessed: 30 November 2025].

Balla, J., Dao, M. H., Truong, T. H., Nguyen, V. D., & Tran, V. T. 2021, June. Firing stability of automatic grenade launcher mounted on tripod. *International Conference on Military Technologies (ICMT)*. IEEE, 2021. p. 1-8 [online]. Available at: https://www.researchgate.net/profile/JiriBalla/publication/353699314_Firing_Stability_of_Automatic_Grenade_Launcher_Mounted_on_Tripod/links/62d2d249a6abd57c6ae9ce15/Firing-Stability-of-Automatic-Grenade-Launcher-Mounted-on-Tripod.pdf. [Accessed: 30 November 2025].

Balla, J., Krist, Z., Racek, F., Melsa, P., Neumann, V., & Le, C. I. 2018. Analysis and parameter identification of automatic cannon carriages. *Defence Science Journal*, 68(6), 525-532. Available at: https://doi.org/10.14429/dsj.68.12395.

Balla, J., Havlicek, M., Jedlicka, L., Krist, Z., & Racek, F. 2011. Firing stability of mounted small arms. *International journal of mathematical models and methods in applied sciences*, 5(3), 412-422 [online]. Available at: https://www.researchgate.net/profile/Jiri-Balla/publication/271752131_Firing_stability_of_mounted_small_arms/links/54d0b16c0cf20323c218bffd/Firing-stability-of-mounted-small-arms.pdf. [Accessed: 30 November 2025].

Bien, V. V., Phon, N. D., & Phu, N. M. 2023. Mathematical model of automatic firing system of gas-operated machine gun. *Applied Engineering Letters*, 8(3), 2023, 91-100. Available at: https://doi.org/10.18485/aeletters.2023.8.3.1.

Bien, V. V., Phuc, T. V., & Macko, M. 2021. Effect of Some Structural Parameters on Firing Stability of Shooter-Weapon System. *Advances in Military Technology*, 16(2), 2021: 235-251. Available at: https://doi.org/10.3849/aimt.01487.

Borkowski, W., Figurski, J., Walentynowicz, J., & Hryciów, Z. 2007. The impact of the cannon on the combat vehicle chassis during firing. *Journal of KONES*, 14, 2007: 49-61 [online]. Available at: https://yadda.icm.edu.pl/baztech/element/bwmeta1.element.baztech-article-BUJ5-0035-

0025/c/httpwww_bg_utp_edu_plartjok12007jo20kones20200720no20120vol201420borkowski20w.pdf. [Accessed: 30 November 2025].

Doan, D. V., Bien, V. V., Quang, M. A., & Phu, N. M. 2023. A Study on Multi-Body Modeling and Vibration Analysis for Twin-Barrel Gun While Firing on Elastic Ground. *Applied Engineering Letters*, 8 (1), 2023. Available at: https://doi.org/10.18485/aeletters.2023.8.1.5.

Dziopa, Z., & Nyckowski, M. 2016. Modal Analysis of a Discrete System in the Form of a Rocket Launcher Installed on a Motor Vehicle. *Problems of Mechatronics, Armament, Aviation, Safety Engineering*, 7(3), 47-58.. Available at: https://doi.org/10.5604/01.3001.0009.2981.

Konečný, P., & Nguyen, D. P. 2021. Effect of Shot Duration on the Firing Accuracy when Burst Fire of Unguided Rockets. *International Conference on Military Technologies (ICMT)*, June 2021, (pp. 1-6). IEEE [online]. Available at: http://eprints.lqdtu.edu.vn/id/eprint/8630/1/Effect%20of%20Shot%20Duration%20on%20the%20Firing%20Accuracy%20when%20Burst%20Fire%20of%20Unguided%20Rockets.pdf. [Accessed: 30 November 2025].

Macko, M., Van VO, B., & Mai, Q. A. 2021. Dynamics of short recoil-operated weapon. Problems of Mechatronics. Armament, Aviation, Safety Engineering, 12(3), 9-26. Available at: https://doi.org/10.5604/01.3001.0015.2432.

Lu, Y., Zhou, K. D., He, L., Li, J. S., & Huang, X. Y. 2019. Research on the floating performance of a novel large caliber machine gun based on the floating principle with complicated boundary conditions. Defence Technology, 15(4), 607-614.. Available at: https://doi.org/10.1016/j.dt.2019.05.001.

Nguyen, D. P., & Macko, M. 2021. Research Technical Solution for Reducing Vibrations of Weapons Mounted on the Vehicle. In 2021 *International Conference on Military Technologies (ICMT),* June 2021, (pp. 1-6). IEEE. Available at: https://doi.org/10.1109/ICMT52455.2021.9502835.

Nguyen, P. D., Vo, B. V., Nguyen, P. M., & Tran, T. H. 2023. Dynamics of Automatic Firing System Type Gas-Operated Weapon. *Problemy Mechatroniki: uzbrojenie, lotnictwo, inżynieria bezpieczeństwa*, 2023, 14. Available at: https://doi.org/10.5604/01.3001.0054.1645.

Nguyen, P. M., Vo, B. V., Dao, D. V., & Nguyen, D. V. 2024. Studying the dynamic characteristics of gas-operated guns using Solidworks Motion software. *Vojnotehnički glasnik/Military Technical Courier*, 2024, 72(3), 1066-1092. Available at: https://doi.org/10.5937/vojtehg72-50987.

Safko, J. L., Goldstein, H., & Poole, C. 2002. *Classical mechanics* [online]. Available at: https://www.academia.edu/download/57055992/Goldstein.pdf. [Accessed: 29 November 2025].

Sun, H. K., Liu, Y. T., & Chen, C. G. 2009. Dynamic Analysis of a Vehicular-mounted Automatic Weapon-Planar Case. Defence Science Journal, 59(3). Available at: https://doi.org/10.14429/dsj.59.1520.

Štiavnický, M., & Lisý, P. 2013. Influence of barrel vibration on the barrel muzzle position at the moment when bullet exits barrel. *Advances in Military Technology*, 8(1), 89-102 [online]. Available at:

https://aimt.cz/index.php/aimt/article/download/1576/57. [Accessed: 30 November 2025].

Thai, D. N., Van, D. N., Van, P. T., & Do Duc, L. 2017, May. Biomechanical analysis of the shooter-weapon system oscillation. *In 2017 International Conference on Military Technologies (ICMT)* (pp. 48-53). IEEE. Available at: https://doi.org/10.1109/MILTECHS.2017.7988729.

Tien, V. D., Macko, M., Procházka, S., & Bien, V. V. 2022. Mathematical Model of a Gas-Operated Machine Gun. Advances in Military Technology, 17 (1). Available at: https://doi.org/10.3849/aimt.01449.

Truong, T. H., Macko, M., Nguyen, D. P., & Vu, D. T. 2021, June. Effect of Some Structural Parameters on the Firing Stability of the PKMS Machine Gun when Firing with Complicated Boundary Conditions. *International Conference on Military Technologies (ICMT)*, 2021, (pp. 1-6). IEEE. Available at: https://doi.org/10.1109/ICMT52455.2021.9502820.

Van Bien, V., Macko, M., Dung, N. T., Phon, N. D., Hai, N. T., & Tuan, B. T. 2021. Dynamic Simulation Analysis and Optimization of Firing Rate of Rocket Launchers on Wheeled Vehicles. *Advances in Military Technology*, 16(1), 2021: 159-175. Available at: https://doi.org/10.3849/aimt.01459.

Vo, B. V., Nguyen, P. D., Nguyen, P. M., & Vu, L. X. 2025. Research into the effect of ammunition belt stiffness on the operation of automatic firing systems using experimental methods. *Vojnotehnički glasnik/Military Technical Courier*, 2025, 73(2), 469-495. Available at: https://doi.org/10.5937/vojtehg73-54574.

Vo, V. B., Macko, M., & Dao, H. M. 2021. Experimental study of automatic weapon vibrations when burst firing. *Problemy Mechatroniki: uzbrojenie, lotnictwo, inżynieria bezpieczeństwa*, 2021, 12. Available at: http://dx.doi.org/10.5604/01.3001.0015.5984

Uticaj elastičnih elemenata na stabilnost gađanja automatskog naoružanja postavljenog na borbena vozila

Ba Ngoc Dang[a], **autor za prepisku**, *Martin* Macko[a], *Frantisek* Racek[a], *Viet Dung* Bui[b], *Quang* A. Mai[b]

[a] University of Defence, Faculty of Military Technology, Department of Weapons and Ammunition, Brno, Czech Republic,

[b] Tran Dai Nghia University, Faculty of Ammunition, Department of of Explosives and Ballistics, Hochiminh, Socialist Republic of Vietnam,

OBLAST: matematika, mašinstvo
KATEGORIJA (TIP) ČLANKA: originalni naučni rad

Sažetak:

Uvod/cilj: Ispitivanje faktora koji utiču na vibracije sistema automatskog naoružanja koje je postavljeno na borbeno vozilo predstavlja važnu naučnu osnovu za unapređenje stabilnosti gađanja, preciznosti i sposobnosti uništavanja ciljeva. Kod automatskog naoružanja sa više cevi, unutrašnja

odstupanja u samom oružju mogu dovesti do asinhronog rada automatskih mehanizama pojedinačnih cevi, a jedan od glavnih razloga za ovu pojavu su razlike u elastičnim elementima svake cevi. Fazna razlika između cevi dovodi do nestabilnosti kako ugla elevacije tako i ugla pravca, čime se smanjuje preciznost gađanja.

Metode: Diferencijalne jednačine sistema rešene su numerički u programu Maple kako bi se utvrdilo na koji način različite vrednosti krutosti povratne opruge izazivaju fazne pomake između dve cevi. Rezultati su eksperimentalno validirani.

Rezultati: Rezultati simulacije ukazuju na značajan uticaj krutosti elastičnog elementa na oscilacije sistema u pravcu. Merenja izvršena brzom kamerom FASTCAM SA1.1 na dvocevnom topu kalibra 37 mm u režimu automatske paljbe pokazuju visok stepen podudarnosti između teorijskog modela i eksperimentalnih rezultata. Karakteristike vibracija sistema, kako u ravni gađanja tako i u horizontalnoj ravni, veoma su bliske stvarnom ponašanju, pri čemu je greška manja od 8,6%.

Zaključak: Dinamički model omogućava optimizaciju konstruktivnih parametara sistema naoružanja. Dobijeni rezultati predstavljaju važnu osnovu za predlaganje rešenja za povećanje brzine paljbe i poboljšanje stabilnosti gađanja sistema naoružanja koja su montirana na vozila, besposadne kopnene platforme i borbene robote.

Ključne reči: dvocevno automatsko naoružanje, stabilnost gađanja, povratna opruga, borbeno vozilo.

Paper received on: 30 November 2025.
Manuscript corrections submitted on: 5 February 2026.
Paper accepted for publishing on: 30 March 2026.

© 2026 The Authors. Published by Vojnotehnički glasnik / Military Technical Courier (www.vtg.mod.gov.rs).This article is an open access article distributed under the terms and conditions of the Creative Commons Attribution license (http://creativecommons.org/licenses/by/4.0/rs/)



Analyzing the belt feed dynamics of gas-operated machine guns

Van Dung Nguyen[a], *Van Bien* Vo[b], *Minh Phu* Nguyen[c], *Xuan Long* Vu[d]

[a] Le Quy Don Technical University, Faculty of Special Equipment, Hanoi, Socialist Republic of Vietnam
e-mail: dungnv@lqdtu.edu.vn,
ORCID iD: https://orcid.org/0000-0003-3460-5238

[b] Le Quy Don Technical University, Faculty of Special Equipment, Hanoi, Socialist Republic of Vietnam
e-mail: vovanbien@lqdtu.edu.vn, **corresponding author**,
ORCID iD: https://orcid.org/0000-0002-1364-2884

[c] Department of Weapons and Ammunition, University of Defence, Brno, Czech Republic
e-mail: minhphu.nguyen@unob.cz,
ORCID iD: https://orcid.org/0009-0000-8599-1445

[d] Tran Dai Nghia University, Ho Chi Minh City, Socialist Republic of Vietnam
e-mail: vuxuanlong@gmail.com,
ORCID iD: https://orcid.org/0009-0005-3633-7902

https://doi.org/10.5937/vojtehg74-60086

FIELD: mathematics, mechanical engineering
ARTICLE TYPE: original scientific paper

Abstract:

Introduction/purpose: This paper introduces a simulation methodology for accurately determining the kinematic parameters of ammunition belts in gas-operated machine guns during short-burst firing.

Methods: The study develops a comprehensive mathematical model grounded in Newton's second law to describe the belt's dynamic behavior. A system of differential equations is established, integrating all relevant forces acting on each belt link under realistic operational conditions to precisely capture the belt's motion. A dynamic simulation of the ammunition belt integrated with the automatic firing mechanism was conducted. The simulation outcomes were subsequently compared with experimental data to verify the model's accuracy. The model is applied for calculations and experimental testing on the PKMS 7.62 mm machine gun.

Results: The simulation results identified the motion patterns of the bolt carrier, the feed pawl, the belt link movements, the belt pulling force, and the elastic forces between the links during burst firing. The calculated results from the theoretical model demonstrate good agreement with the experimental data. The maximum deviation between theoretical predictions and experimental measurements remains within 5.11%.

Conclusion: These findings provide a fundamental theoretical basis for the future design and optimization of gas-operated machine gun systems.

Keywords: ammunition belt dynamics, ammunition belt, 7.62 mm PKMS machine gun, gas-operated machine gun, 7.62x54 mmR ammo.

Introduction

The reliability of gun operation is a critical factor that directly affects a soldier's combat effectiveness on the battlefield. This reliability encompasses various aspects such as firing accuracy, operational stability, and effective performance under diverse combat conditions (Balla et al., 2015; Fiser & Popelinsky, 2007; Allsop, 1997). Among the many factors that influence these aspects, the motion of the ammunition belt plays a significant role. During firing, rounds must be fed precisely and promptly, while minimizing energy consumption in the feeding process. Vibrations and strong impacts on the ammunition should be avoided. If these requirements are not met, undesirable forces may act on the mechanisms of the firing system. This can lead to wear, strong vibrations, unstable firing, and changes in the operational cycle of the automatic system. Consequently, the firing cycle of each shot may also be affected. In more severe cases, this may cause jamming, misfeeding, or even damage to the ammunition belt or the entire firing system, ultimately rendering the weapon unable to fire (Fiser & Popelinsky, 2007).

In automatic artillery weapons, the ammunition feeding mechanism is a crucial component that directly affects the reliability and stability of the weapon system. This mechanism operates either by utilizing the primary energy from the firing process or by using an external power source. In certain cases, when the energy from firing is insufficient, it may be supplemented by external energy sources (Zbigniew et al., 2024; Balla & Mach, 2007). The feeding method determines both the design structure and the operational behavior of the automatic firing system. Currently, there are several commonly used ammunition feeding methods, including clip feeding, magazine feeding, and belt feeding (Fiser & Popelinsky, 2007). Among these, the belt feeding method has the most significant impact on the operation of the automatic firing system and the overall performance of the weapon.

In this paper, the belt feeding method is specifically studied on the PKMS 7.62 mm machine gun (see Figure 1). The lever-type feeding mechanism of the PKMS machine gun is illustrated in Figure 2, and the ammunition belt structure is shown in Figure 3.



Figure 1 - PKMS 7.62 mm machine gun

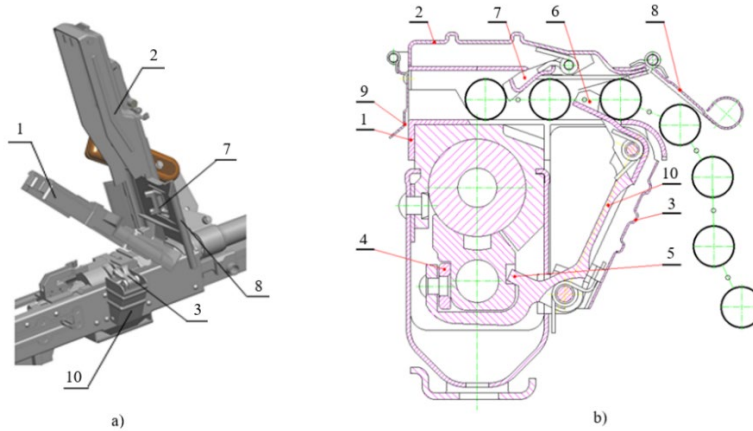


Figure 2 - Diagram of the lever-type ammunition feeding mechanism of the PKMS machine gun
a) General view; b) Cross-section
1. Feeding base; 2. Feed cover; 3. Belt-pulling claw lever; 4. Roller; 5. Pusher lug; 6. Belt-pulling claw; 7. Belt retainer claw; 8. Right dust cover; 9. Left dust cover; 10. Cover for belt-pulling claw lever

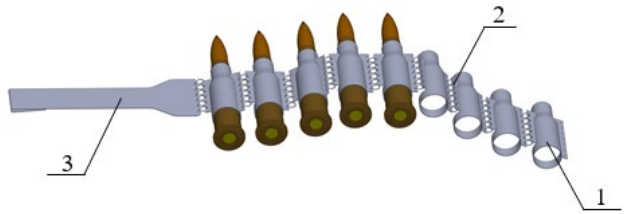


Figure 3 - Ammunition belt
1. Belt link; 2. Belt link connector; 3. Belt leading end

To transmit motion from the driving component of the automatic weapon to the belt-pulling mechanism, cam linkages, levers, or transmission rods are commonly used (P.N. Thieu, 2004; Fiser, 2007). The driving component can be the barrel, the bolt, or the bolt carrier.

- In mechanisms where the barrel serves as the driving component, the operation is stable and reliable. However, due to the barrel's limited movement range, a large transmission force is required, which necessitates larger-sized components to ensure strength and durability. As a result, this type of mechanism is rarely used.

- Mechanisms that use the bolt as the driving component do not suffer from the above size limitation, but their operational reliability is generally lower.

- The most advantageous configuration is the mechanism that uses the bolt carrier as the driving component, which overcomes the aforementioned drawbacks. This configuration is particularly suitable for machine guns operating on the gas-operated principle, and therefore, it is widely adopted in modern machine guns.

The movement of the ammunition belt is closely linked to the automatic firing system; all forces acting on the belt affect the operation of the firing system, and vice versa. If these forces are not properly distributed, they can cause damage to the ammunition belt, jamming, misfeeding, and ultimately prevent the weapon from firing. The motion pattern of the ammunition belt is often uneven and intermittent, varying between individual rounds within the belt as well as between shots in a firing burst. Additionally, the forces acting on each round continuously change, resulting in complex mechanical collisions, which make dynamic calculations highly challenging and require accurate, sophisticated analytical models. In the past, due to the limited development of computer engineering technology and insufficient computational capacity for handling large-scale calculations, numerical models of ammunition belt dynamics were significantly constrained. To simplify the study, some previous research has often modeled the ammunition belt as a soft elastic string with uniformly distributed mass, and its motion was represented by theoretical waveforms, including incident waves and reflected waves acting independently (Han et al., 2011). These studies also indicated that only the incident wave causes elongation forces in the ammunition belt, generating resistance during firing, while the reflected wave serves to reduce this resistance.

In this study, the ammunition belt is modeled as an elastic string of length l, subjected to a belt-pulling force P_T (see Figure 4). The equation of motion for the belt string is expressed as follows:

$$m\frac{\partial^2 u}{\partial t^2} = Ks^2\frac{\partial^2 u}{\partial x^2} \quad (1)$$

where *m* is the mass of an element (consisting of one round and one belt link); *s* is the belt pitch; *K* is the stiffness of the belt link; *x* is the position of the cross-section under consideration, measured from the free end of the belt; *u* is the displacement of the cross-section at position *x*.

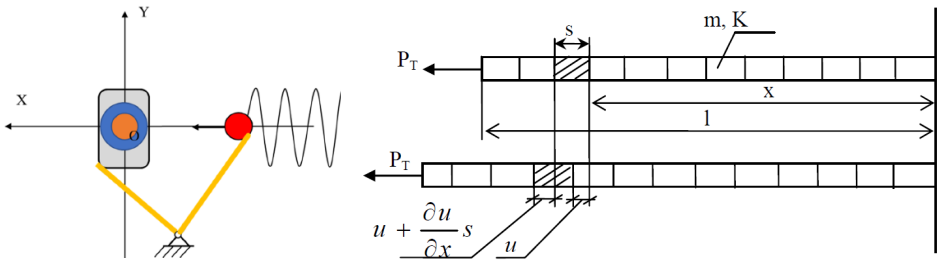


Figure 4 - Dynamic model of the ammunition belt based on wave theory

Regarding the ammunition feeding process, several studies have applied multi-body mechanics theory to investigate the dynamics of the ammunition belt (Van Hung et al., 2024). A dynamic model of the ammunition belt for aircraft-mounted guns was developed, with belt movement simulated using MATLAB software. The dynamic behavior of the ammunition belt for the high-rate-of-fire multi-barrel Gatling machine gun was also studied in Balla & Mach (2007). This research concluded that calculation formulas based on wave theory are unsuitable for analyzing the dynamics of the ammunition belt in such cases. Another related study examined the longitudinal mechanical characteristics of an ammunition belt system using a spiral-type guide mechanism (Zbigniew et al., 2024). To replicate the behavior of the ammunition belt, a virtual spring was employed to connect the two contact points of the belt. A recent study by the authors' group related to the dynamics of the ammunition belt has been published (Vo et al., 2025). In this study, the authors conducted experimental investigations to assess the influence of belt stiffness on the operation of the automatic firing system. They also determined the belt's motion, the displacement velocity of the belt links, and the elastic forces occurring between the links during firing. These findings provide a reliable scientific basis for validating the theoretical calculations and simulation results presented in this paper.

In summary, the dynamic modeling of the ammunition belt for gas-operated machine guns remains a novel research area that requires further investigation. To improve accuracy and reliability in studying the

ammunition belt dynamics, this research focuses on developing a mathematical model describing the three-dimensional motion of the ammunition belt. The simulation results obtained from this model are validated against experimental data previously published by the authors. The 7.62 mm PKMS machine gun was selected as the subject for the ammunition belt dynamic simulation and experimental validation.

For the reader's convenience, this paper is organized as follows: the first section provides a general introduction and a review of related works. The second section describes the dynamic modeling of the ammunition belt during the operation of the firing system. The following section presents the experimental results used to validate the proposed mathematical model. Finally, the last section concludes the paper.

Dynamics of the ammunition belt

Dynamic model of the ammunition belt

Assumptions

To investigate the motion of the ammunition belt during burst firing, forming the foundation for assessing its effect on the reliability of the automatic firing system, the following assumptions are made in this study:

- The gun housing is fixed in a locked position; the ammunition belt's movement during firing is primarily caused by the belt puller claw.
- Rounds number 1 and 2, located within the guide frame of the feed tray, move solely by translation. Rounds from number 3 up to the round at the ejection port move coplanarly in a plane perpendicular to the barrel axis;
- The connections between belt links are assumed to be viscous-elastic joints and frictionless rotary joints, where K_{i} represents the tensile stiffness of the *i*-th belt link connection, C_{i} is the material damping coefficient of the *i*-th belt link connection, and these joints are massless with frictionless rotary movement (see Figure 5);
- Each round installed within a belt link is considered a perfectly rigid body. The distributed mass of the round is replaced by a concentrated mass and moment of inertia located at the centroid of each component in the system. The centroids of all components lie on a plane perpendicular to the barrel axis;
- The belt pulling force generated by the automatic firing system's belt puller claw is applied at the centroid of the first round. Elastic forces between belt links arise when the belt is under tension; if a gap occurs

between the links, the elastic force becomes zero, and the connection acts as a translational joint along the line connecting the two links.

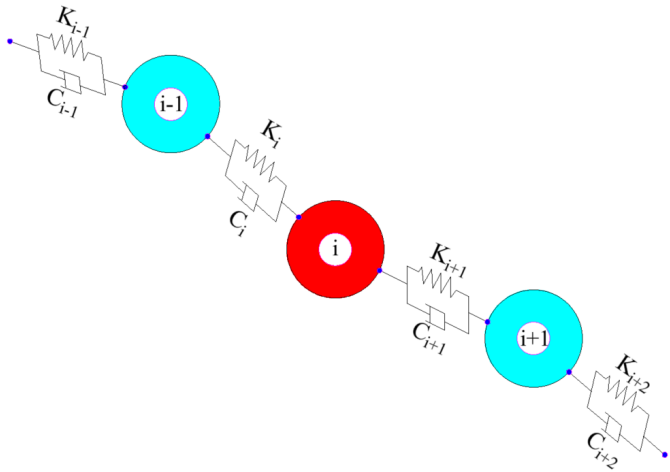


Figure 5 - Discretized model of the ammunition belt

Computational model of ammunition belt motion during firing

Based on the stated assumptions, the schematic of the PKMS machine gun's firing system (Figure 6) and actual combat operating conditions, a dynamic model of the ammunition belt containing n rounds is developed and illustrated in Figure 7.

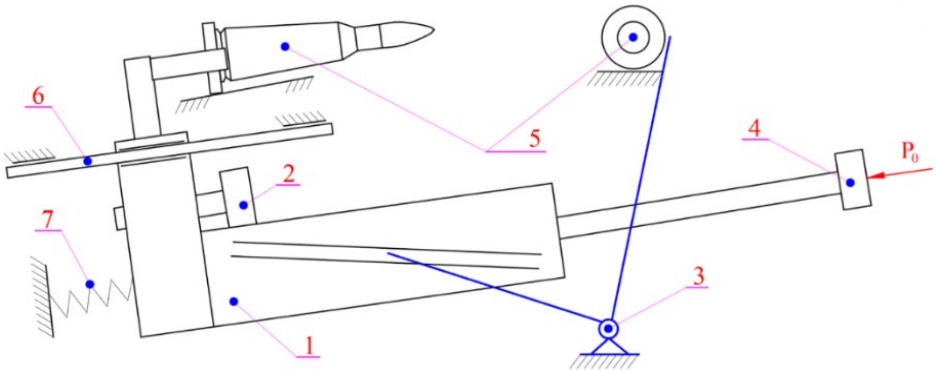


Figure 6 - Diagram of the automatic firing system of the PKMS machine gun
1. Bolt carrier; 2. Bolt; 3. Feed lever; 4. Piston; 5. Cartridge;
6. Guide rail on the weapon casing; 7. Return spring

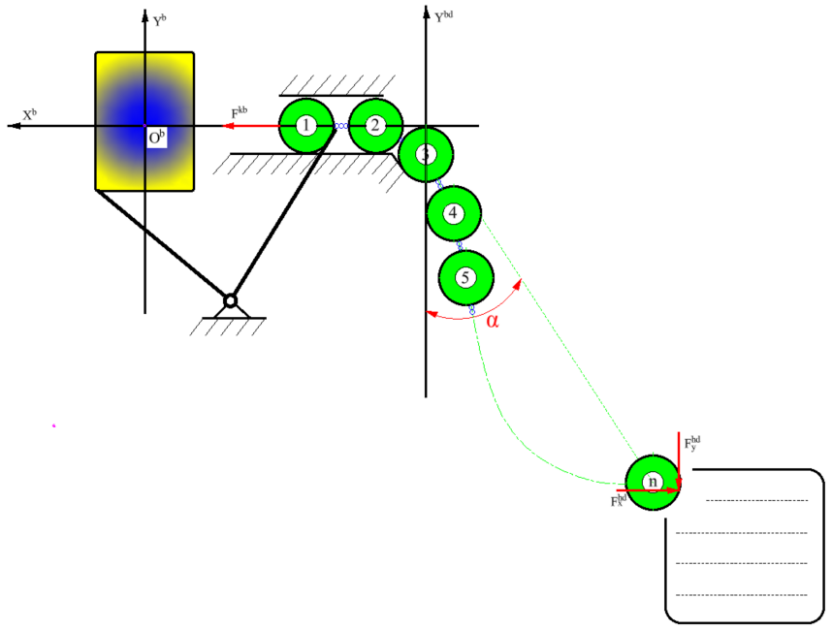
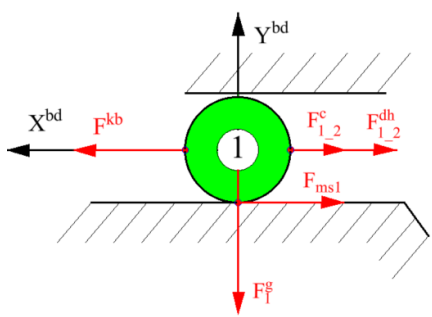


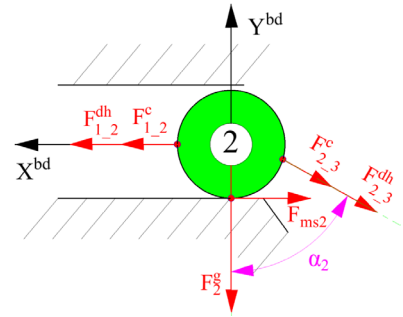
Figure 7 - A computational model of ammunition belt motion during burst firing

Forces acting on the ammunition belt during firing

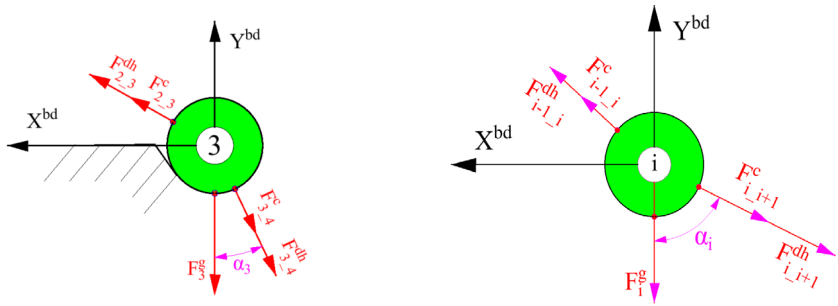
The main forces acting on the discretized ammunition belt are illustrated in Figure 8, including F^{kb} – belt pulling force; F^{ms} – friction force between the cartridge and the feed tray; F^{dh} – elastic force between the belt links; F^{c} – material damping force between the belt links; F^{g} – gravitational force of the cartridge; F^{hd} – the holding force at the ammunition box outlet was experimentally measured by extracting the ammunition belt from the box.



a. Forces acting on the first cartridge



b. Forces acting on the second cartridge



c. Forces acting on the third cartridge *d. Forces acting on the i-th cartridge*

Figure 8 - Forces acting on the cartridge after discretization

- Gravitational Force

The gravitational force is the force acting on the objects (cartridges suspended on the ammunition belt) in a direction perpendicular to the horizontal plane and directed downward. The gravitational force is determined by the following formula:

$$F_i^g = m_i g \tag{2}$$

where m_i is the mass of the *i*-th cartridge and belt link; *g* is the gravitational acceleration.

- Ammunition belt pulling force

The belt-pulling force originates from the motion of the driving component in the automatic firing system and is transmitted through the belt-feeding mechanism to draw the ammunition belt inward. This force is applied directly to the first cartridge in the belt.

Accurately determining the belt pulling force based on the actual configuration of the ammunition belt, considering the presence of clearances and resistance forces acting on the belt links, is a complex task. To simplify the analysis while maintaining the necessary level of accuracy, a computational model is employed to determine the value of the belt pulling force (F^{kb}) (see Figure 9) (Bien et al., 2021; Doan et al., 2023). In this case, the belt-pulling force is calculated using the following equation:

$$F^{kb} = v_b\sqrt{k_b m} + mgn_1(\sin\theta + f\cos\theta) + n_2 mg \tag{3}$$

where v_b - speed of the belt feed part; k_b - stiffness of the belt link; m - mass of the belt link with the cartridge; g - gravitational acceleration; n_1 - number of cartridges on the inclined plane with an inclination angle θ; n_2 - number of cartridges hanging in the ammunition box; f - coefficient of friction between the cartridge and the guide rail.

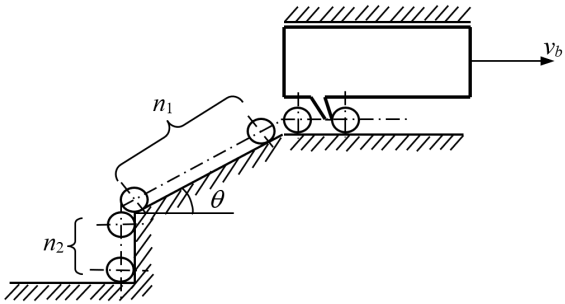


Figure 9 - Diagram for calculating the belt-pulling force

- Friction force between the cartridge and the feed tray

The cartridge moves within the guide channel of the feed tray (the first and second cartridges), always maintaining contact with the guiding frame, which results in the occurrence of a friction force. The friction force is calculated using the following expression:

$$F_{ms} = f_{ms} F_i^g \tag{4}$$

where f_{ms} is the coefficient of friction between the cartridge and the feed tray, F_i^g is the weight of the cartridge and belt link.

- Elastic force between the belt links

Let Δr_{i_i+1} denote the absolute deformation, which equals zero when there is a gap in the connection between two belt links. Let ε_{i_i+1} be the original length of the connection between the *i*-th and (*i*+1)-th belt links. L_{0_i} is the length at the current moment of the two belt links. Based on the assumption of a flexible belt that only undergoes tension and no compression, we have:

$$\varepsilon_{i_i+1} = \begin{cases} \dfrac{\Delta r_{i_i+1}}{L_{0_i}} & \text{when} \quad \Delta r_{i_i+1} \geq 0 \\ 0 & \text{when} \quad \Delta r_{i_i+1} < 0 \end{cases} \tag{5}$$

with: $\Delta r_{i_i+1} = L_{i_i+1} - L_{0_i}$;

$$L_{i_i+1} = \sqrt{\left(X_{b\mathrm{d(i+1)}} - X_{b\mathrm{d(i)}}\right)^2 + \left(Y_{b\mathrm{d(i+1)}} - Y_{b\mathrm{d(i)}}\right)^2}$$

In the case of linear elasticity, the elastic force is determined as follows:

$$F_{i_i+1}^{dh} = K_i \varepsilon_{i_i+1}$$

with $K_i = E_i F_i$; E_i is the elastic modulus of the material; F_i is the cross-sectional area of the element.

In the case of nonlinear elasticity, the elastic force is obtained from the force-deformation curve determined experimentally.

- Material damping force between the belt links

In the general case, the material damping force is taken into account. This force is proportional to the deformation rate of the element and is determined by the following formula:

$$F_{i_i+1}^{c} \begin{cases} C_i \dot{\varepsilon}_{i_i+1} & when \quad \Delta r_{i_i+1} \geq 0 \\ 0 & when \quad \Delta r_{i_i+1} < 0 \end{cases} \tag{6}$$

where C_i is the viscous damping coefficient of the belt.

Formulating the system of differential equations describing the motion of the ammunition belt

System of equations describing the motion of the ammunition belt

Based on Newton's second Law applied to the motion of the center of mass, the system of differential equations describing the translational motion of the cartridges in the ammunition belt in the OXY coordinate system is established as follows:

$$m\vec{a} = \vec{F} \tag{7}$$

where $\vec{a}$ is the acceleration of the object; $\vec{F}$ is the net force acting on the object; m – is the mass of the object.

$$\begin{cases} m_1 \ddot{X}_1 = F^{kb} - F_{1_2}^{dh} - F_{1_2}^{c} - F_{ms1} \\ m_2 \ddot{X}_2 = F_{1_2}^{dh} + F_{1_2}^{c} - \left(F_{2_3}^{dh} + F_{2_3}^{c}\right)\sin\alpha_2 - F_{ms2} \\ m_i \ddot{X}_i = \left(F_{i-1_i}^{dh} + F_{i-1_i}^{c}\right)\sin\alpha_{i-1} - \left(F_{i_i+1}^{dh} + F_{i_i+1}^{c}\right)\sin\alpha_i \quad (i = 3 \div n-1) \\ m_i \ddot{Y}_i = \left(F_{i-1_i}^{dh} + F_{i-1_i}^{c}\right)\cos\alpha_{i-1} - \left(F_{i_i+1}^{dh} + F_{i_i+1}^{c}\right)\cos\alpha_i - F_i^{g} \quad (i = 3 \div n-1) \\ m_n \ddot{X}_n = \left(F_{n-1_n}^{dh} + F_{n-1_n}^{c}\right)\sin\alpha_{n-1} - F_x^{hd} \\ m_n \ddot{Y}_n = \left(F_{n-1_n}^{dh} + F_{n-1_n}^{c}\right)\cos\alpha_{n-1} - F_y^{hd} - F_i^{g} \end{cases} \tag{8}$$

where m_i are the mass of the i-th cartridge and its corresponding link segment.

Auxiliary equations

The motion of the ammunition belt is closely linked to the motion of the firing system, with the forces acting on the belt being generated by the system itself. To comprehensively and accurately study the dynamics of the ammunition belt, it is necessary to simultaneously solve the belt dynamics problem in conjunction with the internal ballistics problem, thermodynamics within the gas chamber, and the dynamic characteristics of the automatic firing mechanism.

- The system of equations for internal ballistics

In this study, the system of differential equations for internal ballistics is adopted based on the models presented in detail in references (Beer et al., 2004; Hu et al., 2019; Kuo et al., 2012). The system of differential equations describing the internal ballistic process is shown in expression (9). The symbols used in equation (9) are explained in detail in references (Beer et al., 2004; Bien et al., 2021).

$$\begin{cases} \dot{l} = v\xi_1\xi_3 \\ \dot{v} = \dfrac{pS}{\varphi m}\xi_1\xi_3 \\ \dot{z} = \dfrac{p}{I_k}\xi_2 \\ \dot{\omega}_k = \xi_2\chi\omega\left(1+2\lambda z\right)\dfrac{p}{I_k} - G_\phi\left(1-\xi_3\right) - G_n\xi_4 \\ \dot{W} = \xi_2\dfrac{1}{\delta}\chi\omega\left(1+2\lambda z\right)\dfrac{p}{I_k} + Sv\xi_3 \\ \dot{p} = \dfrac{1}{W}\left[\begin{array}{l} \xi_2 f\chi\omega\left(1+2\lambda z\right)\dfrac{p}{I_k} - K_t p - K_p p\dot{W} - \\ -K_p G_\phi\left(1-\xi_3\right) - K_p G_n\xi_4 \end{array}\right] \end{cases} \tag{9}$$

- System of thermodynamic equations for the gas chamber

The thermodynamic differential equation system of the gas chamber (10) includes the following equations: the mass conservation equation, the gas chamber volume variation equation, and the energy conservation

equation. This system is presented and explained in detail in references (Hu et al., 2019; Vo et al., 2025).

$$\begin{cases} \dot{\omega}_b = \left(G_\phi - G_\Delta\right)\xi_4 - \xi_5 G_x; \\ \dot{W}_b = S_p v_b \xi_4 \\ \dot{p}_b = \dfrac{1}{W_b}\left[G_\phi kRT - G_\Delta kRT_b - G_x kRT_b - K_{Tb}p_b - kp_b S_b v_b\right]\xi_4 \end{cases} \quad (10)$$

- Dynamic model of the automatic firing system

In this study, the system of differential equations of the firing system dynamics (11), which was developed in detail by the authors in references (Tien et al., 2022; Han et al., 2011; Dingguo, 1996), is used.

$$M_{11}\ddot{x} + M_{12}\dot{x}^2 + c_0 x = P_1 \quad (11)$$

where $M_{11} = m_0 + \sum_{i=1}^{n} \frac{k_i^{\,2}}{\eta_i} m_i$ - is the reduced mass of the operating component of the automatic firing system. $M_{12} = \sum_{i=1}^{n} \frac{k_i}{\eta_i} m_i \frac{dk_i}{dx}$ are the auxiliary moment of inertia of the working components m_i. $P_1 = P_0 - \Pi_0 - \sum_{i=1}^{n} \frac{k_i}{\eta_i} P_i$ is the equivalent force acting on the base component of the automatic firing system.

The differential equation system describing the dynamics of the ammunition belt (8) is solved simultaneously with the internal ballistics equations (9), the thermodynamic chamber equations (10), and the differential equations governing the dynamics of the automatic firing system (11). The block diagram illustrating the solution process for the ammunition belt dynamics problem is shown in Figure 10.

In the block diagram shown in Figure 10, the functions of the blocks are as follows: 1- Input initial conditions; 2 - Determine the forces acting on the base link; 3 - Calculate the values of resistive forces; 4 - Determine the values of K_i and η_i; 5,6- Determine the coefficients ξ_i ; 7 - Check whether a collision occurs; 8 - Calculate the velocity variation due to collision; 9 - Analyze the termination condition of the calculation; 10 - Record the results; 11 - Stop the program.

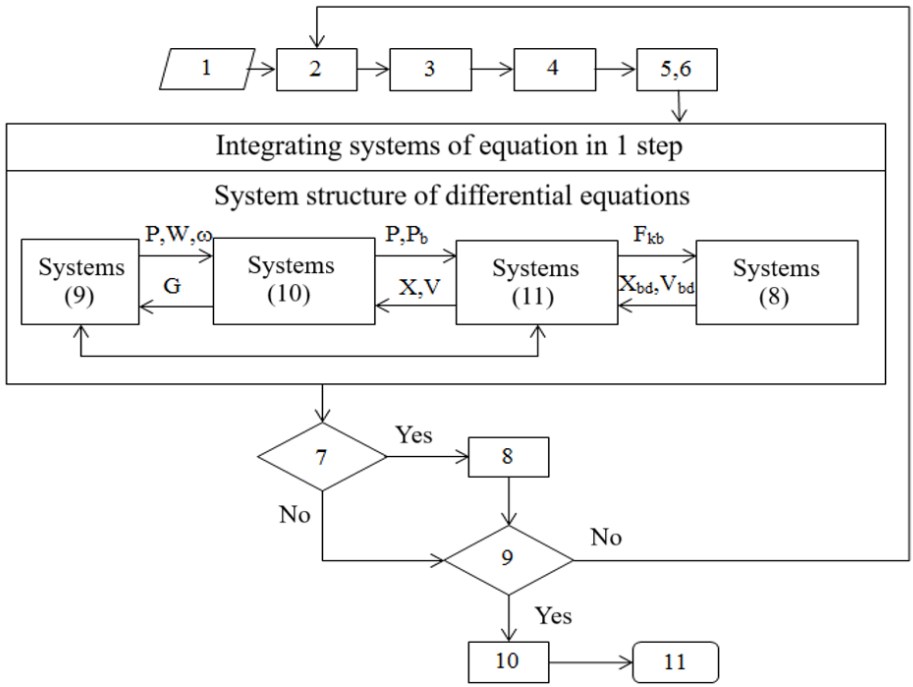


Figure 10 - Block diagram for solving the ammunition belt dynamics problem

To verify the dynamic model of the ammunition belt operating within the firing system, the PKMS 7.62 mm machine gun was chosen for experimental study using 7.62×54 mmR cartridges. Input parameters were determined using various methods. Parameters related to dimensions, mass, and internal ballistics were obtained either through direct measurements of the weapon or from technical documentation. Parameters such as moments of inertia, points of force application, and coordinates of the center of mass were determined using SolidWorks software (Nguyen et al., 2024). In addition to the conditions for solving the dynamic problems of the firing system, when solving the integrated dynamic problem of the ammunition belt, it is important to note that after each shot, the positions of the subsequent rounds are pushed forward to replace the preceding ones. The first and second rounds move only by translation along the X-axis within the feed tray frame, while the remaining rounds move in both the X and Y directions. When there are no more rounds left in the ammunition box, after each shot, the number of motion equations for the belt links decreases by two equations corresponding to the X and Y directions.

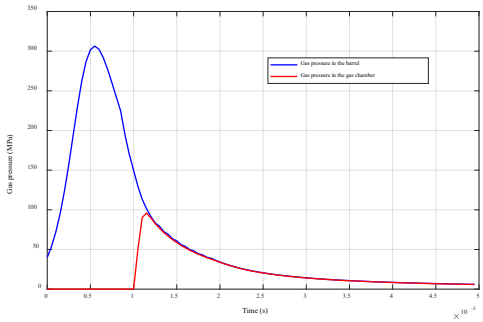


Figure 11 - Propellant gas pressure graph

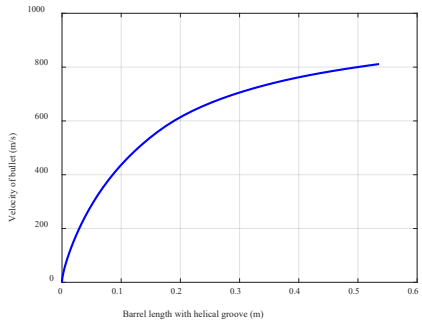


Figure 12 - Velocity of the bullet movement

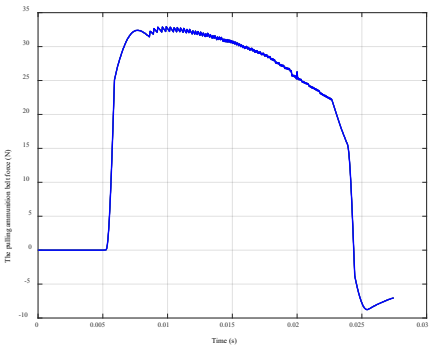


Figure 13 - Graph of the feed belt pulling force

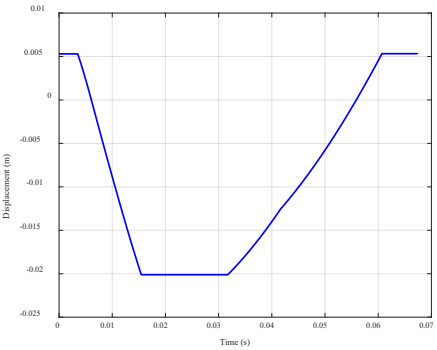


Figure 14 - Movement of the feed lever

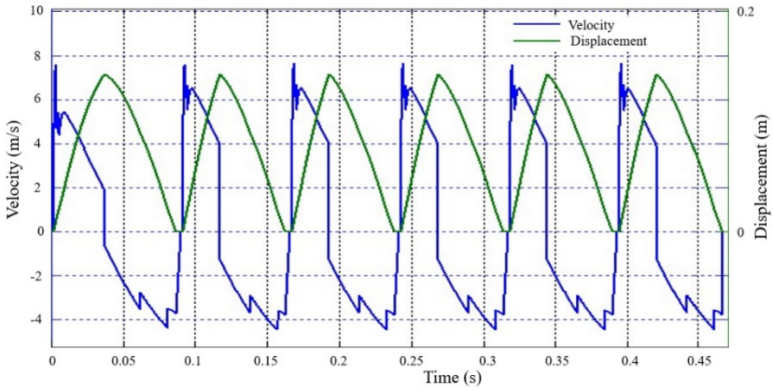


Figure 15 - Displacement and velocity graph of the bolt carrier

After solving the system of equations following the block diagram in Figure 10, several typical results were obtained as follows: the pressure

curves of the propellant gas inside the barrel and the gas chamber are shown in Figure 11; the velocity curve of the bullet movement is shown in Figure 12; the pulling force on the ammunition belt is shown in Figure 13; the feed lever's movement trajectory is shown in Figure 14; the displacement and velocity curves of the bolt carrier during a 6-round burst are shown in Figure 15; the displacement pattern of the ammunition belt is shown in Figure 16; the velocity of the belt links is shown in Figure 17; Figure 18 illustrates the elastic force between the belt links.

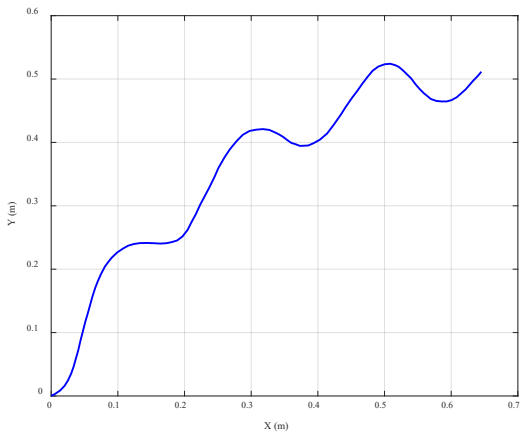


Figure 16 - Displacement of the ammunition belt during firing

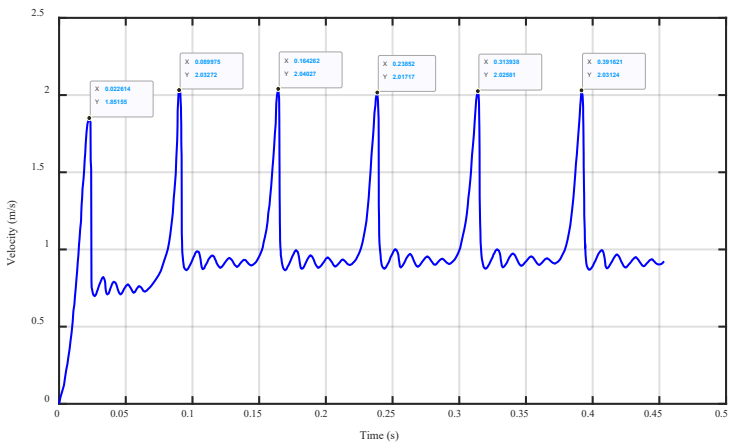


Figure 17 - Belt link velocity during firing

Based on the obtained results, the following observations can be made:

- The pressure variation pattern in the barrel and gas chamber corresponds well to the results published in the design documents (P.N. Thieu, 2004). The calculated propellant gas pressure in the barrel is 306.4 MPa (see Figure 11), while the manufacturer's published data indicates 292.2 MPa, resulting in an error of 4.86%.

- The firing time for one shot is 0.0851 seconds, corresponding to a theoretical firing rate of 705 rounds per minute (see Figure 15); the firing time per shot published in (Bien et al., 2023) is 0.0802 seconds, corresponding to a theoretical firing rate of 748 rounds per minute, with an error of 5.75%.

- During automatic firing, the cartridges suspended on the ammunition belt undergo complex motion, which is strongly influenced by the number of rounds present on the belt. The belt link reaches a maximum velocity of 1.8515 m/s during the first shot, with this value increasing in subsequent shots (see Figure 17). During the initial shot, the elastic force between adjacent belt links attains a maximum value of 171.792 N, which then gradually decreases with subsequent firing (see Figure 18).

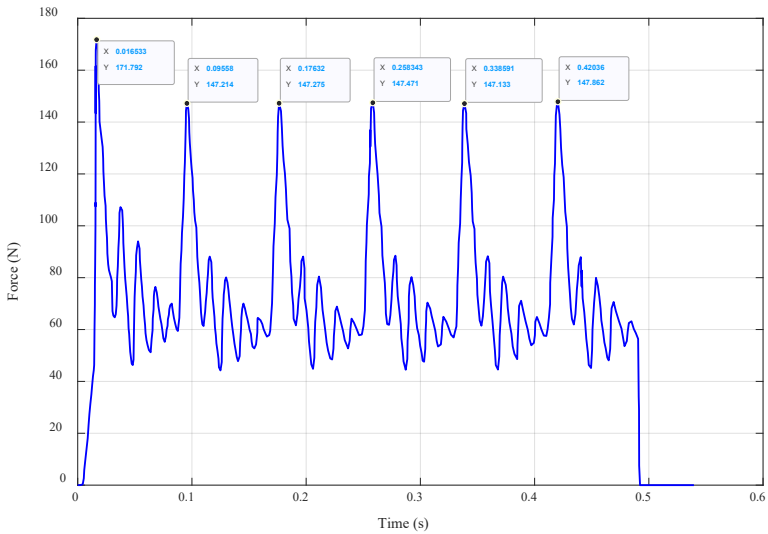


Figure 18 - Graph of elastic forces between belt links during firing

Experimental verification of the model

Many random input variables impact the behavior of the ammunition belt and the reliability of the automatic firing system. No matter how accurate the mathematical model is, it cannot capture all the influencing factors comprehensively. Consequently, experimental investigations play

a vital role in the analysis, design, production, and refinement of current weapon systems. Experiments enable rapid acquisition of necessary data regarding the dynamic parameters of the ammunition belt, as well as the displacement and velocity of the bolt carrier during automatic firing. Data obtained from experiments further demonstrate deviations between theoretical models and real-world measurements. This provides a fundamental basis for evaluating and validating the theoretical computational model. Reference (Vo et al., 2025) presents a comprehensive account of the content, procedures, and testing apparatus used by the research team to evaluate certain motion characteristics of the ammunition belt. The parameters identified through experimentation include:

Determination of the displacement and velocity of the ammunition belt

The displacement and velocity of the ammunition belt were determined using a ballistic camera system. The experimental setup is illustrated in the diagram shown in Figure 19. The recorded motion images of the ammunition belt are presented in Figure 20.

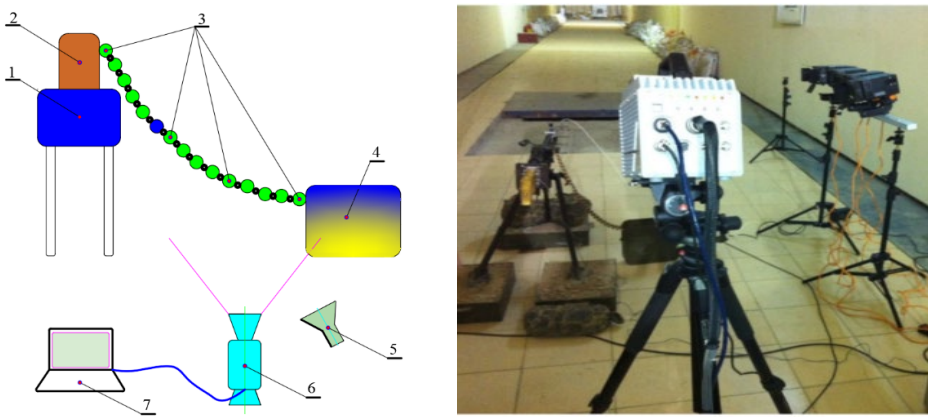


Figure 19 – Schematic diagram of the experimental model (Vo et al., 2025)
1 - Stabilized gun platform; 2 - Machine gun; 3 - Ammunition 7.62x54 mmR;
4 - Ammunition box; 5 - Illumination system;
6 - High-speed imaging system; 7 - Computer



Figure 20 - Images of belt motion under burst-fire conditions

Elastic force analysis between belt links

To assess elastic forces in the ammunition belt during operation, a simulated link equipped with a strain gauge sensor was used (Vo et al., 2025). The experimental setup is illustrated in Figures 21 and 22. During firing, the feed lever pulls the ammunition belt inward to perform the feeding process. When there is no longer a gap between the links, the link is stretched. Deformation detected by the strain gauge on the simulated link is processed by the DEWETRON 4000 system to calculate the corresponding elastic force, with results displayed as data files and force-time graphs.

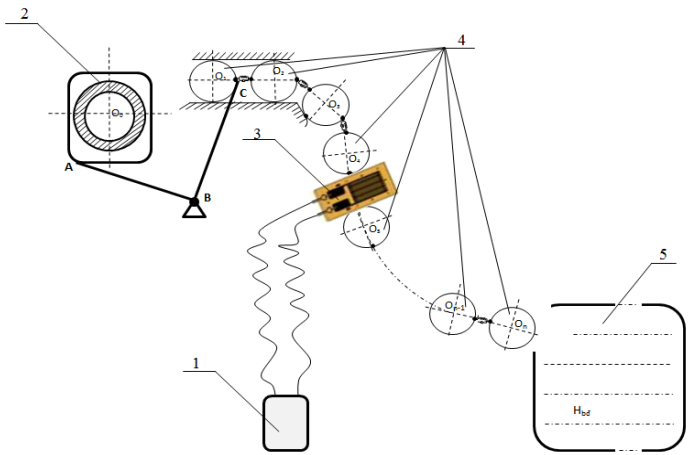


Figure 21 - Diagram of interlink elastic force evaluation (Vo et al., 2025) 1 – Dynamic signal analysis system; 2 –Machine gun; 3 – Simulated belt link integrated within the ammunition belt; 4 – Cartridges positioned on the belt; 5 – Ammunition belt container



Figure 22 - A simulated link mounted within the ammunition belt of the PKMS machine gun (Vo et al., 2025)

Verification of the mathematical model and discussion

To evaluate and validate the proposed mathematical model, experimental data obtained from the study (Vo et al., 2025) were used to compare with the corresponding simulation results. The comparison of the displacement pattern of the ammunition belt during a short burst of 6 rounds is shown in Figure 23. The velocity variation of the belt links is presented in Figure 24 and Table 1. The comparison of the elastic forces between the links during the burst is illustrated in Figure 25 and Table 2.

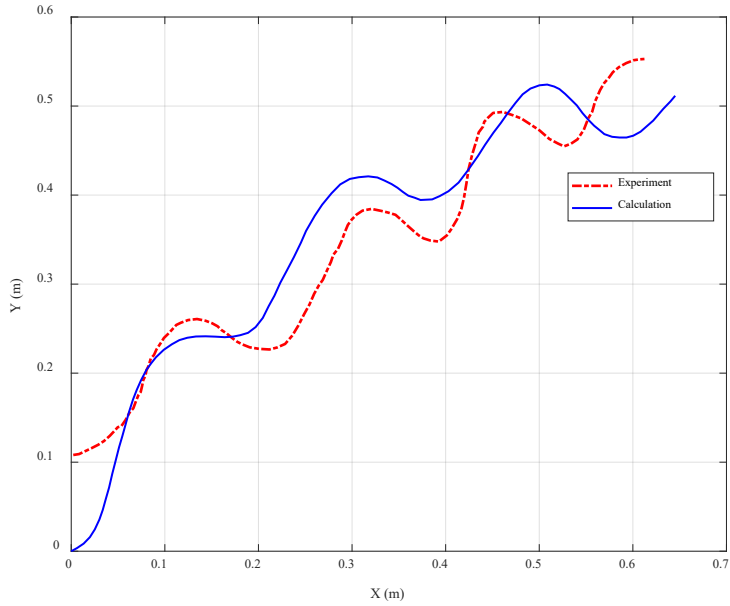


Figure 23 - Comparison of the displacement pattern of the ammunition belt

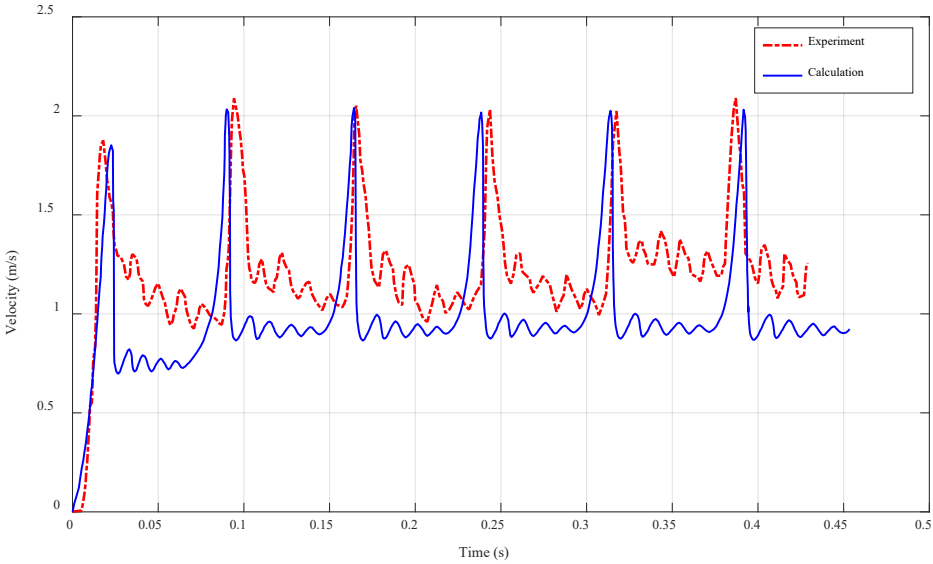


Figure 24 - Comparison of the velocity variation pattern of the belt links

Table 1 - Comparison of theoretical calculation results with experimental results for the velocity of belt links during burst firing

Sequence of fire	Link's maximum velocity [m/s]		
	Theoretical results	Experimental results	Error (%)
1	1.85155	1.876	1.3
2	2.03272	2.089	2.69
3	2.04027	2.051	0.5
4	2.01717	2.033	0.78
5	2.02581	2.025	0.04
6	2.03124	2.09	2.81

The comparison of the elastic forces between the links in the ammunition belt is shown in Figure 25 and Table 2.

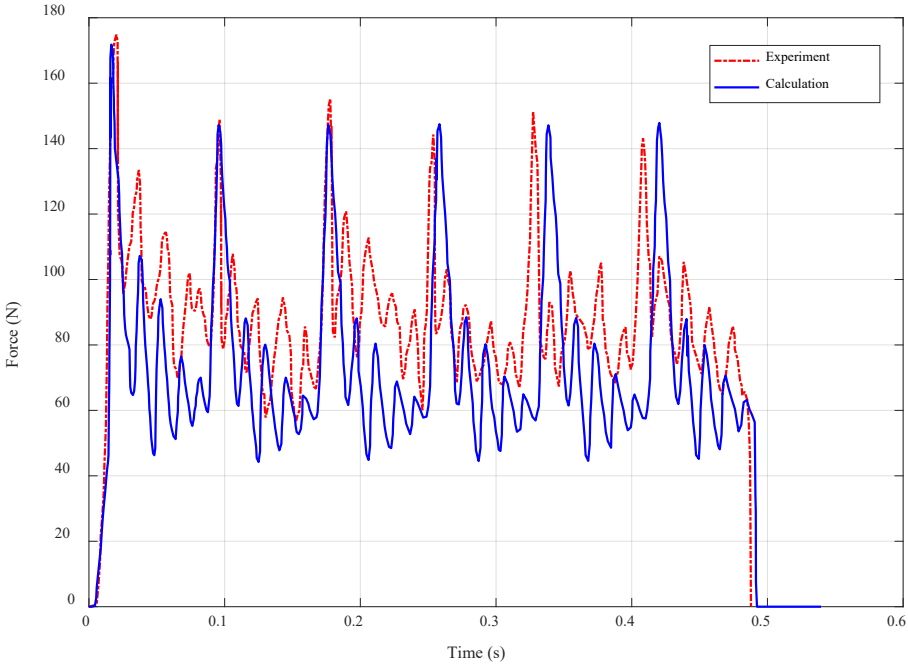


Figure 25 - Comparison of elastic forces between belt links during firing

Table 2 - Theoretical calculation results compared with experimental results of elastic forces between belt links during burst firing

Order of firing sequence	Maximum elastic force [N]		
	Theoretical results	Experimental results	Error (%)
1	171.792	174.9	1.77
2	147.214	149.1	1.26
3	147.275	155.2	5.11
4	147.471	144.3	2.19
5	147.133	151.4	2.82
6	147.826	143.2	3.23

Based on the comparison results obtained, several observations can be made as follows:

- The comparison between theoretical predictions and experimental results demonstrates that the model is highly accurate and comprehensive, as illustrated in Figures 23, 24, and 25. The displacement pattern of the ammunition belt (Figure 23), the velocity variation of the belt links (Figure 24), and the elastic forces between the links (Figure 25)

during burst firing, as calculated by the mathematical model, closely correspond to the experimental observations. The maximum velocity error of the links during burst firing between the theoretical and experimental data does not exceed 2.69% (see Table 1). Correspondingly, the maximum difference between theoretical predictions and experimental measurements of elastic force between links during burst firing remains under 5.11% (see Table 2).

- The analysis results indicate that the established mechanical system model fully corresponds to reality. This model can be used to investigate and evaluate the structural parameters of the weapon to improve firing accuracy, as well as to assess the quality of the weapon after repair or modification.

The difference between theoretical calculation results and measurement results arises from the following reasons:

- Errors in theoretical calculations arise from certain assumptions made to simplify the computation process, as well as from the numerical methods used to solve the problem;

- Experimental errors occur because the ammunition belt was annealed unevenly in terms of stiffness along its entire length, due to limitations in the annealing technique which did not meet the required standards. After annealing, rotational friction appears between the links in the belt loops, hindering the rotational movement of the belt loops. Additionally, experimental measurements are affected by errors inherent in the measuring instruments.

Conclusion

Based on the research results, the authors have successfully developed a dynamic model that integrates the firing system and the ammunition belt during burst firing.

Unlike previous studies, which typically model the ammunition belt as a simplified lumped mass or neglect the detailed interaction between individual rounds, the present work explicitly considers the concentrated mass of each round at the belt link and models the elastic connections with viscous damping between adjacent rounds. The dynamics of the ammunition belt are solved simultaneously and fully coupled with the motion of the automatic firing system through a unified system of differential equations, allowing the forces acting on each belt link to be evaluated under realistic operating conditions.

As a result, the motion characteristics of the bolt carrier, the belt pulling mechanism, the individual belt links, the belt pulling force, and the

elastic interaction forces between belt links during short burst firing are systematically identified and analyzed. This integrated modeling framework provides a more comprehensive and physically representative basis for investigating and evaluating the influence of key structural parameters of the ammunition belt on the performance of the automatic firing system during burst firing, compared with existing approaches.

Furthermore, the proposed mathematical model is experimentally validated by comparing simulation results with measurements obtained from a PKMS 7.62 mm machine gun, demonstrating the accuracy and reliability of the proposed approach relative to previously reported models.

Future research will focus on studying the effects of structural parameters such as belt link stiffness, gaps between links, and the number of rounds in the belt on the operation of the firing system and the weapon's stability during bursts. The goal is to determine the optimal set of structural parameters for belt design, contributing to the improvement and enhancement of machine gun performance based on the operational principle.

The results of this study offer a crucial theoretical basis for the design and enhancement of contemporary machine gun structures, opening new directions for the development of automatic weapon technology.

References

Allsop, D., 1997. *Brassey's Essential Guide to Military Small Arms: Design Principles and Operating Methods* [e-book]. London. ISBN: 1857531078. Available at: https://www.scribd.com/document/712049408/Libro-Military-Small-Arms [Accessed: 22 June 2025].

Balla, J., Krist, Z. & Le, C. L., 2015. Experimental study of turret-mounted automatic weapon vibrations. *International journal of mechanics,* 9(1), pp. 16-25 [online]. Available at: https://www.naun.org/main/NAUN/mechanics/2015/a062003-137.pdf [Accessed: 02 June 2025].

Balla, J. & Mach, R., 2007. Kinematics and dynamics of Gatling weapons. *Advances in Military Technology,* pp. 121-133 [online]. Available at: https://www.aimt.cz/index.php/aimt/article/view/1691/162 [Accessed: 10 June 2025].

Krier, H., & Summerfield, M. 1979. *Interior ballistics of guns*. Progress in astronautics and aeronautics, 66 [e-book]. Available at: https://www.mori.bz.it/Balistica/U.S.ARMY%20Interior%20ballistics.pdf [Accessed: 20 May 2025].

Bien, V. et al., 2021. Effect of Some Structural Parameters on the Firing Stability of the PKMS Machine Gun when Firing with Complicated Boundary

Conditions. *Proceedings of the International Conference on Military Technologies 2021,* pp. 1-6. Available at: https://doi.org/10.1109/ICMT52455.2021.9502820

Bien, V., Macko, M. & Hung, D., 2021. Experimental study of automatic weapons vibrations when firing series. *Problems of Mechatronics. Armament, Aviation, Safety Engineering,* 12(4), pp. 9-28. Available at: https://doi.org/10.5604/01.3001.0015.5984

Bien, V. V., Phon, N. D. & Phu, N. M., 2023. Mathematical model of automatic firing system of gas-operated machine gun. *Applied Engineering Letters,* 8(3), pp. 91-100. Available at: https://doi.org/10.18485/aeletters.2023.8.3.1

Dingguo, Z., 1996. Computer simulation of the motion of the bullet belt of airplane gun. *Applied Mathematics and Mechanics,* 17(11), pp. 1059-1066. Available at: https://doi.org/10.1007/BF00119953

Doan, D., Bien, V., Quang, M. & Phu, N., 2023. A Study on Multi-Body Modeling and Vibration Analysis for Twin-Barrel Gun While Firing on Elastic Ground. *Applied Engineering Letters,* 8(1), pp. 36-43. Available at: https://doi.org/10.18485/aeletters.2023.8.1.5

Balla, J., Krist, Z., Nguyen, M. P., & Vo, V. B., 2021. Study effects of shock absorbers parameters to recoil of automatic weapons. *In 2021 International Conference on Military Technologies (ICMT)*, pp. 1-6. IEEE. Available at: https://doi.org/10.1109/ICMT52455.2021.9502825

Fiser, M. & Popelinsky, L., 2007. *Small Arms* [book]. Brno: University of Defence. ISBN: 978-80-7231-475-1.

Han, X., Bo, Y. & Li, Q., 2011. Dynamic analysis on gas operated device's of internally-powered Gatling weapon. *Proceedings of 2011 International Conference on Electronic & Mechanical Engineering and Information Technology,* Volume 9, pp. 4661-4664. Available at: https://doi.org/10.1109/EMEIT.2011.6024075

Hu, B.C. & Zhang, X., 2019. Influence of multiple structural parameters on interior ballistics based on orthogonal test methods. *Defence Technology,* 15(5), pp. 690-697. Available at: https://doi.org/10.1016/j.dt.2019.06.014

Kuo, C. L., Yuan, C. K. & Liu, B. S., 2012. Using human-centered design to improve the assault rifle. *Applied Ergonomics,* 43(4), pp. 1002-1007. Available at: https://doi.org/10.1016/j.apergo.2012.02.002

Van Hung, N., Van Dung, N., Van Minh, P., Van Ke, T., & Van Thom, D. 2024. Vibration behavior analysis of the ammunition belt of the gas-operated machine gun. *Journal of Vibration Engineering & Technologies*, 12(2), 1563-1575. Available at: https://doi.org/10.1007/s42417-023-00926-4

Nguyen, P. M., Vo, B. V., Dao, D. V. & Nguyen, D. V., 2024. Studying the dynamic characteristics of gas-operated guns using Solidworks Motion software. *Vojnotehnički glasnik/Military Technical Courier,* 72(3), pp. 1066-1092. Available at: https://doi.org/10.5937/vojtehg72-50987

Carlucci, D. E., & Jacobson, S. S. 2025. *Ballistics: theory and design of guns and ammunition* [book]. FL:CRC press. ISBN-13: 978-1-4200-6618-0. Available at:https://ftp.idu.ac.id/wp-content/uploads/ebook/tdg/MILITARY%20PLATFOR

M %20DESIGN/Ballistics%20%20Theory%20and%20Design%20of%20Guns%20and%20Ammunition,%20Third%20Edition.pdf

Tien, V., Macko, M., Procházka, S. & Bien, V., 2022. Mathematical Model of a Gas-Operated Machine Gun. *Advances in Military Technology,* pp. 63–77. Available at: https://doi.org/10.3849/aimt.01449

Vo, B. V., Nguyen, P. D., Nguyen, P. M. & Vu, L. X., 2025. Research into the effect of ammunition belt stiffness on the operation of automatic firing systems using experimental methods. *Vojnotehnički glasnik/Military Technical Courier,* 73(2), pp. 469-495. Available at: https://doi.org/10.5937/vojtehg73-54574

Zbigniew, W., Miroslaw, Z., Tomasz, W. & Ryszard, W., 2024. Analysis of the ammunition belt operation in the 35 mm KDA gun of the OSU-35 Ship Weapons System. *Problemy Mechatroniki: uzbrojenie, lotnictwo, inżynieria bezpieczeństwa,* 15(1), pp. 83-98. Available at: https://doi.org/10.5604/01.3001.0054.4490

Analiza dinamike dovoda redenika kod mitraljeza sa gasnim sistemom

Van Dung Nguyen[a], **autor za prepisku**, *Van Bien* Vo[a], *Minh Phu* Nguyen[b], *Xuan Long* Vu[c]

[a] Le Quy Don Technical University, Faculty of Special Equipment, Hanoi, Socialist Republic of Vietnam
[b] Department of Weapons and Ammunition, University of Defence, Brno, Czech Republic
[c] Tran Dai Nghia University, Ho Chi Minh City, Socialist Republic of Vietnam

OBLAST: matematika, mašinstvo
KATEGORIJA (TIP) ČLANKA: originalni naučni rad

Sažetak:

Uvod/cilj: U radu je predstavljena metodologija simulacije za precizno određivanje kinematičkih parametara redenika kod mitraljeza sa gasnim sistemom tokom kratkih rafala.

Metode: Razvijen je sveobuhvatan matematički model zasnovan na Drugom Njutnovom zakonu kojim se opisuje dinamičko ponašanje redenika. Formiran je sistem diferencijalnih jednačina koji obuhvata sve relevantne sile koje deluju na svaku kariku redenika u realnim radnim uslovima kako bi se precizno opisalo kretanje redenika. Izvršena je dinamička simulacija redenika integrisanog sa mehanizmom automatskog punjenja. Rezultati simulacije su potom upoređeni sa eksperimentalnim podacima radi verifikacije tačnosti modela. Model je primenjen za proračune i eksperimentalna ispitivanja na mitraljezu PKMS kalibra 7,62 mm.

Rezultati: Rezultati simulacije pokazali su obrasce kretanja nosača zatvarača, poluge za dovod, kretanja karika redenika, sile povlačenja redenika i elastičnih sila između karika tokom rafalne paljbe. Rezultati proračuna dobijeni teorijskim modelom pokazuju dobro slaganje sa

eksperimentalnim podacima. Maksimalno odstupanje između teorijskih predviđanja i eksperimentalnih merenja iznosi 5,11%.

Zaključak: Dobijeni rezultati predstavljaju teorijsku osnovu za buduće projektovanje i optimizaciju sistema automatike mitraljeza sa gasnim pogonom.

Ključne reči: dinamika redenika, redenik, mitraljez PKMS 7,62 mm, mitraljez sa gasnim sistemom automatike, municija 7,62×54 mmR.

Paper received on: 5 June 2025.
Manuscript corrections submitted on: 1 January 2026.
Paper accepted for publishing on: 25 January 2026.

© 2026 The Authors. Published by Vojnotehnički glasnik / Military Technical Courier (www.vtg.mod.gov.rs). This article is an open access article distributed under the terms and conditions of the Creative Commons Attribution license (http://creativecommons.org/licenses/by/4.0/rs/).

Functional hierarchy using GIS: Diagnosis and traffic regulation solutions in Batna City (Northeastern Algeria)

Sonia Adjroud[a], *Samir* Djenba[b], *Abdelhamid* Khedidja[c], *Hamza* Amireche[d]

[a] University of Batna 02, Institute of Earth and Universe Sciences, Department of Geography and Territorial Planning, Laboratory of Natural Hazards and Land Use (LRNAT), Batna, People's Democratic Republic of Algeria
e-mail: adjroudsonia@yahoo.fr, s.adjroud@univ-batna2.dz, **corresponding author**,
ORCID ID: https://orcid.org/0009-0000-5904-2895

[b] University of Batna 02, Institute of Earth and Universe Sciences, Department of Geology, Laboratory for Water Resource Mobilization and Management (LMGRE), Batna, People's Democratic Republic of Algeria
e-mail: s.djenba@univ-batna2.dz,
ORCID ID: https://orcid.org/0000-0002-4789-6866

[c] University of Batna 02, Institute of Earth and Universe Sciences, Department of Geology, Laboratory for Water Resource Mobilization and Management (LMGRE), Batna, People's Democratic Republic of Algeria
e-mail: a.khedidja@univ-batna2.dz,
ORCID ID: https://orcid.org/0000-0001-7085-3795

[d] University of Constantine 03, Institute of Urban Technology Management, Laboratory of resilient and intelligent dynamic regions (LRIDR), Constantine, People's Democratic Republic of Algeria
e-mail: Hamza-amireche@univ-constantine3.dz,
ORCID ID: https://orcid.org/0009-0001-7744-1723

https://doi.org/10.5937/vojtehg74-62399

FIELD: geosciences
ARTICLE TYPE: original scientific paper

Abstract:

Introduction/purpose: The city of Batna in northeastern Algeria has experienced rapid population expansion. This growth has intensified mobility needs and placed significant pressure on a limited and aging road network. Congestion now affects the main urban corridors and central districts. The study aims to diagnose these dysfunctions and propose a strategic framework for improving traffic circulation. It also evaluates the effectiveness of GIS-based spatial analysis for urban mobility planning.

Methods: The research uses Geographic Information Systems and satellite imagery to analyze Batna's transportation system. The study area covers

primary and secondary road axes within the urban core. Data include topographic maps, demographic layers, land use, and field observations. ArcGIS tools were applied to identify congestion hotspots, measure network accessibility, evaluate hierarchy consistency, and model current and future mobility scenarios.

Results: The results reveal recurrent congestion along Avenue de l'Indépendance, Route de Biskra, and the northern ring road. Several intersections show saturation levels exceeding functional thresholds. The analysis highlights structural discontinuities, insufficient road widths, and poorly connected radial axes. Spatial correlations indicate that high-density zones and commercial clusters strongly influence traffic bottlenecks. The maps produced reveal gaps in east–west connectivity and limited alternatives for bypassing the city center.

Conclusion: The findings support a set of targeted interventions, including new link roads, optimized junctions, and redistribution of traffic flows. The results confirm that GIS enhances diagnostic accuracy and supports evidence-based planning. The proposed framework offers a scalable method for improving mobility in rapidly urbanizing cities. The study demonstrates that integrating spatial modeling with strategic planning leads to more resilient and adaptive transportation systems aligned with sustainable development goals.

Keywords: urban road network, functional hierarchy, traffic regulation, GIS analysis, Batna, Algeria.

Introduction

The socio-economic dynamics of Batna, Algeria, have spurred rapid urban expansion driven by population growth, intensified economic activities, and the city's strategic geographical position (Tout, 2024). This expansion presents two contrasting trends. On one hand, Batna has retained its historic core and central urban fabric, underscoring its cultural and administrative significance. On the other hand, the emergence of new mobility patterns, most notably the increasing dependence on private vehicles, has profoundly reshaped travel behavior and intensified pressure on existing transport infrastructure.

Despite these transformations, the city's road network has not developed in parallel. As one approaches the city center, urban infrastructure becomes progressively insufficient to accommodate the growing volume of motorised traffic. The concentration of commercial, administrative, and service activities within the core area generates heavy traffic flows, leading to recurrent congestion and inefficiencies, especially during peak hours. These conditions strain mobility, reduce accessibility, and diminish residents' quality of life (Faheem, 2024).

This disparity between evolving mobility demands and the limited capacity of the road network underscores the urgent need for data-informed planning and intervention. Conventional traffic management strategies have proven inadequate to address these complex challenges effectively. Consequently, this study explores the use of geomatics tools, particularly Geographic Information Systems (GIS) and remote sensing, to develop an integrated and evidence-based framework for analysis. By leveraging these tools, the research aims to classify, assess, and optimise Batna's road network to mitigate congestion and promote sustainable urban mobility.

The primary objective is to apply ArcGIS-based analysis to establish a functional classification of the city's road network. This classification will not only differentiate roads according to their capacity and function but also pinpoint critical areas requiring intervention. The resulting framework will support the efficient management of traffic flows and guide the strategic planning of future infrastructure development (Metz, 2024).

Geomatics and remote sensing technologies offer distinctive advantages in addressing these urban challenges. They facilitate the integration of heterogeneous datasets such as population density, traffic intensity, and land use into a unified analytical environment (Khireddine & Aichour, 2022).This integration enables evidence-based decision-making, allowing planners to design targeted, equitable, and environmentally sustainable mobility solutions. Furthermore, GIS methods provide powerful visual and analytical representations of traffic dynamics, congestion hotspots, and the hierarchical structure of road systems, enhancing both diagnosis and planning capabilities.

The analysis of Batna's road network thus serves as a case study illustrating the potential of GIS-driven methodologies for addressing urban mobility issues. By focusing on the specific context of Batna, this research contributes to a broader understanding of how integrated spatial analyses can foster resilient, efficient, and sustainable transportation systems in rapidly expanding urban environments.

Materials and methods

Overview of the study area

The city of Batna, acknowledged as both the capital of the Aurès region and the administrative center of the Wilaya of Batna, occupies a pivotal position within eastern Algeria. Situated approximately 435 kilometers southeast of Algiers and 113 kilometers southwest of Constantine, the city extends over a total area of 11.641 hectares. Its

geographical configuration places it at the heart of the northeastern part of the wilaya, where it stands at the junction of major regional and national transportation corridors linking Constantine, Biskra, and Khenchela. This advantageous location has historically fostered Batna's emergence as a strategic urban center and a hub of socio-economic interaction in the Aurès.

Geographically, Batna's coordinates range from 6°7'59'' to 6°13'31" East Longitude and 35°31'26" to 35°34'23'' North Latitude, with an average altitude of 1.040 meters above sea level. Its elevated topography, combined with its centrality in the regional landscape, enhances its climatic distinctiveness and strengthens its function as a key crossroads within Algeria's transportation network. The city's strategic importance is further emphasized by its integration into two major infrastructural axes that structure the national transport framework:

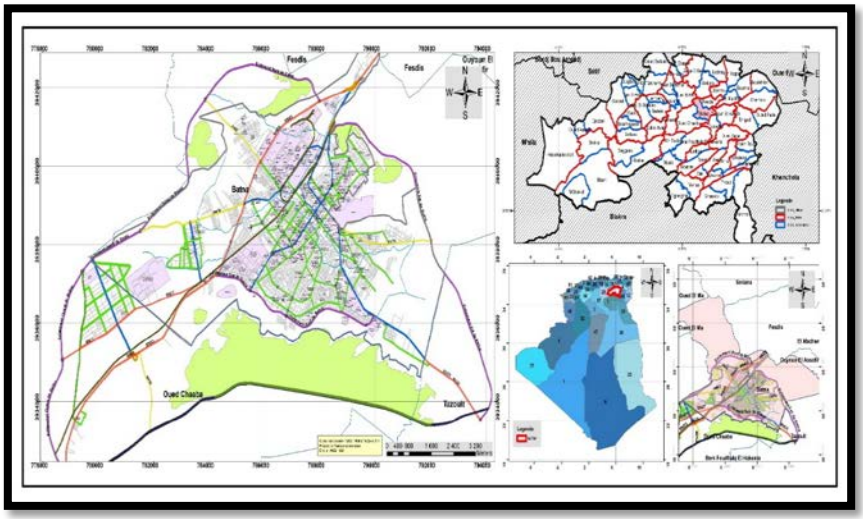


Figure 1 - Map 1, overview of the study area

The North–South corridor, which consolidates connectivity between Algeria's northern coastal regions and the southern arid zones; and the East–West axis, which traverses the high plateaus, ensuring continuity and accessibility between the eastern and western territories of the country.

Through this dual orientation, Batna plays a crucial role in regional and national mobility, serving as both a gateway for economic exchange and a vector of territorial cohesion. Its positioning within this multidirectional transport system makes it a focal point for infrastructure planning, urban development, and traffic management policies.

Population

The demographic expansion of the city of Batna mirrors a broader trend affecting numerous Algerian urban centers, reflecting the combined effects of natural growth, rural–urban migration, and inter-wilaya mobility. Together, these forces have profoundly reconfigured the city's population dynamics and urban morphology over recent decades.

A primary driver of this expansion is the natural increase in population, resulting from a persistently high birth rate and notable improvements in public health services, which have contributed to a marked decline in mortality rates. This demographic context has sustained continuous population growth, fostering both spatial and social transformations within the urban fabric.

In addition, Batna experienced a significant influx of rural migrants during the period of rural exodus, particularly throughout Algeria's "black decade" of the 1990s. In this era of sociopolitical turmoil and rural insecurity, many individuals and families sought refuge in relatively stable urban centers such as Batna. The city's perceived safety, coupled with better access to essential services, employment, and educational infrastructure, reinforced its attractiveness as a destination for internal migration (Aicha, 2022).

A further dimension of Batna's demographic evolution is inter-wilaya migration, driven by the pursuit of enhanced economic opportunities, academic institutions, and living conditions. Batna's strategic geographic position at the intersection of major economic and administrative axes has consolidated its status as a regional magnet for population movements, intensifying its urban growth (Pisarevskaya & Scholten, 2022).

Collectively, these interacting demographic forces have produced a complex pattern of urban expansion, leading to accelerated urbanization and mounting pressure on infrastructure systems, particularly the road and transport networks. A comprehensive understanding of these dynamics is therefore essential for urban planners and policymakers, as it underpins the formulation of sustainable development strategies, infrastructure enhancement programs, and effective mobility and traffic management frameworks.

Population density

Population density constitutes a fundamental indicator of urban balance and service efficiency, particularly in relation to traffic management and mobility planning. Variations in density—whether excessive, uneven or insufficient—have a direct impact on traffic

circulation, infrastructure demand, and the overall performance of urban systems. In the case of Batna, the close interdependence between population concentration and mobility patterns reveals the complexity of the city's traffic and transport challenges.

High-density areas tend to generate significant mobility needs, as they usually coincide with the concentration of residential, economic, administrative, and social functions. These overlapping activities intensify congestion during peak hours, placing considerable pressure on the existing road infrastructure and public transport systems. In contrast, low-density zones often suffer from limited accessibility and the underutilization of transport facilities, which undermines the efficiency and integration of the overall urban network.

In Batna, the population is distributed across ten distinct urban sectors, each characterized by specific density profiles and spatial arrangements. These range from highly compact central districts—such as Bouakal and the city's traditional core—to more dispersed peripheral sectors like Bouzourane and the Tazoult Road area. For instance, Bouakal, with an estimated density of around 310 inhabitants per hectare, exemplifies zones with intense mobility demand and high pressure on public services. Conversely, ZHUN II, where the density reaches only 47 inhabitants per hectare, reflects a fragmented settlement pattern marked by issues of connectivity, accessibility, and service provision.

The table below presents the detailed distribution of population density across Batna's ten sectors, providing a clear overview of the spatial disparities that shape mobility dynamics and guide infrastructure planning within the city.

The variation in population density across Batna's urban sectors underscores the complexity of traffic management and road network planning within the city. In high-density areas, targeted interventions such as increasing road capacity, establishing dedicated public transport lanes and implementing advanced traffic flow optimization systems are essential to mitigate congestion and enhance overall mobility performance. Conversely, low-density sectors call for improved connectivity through the development of secondary and feeder roads, ensuring equitable access to essential services and economic opportunities.

Addressing these disparities necessitates a comprehensive and sector-specific planning approach that integrates population density analysis with the functional classification of the road network (Kalla, 2015). Such an integrated framework enables the urban mobility system to respond effectively to the distinct needs of each sector, thereby enhancing

traffic efficiency, accessibility, and the long-term resilience of Batna's urban structure (Ben Yahia, 2023).

Sector	Population (2010)	Density (Hab/ha)	Area (ha)	Classification by sector
Downtown	22.057	98	225.52	05
Traditional neighborhoods	32.914	293	112.26	02
Bouakal	66.180	310	223.33	01
Kechida	42.647	122	349.19	04
Feeding area	46.377	106	437.40	07
Bouzourane	12.015	50	239.83	09
Shouhada	25.800	181	142.88	03
Route of Tazoult	36.560	157	282.85	10
ZHUN I	31.589	96	330.77	06
ZHUN II	20.800	47	403.79	08

Table 1- Distribution of population density across Batna's urban sectors

Population evolution and forecasts

The city of Batna, like many other major Algerian urban centers, has undergone remarkable population growth over recent decades. This rapid demographic expansion has profoundly influenced the city's spatial equilibrium and the quality of urban services, particularly those related to mobility and traffic management. The increasing population has exerted growing pressure on Batna's road infrastructure, often surpassing its design capacity and generating considerable challenges in meeting escalating transport demands.

An examination of population density patterns, as illustrated in the map below, reveals a pronounced spatial imbalance among the city's sectors. While certain districts such as Bouakal and other historic neighborhoods record densities exceeding 70.000 inhabitants, others, including Bouzourane and the industrial zone, remain sparsely populated.

This uneven distribution presents a dual challenge for urban planners: high-density areas experience recurrent congestion and infrastructure strain, whereas low-density sectors suffer from weak connectivity and underutilized resources.

Population trends and forecast data underscore these spatial disparities and their implications for urban mobility. As Batna's population grows, such imbalances are expected to intensify, heightening the need for targeted interventions that ensure equitable access to transportation

and urban services. The spatial analysis highlights the necessity of sector-specific strategies where densely populated zones require expanded infrastructure and enhanced public transport, while peripheral areas demand improved connectivity through feeder and collector roads.

To effectively manage these challenges, a data-driven and forward-looking approach to urban and mobility planning is essential. Incorporating demographic projections into road network classification and management enables planners to design a transport system capable of balancing mobility needs across the city. In this context, high-density sectors should prioritize the development of mass transit systems, congestion mitigation measures, and pedestrian-friendly zones, whereas low-density sectors should focus on improving accessibility via secondary and connecting roads.

By addressing these disparities through integrated planning, the city of Batna can foster a resilient, efficient, and equitable urban mobility system that supports sustainable growth and enhances the overall quality of life for its residents. Moreover, by integrating demographic trends into the planning of future road networks, this approach provides a solid basis for developing a city that is not only well connected but also capable of adapting to the evolving challenges of urban growth and transformation.

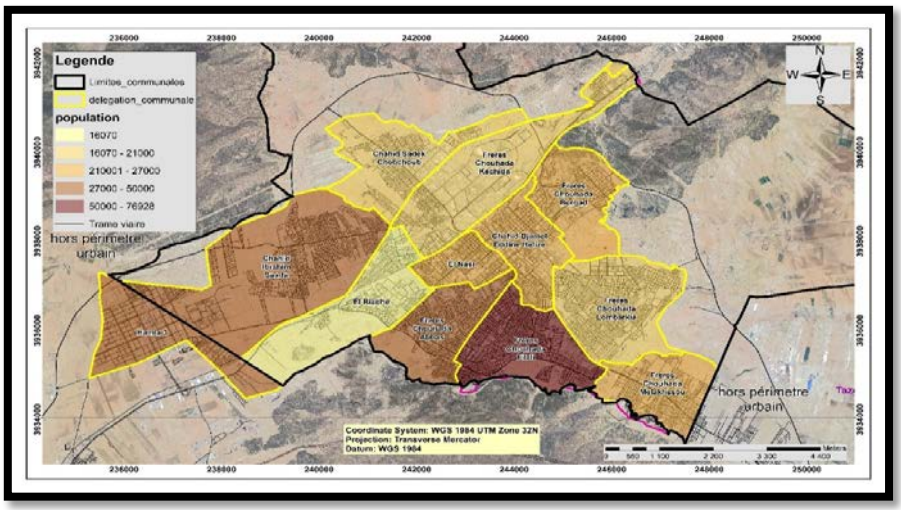


Figure 2 - Map 2, distribution of the population by sector

Urban roads

The road infrastructure of the city of Batna has been developed to accommodate a broad spectrum of traffic demands, addressing both local

mobility requirements and regional transportation flows. This dual functionality stems from Batna's strategic geographical position at the intersection of two major national transportation corridors: RN3, a key north–south axis, and RN31, which ensures east–west connectivity across the highlands. Together, these routes establish Batna as a vital hub for economic exchange, trade, and goods and people throughout Algeria.

City bypasses

Bypasses are designed to divert regional and long-distance traffic away from the congested urban core. They facilitate smoother transit around the city, thereby reducing inner-city congestion and preventing heavy freight vehicles and through-traffic from disrupting local mobility. However, their effectiveness is often constrained by factors such as limited access points, inadequate maintenance, and insufficient integration with the inner urban road network. Enhancing these aspects is crucial to ensure that bypasses fully achieve their decongestion and connectivity objectives.

Urban routes (local road network)

This component of Batna's infrastructure supports intra-urban mobility, linking residential neighborhoods with commercial, industrial, and administrative areas, thus forming the backbone of daily urban activity. These routes must balance multiple demands, including pedestrian circulation, public transport operations, and private vehicle use. Such complexity frequently results in congestion, particularly in high-density zones and during peak travel periods. The efficiency of these routes is further strained by the city's rapid demographic and spatial expansion, which continually amplifies mobility demand.

Challenges and planning perspectives

Despite its strategic layout, Batna's road network faces several structural and operational challenges that undermine its overall performance. Rising traffic volumes, insufficient coordination between bypasses and urban routes, and the absence of intelligent traffic management systems have led to recurrent bottlenecks and travel delays (Efrat, 2024). Additionally, ongoing urban sprawl has intensified pressure on existing infrastructure, underscoring the urgent need for targeted upgrades and adaptive planning.

Addressing these challenges requires a comprehensive and integrated planning approach that harmonizes the functions of bypasses and urban routes within a unified mobility framework. Investments in Intelligent Transport Systems (ITS), systematic road maintenance, and the

strategic extension of bypass infrastructure could substantially enhance the network's capacity to accommodate both local and regional traffic flows. Moreover, implementing a hierarchical road classification system would help prioritize interventions, ensuring that each road category effectively fulfills its designated role. By reinforcing the synergy between bypasses and urban routes, Batna can develop a resilient, efficient, and adaptive road network—one capable of responding to present mobility demands while anticipating future urban growth.

Classification of urban roads

a. Administrative classification of urban roads

The classification of urban roads constitutes a fundamental component of urban mobility planning, offering a structured framework for the organization and management of road networks. In the case of Batna, urban roads are classified according to two main criteria, ensuring a clear understanding of their design, function, and administrative jurisdiction.

1. Technical criterion

Motorways: High-capacity roads designed for long-distance travel, featuring controlled access points and minimal intersections. They facilitate the rapid and uninterrupted movement of heavy traffic between major cities and regions.

Expressways: Similar in function to motorways but primarily serving urban and peri-urban areas. They accommodate substantial traffic volumes over shorter distances, ensuring efficient connectivity between key urban zones.

2. Administrative and legal criterion

This classification is based on the governance structure and legal jurisdiction under which roads operate, clarifying responsibilities for their management and maintenance. Roads are thus classified into:

Highways: Managed at the national level, connecting major cities and forming the backbone of inter-regional transport.

Urban Highways: Designed for high-speed traffic within city limits, providing seamless links between the urban core and peripheral areas.

National Roads (NR): Connecting Batna to neighboring wilayas, these roads serve both regional and urban transport functions.

Wilaya Roads (WR): Secondary routes linking smaller towns and rural areas to Batna, playing a crucial role in regional accessibility.

Municipal Roads (MR): Local roads serving neighborhoods and districts, facilitating everyday mobility and access to essential services within the city.

The spatial distribution and hierarchy of these road types are illustrated in Map N°3, which depicts how each category integrates into Batna's overall transport network, emphasizing the interaction between technical functionality and administrative jurisdiction.

3. Significance and implications

This dual classification system is vital for effective traffic management and strategic urban planning. Motorways and expressways are prioritized for intercity and high-speed mobility, thereby reducing congestion and enhancing regional connectivity (Wang, 2024). Conversely, Wilaya and municipal roads meet local mobility needs, ensuring equitable access to services and improving residents' quality of life. The integration of Geographic Information Systems (GIS) into this framework enables planners to identify congestion points, optimize traffic circulation, and prioritize road maintenance activities. Through these tools, Batna can develop a resilient, adaptive transport system capable of meeting current demands while accommodating future urban growth. This classification not only establishes an organizational structure for the city's roads but also serves as a strategic basis for implementing targeted interventions aligned with Batna's socio-economic and mobility objectives.

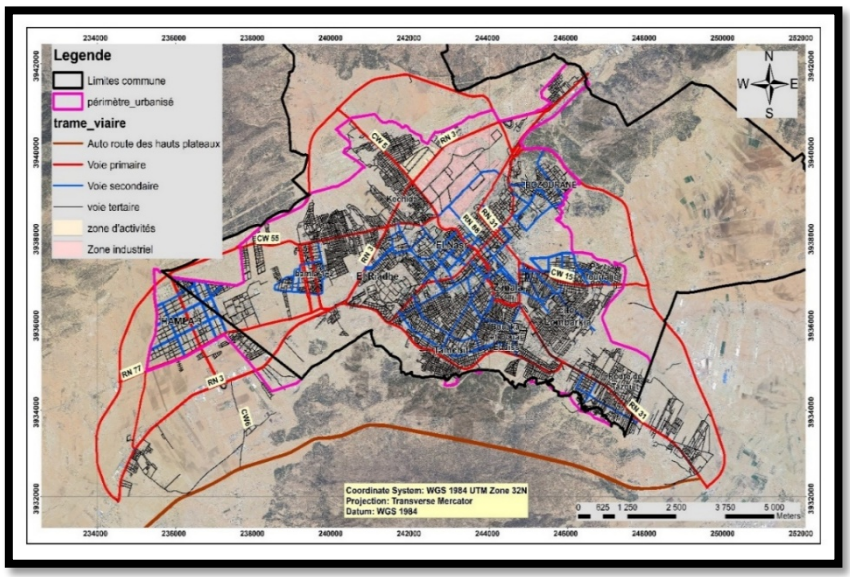


Figure 3 – Map 3, urban roads classification 1

b. Functional classification of urban roads

The functional classification of road networks is a critical planning tool that categorizes streets based on their purpose, traffic volume, and connectivity within the urban structure. In Batna, the network can be broadly divided into three categories: local (deserted) streets, arterial roads, and rapid urban roads.

This approach provides insight into the operational dynamics of the city's transport grid and serves as a foundation for optimizing traffic efficiency and prioritizing infrastructure investment.

1. Local (deserted) streets

These streets represent the most localized level of the urban network, serving low-density residential areas with minimal traffic demand. They generally have low vehicular volumes and limited connectivity to larger roads. While primarily intended to ensure local access, they play an important role in maintaining accessibility in the city's peripheral and less densely populated zones.

2. Arterial roads

Arterial roads form the backbone of Batna's transport system, facilitating the movement of medium to high traffic volumes between residential, commercial, and industrial areas. They balance accessibility with mobility.

In Batna, they link the city center to surrounding neighborhoods, distributing traffic efficiently and mitigating congestion. Proper planning and maintenance of these roads are crucial for supporting socio-economic activities.

3. Rapid urban roads

Designed as expressways or high-capacity corridors, these roads prioritize high-speed travel across and beyond the city. Characterized by minimal intersections and uninterrupted flow, they connect major urban zones with external regions.

In Batna, rapid urban roads facilitate intercity mobility, reduce travel times, and divert transit traffic away from congested centers, thus contributing to economic productivity and regional integration.

Map N°4 illustrates the evolution of Batna's functional road hierarchy, revealing a clear shift toward expanding arterial and rapid urban roads to accommodate growing traffic demands. This evolution underscores the city's adaptation to urban growth and changing mobility needs.

By leveraging this classification, planners can identify priority investment areas, optimize traffic distribution, and promote sustainable long-term development.

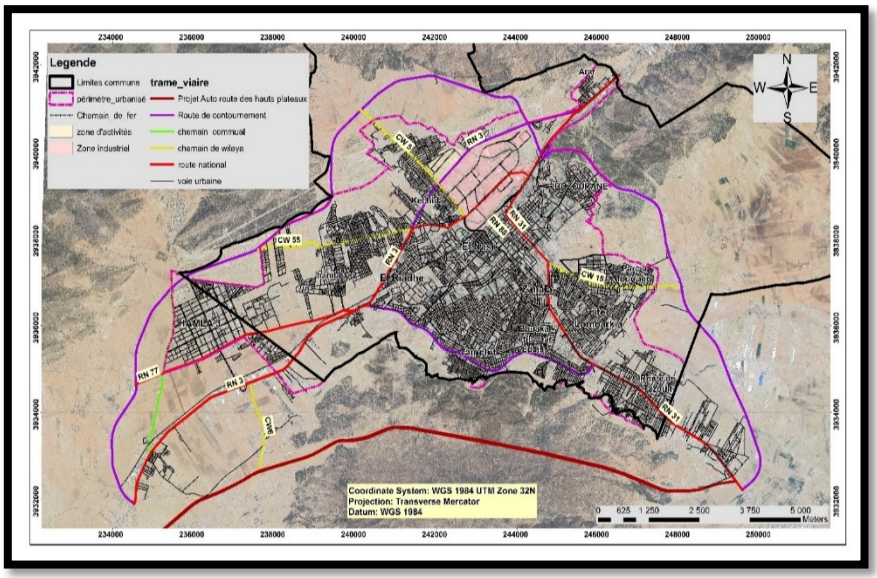


Figure 4 - Map 4, urban road classification 2

c. Diachronic classification of urban roads

Over the past two decades, Batna's road network has undergone major transformation driven by rapid urbanization, demographic growth, and rising mobility demands (Khireddine & Aichour, 2022). This diachronic analysis traces the network's evolution between 2000 and 2018, highlighting key spatial and functional developments.

In 2000, the road network was strongly centralized, with the city center functioning as the primary traffic hub. The absence of bypasses and peripheral connections led to frequent congestion and restricted access to suburban areas (Khireddine & Aichour, 2022).

By 2018, the construction of new arterials, bypasses, and secondary routes had decentralized traffic, improved accessibility, and strengthened connections between the urban core and peripheral areas. Maps reveal both quantitative growth in road length and qualitative improvement in network hierarchy.

Despite these advances, challenges remain: peripheral districts are still under-connected, and the absence of adaptive traffic management

limits the system's responsiveness (Louati & Rafik, 2024). Some expansions also lack integration within the broader mobility framework.

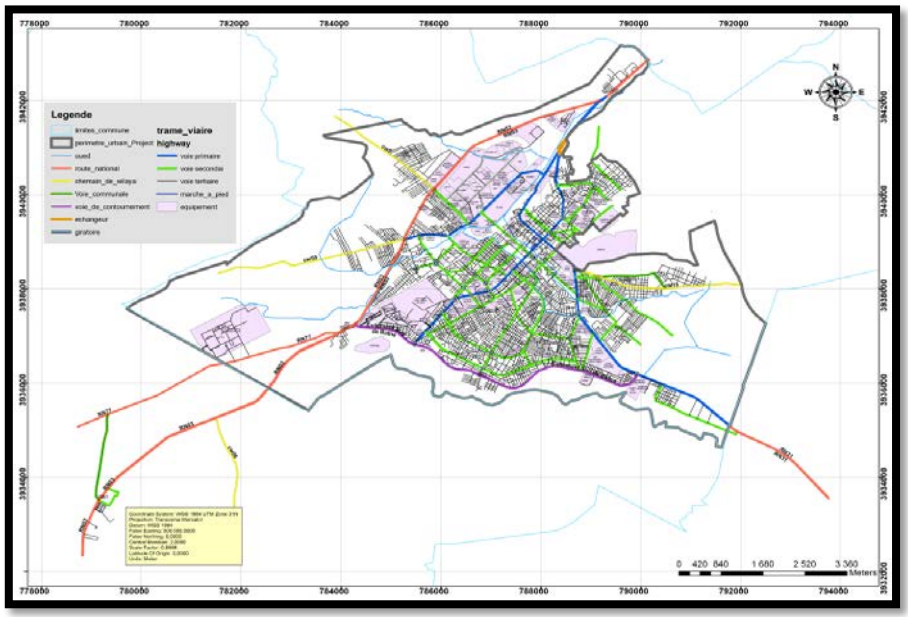


Figure 5 – Map 5, evolution of the city of Batna (2000)

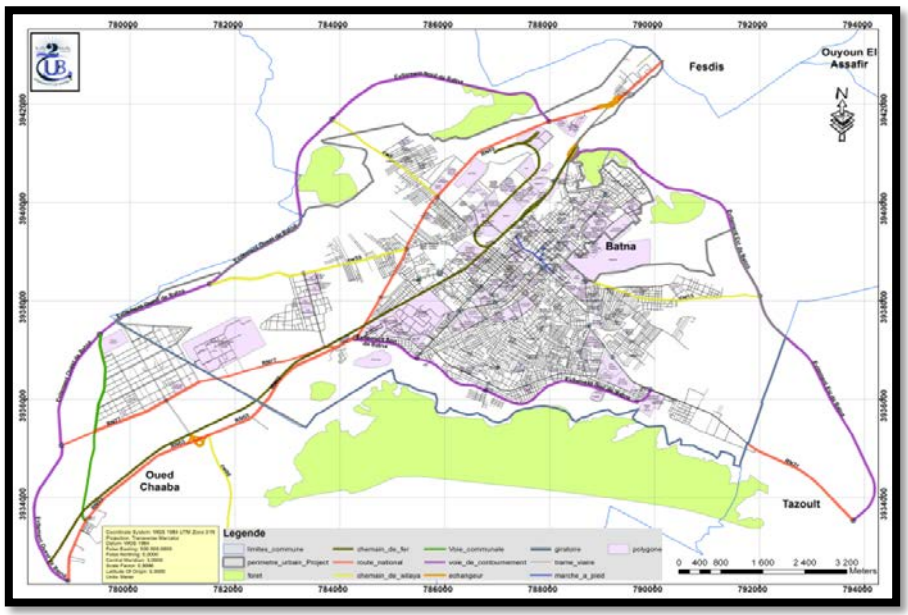


Figure 6 - Map 6, evolution of the city of Batna (2018)

A forward-looking strategy should therefore focus on strengthening peripheral connectivity, adopting intelligent traffic management, and promoting sustainable, balanced urban growth.

Overall, Batna's road network evolution between 2000 and 2018 demonstrates clear progress toward a more efficient and resilient urban transport system.

d. Town and country planning and the role of GIS

Town and country planning, as a multidisciplinary domain, plays a crucial role in structuring the spatial organization of human activities. It entails the systematic consideration of spatial rela-tions, land-use dynamics, accessibility, and socio-economic interdependencies to promote efficient resource allocation and sustainable development. The objective is to design spatial frameworks that balance urban, suburban, and rural functions, fostering inclusive, resilient, and environmentally responsible territories (Metz, 2024).

Over the past few decades, the emergence of Geographic Information Systems (GIS) has profoundly transformed spatial planning and development practices (Reddy, 2021). These sophisticated computer-based systems surpass traditional cartographic methods by allowing planners to visualize, analyze, and interpret complex spatial datasets with exceptional accuracy. GIS facilitates the integration of heterogeneous information — including demographic profiles, transportation networks, environmental conditions, and land-use patterns into coherent analytical models that support evidence-based decision-making.

Unlike static mapping techniques, GIS enables dynamic, multi-layered representations of spatial phenomena, empowering planners to simulate scenarios and forecast potential outcomes. For example, GIS can assess the impact of new infrastructure on traffic distribution, identify zones at risk of flooding or pollution, and evaluate the implications of zoning modifications. Such capabilities enhance the strategic dimension of planning by ensuring that proposed interventions are both feasible and aligned with long-term sustainability objectives.

Furthermore, GIS has become an essential instrument for addressing complex challenges in spatial management and governance. By providing analytical precision and transparency, it supports the identification of urban sprawl patterns, transportation bottlenecks, and land-use conflicts. Through this, planners and policymakers can design targeted, equitable, and efficient solutions to optimize the use of space and resources.

In conclusion, the integration of Geographic Information Systems (GIS) into town and country planning represents a significant paradigm

shift in contemporary spatial management. By bridging the gap between theoretical frameworks and practical implementation, GIS enhances the analytical and decision-making capacities of planners, enabling them to address complex, multidimensional challenges more effectively. This integration fosters the formulation of intelligent, adaptive, and sustainable spatial development strategies that support long-term territorial resilience and balanced growth.

In contemporary planning practice, GIS extends beyond visualization to encompass predictive modeling, real-time monitoring, and participatory planning. These functions enable adaptive management of territories in response to rapid urbanization, environmental degradation, and climate change (Reddy, 2021). As such, GIS not only strengthens spatial analysis but also facilitates collaborative decision-making among planners, institutions, and communities.

Results and discussion

Diachronic monitoring of Batna's urban evolution (2000 and 2018)

The diachronic analysis of Batna's urban evolution between 2000 and 2018 provides insights into the structural transformation of both the city's urban fabric and its road network. Over this period, rapid urbanization and uncoordinated spatial expansion have contributed to the fragmentation of the urban fabric, resulting in multiple functional inconsistencies.

These include the emergence of disconnected neighborhoods, unequal accessibility, and a growing disparity between central and peripheral zones. Such fragmentation illustrates the challenges associated with unmanaged urban growth and the absence of integrated spatial planning strategies.

Concurrently, Batna's road network underwent significant spatial and functional restructuring during this 18-year period. As illustrated in the accompanying maps, this evolution is marked by an expansion in total road length and the reorganization of the network's hierarchical structure. The development of arterial corridors, bypasses, and secondary roads reflects efforts to accommodate rising mobility demands and support the city's expanding urban footprint.

The 2000 map depicts a highly centralized network, concentrated around the urban core, which served as the main hub for both local and regional traffic. This configuration led to severe congestion, particularly during peak hours, as peripheral districts remained insufficiently connected to the main transportation system. The absence of bypass

routes exacerbated these bottlenecks by channeling intercity traffic through the already congested downtown area.

By contrast, the 2018 map reveals a more decentralized network structure, characterized by the emergence of peripheral roads and bypasses designed to redistribute traffic flows. This evolution demonstrates a deliberate planning effort to reduce dependence on central arteries, improve access to suburban areas, and facilitate urban expansion into newly developed zones. Quantitative analysis further indicates a notable increase in road network density, reflecting the city's response to rising population pressures and economic growth.

Despite these advances, several challenges persist. The expansion of the road network has not entirely mitigated the fragmentation of the urban fabric, as some recently urbanized areas remain poorly integrated into the overall transport system. Moreover, functional disparities continue to affect network performance due to the lack of adaptive traffic management systems and uneven infrastructure quality across districts.

From a planning perspective, the diachronic monitoring of Batna underscores the need for a comprehensive and integrated urban development strategy. To address the persistent issues of fragmentation and inefficiency, future interventions should prioritize:

Enhanced Strategic Connectivity: Strengthening linkages between central and peripheral areas through well-coordinated arterial and secondary road systems.

Adaptive Traffic Management: Implementing intelligent transportation technologies to regulate congestion and optimize traffic flows in real time.

Sustainable Urban Growth: Aligning transport infrastructure development with broader spatial planning objectives to promote balanced, inclusive, and environmentally responsible growth.

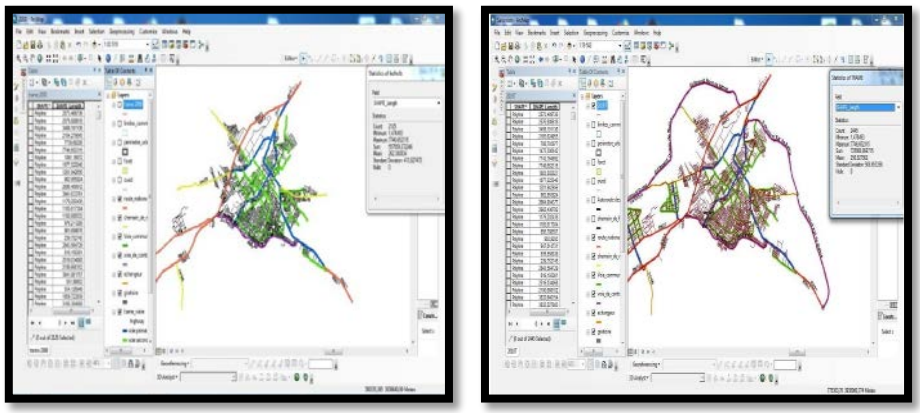


Figure 7 - Diachronic monitoring of the city of Batna (2000-2018)

Results of the urban road classification in Batna

The analysis of the urban road classification in Batna reveals a series of structural dynamics and functional challenges directly influencing traffic regulation and mobility efficiency. The existing road network, composed of bypass routes, exchange roads, and arterial roads, provides a foundational framework for urban mobility. However, it remains insufficient to accommodate the city's rapidly evolving transportation demands (Metz, 2024).

1. Connectivity disparities

Recently urbanized peripheral areas exhibit limited connectivity with the city center and other strategic zones. This deficiency stems from the fragmentation of the road network, which hinders the functional integration of different urban sectors and restricts mobility flows.

2. Central area congestion:

Persistent traffic congestion in the city center, particularly during peak hours, continues to generate major bottlenecks. The saturation of principal roads is exacerbated by the absence of adaptive traffic management systems capable of dynamically redistributing flows across the network.

3. Underutilization of bypass routes:

Although the northern and southern bypasses were designed to divert transit traffic from the central core, their actual use remains limited. This underutilization is largely attributed to insufficiently developed access points, inadequate directional signage, and a lack of integration with primary road arteries.

4. Network-wide congestion propagation:

Localized congestion frequently produces a chain reaction across the urban network. Traffic delays originating at specific intersections propagate upstream, affecting adjacent routes and amplifying network-wide inefficiencies.

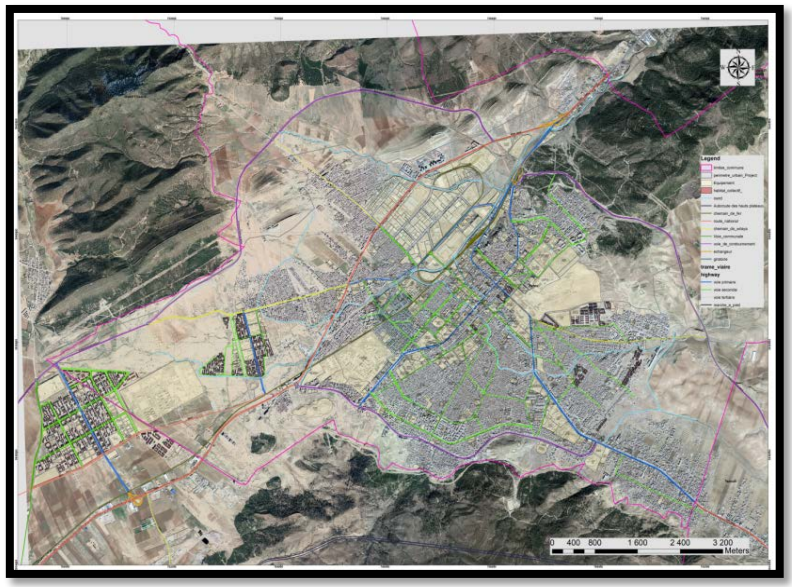


Figure 8 - Map 7, hierarchy of urban roads

Functional classification in planning

Effective planning of Batna's overall road network requires a functional classification of its roads. This classification prioritizes routes based on demographic and socio-economic criteria, as well as their functionality within the city's broader urban transport system. Roads are categorized primarily by their role in facilitating connectivity, with motorways being the exception, where design parameters serve as the primary determinant. Additional factors, such as traffic volume and road quality, are used as secondary criteria to characterize and prioritize main roads.

By employing this approach, Batna's road network is designed to optimize traffic flow and address congestion issues strategically. Roads serving higher traffic densities and critical urban zones are prioritized for upgrades, ensuring that key transportation corridors remain efficient and effective.

Implementation of "taps" access control

To further enhance traffic management, Batna has implemented a regulatory strategy utilizing an access control system known as "taps."

These "taps" consist of strategically located traffic lights placed along penetration axes (exchange lanes) at intersections with the internal ring

road and at entry points to the city center. Their primary function is to manage the flow of vehicles into the city center during periods of high congestion (Gwalani, 2024).

By temporarily holding back vehicles attempting to enter the city, these access control measures help maintain traffic fluidity within the hyper-center. Vehicles are delayed upstream but eventually navigate through the improved flow conditions within the central network.

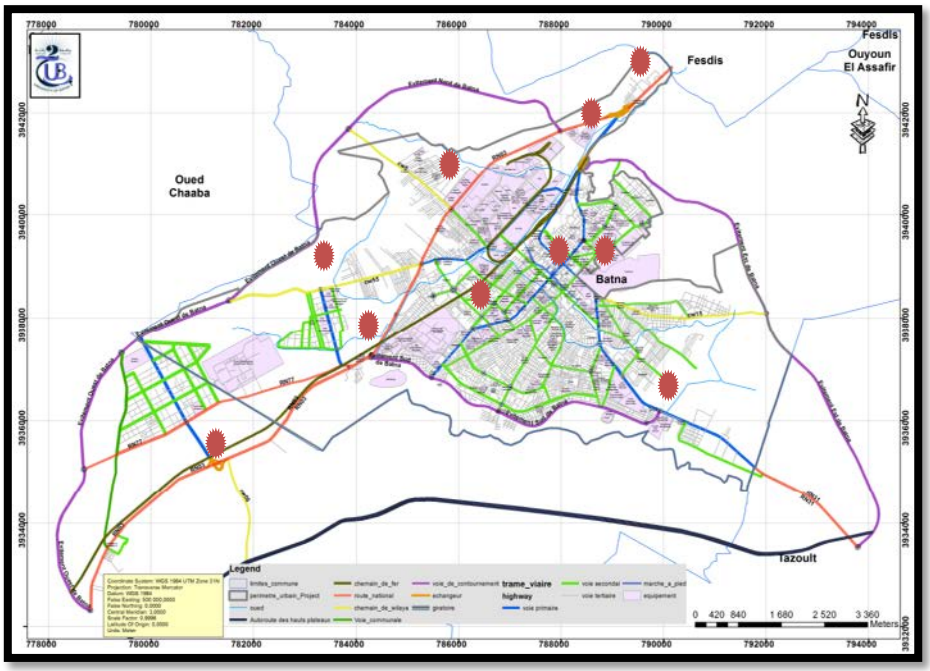


Figure 9 - Map 8, taps control

Structure and congestion in Batna's road network

Batna's road network exhibits a dense and highly interconnected structure, composed of several key components:

Bypasses (northern and southern), designed to divert transit and heavy vehicles away from the urban core;

Exchange roads, which penetrate the city and connect peripheral districts to central areas;

Arterial and distribution roads, ensuring internal accessibility and linking major functional zones within the city.

Together, these elements form a relatively extensive and integrated transportation framework that supports mobility across Batna's urban fabric.

However, despite this structural connectivity, the network frequently experiences reduced operational efficiency due to recurrent congestion.

Traffic saturation often generates chain reactions, where queues originating at one intersection propagate upstream to neighboring junctions, resulting in interdependent and widespread delays throughout the network.

These cascading effects considerably undermine the overall performance and reliability of Batna's road system.

Conclusion

The functional classification of Batna's urban road network provides a coherent framework for analyzing traffic dynamics and improving mobility efficiency. By distinguishing between bypass, exchange, arterial, and local roads, it clarifies network hierarchies and supports targeted planning interventions.

Findings reveal that while the network is well connected, persistent issues such as the underuse of bypasses, congestion in central arteries, and insufficient local infrastructure continue to limit efficiency. Addressing these requires coordinated interventions that strengthen primary routes, modernize secondary roads, and integrate multimodal options such as public transport, cycling, and walking.

Regular updates to road classifications and their integration into zoning and urban planning policies are essential to ensure responsiveness to demographic and spatial change. GIS technologies further enhance this process by identifying congestion hotspots, modeling future scenarios, and linking mobility data with socio-economic and geographic factors.

Despite these advances, network fragmentation and localized congestion remain significant challenges. An adaptive, data-driven approach to planning and regulation is therefore crucial. Overall, the combination of functional classification and GIS offers a replicable model for developing efficient, resilient, and sustainable urban transport systems—both in Batna and comparable urban contexts.

References

Anu, M.R., 2022. Cities of migration. In: Cities of Migration. Springer, pp.331–349. Available at: https://doi.org/10.1007/978-3-030-92377-8_16

Aryan, G., Abhishek, P., Adish, P., Prasenjit, B. and Kailas, D., 2024. Prediction and management of traffic congestion in urban environments. In: *Proceedings of the International Conference on Computing, Communication, and Networking Technologies*. IEEE, pp.1–6. Available at: https://doi.org/10.1109/icccnt61001.2024.10724090

Chetara, A., Benabbas, M. and Djaghrouri, D., 2022. The effect of sky view factor on the thermic ambiances: Case of Batna city. *International Journal of Innovative Studies in Sociology and Humanities*, 7(8), pp.20–30. Available at: https://doi.org/10.20431/2456-4931.070820

Efrat, B.-L., Nimrod, S., Jinxiao, D., Guanwen, Z. and Shlomo, H., 2024. Addressing the urban congestion challenge based on traffic bottlenecks. *Philosophical Transactions of the Royal Society A*, 382(2282), Article 20240095. Available at: https://doi.org/10.1098/rsta.2024.0095

Faicel, T., 2024. Assessing urban vulnerability to flood risk: A case study in Batna city, northeast Algeria. *Cuadernos de Geografía*, (111), Article 26271. Available at: https://doi.org/10.7203/CGUV.111.26271

Gerardo, G.-R., 2023. Road traffic density classification to improve traffic systems using convolutional neural networks (CNN). In: *Advances in Computing and Intelligent Systems. Springer*, pp.435–448. Available at: https://doi.org/10.1007/978-981-19-8825-7_34

Hamdy, F., Amira, M.E.S. and Mohamed, E.G., 2024. Impact of traffic congestion on transportation systems: Challenges and remediations – *A review. Majallat Kulliyyat Dar Al-Ulum*, (83), pp.1–25. Available at: https://doi.org/10.58491/2735-4202.3191

Khireddine, D. and Aichour, B., 2022. Batna city from organized planning to distortion (Case study Biskra road axis – Algeria). *Mediterranean Journal of Social Sciences*, 13(1), pp.79–94. Available at: https://doi.org/10.36941/mjss-2022-0008

Pamireddy, S.R., 2021. Implication of GIS on sustainable urban planning and management in Uganda. *International Journal of Town Planning and Management*, 7(1), pp.1–12. Available at: https://doi.org/10.47604/IJTS.1268

Rafik, L., Mariem, T. and Nabil, T., 2024. An adaptive data rate scheme for multi-hop forwarding in LoRaWAN networks. In: *Proceedings of the International Wireless Communications and Mobile Computing Conference*. IEEE, pp.109–114. Available at: https://doi.org/10.1109/iwcmc61514.2024.10592512

Sadok, B.Y., 2023. Data-driven approaches for resilient and sustainable urban mobility. In: *Proceedings of the International Conference on Intelligent Systems and New Applications. IEEE*, pp.1–6. Available at: https://doi.org/10.1109/icnas59892.2023.10330531

Wang, X., Zhuocheng, Y., Hengbo, Z., Yiming, L., Xinke, W. and Wei, C., 2024. Research on traffic congestion active control technology for expressway. In: *Proceedings of the International Conference on Machine Learning and Data*

Engineering. ACM, pp.19–24. Available at: https://doi.org/10.1145/3665348.3665351

Yannick, M., Dennis, A., Daniel, A.K. and Michael, F., 2024. *Interactive public transport infrastructure analysis through mobility profiles*: Making the mobility transition transparent. arXiv. Available at: https://doi.org/10.48550/arxiv.2407.10791

Artem, B., Bohdan, S., Mykhailo, D., Nataliia, M. and Taras, P., 2024. Conceptual framework for determining the effectiveness of tasks and measures implementation in state targeted development programs to improve road management efficiency. *Dorogi i Mosti*, (30), pp.13–25. Available at: https://doi.org/10.36100/dorogimosti2024.30.013

Funkcionalna hijerarhija primenom GIS-a: dijagnostika i rešenja za regulaciju saobraćaja u gradu Batna (severoistočni Alžir)

Sonia Adjroud[a], **autor za prepisku**, *Samir* Djenba[b], *Abdelhamid* Khedidja[b], *Hamza* Amireche[c]

[a] University of Batna 02, Institute of Earth and Universe Sciences, Department of Geography and Territorial Planning, Laboratory of Natural Hazards and Land Use (LRNAT), Batna, People's Democratic Republic of Algeria

[b] University of Batna 02, Institute of Earth and Universe Sciences, Department of Geology, Laboratory for Water Resource Mobilization and Management (LMGRE), Batna, People's Democratic Republic of Algeria

[c] University of Constantine 03, Institute of Urban Technology Management, Laboratory of resilient and intelligent dynamic regions (LRIDR), Constantine, People's Democratic Republic of Algeria

OBLAST: geonauke
KATEGORIJA (TIP) ČLANKA: originalni naučni rad

Sažetak:

Uvod/cilj: Grad Batna u severoistočnom Alžiru beleži ubrzan rast broja stanovnika, što je povećalo potrebe za mobilnošću i doveo do značajanog pritiska na ograničenu i dotrajalu putnu mrežu. Zagušenja utiču na glavne gradske saobraćajne koridore i centralne gradske zone. Cilj ovog istraživanja je da dijagnostikuje ove disfunkcionalnosti i predloži strateški okvir za unapređenje odvijanja saobraćaja. U radu se takođe procenjuje efikasnost prostorne analize zasnovane na GIS-u za potrebe planiranja urbane mobilnosti.

Metode: U istraživanju se koriste geografski informacioni sistemi (GIS) i satelitski snimci za analizu saobraćajnog sistema Batne. Područje istraživanja obuhvata primarne i sekundarne saobraćajne pravce unutar urbanog jezgra. Podaci obuhvataju topografske karte, demografske slojeve, namenu zemljišta i terenska opažanja. Alati ArcGIS koriste se za prepoznavanje kritičnih tačaka saobraćajnih zagušenja, merenje

pristupačnosti mreže, procenu usklađenosti hijerarhije puteva i modelovanje sadašnjih i budućih scenarija mobilnosti.

Rezultati: Rezultati ukazuju na ponavljajuća saobraćajna zagušenja duž puta Avenue de l'Indépendance, puta za Biskru i severne obilaznice. Na nekoliko raskrsnica utvrđeni su nivoi zasićenja koji prelaze funkcionalne pragove. Analiza ukazuje na strukturne diskontinuitete, nedovoljnu širinu kolovoza i slabo povezane radijalne pravce. Prostorne korelacije ukazuju na snažan uticaj zona velike gustine naseljenosti i komercijalne koncentracije na pojavu saobraćajnih uskih grla. Izrađene karte otkrivaju nedostatke u povezivanju u pravcu istok–zapad i ograničene mogućnosti za zaobilaženje gradskog centra.

Zaključak: Rezultati podržavaju niz ciljanih intervencija, uključujući izgradnju novih poveznih saobraćajnica, optimizaciju raskrsnica i preraspodelu saobraćajnih tokova. Rezultati potvrđuju da GIS unapređuje preciznost dijagnostike i podržava planiranje zasnovano na dokazima. Predloženi okvir predstavlja skalabilan metod za unapređenje mobilnosti u gradovima koji se ubrzano urbanizuju. Istraživanje pokazuje da integracija prostornog modelovanja sa strateškim planiranjem vodi ka otpornijim i adaptivnijim saobraćajnim sistemima koji su usklađeni sa ciljevima održivog razvoja.

Ključne reči: urbana putna mreža, funkcionalna hijerarhija, regulacija saobraćaja, GIS analiza, Batna, Alžir.

Paper received on: 25 November 2025.
Manuscript corrections submitted on: 5 May 2026.
Paper accepted for publishing on: 6 June 2026.

© 2026 The Authors. Published by Vojnotehnički glasnik / Military Technical Courier (www.vtg.mod.gov.rs).This article is an open access article distributed under the terms and conditions of the Creative Commons Attribution license (http://creativecommons.org/licenses/by/4.0/rs/)

Influence of visco-Pasternak foundation parameters on the bending and vibrational behavior of thick isotropic plates

Hebali Habib[a], *Djidar* Fatima Zohra[b], *Derras* Abdelhak[c]

[a] Mustapha Stambouli University, Department of Civil Engineering, Mascara, People's Democratic Republic of Algeria
e-mail: habib.hebali@univ-mascara.dz,
ORCID iD: https://orcid.org/0009-0001-1309-2595

[b] Mustapha Stambouli University, Department of Civil Engineering, Mascara, People's Democratic Republic of Algeria +
Smart Structures Laboratory (SSL), University of Ain Temouchent, Ain Temouchent, People's Democratic Republic of Algeria
e-mail: fatima.djidar@univ-mascara.dz, **corresponding author**,
ORCID iD: https://orcid.org/0009-0006-6361-073X

[c] Ahmed Ben Bella University – Oran 1, Department of Chemistry, Oran, People's Democratic Republic of Algeria +
Smart Structures Laboratory (SSL), University of Ain Temouchent, Ain Temouchent, People's Democratic Republic of Algeria
e-mail: abdelhakderrasderras@gmail.com,
ORCID iD: https://orcid.org/0009-0006-2459-6461

https://doi.org/10.5937/vojtehg74-59632

FIELD: civil engineering
ARTICLE TYPE: original scientific paper

Abstract:

Introduction/purpose: This study primarily aims to investigate the effect of viscoelastic Pasternak foundation parameters on the bending and free vibrational behavior of simply supported thick isotropic plates using a two-variable high-order shear deformation theory (HSDT). The theory adopted in this study uses a limited number of unknowns and avoids the use of shear correction factors to ensure zero transverse shear stresses at the surface of the plates, which is not the case with other higher-order theories that generally involve four or five unknowns. In addition, the stress and displacement responses are analyzed under uniformly distributed loads (UDLs) and sinusoidally distributed loads (SDLs). Moreover, natural frequencies corresponding to both bending and thickness-shear modes are provided to demonstrate the accuracy of the proposed model in predicting the dynamic behavior of simply supported isotropic square and rectangular plates.

Methods: The main contribution of this work lies in the integration of the effects of elastic foundation parameters and damping coefficients on the bending and vibration responses of simply supported thick isotropic plates, using a refined two-variable high-order shear deformation theory. In

addition, the formulation of the displacement field introduces a number of undetermined integral terms, hence reducing the number of unknowns. The governing equations are derived using Hamilton's principle. Moreover, Navier's method is utilized to determine the analytical solutions for simply supported plates, while natural frequencies are calculated by solving the corresponding eigenvalue problem.

Results: The analytical results are validated against several established higher-order shear deformation theories (ESDT, HSDT, TSDT), the first-order shear deformation theory (FSDT), and the classical plate theory (CPT). The findings show excellent agreement when viscoelastic and foundation effects are not taken into account. It is important to emphasize that when these effects are considered, the results show increased plate stiffness, leading to lower deflections and higher natural frequencies.

Conclusion: The proposed theory provides results in close agreement with those obtained from existing models. It also clearly highlights the significant influence of viscoelastic foundation parameters on both the static and dynamic behavior of isotropic plates.

Key words: bending, vibration, isotropic plate, visco-Pasternak foundations.

Introduction

Nowadays, plates are widely used in industry and several emerging technological fields, such as aeronautics, marine engineering, civil engineering, and mechanical engineering. It has been revealed that transverse shear and normal deformation effects are quite significant in shear-flexible plates. These plates can be made of isotropic, orthotropic, anisotropic, or laminated composite materials.

Furthermore, the behavior of plates subjected to mechanical and thermal loads can generally be predicted using either a three-dimensional (3D) elasticity theory or other equivalent single-layer (ESL) elasticity theories. These ESL theories can take into account the transverse shear and normal deformation effects, depending on the assumptions considered. It should be noted that the classical plate theory (CPT) is the simplest ESL model. It can solely be applied to thin plates for which the shear deformation and transverse normal effects are negligible.

The first-order shear deformation theory (FSDT), which is commonly referred to as the Reissner-Mindlin theory, is the next level in the hierarchy of ESL models. This FSDT theory takes into account the shear deformation effects by assuming a linear variation of displacements through the thickness of the plate, which requires the use of a shear correction factor. According to the findings of Lanhe (2004), Chen (2005),

Park and Kim (2006), Bouazza et al. (2010), Kiani and Eslami (2012), and Yaghoobi & Yaghoobi (2013), this theory is widely used to analyze the behavior of functionally graded material (FGM) plates.

The limitations of CPT and FSDT theories have led to the development of higher-order shear deformation theories (HSDT) which eliminate the need for shear correction factors and provide a more realistic representation of shear deformation and stress variation through the plate thickness. In this regard, various applications of this theory to thick isotropic plates have been explored by Levy (1877), Stein (1986, 1989), Lee et al. (1989), Stein et al. (1990), Shimpi (2002), Ghugal and Pawar (2011), Ghugal and Sayyad (2011), Sayyad and Ghugal (2012), and Djidar et al. (2022).

Likewise, Soldatos (1992), Chen et al. (2009), Xiang et al. (2011), Mantari et al. (2012), Mantari and Guedes Soares (2012), Xiang and Kang (2013), Wattanasakulpong et al. (2013), Grover et al. (2013), and Mantari et al. (2014) carried out a large number of studies to investigate composite and functional gradient (FG) plates using higher-order shear deformation theories (HSDT).

It is worth noting that plates resting on elastic foundations are commonly encountered in various civil and structural engineering sectors. It has been established that the simplest and most commonly used model for characterizing the interaction between the plate and supporting medium is that of Winkler, as this model represents the foundation as an array of independent vertical springs without any shear interaction (Winkler, 1867).

On the other hand, to make this approach more realistic, Pasternak (1954) introduced a two-parameter foundation model by adding a shear layer to the stiffness of the vertical spring, which allows for interaction between adjacent springs.

Likewise, several research studies have been conducted by Huang et al. (2008), Amini et al. (2009), Ait Atmane et al. (2010), Ameur et al. (2011), Baferani et al. (2011), Fallah et al. (2013), Sobhy (2013), Hebali et al. (2014), Mahi et al. (2015), Saidi et al. (2016), and Benahmed et al. (2017) to examine the mechanical behavior of functionally graded (FG) plates resting on a Winkler-Pasternak foundation.

More recently, attention has turned towards viscoelastic foundations, which extend the Pasternak foundation model by introducing time-dependent behavior. In addition, numerous studies have explored the mechanical response of FG beams and plates resting on viscoelastic foundations under various loading and boundary conditions.

Zeighampour and Beni (2015), they analyzed the vibrational behavior of axially functionally graded (AFG) nanobeams resting on a viscoelastic Pasternak foundation. Arani and Kiani (2018), they conducted a nonlinear free and forced vibration analysis of microbeams resting on a nonlinear orthotropic visco-Pasternak foundation, while considering various boundary conditions. Similarly, Arshid et al. (2019) employed the classical and some higher-order plate theories, such as CPT, FSDT, and TSDT, to investigate the effect of porosity on the free vibration of SPFG circular plates resting on viscoelastic Pasternak foundations. Boulefrakh et al. (2019), they mainly focused on the bending and vibration behaviors of thick FG plates, while highlighting the effect of viscoelastic foundation parameters. In this context, Bounouara et al. (2023) conducted two distinct studies. In the first one, the authors analyzed the impact of viscoelastic Pasternak foundations on the free vibration behavior of exponentially graded sandwich plates under various boundary conditions, while in the second, they primarily focused on the thermo-mechanical bending responses of anisotropic thick laminated composite plates resting on a viscoelastic foundation.

Furthermore, Bennedjadi et al. (2023) employed a refined shear deformation theory to investigate the buckling response of exponentially graded sandwich plates supported by viscoelastic foundations. Likewise, I.M. Mudhaffar (2023) proposed a quasi-3D shear deformation theory with four variables to study the bending behavior of FG plates subjected to hygro-thermo-mechanical loading and supported by viscoelastic foundations. Similarly, Frahlia (2023) used the four-unknown high-order shear deformation theory to assess the effects of viscoelastic foundation parameters on the dynamic response of FG plates.

The present study essentially aims to analyze the bending and free vibration behavior of simply supported thick isotropic plates resting on a viscoelastic Pasternak foundation. To achieve this, it was deemed appropriate to adopt a simplified higher-order shear deformation theory with only two unknowns. The viscoelastic foundation model incorporates the damping effects into the classical Pasternak foundation that is characterized by the Winkler-Pasternak shear modulus. Then, a validation study was carried out in order to assess the accuracy and reliability of the proposed theory. The results obtained showed excellent agreement with those reported in the literature.

It is worth emphasizing that, though Djidar et al. (2022) utilized the same higher-order shear deformation theory, their study did not consider plates resting on a viscoelastic foundation. The present work seeks to extend the theory to include this effect, while incorporating the Winkler

modulus (Kw), the Pasternak shear modulus (Ks), and the viscoelastic damping coefficient (Ct). In addition, a comprehensive parametric study is conducted to investigate the impact of these three viscoelastic parameters on plate deflection and natural frequencies, thereby highlighting the novelty and significance of the present research.

Theoretical formulations

Plate under consideration

An isotropic plate of length a, width b, and thickness h is considered in this study, as illustrated in Figure 1.

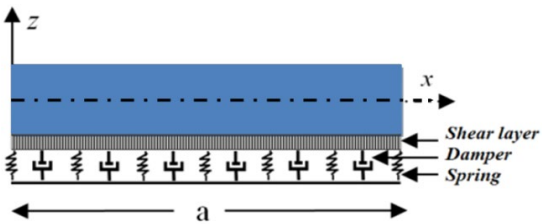


Figure 1 – Schematic of an isotropic plate resting on visco-Pasternak foundation

Kinematics and strains

The displacement field adopted for the model under consideration is based on the formulation presented by Djidar et al. (2022). Hence,

$$\begin{aligned} u(x,y,z,t) &= -z\frac{\partial w_0}{\partial x} + K_1 f(z)\int \theta(x,y,t)\,dx \\ v(x,y,z,t) &= -z\frac{\partial w_0}{\partial y} + K_2 f(z)\int \theta(x,y,t)\,dy \\ w(x,y,z,t) &= w_0(x,y,t) \end{aligned} \tag{1}$$

where:

u, v, and w are the displacement components along the x, y, and z directions, respectively,

w_0 is the transverse displacement of a mid-line point of the plate, and

θ represents the rotation of the plate's cross-section due to transverse shear deformation, at the neutral axis.

In this study, the transverse shear function takes the following form, which was proposed by Karama et al. (2003):

$$f(z) = z\exp\left[-2\left(\frac{z}{h}\right)^2\right] \tag{2}$$

It is important to emphasize that the coefficients K_1 and K_2, given in (1), closely depend on the plate geometry. It is also noted that the kinematics

of Eq. (1) introduces only two unknowns (w_0 and θ). The strain-displacement relations used in the theoretical framework adopted in this study may therefore be expressed as:

$$\begin{cases} \varepsilon_x = \dfrac{\partial u}{\partial x} = -z\dfrac{\partial^2 w_0}{\partial x^2} + k_1\theta f(z)\,, \varepsilon_y = \dfrac{\partial v}{\partial y} - z\dfrac{\partial^2 w_0}{\partial y^2} + k_2\theta f(z) \\ \gamma_{xy} = \dfrac{\partial u}{\partial y} + \dfrac{\partial v}{\partial x} = -\dfrac{\partial^2 w_0}{\partial x \partial y} + k_1\dfrac{\partial}{\partial y}\int \theta\, dx + k_2\dfrac{\partial}{\partial x}\int \theta\, dy f(z) \\ \gamma_{yz} = \dfrac{\partial v}{\partial z} + \dfrac{\partial w}{\partial y} = k_2\int \theta\, dy \dfrac{df(z)}{dz}, \gamma_{xz} = \dfrac{\partial u}{\partial z} + \dfrac{\partial w}{\partial x} = k_1\int \theta\, dx \dfrac{df(z)}{dz} \end{cases} \quad (3)$$

$$\begin{Bmatrix} \varepsilon_x \\ \varepsilon_y \\ \gamma_{xy} \end{Bmatrix} = z\begin{Bmatrix} k_x^b \\ k_y^b \\ k_{xy}^b \end{Bmatrix} + f(z)\begin{Bmatrix} k_x^s \\ k_y^s \\ k_{xy}^s \end{Bmatrix}, \begin{Bmatrix} \gamma_{yz} \\ \gamma_{xz} \end{Bmatrix} = g(z)\begin{Bmatrix} \gamma_{yz}^0 \\ \gamma_{xz}^0 \end{Bmatrix} \quad (4)$$

where:

$$\begin{Bmatrix} k_x^b \\ k_y^b \\ k_{xy}^b \end{Bmatrix} = \begin{Bmatrix} -\dfrac{\partial^2 w_0}{\partial x^2} \\ -\dfrac{\partial^2 w_0}{\partial y^2} \\ -\dfrac{\partial^2 w_0}{\partial x \partial y} \end{Bmatrix}, \begin{Bmatrix} k_x^s \\ k_y^s \\ k_{xy}^s \end{Bmatrix} = \begin{Bmatrix} k_1\theta \\ k_2\theta \\ k_1\dfrac{\partial}{\partial y}\int \theta\, dx + k_2\dfrac{\partial}{\partial x}\int \theta\, dy \end{Bmatrix} \quad (5)$$

$$\begin{Bmatrix} \gamma_{yz}^0 \\ \gamma_{xz}^0 \end{Bmatrix} = \begin{Bmatrix} k_2\int \theta\, dy \\ k_1\int \theta\, dx \end{Bmatrix}, g(z) = \frac{df(z)}{dz}$$

Navier's solution is determined in order to identify the integrals used in the proposed kinematics. This solution is thus given by the following expressions:

$$\frac{\partial}{\partial y}\int \theta\, dx = \acute{A}\frac{\partial^2\theta}{\partial x \partial y}\,, \frac{\partial}{\partial x}\int \theta\, dy = \acute{B}\frac{\partial^2\theta}{\partial x \partial y}\,, \int \theta\, dx = \acute{A}\frac{\partial\theta}{\partial x}\,, \int \theta\, dy = \acute{B}\frac{\partial\theta}{\partial y} \quad (6)$$

According to Eq. (6), in the case of the Navier approach, the coefficients A' and B' are taken into account depending on the type of solution used. Hence, A', B', k_1, and k_2 may be expressed as:

$$\acute{A} = -\frac{1}{\lambda^2}\,, \acute{B} = -\frac{1}{\mu^2}\,, k_1 = \lambda^2\,, k_2 = \mu^2 \quad (7)$$

where λ and μ are defined in Eq.(27).

For an isotropic elastic material plate with uniform thickness, the contribution of the transverse normal stress σ_z to the global structural response is considered negligible compared with the in-plane stresses σ_x and σ_y. Moreover, the assumption of linear elasticity allows asserting that the in-plane stresses σ_x and σ_y are directly associated with the normal strains ε_x and ε_y, while the shear stresses τ_{xy}, τ_{yz} and τ_{xz} are related to the corresponding shear strains γ_{xy}, γ_{yz} and γ_{xz} through the constitutive relations given below.

$$\begin{aligned}\sigma_x &= \frac{E}{(1-\nu^2)}\left[\varepsilon_x + \nu\varepsilon_y\right] = \frac{E}{(1-\nu^2)}\varepsilon_x + \frac{E\nu}{(1-\nu^2)}\varepsilon_y \\ \sigma_y &= \frac{E}{(1-\nu^2)}\left[\varepsilon_y + \nu\varepsilon_x\right] = \frac{E}{(1-\nu^2)}\varepsilon_y + \frac{E\nu}{(1-\nu^2)}\varepsilon_x \\ \tau_{xy} &= \frac{E}{2(1+\nu)}\gamma_{xy}, \tau_{xz} = \frac{E}{2(1+\nu)}\gamma_{xz}, \tau_{yz} = \frac{E}{2(1+\nu)}\gamma_{yz}\end{aligned} \tag{8}$$

C_{ij} can be expressed as follows:

$$\frac{E}{1-\nu^2} = C_{11} = C_{22}, \frac{\nu E}{1-\nu^2} = C_{12}, \frac{E}{2(1+\nu)} = C_{44} = C_{55} = C_{66} \tag{9}$$

Equations of motion

The isotropic plate considered in this study rests on a homogeneous viscoelastic foundation that is defined by three parameters, namely, the linear Winkler modulus Kw, Pasternak shear modulus Ks, and damping coefficient of the viscoelastic medium Ct.

In the case of an unglued contact, i.e. when there is no adhesion, between the isotropic plate and the support, the interaction follows the three-parameter visco-Pasternak foundation model, similar to that established by Zenkour (2016).

It is noteworthy that the vertical reaction R_f of the viscoelastic foundation is expressed as:

$$R_f = \left(k_w - k_s\nabla^2 + C_t\frac{\partial}{\partial t}\right)w \tag{10}$$

On the other hand, the Hamilton's principle is employed to derive the equations of motion. Hence:

$$0 = \int_0^t \left(\delta U + \delta V - \delta K + \delta R_f\right)dt \tag{11}$$

Here, δU denotes the strain energy variation, δV the potential energy variation, and δK the kinetic energy variation.

The above strain energy variation for an isotropic plate may be written as:

$$\delta U = \int_V \left[\sigma_x \delta\varepsilon_x + \sigma_y \delta\varepsilon_y + \tau_{xy}\delta\gamma_{xy} + \tau_{yz}\delta\gamma_{yz} + \tau_{xz}\delta\gamma_{xz}\right] dV$$

$$= \int_A \left[M_x \delta k_x^b + M_y \delta k_y^b + M_{xy}\delta k_{xy}^b + N_{sx}\delta k_x^s + N_{sy}\delta k_y^s + N_{sxy}\delta k_{xy}^s + N_{Tcx}\delta\gamma_{xz}^0 + N_{Tcy}\delta\gamma_{yz}^0\right] dV \quad (12)$$

where A is the top surface. The stress resultants M and N are given by:

$$\left(M_x, M_y, M_{xy}\right) = \int_{-h/2}^{h/2} \left(\sigma_x, \sigma_y, \tau_{xy}\right) z dz \ , \left(N_{sx}, N_{sy}, N_{sxy}\right)$$

$$= \int_{-h/2}^{h/2} \left(\sigma_x, \sigma_y, \tau_{xy}\right) f(z) dz \quad (13)$$

$$\text{and } \left(N_{Tcx}, N_{Tcy},\right) = \int_{-h/2}^{h/2} \left(\tau_{xz}, \tau_{yz}\right) g(z) dz$$

Likewise, the variation of external work can be written as:

$$\delta V = -\int_A q \delta w_0 dA \quad (14)$$

Similarly, the variation of kinetic energy of the plate is given by:

$$\delta K = \int_V \left(\ddot{u}\ \delta u + \ddot{v}\ \delta v + \ddot{w}\ \delta w\right) \rho dV$$

$$\delta K = \int_A \left\{ I_1 \ddot{w}_0 \partial\ddot{w}_0 + I_2 \left(\frac{\partial\ddot{w}_0}{\partial x}\frac{\partial\delta w_0}{\partial x} + \frac{\partial\ddot{w}_0}{\partial y}\frac{\partial\delta w_0}{\partial y}\right) - I_3 - I_3\left(K_1\acute{A}\frac{\partial\ddot{w}_0}{\partial x}\frac{\partial\delta\theta}{\partial x} + K_1\acute{A}\frac{\partial\ddot{\theta}}{\partial x}\frac{\partial\delta w_0}{\partial x} + K_2\acute{B}\frac{\partial\ddot{w}_0}{\partial y}\frac{\partial\delta\theta}{\partial y} + K_2\acute{B}\frac{\partial\ddot{\theta}}{\partial y}\frac{\partial\delta w_0}{\partial y}\right) + I_4\left(\left(K_1\acute{A}\right)^2\frac{\partial\ddot{\theta}}{\partial x}\frac{\partial\delta\theta}{\partial x} + \left(K_2\acute{B}\right)^2\frac{\partial\ddot{\theta}}{\partial y}\frac{\partial\delta\theta}{\partial y}\right)\right\} dA \quad (15)$$

The dot superscript indicates differentiation with respect to time t, ρ is the mass density, and I_i denotes the mass inertias, as expressed below:

$$(I_1, I_2, I_3, I_4) = \int_{-h/2}^{h/2} (1, z^2, zf(z), f(z)^2)\rho dz \tag{16}$$

Substitution of Eqs. (12), (14) and (15) into Eq. (11) leads to the following equations of motion:

$$\begin{aligned}
\delta w_0: & -\frac{\partial^2 M_x}{\partial x^2} - \frac{\partial^2 M_y}{\partial y^2} - 2\frac{\partial^2 M_{xy}}{\partial x \partial y} + q + k_w w_0 - k_s^x \frac{\partial^2 w_0}{\partial x^2} - k_s^y \frac{\partial^2 w_0}{\partial y^2} \\
& + k_w + c_t * \frac{\partial w_0}{\partial t} \\
& = -I_1 \frac{\partial^2 w_0}{\partial t^2} + I_2 \left(\frac{\partial^4 w_0}{\partial x^2 \partial t^2} + \frac{\partial^4 w_0}{\partial y^2 \partial t^2} \right) \\
& - I_3 \left(K_1 \acute{A} \frac{\partial^4 \theta}{\partial x^2 \partial t^2} + K_2 \acute{B} \frac{\partial^4 \theta}{\partial y^2 \partial t^2} \right) \\
\delta\theta: & K_1 \acute{A} \frac{\partial^2 N_{sx}}{\partial x^2} + K_2 \acute{B} \frac{\partial^2 N_{sy}}{\partial y^2} + \left(K_1 \acute{A} + K_2 \acute{B} \right) \frac{\partial^2 N_{sxy}}{\partial x \partial y} - K_1 \acute{A} \frac{\partial N_{Tcx}}{\partial x} \\
& - K_2 \acute{B} \frac{\partial N_{Tcy}}{\partial y} \\
& = -I_3 \left(K_1 \acute{A} \frac{\partial^4 w_0}{\partial x^2 \partial t^2} + \quad K_2 \acute{B} \frac{\partial^4 w_0}{\partial y^2 \partial t^2} \right) \\
& + I_4 \left(\left(K_1 \acute{A} \right)^2 \frac{\partial^4 \theta}{\partial x^2 \partial t^2} + \left(K_2 \acute{B} \right)^2 \frac{\partial^4 \theta}{\partial y^2 \partial t^2} \right)
\end{aligned} \tag{17}$$

Similarly, substituting Eq. (4) into Eq. (8) and incorporating the resulting expressions into Eqs. (13) allows deriving the equations of motion in terms of displacements, in the following compact form:

$$\begin{Bmatrix} M \\ N_S \end{Bmatrix} = \begin{Bmatrix} A & B \\ B & A_s \end{Bmatrix} \begin{Bmatrix} k^b \\ k^s \end{Bmatrix}, \; N_{Tc} = H\gamma \tag{18}$$

in which

$$\begin{gathered}
M = \left\{ M_x, M_y, M_{xy} \right\}^t, N_s = \left\{ N_{sx}, N_{sy}, N_{sxy} \right\}^t \\
k^b = \left\{ k_x^b, k_y^b, k_{xy}^b \right\}^t, k^s = \left\{ k_x^s, k_y^s, k_{xy}^s \right\}^t
\end{gathered} \tag{19}$$

$$\text{with } A = \begin{bmatrix} A_{11} & A_{12} & 0 \\ A_{12} & A_{22} & 0 \\ 0 & 0 & A_{66} \end{bmatrix}, B = \begin{bmatrix} B_{11} & B_{12} & 0 \\ B_{12} & B_{22} & 0 \\ 0 & 0 & B_{66} \end{bmatrix}, \quad A_s = \begin{bmatrix} A_{s11} & A_{s12} & 0 \\ A_{s12} & A_{s22} & 0 \\ 0 & 0 & A_{s66} \end{bmatrix} \tag{20}$$

$$N_{Tc} = \{N_{Tcx}, N_{Tcy}\}^t, \gamma = \{\gamma_{xz}^0, \gamma_{yz}^0\}^t,$$
$$H = \begin{bmatrix} H_{44} & 0 \\ 0 & H_{55} \end{bmatrix}$$

Likewise, the stiffness components are defined as follows:

$$\left(A_{ij}, B_{ij}, A_{sij}\right) = \int_{-h/2}^{h/2} (z^2, zf(z), f(z)^2) C_{ij} dz \ , (\ i,j = 1,2,6)$$
$$H_{ij} = \int_{-h/2}^{h/2} \acute{f}(z)^2 C_{ij} dz \ , (\ i,j = 4,5) \tag{21}$$

Thus, substituting Eq. (18) into Eq. (17) allows formulating the equations of motion in terms of displacements (w_0, θ). The resulting governing equations may then be written in the following form:

$$\begin{aligned}
&A_{11}d_{1111}w_0 - B_{11}K_1\acute{A}d_{1111}\theta + 2A_{12}d_{1122}w_0 \\
&\quad - B_{12}\left(K_1\acute{A} + K_2\acute{B}\right)d_{1122}\theta + A_{22}d_{2222}w_0 \\
&\quad - \ B_{22}K_2\acute{B}d_{2222}\theta + 4A_{66}d_{1122}w_0 \\
&\quad - 2B_{66}\left(K_1\acute{A} + K_2\acute{B}\right)d_{1122}\theta + q + k_w w_0 - k_s^x d_{11}w_0 \\
&\quad - k_s^y d_{22}w_0 + c_t * \dot{w}_0 \\
&\quad = -I_1\ddot{w}_0 + I_2(d_{11}\ddot{w}_0 + \ d_{22}\ddot{w}_0) \\
&\quad - \ I_3\left(K_1\acute{A}d_{11}\ddot{\theta} + K_2\acute{B}d_{22}\ddot{\theta}\right) \\
&\left(-B_{11}d_{1111}w_0 + A_{s11}K_1\acute{A}d_{1111}\theta - B_{12}d_{1122}w_0\right. \\
&\quad \left. + A_{s12}K_2\acute{B}d_{1122}\theta\right)K_1\acute{A} \\
&\quad + \left(-B_{12}d_{1122}w_0 + \ A_{s12}K_1\acute{A}d_{1122}\theta - B_{22}d_{2222}w_0\right. \\
&\quad \left. + A_{s22}K_2\acute{B}d_{2222}\theta\right)K_2\acute{B} \\
&\quad + \left(-2B_{66}d_{1122}w_0\right. \\
&\quad \left. + A_{s66}\left(K_1\acute{A} + \ K_2\acute{B}\right)d_{1122}\theta\right)\left(K_1\acute{A} + K_2\acute{B}\right) \\
&\quad - \left(K_1\acute{A}\right)^2 H_{55}d_{11}\theta - \left(K_2\acute{B}\right)^2 H_{44}d_{22}\theta \\
&\quad = -I_3\left(K_1\acute{A}d_{11}\ddot{w}_0 + \ K_2\acute{B}d_{22}\ddot{w}_0\right) \\
&\quad + I_4\left(\left(K_1\acute{A}\right)^2 d_{11}\ddot{\theta} + \left(K_2\acute{B}\right)^2 d_{22}\ddot{\theta}\right)
\end{aligned} \tag{22}$$

where d_{ij}, d_{ijl} and d_{ijlm} represent the following differential operators:

$$d_{ij} = \frac{\partial^2}{\partial x_i \partial x_j}, d_{ijl} = \frac{\partial^3}{\partial x_i \partial x_j \partial x_l}, d_{ijlm} = \frac{\partial^4}{\partial x_i \partial x_j \partial x_l \partial x_m}, d_i = \frac{\partial}{\partial x_i}, \quad (\ i,j,l,m = 1,2) \tag{23}$$

Regarding the shear stresses $\left(\tau_{xz}, \tau_{yz}\right)$, they can be expressed either by the constitutive relations in Eq. (8), or by integrating the 3D elasticity equilibrium equations with respect to the thickness coordinate, as previously reported by Younsi et al. (2018) and Boulefrakh et al. (2019).

$$\frac{\partial \sigma_x}{\partial x}+\frac{\partial \tau_{xy}}{\partial y}+\frac{\partial \tau_{xz}}{\partial z}=0 \text{ and } \frac{\partial \tau_{xy}}{\partial x}+\frac{\partial \sigma_y}{\partial y}+\frac{\partial \tau_{yz}}{\partial z}=0 \quad (24)$$

Then, integrating Eq. (24) with respect to the thickness coordinate z, and applying appropriate boundary conditions at the upper and lower surfaces of the plate, yields:

$$[\tau_{xz}]_{z=\pm h/2}=0\,, \qquad [\tau_{yz}]_{z=\pm h/2}=0 \quad (25)$$

It is important to note that, in this study, τ_{xz}^{CR} and τ_{yz}^{CR} are the stresses obtained by the constitutive relations, while $(\tau_{xz}^{EE}, \tau_{yz}^{EE})$ are the stresses calculated using the equilibrium equations.

Analytical solution for simply-supported FG plates

The analytical Navier solution method is adopted to obtain analytical solutions in which the displacement components are represented by the product of arbitrary parameters and some known trigonometric functions. This approach ensures that the governing equations of motion and the associated boundary conditions are both satisfied.

$$\begin{Bmatrix} w_0 \\ \theta \end{Bmatrix}=\sum_{m=1}^{\infty}\sum_{n=1}^{\infty}\begin{Bmatrix} w_{mn}e^{i\omega t}sin(\lambda x)sin(\mu y) \\ \theta_{mn}e^{i\omega t}sin(\lambda x)sin(\mu y) \end{Bmatrix} \quad (26)$$

Here, ω is the frequency of the plate's free vibration, and $\sqrt{i}=-1$ represents the imaginary unit.

with

$$\lambda=\frac{m\pi}{a} \quad , \qquad \mu=\frac{n\pi}{b} \quad (27)$$

The transverse load q is expanded in the double-Fourier sine series as:

- Bending analysis of isotropic plates subjected to a uniformly distributed load:

$$q(x,y)=\sum_{m=1}^{\infty}\sum_{n=1}^{\infty}q_{mn}sin\left(\frac{m\pi}{a}x\right)sin\left(\frac{n\pi}{b}y\right)$$

where

$$q_{mn}=\frac{16q_0}{mn\pi^2}\ for\ m=1,3,5,\ldots\ldots and\ \ n=1,3,5,\ldots. \quad (28)$$

$$q_{mn}=0\ \ for\ m=2,4,4,\ldots\ldots and\ \ n=2,4,4,\ldots\ldots$$

-Bending analysis of isotropic plates subjected to a sinusoidally distributed load:

$$q(x,y)=q_0sin\left(\frac{\pi}{a}x\right)sin\left(\frac{n\pi}{b}y\right) \quad (29)$$

Substitution of Eq. (26) into Eq. (22) leads to the following analytical solution:

$$\left(\begin{bmatrix} K_{11} & K_{12} \\ K_{12} & K_{22} \end{bmatrix} - \omega^2 \begin{bmatrix} m_{11} & m_{12} \\ m_{12} & m_{22} \end{bmatrix}\right) \begin{Bmatrix} w_{mn} \\ \theta_{mn} \end{Bmatrix} = \begin{Bmatrix} q_{mn} \\ 0 \end{Bmatrix} \tag{30}$$

where

$$\begin{aligned}
K_{11} &= 2(2A_{66} + A_{12})\lambda^2\mu^2 + A_{22}\mu^4 + A_{11}\lambda^4 + k_s^x\lambda^2 + k_s^y\mu^2 + k_w \\
&\quad - c_t * \omega \\
K_{12} &= -2\left(K_1\acute{A} + K_2\acute{B}\right)B_{66}\lambda^2\mu^2 - \left(K_1\acute{A} + K_2\acute{B}\right)B_{12}\lambda^2\mu^2 \\
&\quad - K_1\acute{A}B_{11}\lambda^4 - K_2\acute{B}B_{22}\mu^4 \\
K_{22} &= \left(K_1\acute{A}\lambda^4 A_{s11} + K_2\acute{B}\lambda^2\mu^2 A_{s12}\right)K_1\acute{A} + \left(K_1\acute{A}\right)^2\lambda^2 H_{55} \\
&\quad + \left(K_1\acute{A}\lambda^2\mu^2 A_{s12} + K_2\acute{B}\mu^4 A_{s22}\right)K_2\acute{B} \\
&\quad + \left(K_2\acute{B}\right)^2\mu^2 H_{44} \\
&\quad + \left(K_1\acute{A}\lambda^2\mu^2 A_{s66} + K_2\acute{B}\lambda^2\mu^2 A_{s66}\right)\left(K_1\acute{A} + K_2\acute{B}\right) \\
m_{11} &= I_1 + I_2(\lambda^2 + \mu^2) \\
m_{12} &= -I_3\left(K_1\acute{A}\lambda^2 + K_2\acute{B}\mu^2\right) \\
m_{22} &= I_4\left(\left(K_1\acute{A}\right)^2\lambda^2 + \left(K_2\acute{B}\right)^2\mu^2\right)
\end{aligned} \tag{31}$$

Numerical results and discussion

Various numerical examples are provided and discussed in prder to demonstrate the effect of the visco-Pasternak foundation on the bending and free vibration responses of simply supported thick isotropic square and rectangular plates.

Then, the results obtained by means of the present high-order shear deformation theory (HSDT) are compared with those derived from other well-established HSDTs, including those proposed by Reddy (1984), Ghugal and Sayyad (2010), Ghugal and Pawar (2011), Sayyad and Ghugal (2012), and Djidar et al. (2022). Moreover, some additional comparisons are made with the predictions of the first-order shear deformation theory (FSDT) previously developed by Mindlin (1951), the classical plate theory (CPT) of Kirchhoff (1850), and the exact elasticity solution of Pagano (1970).

For the sake of consistency, the numerical results related to bending and free vibration are presented in a non-dimensional form, using the following relations:

$$\begin{aligned}
&\bar{u} = \frac{uE_2}{qhS^3}, \bar{w} = \frac{100Ew}{qhS^4}, \left(\bar{\sigma}_x, \bar{\sigma}_y\right) = \frac{\left(\sigma_x, \sigma_y\right)}{qS^2}, \bar{\tau}_{zx} = \frac{\tau_{xz}}{qS}, \\
&\bar{\omega} = \omega_{mn}h\sqrt{\rho/G}, \quad \bar{c}_t = \frac{a^4 c_t}{10^3 D_c}, \qquad K_w = \frac{k_w a^4}{h^3}, \quad K_s = \frac{k_s a^2}{h^3 v}
\end{aligned} \tag{32}$$

where S (a/h) represents the thickness ratio.

The properties of the isotropic plate material are:

$$E = 210GPa, \qquad v = 0.3, \qquad G = \frac{E}{2(1+v)} \text{ and } \rho = 7800\,Kg/m^3$$

where E is Young's modulus, G is the shear modulus, v is Poisson's ratio and ρ is the material's density.

Bending analysis

In the first example, the displacements and stresses for the isotropic square plate simply supported on a viscoelastic foundation and subjected to a uniformly distributed load for both aspect ratios *(a/h)*, i.e. 4 and 10, are compared in Table 1 with those previously published. It can be readily observed that when the viscosity term $\bar{C}_t$ and elastic foundation parameters K_w, K_S are omitted, good agreement between the results is then obtained. It may also be noted that the displacements and stresses decrease with the incorporation of the viscoelastic foundation parameters. Moreover, when the visco-Winkler-Pasternak foundation parameters $\bar{C}_t$,K_w and $K_S$increase, the displacements and stresses decrease. However, it is important to emphasize that the effect of the Pasternak shear modulus parameter (K_s) is more significant than that of Winkler modulus parameter K_w.

In the second example, Table 2 presents a comparison between the displacements and stresses obtained using the proposed theory and others reported in the literature. The results are provided for the isotropic square plate simply supported on a viscoelastic foundation and subjected to a sinusoidally distributed load for different values of K_w, K_S and $\bar{C}_t$. It turns out that in the case where the damping coefficient $\bar{C}_t$ and elastic foundation parameters K_w and K_S are equal to zero, the different theories are in excellent agreement. It was also found that using visco-Winkler-Pasternak foundations leads to smaller displacements and stresses.

Furthermore, it was revealed that high values of the elastic foundation modulus and damping coefficient enhance the bending rigidity of the isotropic plate.

Table 1 – Comparison of non-dimensional in-plane displacement $(\bar{u})$ *at* $(x = 0,\ y = b/2, z = \pm h/2)$*, transverse displacement* $(\bar{w})(x = a/2, y = b/2, z = 0)$*, in-plane normal stress* $(\bar{\sigma}_x)(x = a/2, y = b/2, z = \pm h/2)$*, in-plane shear stress* $(\bar{\sigma}_{xy})(x = 0, y = 0, z = \pm h/2)$*, and transverse shear stress* $(\bar{\sigma}_{zx})(x = 0, y = b/2, z = 0)$ *in an isotropic square plate subjected to a uniformly distributed load*

S	Theory	Model	K_w	K_s	$\bar{C}_t$	$\bar{u}$	$\bar{w}$	$\bar{\sigma}_x$	$\bar{\sigma}_{xy}$	$\bar{\tau}_{zx}^{EE}$
4	A.S.Sayyad (2012)	ESDT	0	0	0	0.079	5.816	0.3	0.223	0.472
	Reddy (1984)	HSDT				0.079	5.869	0.299	0.218	0.452
	Ghugal & Sayyad (2011)	TSDT				0.074	5.68	0.318	0.208	0.42
	Ghugal & Pawar (2011)	HPSDT				0.079	5.858	0.297	0.185	0.451
	Mindlin (1951)	FSDT				0.074	5.633	0.287	0.195	0.495
	Kirchhoff (1850)	CPT				0.074	4.436	0.287	0.195	0.495
	Pagano (1970)	Elasticity				0.072	5.694	0.307	–	–
	Djidar et al. (2022)	ESDT				0.079	5.858	0.300	0.223	0.4504
	Present	ESDT	0	0	0	**0.079**	**5.858**	**0.300**	**0.223**	**0.4504**
			5	0	0.01	**0.077**	**5.654**	**0.289**	**0.218**	**0.4375**
					0.05	**0.072**	**5.284**	**0.269**	**0.206**	**0.414**
					0.1	**0.067**	**4.883**	**0.246**	**0.194**	**0.389**
			0	5	0.01	**0.059**	**4.274**	**0.215**	**0.172**	**0.342**
					0.05	**0.056**	**4.057**	**0.2035**	**0.165**	**0.329**
					0.1	**0.053**	**3.814**	**0.190**	**0.157**	**0.313**
			5	5	0.01	**0.058**	**4.218**	**0.212**	**0.170**	**0.339**
					0.05	**0.056**	**4.006**	**0.201**	**0.163**	**0.325**
					0.1	**0.053**	**3.768**	**0.188**	**0.156**	**0.310**
10	A.S.Sayyad (2012)	ESDT	0	0	0	0.075	4.658	0.289	0.204	0.49
	Reddy (1984)	HSDT				0.075	4.666	0.289	0.203	0.486
	Ghugal & Sayyad (2011)	TSDT				0.073	4.625	0.307	0.195	0.481
	Ghugal & Pawar (2011)	HPSDT				0.074	4.665	0.289	0.193	0.486
	Mindlin (1951)	FSDT				0.074	4.67	0.287	0.195	0.495
	Kirchhoff (1850)	CPT				0.074	4.436	0.287	0.195	0.495
	Pagano (1970)	Elasticity				0.073	4.639	0.289	–	–
	Djidar et al (2022)	ESDT				0.074	4.664	0.289	0.200	0.484
	Present	ESDT	0	0	0	**0.074**	**4.664**	**0.289**	**0.200**	**0.484**
			5	0	0.01	**0.073**	**4.538**	**0.281**	**0.196**	**0.474**
					0.05	**0.069**	**4.304**	**0.265**	**0.187**	**0.455**
					0.1	**0.065**	**4.043**	**0.248**	**0.178**	**0.434**
			0	5	0.01	**0.059**	**3.6205**	**0.221**	**0.161**	**0.395**
					0.05	**0.056**	**3.469**	**0.2105**	**0.1555**	**0.383**
					0.1	**0.054**	**3.296**	**0.199**	**0.149**	**0.369**
			5	5	0.01	**0.058**	**3.581**	**0.218**	**0.160**	**0.392**
					0.05	**0.056**	**3.433**	**0.208**	**0.154**	**0.380**
					0.1	**0.053**	**3.263**	**0.197**	**0.148**	**0.366**

Table 2 – Comparison of non-dimensional in-plane displacement $(\bar{u})$ *at* $(x = 0, y = b/2, z = \pm h/2)$*, transverse displacement* $(\bar{w})$ *at* $(x = a/2, y = b/2, z = 0)$*, in-plane normal stress* $(\bar{\sigma}_x)$ *at* $(x = a/2, y = b/2, z = \pm h/2)$*, in-plane shear stress* $(\bar{\sigma}_{xy})$ *at* $(x = 0, y = 0, z = \pm h/2)$ *and transverse shear stress* $(\bar{\sigma}_{zx})$ *at* $(x = 0, y = b/2, z = 0)$ *in an isotropic square plate subjected to a sinusoidal load.*

S	Theory	Model	K_w	K_s	$\bar{C}_t$	$\bar{u}$	$\bar{w}$	$\bar{\sigma}_x$	$\bar{\sigma}_{xy}$	$\bar{\tau}_{zx}^{EE}$
4	A.S.Sayyad (2012)	ESDT	0	0	0	0.046	3.748	0.213	0.114	0.236
	Reddy (1984)	HSDT				0.046	3.787	0.209	0.112	0.226
	Ghugal & Sayyad (2011)	TSDT				0.044	3.653	0.226	0.133	0.232
	Ghugal & Pawar (2011)	HPSDT				0.047	3.779	0.209	0.112	0.235
	Mindlin (1951)	FSDT				0.044	3.626	0.197	0.106	0.239
	Kirchhoff (1850)	CPT				0.044	2.803	0.197	0.106	0.238
	Pagano (1970)	Elasticity				0.049	3.662	0.217	–	–
	Djidar et al. (2022)	ESDT				0.046	3.778	0.21	0.113	0.234
	Present	ESDT	0	0	0	**0.046**	**3.778**	**0.21**	**0.113**	**0.234**
			5	0	0.01	**0.045**	**3.652**	**0.203**	**0.110**	**0.226**
					0.05	**0.042**	**3.423**	**0.191**	**0.103**	**0.212**
					0.1	**0.039**	**3.174**	**0.177**	**0.095**	**0.197**
			0	5	0.01	**0.035**	**2.781**	**0.155**	**0.083**	**0.172**
					0.05	**0.033**	**2.646**	**0.147**	**0.079**	**0.164**
					0.1	**0.031**	**2.495**	**0.139**	**0.075**	**0.155**
			5	5	0.01	**0.034**	**2.746**	**0.153**	**0.082**	**0.170**
					0.05	**0.032**	**2.614**	**0.146**	**0.078**	**0.162**
					0.1	**0.031**	**2.467**	**0.137**	**0.074**	**0.153**
10	A.S.Sayyad (2012)	ESDT	0	0	0	0.044	2.954	0.2	0.108	0.238
	Reddy (1984)	HSDT				0.044	2.961	0.199	0.107	0.229
	Ghugal & Sayyad (2011)	TSDT				0.044	2.933	0.212	0.11	0.235
	Ghugal & Pawar (2011)	HPSDT				0.044	2.959	0.199	0.107	0.238
	Mindlin (1951)	FSDT				0.044	2.934	0.197	0.106	0.239
	Kirchhoff (1850)	CPT				0.044	2.802	0.197	0.106	0.238
	Pagano (1970)	Elasticity				0.044	2.942	0.2	–	–
	Djidar et al. (2022)	ESDT				0.044	2.959	0.200	0.108	0.238
	Present	ESDT	0	0	0	**0.044**	**2.959**	**0.200**	**0.108**	**0.238**
			5	0	0.01	**0.043**	**2.881**	**0.194**	**0.105**	**0.232**
					0.05	**0.041**	**2.737**	**0.185**	**0.099**	**0.220**
					0.1	**0.039**	**2.576**	**0.174**	**0.094**	**0.207**
			0	5	0.01	**0.035**	**2.310**	**0.156**	**0.084**	**0.186**
					0.05	**0.033**	**2.217**	**0.150**	**0.081**	**0.178**
					0.1	**0.032**	**2.109**	**0.142**	**0.077**	**0.170**
			5	5	0.01	**0.034**	**2.286**	**0.154**	**0.083**	**0.184**
					0.05	**0.033**	**2.194**	**0.148**	**0.080**	**0.176**
					0.1	**0.031**	**2.089**	**0.141**	**0.076**	**0.168**

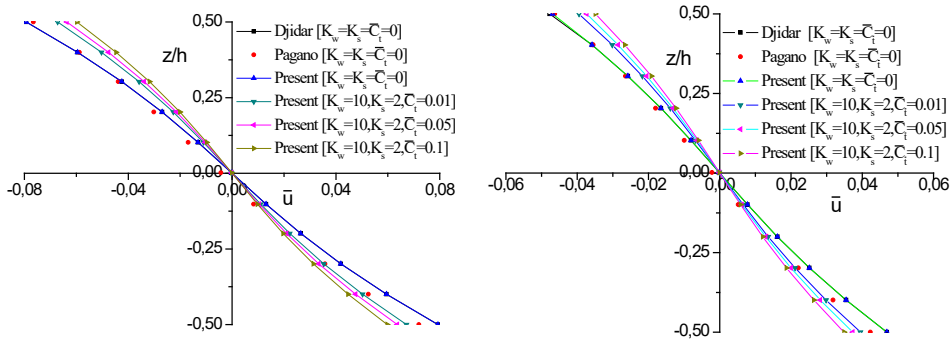


Figure 2 – Variation of the in-plane displacement as a function of the thickness of an isotropic plate subjected successively to a uniformly distributed load and a single sinusoidal load for different values of $\bar{C}_t$, K_w and K_s (a/h= 4)

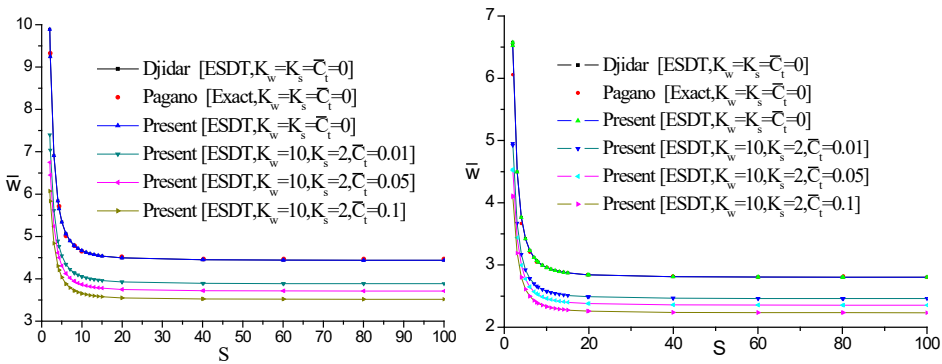


Figure 3 – Variation of the transverse displacement as a function of the thickness of an isotropic plate subjected successively to a uniformly distributed load and a single sinusoidal load for different values of $\bar{C}_t$, K_w and K_s

Figure 2 presents the in-plane displacement $\bar{u}$ through the thickness of the isotropic plate subjected to a uniformly distributed load (UDL) and a sinusoidally distributed load (SDL), successively, for different values of the viscosity term $\bar{C}_t$ and elastic foundation parameters K_w and K_S. This figure clearly indicates that increasing $\bar{C}_t$, K_w, and K_S induces a reduction in the in-plane displacement of the isotropic plate. Furthermore, the plots in this same figure also show that the $\bar{u}$ values obtained with the method proposed in this work, in which the effect of viscoelastic foundation parameters is taken into account, are smaller than those previously found

by Djidar et al. and Pagano, who had neglected the parameters K_w, K_S and $\overline{C}_t$.

Figure 3 displays the variations of the transverse displacement $\overline{w}$ of the isotropic plate subjected to a UDL and a SDL, successively, versus the aspect ratio (a/h), for different values of K_w, K_S and $\bar{C}_t$. It is clearly shown that the transverse displacement $\overline{w}$ decreases as the aspect ratio (a/h) increases. Moreover, the resulting curves suggest that the presence of viscoelastic foundations leads to a decline in the transverse displacement $\overline{w}$ of the isotropic plate. In addition, it is also observed, as expected, that the results obtained indicate that the Pagano and Djidar models generate larger transverse displacements, as these two models do not take into account the effects of the parameters K_w, K_S and $\bar{C}_t$.

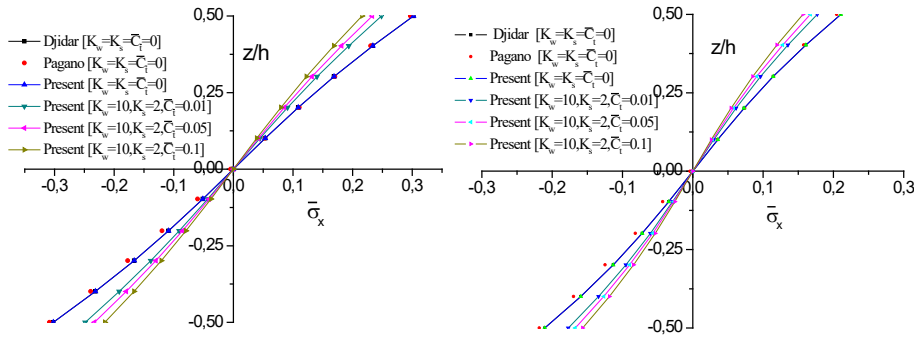


Figure 4 – Variation of the in-plane normal stress as a function of the thickness of an isotropic plate subjected successively to a uniformly distributed load and a single sinusoidal load for different values of $\bar{C}_t$, K_w and K_s (a/h= 4)

Figure 4 depicts the graphical variations of the in-plane normal stresses $\bar{\sigma}_x$ across the thickness of the isotropic plate, successively under UDL and SDL, for different values of the damping coefficient $\bar{C}_t$ and elastic foundation parameters K_w and K_S. This figure explicitly indicates that the maximum tensile stresses occur at a point near the bottom surface of the isotropic plate, while the maximum compressive stresses occur at a point near the upper surface. In addition, the curves in this figure suggest that the visco-elastic foundation has a significant impact on the in-plane normal stress values.

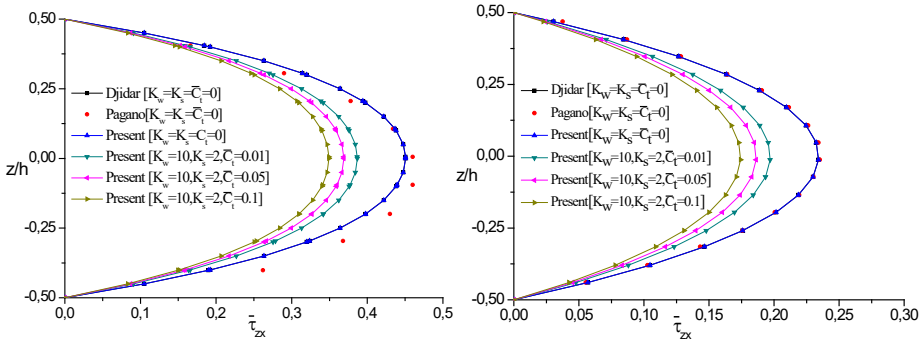


Figure 5 – Variation of the transverse shear stress as a function of the thickness through an isotropic plate subjected successively to a uniformly distributed load and a single sinusoidal load for different values of $\bar{C}_t$, K_w and K_s (a/h= 4)

Figure 5 depicts the through-the-thickness distributions of transverse shear stresses within the square isotropic plate, successively under UDL and SDL. The aspect ratio (a/h) is taken as equal to 4. It is clearly established that the zero shear stress condition at the upper and lower faces of the plate is fully satisfied. It is also observed that the transverse shear stress increases gradually as the $\bar{C}_t$, K_w and K_S values decrease. It can therefore be inferred that the introduction of large visco-elastic foundation parameters can enhance the bending rigidity of the isotropic plate.

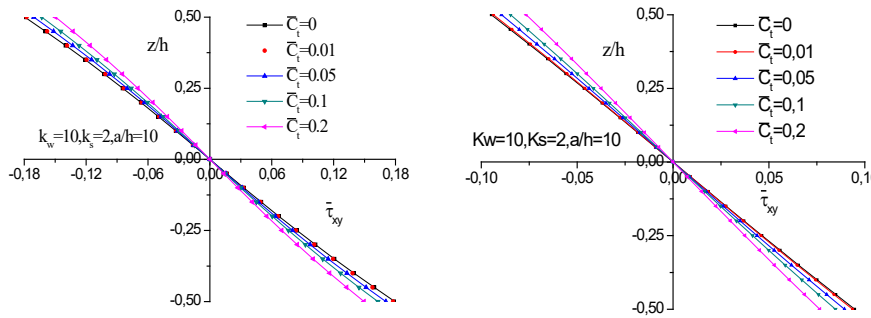


Figure 6 – Variation of the in-plane shear stress as a function of the thickness across an isotropic plate, successively subjected to a uniformly distributed load and a single sinusoidal load for different values of $\bar{C}_t$ (a/h = 10, $K_w = 10$ and, $K_s = 2$) (a/h = 10, $K_w = 10$ and, $K_s = 2$)

Figure 6 presents the variations of the in-plane shear stresses $\bar{\tau}_{xy}$ through the thickness of the isotropic plate, successively subjected to UDL

and SDL, for different values of the viscosity term $\bar{C}_t$. The results obtained reveal that the in-plane compressive and tensile shear stress values are maximum at points near the top and bottom surfaces of the isotropic plate, respectively.

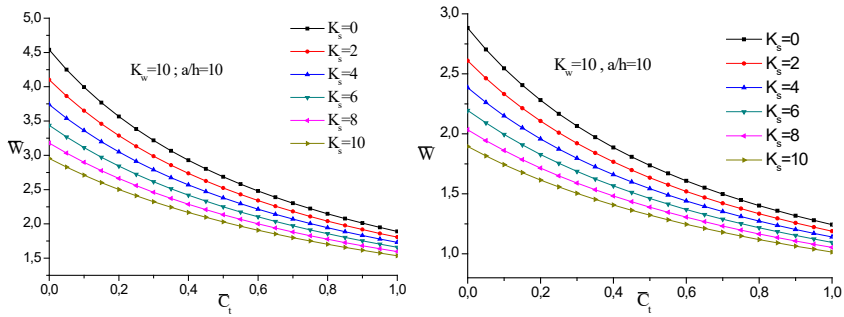


Figure 7 – Effect of damping coefficient and Pasternak shear modulus parameter on the transverse displacement of an isotropic plate, successively subjected to uniformly distributed load and single sine load for different values of K_s (a/h = 10, $K_w = 10$)

Figure 7 presents the variation of the transverse displacement $\bar{w}$ of the isotropic plate successively subjected to a uniformly distributed load and a single sine load versus the damping coefficient $\bar{C}_t$ for various values of the Pasternak shear modulus parameter K_S. It is clearly observed that when the viscosity term is taken into account, the transverse displacement $\bar{w}$ declines due to the damping effect. This same figure also shows that when the parameter K_S increases, the transverse displacement of the isotropic plate diminishes.

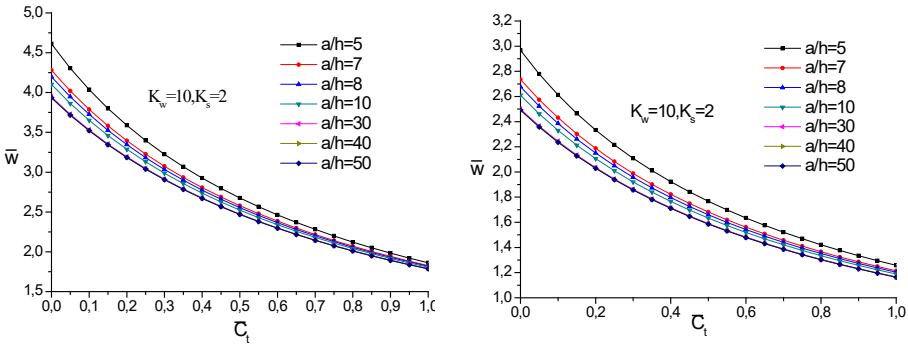


Figure 8 – Effect of damping coefficient on the transverse displacement of the isotropic plate, successively subjected to uniformly distributed load and single sine load for different values of a/h ($K_w = 10$, $K_s = 2$)

Likewise, Figure 8 illustrates the variation of the transverse

displacement $\overline{w}$ of the isotropic plate, successively subjected to UDL and SDL, as a function of the damping coefficient $\bar{C}_t$ for various aspect ratios (a/h). This figure also indicates that the transverse displacement $\overline{w}$ diminishes as the aspect ratio (a/h) rises. It should be emphasized that increasing the damping coefficient leads to a more rigid plate.

Vibration analysis

In this section, two numerical examples are presented and discussed to assess the accuracy of the proposed theory in predicting the dynamic response of plates.

Table 3 – Comparison between natural bending mode frequencies $(\overline{\omega}_w)$ and thickness shear mode frequencies $(\overline{\omega}_\theta)$ for simply supported isotropic square plates $(S = 10)$.

a/b	w	Theory	Kw	Ks	$\bar{C}_t$	(m.n)						
						1.1	1.2	1.3	2.2	2.3	2.4	4.4
		CPT (1850)				0.0955	0.236	0.4629	0.3732	0.5951	0.8926	1.3716
		Mindlin (1951)				0.0930	0.2219	0.4149	0.3406	0.5206	0.7446	1.0764
		Reddy (1984)				0.0931	0.2219	0.4150	0.3406	0.5208	0.7453	1.0785
		Ghugal & Sayyad (2011)	0	0	0	0.0933	0.2231	0.4184	0.3431	0.5258	0.7542	1.0945
		Sayyad & Ghugal (2012)				0.0931	0.2223	0.4163	0.3415	0.5228	0.7499	1.0872
	w_w	Exact (1970)				0.0932	0.2226	0.4171	0.3421	0.5239	0.7511	1.0889
		Djidar et al. (2022)				0.0930	0.2220	0.4153	0.3408	0.5213	0.7464	1.0807
			0	0	0	**0.0930**	**0.2220**	**0.4153**	**0.3408**	**0.5213**	**0.7464**	**1.0807**
		Present	10	2	0.01	**0.0997**	**0.2279**	**0.4211**	**0.3466**	**0.5271**	**0.7525**	**1.0873**
					0.05	**0.1020**	**0.2289**	**0.4217**	**0.3472**	**0.5276**	**0.7528**	**1.0875**
					0.1	**0.1048**	**0.2301**	**0.4223**	**0.3480**	**0.5281**	**0.7531**	**1.0877**
		CPT (1850)				--	--	--	--	--	--	--
		Mindlin (1951)				3.2538	3.4112	3.6510	3.558	3.7842	4.072	4.5098
		Reddy (1984)				3.2555	3.4125	3.6517	3.5589	3.7848	4.072	4.5092
		Ghugal & Sayyad (2011)	0	0	0	3.2469	3.394	3.6178	3.5312	3.7414	4.0082	4.4102
		Sayyad & Ghugal (2012)				3.2428	3.3994	3.6381	3.5455	3.7709	4.0576	4.4944
	$w\theta$	Exact (1970)				3.2465	3.3933	3.6160	3.5298	3.7393	4.0037	4.4013
		Djidar et al. (2022)				3.2555	3.4123	3.6513	3.5586	3.7842	4.0712	4.5082
			0	0	0	**3.2555**	**3.4123**	**3.6513**	**3.5586**	**3.7842**	**4.0712**	**4.5082**
		Present	10	2	0.01	**3.2555**	**3.4123**	**3.6513**	**3.5586**	**3.7842**	**4.0712**	**4.5082**
					0.05	**3.2555**	**3.4123**	**3.6513**	**3.5586**	**3.7842**	**4.0712**	**4.5082**
1					0.1	**3.2555**	**3.4123**	**3.6513**	**3.5586**	**3.7842**	**4.0712**	**4.5082**

Table 3 presents a comparison between the natural bending mode (NBM) frequencies and thickness shear mode (TSM) frequencies for simply supported isotropic square plates resting on a viscoelastic foundation. It is observed that the inclusion of viscosity leads to larger frequency values, indicating that the viscoelastic effect contributes to the stiffening of the plate.

Table 4 – Comparison between the natural bending mode frequencies $(\bar{\omega}_w)$ *and others found in others works, of simply supported isotropic rectangular plates*$(S = 10)$

a/b	w	Theory	Kw	Ks	$\bar{C}_t$	(m.n)						
						1.1	1.2	1.3	2.2	2.3	2.4	3.2
√2	ww	CPT (1850)	0	0	0	0.0718	0.1427	0.2591	0.2821	0.3958	0.5513	0.5073
		Mindlin (1951)				0.0703	0.1373	0.2424	0.2625	0.3595	0.4861	0.4509
		Reddy (1984)				0.0704	0.1374	0.2426	0.2628	0.3601	0.4874	0.4520
		Ghugal & Sayyad (2011)				0.0705	0.1393	0.2438	0.2642	0.3623	0.4906	0.4550
		Sayyad & Ghugal (2012)				0.0704	0.1376	0.2433	0.2639	0.3639	0.4928	0.4552
		Exact (1970)				0.0704	0.1376	0.2431	0.2634	0.3612	0.4890	0.4535
		Djidar et al. (2022)				0.0703	0.1373	0.2425	0.2627	0.3598	0.4867	0.4514
		Present	0	0	0	**0.0703**	**0.1373**	**0.2425**	**0.2627**	**0.3598**	**0.4867**	**0.4514**
			10	2	0.01	**0.0767**	**0.1419**	**0.2462**	**0.2676**	**0.3641**	**0.4907**	**0.4567**
					0.05	**0.0797**	**0.1435**	**0.2471**	**0.2684**	**0.3648**	**0.4912**	**0.4572**
					0.1	**0.0833**	**0.1455**	**0.2483**	**0.2695**	**0.3655**	**0.4917**	**0.4578**

Table 5 - Non-dimensional fundamental frequencies $\bar{\omega}$ *for isotropic square plates resting on the Visco-Winkler-Pasternak foundations (a/h = 5, i = j = 1).*

K_w	K_s	Matsunaga (2000)	Thai and Choi (2012)	Mantari (2014)	Present			
					$\bar{C}_t$=0	$\bar{C}_t$=0.5	$\bar{C}_t$=1	$\bar{C}_t$=1.5
0	**0**	**17.526**	**17.4523**	**17.5271**	**17.45234**	**-**	**-**	**-**
10		**17.7847**	**17.7248**	**17.7858**	**17.72445**	**17.72945**	**17.73445**	**17.73945**
10^2		**19.9528**	**20.0076**	**19.9613**	**20.00731**	**20.01174**	**20.01616**	**20.02059**
10^3		**34.3395**	**35.5039**	**34.7796**	**35.50397**	**35.50646**	**35.50895**	**35.51144**
0	**10**	**22.0429**	**22.2145**	**22.0707**	**22.21443**	**22.21842**	**22.22240**	**22.22639**
10		**22.2453**	**22.4286**	**22.2757**	**22.42873**	**22.43268**	**22.43663**	**22.44057**
10^2		**23.983**	**24.2723**	**24.0401**	**24.27221**	**24.27586**	**24.27950**	**24.28315**
10^3		**36.6276**	**38.065**	**37.2169**	**38.06470**	**38.06702**	**38.06934**	**38.07166**

Table 4 shows a comparison between the natural bending mode frequencies obtained with the model proposed in this study and those

reported in the literature for simply supported isotropic rectangular plates. The results obtained turn out to be in good agreement with those reported in other studies in which the viscosity term and elastic foundation parameters were neglected. Once again, increasing the damping coefficient leads to a stiffer plate response, with greater rigidity.

To further assess the accuracy of the proposed model, the first two non-dimensional natural frequencies of a thick square plate (a/h=5) resting on an elastic foundation are reported. In this context, the following parameters are considered:

$$\widetilde{\omega} = \omega a^2\sqrt{\rho_0 h/D_0}\,, D_0 = \frac{Eh^3}{12(1-\nu^2)}\,, K_w = \frac{k_w a^4}{D_0}\,, K_s = \frac{k_s a^2}{D_0}$$

$$f(z) = h\sinh\left(\frac{z}{h}\right) - \frac{4z^3}{3h^2}\cosh\left(\frac{1}{2}\right)$$

Tables 5 and 6 illustrate the validation of the proposed theory through a comparison with other higher-order shear deformation theories reported in the literature, specifically those by Thai and Choi (2012), Matsunaga (2000), and Mantari et al. (2014). The fundamental frequencies corresponding to the first mode (i=j=1), denoted by ω_{11}, are presented in Table 5, whereas the natural frequencies ω_{12} are listed in Table 6.

Table 6 - Non-dimensional fundamental frequencies $\widetilde{\omega}$ for isotropic square plates resting on the Visco-Winkler-Pasternak foundations (a/h = 5, i = j = 2).

K_w	K_s	Matsunaga (2000)	Thai and Choi (2012)	Mantari (2014)	Present			
					$\bar{C}_t$=0	$\bar{C}_t$=1	$\bar{C}_t$=2	$\bar{C}_t$=3
0		**38.4827**	**38.1883**	**38.4991**	**38.18838**	**—**	**—**	**—**
10	**0**	**38.5929**	**38.3098**	**38.6093**	**38.31023**	**38.31474**	**38.31924**	**38.32375**
10^2		**39.5669**	**39.3895**	**39.586**	**39.38973**	**39.39412**	**39.39850**	**39.40288**
10^3		**47.8667**	**48.8772**	**48.1688**	**48.87732**	**48.88084**	**48.88436**	**48.88788**
0		**43.4816**	**43.7943**	**43.5741**	**43.79477**	**43.79870**	**43.80264**	**43.80657**
10	**10**	**43.5747**	**43.9009**	**43.6701**	**43.90089**	**43.90482**	**43.90874**	**43.91267**
10^2		**44.3994**	**44.8445**	**44.5241**	**44.84454**	**44.84839**	**44.85223**	**44.85607**
10^3		**51.6029**	**53.358**	**52.2029**	**53.35832**	**53.36154**	**53.36476**	**53.36798**

According to the results presented in Table 5, the fundamental frequencies obtained by the present model show very good agreement with the results of Thai and Choi (2014), particularly when the viscosity coefficient is zero. They are also slightly higher than those reported by Matsunaga (2000) and Mantari et al. (2014) for high values of the first coefficient of the parameter K_w. In addition, the fundamental frequencies

increase with the increase of the viscoelastic foundation parameters K_w, K_s and $\bar{C}_t$. On the other hand, Table 6 also indicates that the results from the present shear deformation theory closely match those of the higher-order theories by Thai and Choi (2014), Matsunaga (2000), and Mantari et al. (2014). According to this comparison, taking into account the viscoelastic foundation parameters stiffens the plate, thereby increasing its fundamental frequencies.

Conclusion

This study investigated the bending and free vibration behavior of simply supported isotropic plates resting on a viscoelastic Winkler–Pasternak foundation, using a refined two-variable higher-order shear deformation theory. The stress and displacement responses of the plates subjected to uniformly distributed loads (UDLs) and sinusoidally distributed loads (SDLs) were analyzed.

The proposed formulation was then validated against reported solutions. It showed excellent agreement with existing findings when the viscoelastic effects (*Kw*, *Ks*, *Ct*) are neglected.

It was found that when the above-mentioned effects are included, the displacements and stresses are significantly reduced. In this case, the influence of the Pasternak shear modulus (*Ks*) is more significant than that of the Winkler modulus (*Kw*). Moreover, the inclusion of viscosity leads to increased natural frequencies, highlighting the stiffening effect of the viscoelastic foundation.

The present study, which demonstrates clear novelty and practical relevance, is an extension of previous works, such as that carried out by Djidar et al. (2022), as it performs a comprehensive parametric analysis and provides essential insights for the analysis of plates resting on viscoelastic foundations.

References

Ait Atmane, H., Tounsi, A., Mechab, I., & Adda Bedia, E. A. (2010). Free vibration analysis of functionally graded plates resting on Winkler–Pasternak elastic foundations using a new shear deformation theory. *International Journal of Mechanics and Materials in Design*, 6, 113-121. Available at: https://doi.org/10.1007/s10999-010-9110-x

Ameur, M., Tounsi, A., Mechab, I., & El Bedia, A. A. (2011). A new trigonometric shear deformation theory for bending analysis of functionally graded plates resting on elastic foundations. *KSCE Journal of Civil Engineering*, *15*(8), 1405-1414.Available at: https://doi.org/10.1007/s12205-011-1361-z

Amini, M. H., Soleimani, M., &Rastgoo, A. (2009). Three-dimensional free vibration analysis of functionally graded material plates resting onan elastic foundation. *Smart Materials and Structures*, *18*(8), 085015.Available at: https://doi.org/10.1088/0964-1726/18/8/085015

Arani, A. G., &Kiani, F. (2018). Nonlinear free and forced vibration analysis of microbeams resting on the nonlinear orthotropic visco-Pasternak foundation with different boundary conditions. *Steel and Composite Structures*, *28*(2), 149-165. Available at: https://doi.org/10.12989/scs.2018.28.2.149.

Arshid, E., Khorshidvand, A. R., &Khorsandijou, S. M. (2019). The effect of porosity on free vibration of SPFG circular plates resting on visco-Pasternak elastic foundation based on CPT, FSDT and TSDT. *Structural Engineering and Mechanics, An Int'l Journal*, *70*(1), 97-112. Available at: https://doi.org/10.12989/sem.2019.70.1.097.

Baferani, A. H., Saidi, A. R., &Ehteshami, H. (2011). Accurate solution for free vibration analysis of functionally graded thick rectangular plates resting on elastic foundation. *Composite Structures*, *93*(7), 1842-1853. Available at: https://doi.org/10.1016/j.compstruct.2011.01.020

Benahmed, A., Houari, M. S. A., Benyoucef, S., Belakhdar, K., &Tounsi, A. (2017). A novel quasi-3D hyperbolic shear deformation theory for functionally graded thick rectangular plates on elastic foundation. *Geomech. Eng*, *12*(1), 9-34. Available at: https://doi.org/10.12989/gae.2017.12.1.009

Bennedjadi, M., Aldosari, S. M., Chikh, A., Kaci, A., Bousahla, A. A., Bourada, F., ... &Tounsi, A. (2023). Visco-elastic foundation effect on buckling response of exponentially graded sandwich plates under various boundary conditions. *Geomechanics and Engineering*, *32*(2), 159-177. Available at: https://doi.org/10.12989/gae.2023.32.2.159

Bouazza, M., Tounsi, A., Adda-Bedia, E. A., &Megueni, A. (2010). Thermoelastic stability analysis of functionally graded plates: An analytical approach. *Computational Materials Science*, *49*(4), 865-870. Available at: https://doi.org/10.1016/j.commatsci.2010.06.038

Boulefrakh, L., Hebali, H., Chikh, A., Bousahla, A. A., Tounsi, A., & Mahmoud, S. R. (2019). The effect of parameters of visco-Pasternak foundation on the bending and vibration properties of a thick FG plate. *Geomechanics and Engineering*, *18*(2), 161-178. Available at: https://doi.org/10.12989/gae.2019.18.2.161

Bounouara, F., Aldosari, S. M., Chikh, A., Kaci, A., Bousahla, A. A., Bourada, F., ... &Albalawi, H. (2023). The effect of visco-Pasternak foundation on the free vibration behavior of exponentially graded sandwich plates with various boundary conditions. *Steel and Composite Structures, An International Journal*, *46*(3), 367-383.Available at: https://doi.org/10.12989/scs.2023.46.3.367

Bounouara, F., Sadoun, M., Saleh, M. M. S., Chikh, A., Bousahla, A. A., Kaci, A., ... &Tounsi, A. (2023). Effect of visco-Pasternak foundation on thermo-mechanical bending response of anisotropic thick laminated composite plates. *Steel and Composite Structures*, *47*(6), 693-707. Available at: https://doi.org/10.12989/scs.2023.47.6.693

Chen, C. S. (2005). Nonlinear vibration of a shear deformable functionally graded plate. *Composite Structures*, *68*(3), 295-302. Available at: https://doi.org/10.1016/j.compstruct.2004.03.022

Chen, C. S., Hsu, C. Y., &Tzou, G. J. (2009). Vibration and stability of functionally graded plates based on a higher-order deformation theory. *Journal of reinforced plastics and composites*, *28*(10), 1215-1234. Available at: https://doi.org/10.1177/0731684408088884

Djidar, F. Z., Hebali, H., Amara, K., Touns, A., Bendaho, B., Ghazwani, M. H., & Hussain, M. (2022). Flexural and free vibration responses of thick isotropic bridge deck using a novel two variable refined plate theory. Available at: https://doi.org/10.12989/sem.2022.82.6.725

Fallah, A., Aghdam, M. M., &Kargarnovin, M. H. (2013). Free vibration analysis of moderately thick functionally graded plates on elastic foundation using the extended Kantorovich method. *Archive of Applied Mechanics*, *83*(2), 177-191. Available at: https://doi.org/10.1007/s00419-012-0645-1

Frahlia, H., Bennai, R., Nebab, M., AitAtmane, H., &Tounsi, A. (2023). Assessing effects of parameters of viscoelastic foundation on the dynamic response of functionally graded plates using a novel HSDT theory. *Mechanics of Advanced Materials and Structures*, *30*(13), 2765-2779. Available at: https://doi.org/10.1080/15376494.2022.2062632

Ghugal, Y. M., & Sayyad, A. S. (2011). Free vibration of thick orthotropic plates using trigonometric shear deformation theory. *Latin American Journal of Solids and Structures*, *8*, 229-243. Available at: https://doi.org/10.1590/S1679-78252011000300002

Ghugal, Y. M., &Pawar, M. D. (2011). Buckling and vibration of plates by hyperbolic shear deformation theory. *Journal of Aerospace Engineering and Technology*, *1*(1), 1-12. [online]. Available at: https://www.researchgate.net/profile/Yuwaraj-Ghugal/publication/285467416_Buckling_and_vibration_of_plates_by_hyperbolic_shear_deformation_theory/links/568113cb08ae051f9aec2333/Buckling-and-vibration-of-plates-by-hyperbolic-shear-deformation-theory.pdf [Accessed: 03 January 2025].

Grover, N., Maiti, D. K., & Singh, B. N. (2013). A new inverse hyperbolic shear deformation theory for static and buckling analysis of laminated composite and sandwich plates. *Composite Structures*, *95*, 667-675. Available at: https://doi.org/10.1016/j.compstruct.2012.08.012

Hebali, H., Tounsi, A., Houari, M. S. A., Bessaim, A., &Bedia, E. A. A. (2014). New quasi-3D hyperbolic shear deformation theory for the static and free vibration analysis of functionally graded plates. *Journal of Engineering Mechanics*, *140*(2), 374-383. Available at: https://doi.org/10.1061/(ASCE)EM.1943-7889.0000665

Huang, Z. Y., Lü, C. F., & Chen, W. Q. (2008). Benchmark solutions for functionally graded thick plates resting on Winkler–Pasternak elastic foundations. *Composite Structures*, *85*(2), 95-104. Available at: https://doi.org/10.1016/j.compstruct.2007.10.010

Karama, M., Afaq, K.S., Mistou, S. (2003), Mechanical behaviour of laminated composite beam by the new multilayered laminated composite structures model with transverse shear stress continuity. *Int. J. Solids Struct.*, 40(6), 1525–1546. Available at: https://doi.org/10.1016/S0020-7683(02)00647-9

Kiani, Y., &Eslami, M. R. (2012). Thermal buckling and post-buckling response of imperfect temperature-dependent sandwich FGM plates resting on elastic foundation. *Archive of Applied Mechanics*, *82*(7), 891-905. Available at: https://doi.org/10.1007/s00419-011-0599-8

Kirchhoff, G. (1850). Über das Gleichgewicht und die BewegungeinerelastischenScheibe. *Journal für die reine und angewandte Mathematik (Crelles Journal)*, *1850*(40), 51-88. Available at: https://doi.org/10.1515/crll.1850.40.51

Kirchhoff, G. (1850). Ueber die Schwingungen einer kreisförmigen elastischen Scheibe. *Annalen der PhysikundChemie*, *81*, 258-264. Available at: https://doi.org/10.1002/andp.18501571005

Lanhe, W. (2004). Thermal buckling of a simply supported moderately thick rectangular FGM plate. *Composite Structures*, *64*(2), 211-218. Available at: https://doi.org/10.1016/j.compstruct.2003.08.004

Lee, K. H., Senthilnathan, N. R., Lim, S. P., and Chow, S. T. (1989). A simple Higher Order Nonlinear Shear Deformation Plate Theory. *International Journal of Nonlinear Mechanics,* 24 (2), 127–137. Available at: https://doi.org/10.1016/0020-7462(89)90004-8

Levy, M. (1877). Mémoire sur la théorie des plaques élastiques planes. *Journal de mathématiques pures et appliquées*, 30, 219-306. [online]. Available at: https://www.numdam.org/item/JMPA_1877_3_3__219_0.pdf [Accessed: 01 May 2025].

Mahi, A., El Abbas,A.B., Tounsi, A. (2015). A new hyperbolic shear deformation theory for bending and free vibration analysis of isotropic, functionally graded, sandwich and laminated composite plates. *Applied Mathematical Modelling*, 39(9), 2489–2508. Available at: https://doi.org/10.1016/j.apm.2014.10.045

Mantari, J. L., Oktem, A. S., &Soares, C. G. (2012). A new trigonometric shear deformation theory for isotropic, laminated composite and sandwich plates. *International Journal of Solids and Structures*, *49*(1), 43-53. Available at: https://doi.org/10.1016/j.ijsolstr.2011.09.008

Mantari, J. L., &Soares, C. G. (2012). Bending analysis of thick exponentially graded plates using a new trigonometric higher order shear deformation theory. *Composite Structures*, *94*(6), 1991-2000. Available at: https://doi.org/10.1016/j.compstruct.2012.01.005

Mantari, J. L., Granados, E. V., &Soares, C. G. (2014). Vibrational analysis of advanced composite plates resting on elastic foundation. *Composites Part B: Engineering*, *66*, 407-419. Available at: https://doi.org/10.1016/j.compositesb.2014.05.026

Mantari, J. L., Granados, E. V., Hinostroza, M. A., & Soares, C. G. (2014). Modelling advanced composite plates resting on elastic foundation by using a

quasi-3D hybrid type HSDT. *Composite Structures*, 118, 455-471. Available at: http://dx.doi.org/10.1016/j.compstruct.2014.07.039

Matsunaga, H. (2000). Vibration and stability of thick plates on elastic foundations. *Journal of engineering mechanics,* 126(1), 27-34. Available at: https://doi.org/10.1061/(ASCE)0733-9399(2000)126:1(27)

Mindlin, R. (1951). Influence of rotatory inertia and shear on flexural motions of isotropic, elastic plates.*J. of Appl. Mechanics,* 18, 31-38 .Available at: https://doi.org/10.1115/1.4010217

Mudhaffar, I. M., Chikh, A., Tounsi, A., Al-Osta, M. A., Al-Zahrani, M. M., & Al-Dulaijan, S. U. (2023). Impact of viscoelastic foundation on bending behavior of FG plate subjected to hygro-thermo-mechanical loads. *Structural Engineering and Mechanics, An Int'l Journal*, *86*(2), 167-180. Available at: https://doi.org/10.12989/sem.2023.86.2.167

Pagano, N. J. (1970). Exact solutions for bidirectional composites and sandwich plates. *Journal of Composite Materials*, 4(1), 20–34. Available at: https://doi.org/10.1177/002199837000400102

Park, J. S., & Kim, J. H. (2006). Thermal postbuckling and vibration analyses of functionally graded plates. *Journal of Sound and Vibration*, *289*(1-2), 77-93. Available at: https://doi.org/10.1016/j.jsv.2005.01.031

Reddy, J. N. (1984). A simple higher-order theory for laminated composite plates.*ASME Journal of Applied Mechanics*, 51, 745–752. Available at: https://doi.org/10.1115/1.3167719

Saidi, H., Tounsi, A., &Bousahla, A. A. (2016). A simple hyperbolic shear deformation theory for vibration analysis of thick functionally graded rectangular plates resting on elastic foundations. *Geomechanics & engineering*, *11*(2), 289-307. Available at: https://doi.org/10.12989/gae.2016.11.2.289

Sayyad, A. S., &Ghugal, Y. M. (2012). Bending and free vibration analysis of thick isotropic plates by using exponential shear deformation theory. *Applied and Computational mechanics*, *6*(1). [online]. Available at: https://acm.kme.zcu.cz//article/view/171 [Accessed: 05 January 2025].

Shimpi, R. P. (2002). Refined plate theory and its variants. *AIAA journal*, *40*(1), 137-146.Available at: https://doi.org/10.2514/2.1622

Sobhy, M. (2013). Buckling and free vibration of exponentially graded sandwich plates resting on elastic foundations under various boundary conditions. *Composite Structures*, *99*, 76-87. Available at: https://doi.org/10.1016/j.compstruct.2012.11.018

Soldatos, K. (1992). A transverse shear deformation theory for homogeneous monoclinic plates. *Acta Mechanica*, *94*(3), 195-220. Available at: https://doi.org/10.1007/BF01176650

Stein, M. (1986). Nonlinear theory for plates and shells including the effects of transverse shearing. *AIAA journal*, *24*(9), 1537-1544. Available at: https://doi.org/10.2514/3.9477

Stein, M. (1989). Vibration of beams and plate strips with three-dimensional flexibility. *ASME Journal of Applied Mechanics,* Brief Notes,56(1), 228–231. Available at: https://doi.org/10.1115/1.3176054

Stein, M., Sydow, P. D., &Librescu, L. (1990). Postbuckling of long thick plates in compression including higher order transverse shearing effects. In *Studies in Applied Mechanics*, (24), 63-86. Elsevier. Available at: https://doi.org/10.1016/B978-0-444-88366-7.50008-7

Thai, H. T., & Choi, D. H. (2012). A refined shear deformation theory for free vibration of functionally graded plates on elastic foundation. *Composites Part B: Engineering*, 43(5), 2335-2347. Available at: https://doi.org/10.1016/j.compositesb.2011.11.062

Wattanasakulpong, N., Prusty, G. B., & Kelly, D. W. (2013). Free and forced vibration analysis using improved third-order shear deformation theory for functionally graded plates under high temperature loading. *Journal of Sandwich Structures & Materials*, *15*(5), 583-606. Available at: https://doi.org/10.1177/1099636213495751

Winkler, E. (1867). *Die Lehre von der Elasticitaet und Festigkeit*, Prag Dominicus. [e-book]. Available at: https://books.google.com/books?id=i2kSAAAAIAAJ [Accessed: 15 March 2025].

Xiang, S., Jin, Y. X., Bi, Z. Y., Jiang, S. X., & Yang, M. S. (2011). A n-order shear deformation theory for free vibration of functionally graded and composite sandwich plates. *Composite Structures*, *93*(11), 2826-2832.Available at: https://doi.org/10.1016/j.compstruct.2011.05.022

Xiang, S., & Kang, G. W. (2013). Static analysis of functionally graded plates by the various shear deformation theory. *Composite Structures*, *99*, 224-230. Available at: https://doi.org/10.1016/j.compstruct.2012.11.021

Yaghoobi, H., &Yaghoobi, P. (2013). Buckling analysis of sandwich plates with FGM face sheets resting on elastic foundation with various boundary conditions: an analytical approach. *Meccanica*, *48*(8), 2019-2035. Available at: https://doi.org/10.1007/s11012-013-9720-0

Younsi, A., Tounsi, A., Zaoui, F. Z., Bousahla, A. A., & Mahmoud, S. R. (2018). Novel quasi-3D and 2D shear deformation theories for bending and free vibration analysis of FGM plates. *Geomechanics & engineering*, *14*(6), 519-532. Available at: https://doi.org/10.12989/gae.2018.14.6.519.

Zeighampour, H., &Beni, Y. T. (2015). Free vibration analysis of axially functionally graded nanobeam with radius varies along the length based on strain gradient theory. *Applied Mathematical Modelling*, *39*(18), 5354-5369. Available at: https://doi.org/10.1016/j.apm.2015.01.015

Zenkour, A. M. (2016). Buckling of a single-layered graphene sheet embedded in visco-Pasternak. *Advances in nano research*, *4*(4), 309. Available at: https://doi.org/10.12989/anr.2016.4.4.309.

Uticaj parametara viskoelastične Pasternakove osnove na savijanje i vibraciono ponašanje debelih izotropnih ploča

Hebali Habib[a], *Djidar* Fatima Zohra[b], **autor za prepisku**, *Derras* Abdelhak[c]

[a] Mustapha Stambouli University, Departement of Civil Engineering, Mascara, People's Democratic Republic of Algeria

[b] Mustapha Stambouli University, Department of Civil Engineering, Mascara, People's Democratic Republic of Algeria +
Smart Structures Laboratory (SSL), University of Ain Temouchent, Ain Temouchent, People's Democratic Republic of Algeria

[c] Ahmed Ben Bella University – Oran 1, Department of Chemistry, Oran, People's Democratic Republic of Algeria +
Smart Structures Laboratory (SSL), University of Ain Temouchent, Ain Temouchent, People's Democratic Republic of Algeria

OBLAST: građevinarstvo
KATEGORIJA (TIP) ČLANKA: originalni naučni rad

Sažetak:

Uvod/cilj: Primarni cilj ove studije je ispitivanje uticaja parametara viskoelastične Pasternakove podloge na ponašanje debelih izotropnih ploča sa prostim oslanjanjem pri savijanju i slobodnim vibracijama primenom teorije smične deformacije višeg reda sa dve nepoznate veličine (eng. HSDT). Usvojena teorija koristi ograničen broj nepoznatih i izbegava upotrebu korekcionih faktora smicanja kako bi poprečni smični naponi na površinama ploče bili jednaki nuli, što nije slučaj kod drugih teorija višeg reda koje uglavnom obuhvataju četiri ili pet nepoznatih. Pored toga, analiziraju se naponski i pomerajni odzivi pri dejstvu ravnomerno raspodeljenih opterećenja (eng. UDL) i sinusoidalno raspodeljenih opterećenja (eng. SDL). Takođe, prikazane su sopstvene frekvencije koje odgovaraju kako modovima savijanja tako i modovima smicanja po debljini kako bi se pokazala tačnost predloženog modela u predviđanju dinamičkog ponašanja kvadratnih i pravougaonih izotropnih ploča sa prostim oslanjanjem.

Metode: Glavni doprinos ovog rada ogleda se u uključivanju uticaja parametara elastične podloge i koeficijenata prigušenja na odzive debelih izotropnih ploča sa prostim oslanjanjem pri savijanju i vibracijama primenom usavršene teorije smične deformacije višeg reda sa dve nepoznate veličine. Pored toga, formulacija polja pomeranja uvodi određeni broj neodređenih integralnih članova, čime se smanjuje broj nepoznatih. Osnovne jednačine izvode se primenom Hamiltonovog principa. Zatim se koristi Navijeov metod za određivanje analitičkih rešenja za ploče sa prostim oslanjanjem, dok se sopstvene frekvencije izračunavaju rešavanjem odgovarajućeg problema sopstvenih vrednosti.

Rezultati: Analitički rezultati validirani su poređenjem sa nekoliko poznatih teorija smične deformacije višeg reda (eng. ESDT, HSDT, TSDT), teorijom

smične deformacije prvog reda (eng. FSDT) i klasičnom teorijom ploča (eng. CPT). Rezultati pokazuju odlično slaganje kada se viskoelastični efekti i efekti podloge ne uzimaju u obzir. Važno je naglasiti da rezultati pokazuju povećanu krutost ploče kada se ovi efekti uzmu u obzi, što dovodi do manjih ugiba i viših sopstvenih frekvencija.

Zaključak: Predložena teorija daje rezultate koji se dobro podudaraju sa rezultatima dobijenim primenom postojećih modela. Takođe, teorija jasno ukazuje na značajan uticaj parametara viskoelastične podloge na statičko i dinamičko ponašanje izotropnih ploča.

Ključne reči: savijanje, vibracije, izotropna ploča, visko-Pasternakove podloge.

Paper received on: 20 June 2025.
Manuscript corrections submitted on: 21 November 2025.
Paper accepted for publishing on: 23 January 2026.

© 2026 The Authors. Published by Vojnotehnički glasnik / Military Technical Courier (www.vtg.mod.gov.rs). This article is an open access article distributed under the terms and conditions of the Creative Commons Attribution license (http://creativecommons.org/licenses/by/4.0/rs/).

AHP-based seismic vulnerability index for critical urban water and sanitation infrastructure

Fatma Zohra Halfaya[a], *Mahmoud* Bensaibi[b]

[a] University of Blida 1, Civil Department, People's Democratic Republic of Algeria,

e-mail: fz_halfaya@yahoo.fr, **corresponding author**,

ORCID iD: https://orcid.org/0009-0009-6030-3664

[b] Infrastructure Studies Control and Assistance Group, GEICA, People's Democratic Republic of Algeria,

e-mail:bensaibim@gmail.com,

ORCID iD: https://orcid.org/0000-0003-1409-4610

https://doi.org/10.5937/vojtehg74-61277

FIELD: civil engineering
ARTICLE TYPE: original scientific paper

Abstract:

Introduction/purpose: This research develops a systematic methodology for assessing the seismic vulnerability of buried water supply and wastewater pipeline networks. The objective is to integrate geological, geotechnical, and structural parameters within a unified decision-support framework, thus enabling infrastructure managers to identify and prioritize vulnerable segments in earthquake-prone regions.

Methods: The methodology combines the Vulnerability Index (VI) approach with the Analytic Hierarchy Process (AHP) to assign relative weights to factors such as pipe material, diameter, age, burial depth, soil type, liquefaction potential, seismic intensity, and fault crossings. Expert judgment and pairwise comparisons are used to determine these weights. Geographic Information System (GIS) tools and field surveys support the spatial analysis. The approach is applied to the city of Blida, Algeria, characterized by high seismic hazard and diverse soil conditions.

Results: The AHP-based VI approach produced detailed vulnerability maps for both water and sewer networks, classifying pipeline segments into low, medium, and high vulnerability levels. The method demonstrated higher precision and contextual relevance compared to empirical assessments, revealing material brittleness, diameter, and geotechnical conditions as key determinants.

Conclusion: The AHP–VI framework provides a robust, adaptable, and transparent tool for seismic risk assessment of lifeline infrastructure. Its applicability extends to both civilian and military contexts, supporting

strategic planning, targeted mitigation, and resilience enhancement of critical buried pipelines in seismically active regions.

Key words: Analytic Hierarchy Process (AHP), vulnerability index, water supply network, wastewater network, seismic risk, GIS.

Introduction

Assessing the seismic vulnerability of buried pipelines in water supply and wastewater systems is a key concern in the broader context of disaster risk reduction and infrastructure resilience. Earthquakes can cause significant damage to these essential systems, jeopardizing the delivery of potable water and the functioning of sanitation services in affected areas. Accordingly, establishing a systematic and robust methodology for vulnerability assessment is crucial for strengthening the seismic resilience of these networks (Farahmandfar et al, 2016; Bata et al, 2022; Hou et al, 2023; Boskabadi et al, 2020).

This study presents a methodological framework based on the Vulnerability Index (VI) for evaluating the seismic susceptibility of buried pipelines (Adafer & Bensaibi, 2017). To improve the precision of this assessment, the Analytic Hierarchy Process (AHP) is integrated to assign relative weights to the different parameters that influence pipeline behavior under seismic loading conditions (Saaty, 1987; Bernasconi et al, 2010; Omkarprasad & Sushil, 2006; Bhushan & Rai, 2004; Roy et al, 2023; Sharveen et al, 2022). By combining the structured decision-making capabilities of AHP with the implementation of the VI, this approach offers an effective tool for assessing and ranking pipeline vulnerability.

Previous research has increasingly emphasized the importance of assessing the seismic vulnerability of lifeline infrastructure, particularly in seismically active regions. Numerous studies highlight the necessity of incorporating the specific characteristics of water distribution systems into such evaluations (Halfaya, 2013; Halfaya et al, 2017; Germoso et al, 2021; Ballantyne, 2010; Tucker, 2010; O'Rourke & Deyoe, 2004; O'Rourke, 2009; Maruyama et al 2011; Christodoulou & Fragiadakis, 2015; Braun et al, 2020; Roy et al, 2021; Roy et al, 2022). Additionally, several investigations have examined the seismic performance of wastewater pipeline networks (Matsuhashi et al, 2014; Baris et al, 2021; Giovinazzi et al, 2015; Kerpelis et al, 2021; Rahimi & Rezaii, 2021).

Globally, numerous comprehensive studies have addressed the seismic resilience of urban infrastructure, with particular emphasis on water and wastewater systems (ATC25, 1991; ATC25-1, 1991; FEMA,

1997; FEMA, 2000; OYO Corporation, 1999; RISK-UE, 2003). The present research builds on the recommendations from these studies and adapts the methodology to real-world contexts, particularly potable water pipelines in seismically active areas (Ansal, 2008) with the aim of improving preparedness and enhancing the reliability of water and sanitation services during seismic events. Furthermore, the validation of the methodology for wastewater networks broadens its applicability to other underground utilities, enhancing its relevance for diverse urban environments.

This research proposes a novel and practical framework for seismic vulnerability assessment of buried pipelines, combining the analytical strength of AHP with the operational value of the Vulnerability Index. The application of the methodology to the water and wastewater infrastructure of Blida, Algeria, provides actionable insights to support the resilience of vital public services in earthquake-sensitive regions.

Vulnerability Index (VI) methodology

The Vulnerability Index (VI) method offers a structured and quantitative approach for evaluating seismic risk in buried water and wastewater pipeline systems. The methodology is composed of four key stages:

Identification of relevant factors

The initial step involves identifying the critical factors that influence pipeline performance under seismic loading. These typically include structural and geotechnical attributes such as pipe material, diameter, burial depth, soil type, liquefaction potential, and the age of the infrastructure. Each factor contributes uniquely to the pipeline's response to seismic activity, necessitating careful and context-specific consideration.

Assignment of weighting factors

In the second stage, the Analytic Hierarchy Process (AHP) — a well-established multi-criteria decision-making (MCDM) method, is employed to assign weights to the identified factors. AHP facilitates a structured comparison of the relative importance of each parameter through expert judgment and pairwise comparisons. This ensures that the final weighting reflects the actual influence of each factor on seismic vulnerability, while accounting for potential interdependencies among variables.

Formulation of the vulnerability index

The third step involves integrating the weighted factors into a single analytical expression to compute the Vulnerability Index. This index serves as a quantitative indicator of the relative seismic risk of different pipeline segments. The shift from qualitative assessments to a numerical index enables objective comparisons between network components and supports data-driven decision-making.

Classification of pipeline segments

The final stage consists of classifying pipeline segments according to their calculated Vulnerability Index values. They are typically grouped into discrete vulnerability levels such as low, moderate, high, and very high, providing infrastructure managers with a transparent and actionable framework for prioritizing interventions. This classification facilitates effective resource allocation, risk mitigation planning, and long-term infrastructure resilience strategies.

Overview of the analytic hierarchy process (AHP)

The Analytic Hierarchy Process (AHP), developed by Thomas L. Saaty in the 1970s, is a widely adopted multi-criteria decision-making methodology. It is particularly effective in addressing complex decision problems that involve multiple, and sometimes conflicting, criteria. AHP decomposes such problems into a hierarchical structure, enabling systematic analysis and prioritization based on expert judgments.

Hierarchical structure

The AHP manages the decision-making problem as a multi-level hierarchy with three key components:

- Goal/Objective: This represents the overall target of the analysis in this case, assessing the seismic vulnerability of buried pipelines.
- Criteria: These are the factors that influence the achievement of the goal. Relevant criteria include pipe material, diameter, burial depth, age, soil type, and liquefaction potential.
- Alternatives: These refer to the different pipeline segments or configurations under evaluation.

This hierarchical organization provides a transparent structure for breaking down and analyzing complex problems in a logical and systematic manner.

Pairwise comparisons

A fundamental component of AHP is the use of pairwise comparisons to assess the relative importance of criteria and alternatives. Decision-makers evaluate each pair of elements at a given level of the hierarchy using expert judgment. This technique captures both qualitative preferences and quantitative significance, offering a nuanced view of relative priority.

Saaty's fundamental scale

To support pairwise comparisons, AHP employs Saaty's fundamental scale, which ranges from 1 to 9. A value of 1 denotes equal importance between two elements, while a value of 9 indicates an extreme preference for one element over the other. Intermediate values (2, 4, 6, 8) allow for graded distinctions between judgments. Reciprocals are automatically applied for inverse comparisons.

Table 1 – Saaty's fundamental scale for pairwise comparison

Intensity of importance on an absolute scale	Definition	Explanation
1	Equal importance	Two elements contribute equally to the objective
3	Moderate importance	Experience or judgment slightly favors one element
5	Strong importance	Clear and consistent preference for one element
7	Very strong importance	One element is strongly favored, with demonstrated dominance
9	Extreme importance	Evidence overwhelmingly favors one element
2,4,6,8	Intermediate values	Used when compromise or uncertainty exists between two adjacent levels
Reciprocals	Inverse values (1/x)	Applied to the opposite comparison

*Consistency c*heck

To ensure logical coherence in the judgment matrix, AHP incorporates a consistency check by computing the Consistency Ratio (CR). A CR value below 0.10 is generally considered acceptable. If the ratio exceeds this threshold, the decision-maker should revise the judgments to improve consistency and reliability.

Computing of relative ponderations

The ponderations of criteria and alternatives are derived mathematically, typically using eigenvector calculations based on the pairwise comparison matrices. These weights reflect the relative importance of each element in contributing to the overall objective and form the basis for aggregating judgments across the hierarchy.

Synthesis and decision-making

In the final step, the results from all hierarchical levels are aggregated to obtain a ranked list of alternatives. The synthesis of calculated weights enables a comprehensive evaluation of options, facilitating well-informed and justifiable decision-making based on a structured analytical foundation.

Seismic vulnerability of the water supply network

The developed methodology is applied to assess the seismic vulnerability of the water supply network through a hierarchical structure based on the Analytic Hierarchy Process (AHP). This structure consists of three levels, each designed to capture different aspects of vulnerability.

Hierarchical structure of parameters

The AHP-based evaluation of seismic vulnerability in the service drinking water network is structured across three hierarchical levels.

Level 1 – Parameters: Three key parameters are selected for the vulnerability assessment: structural, ground-related, and seismic hazard parameters;

Level 2 – Factors: Each parameter is subdivided into specific factors that characterize different physical or environmental conditions influencing pipeline vulnerability;

Level 3 – Categories: Each factor is further broken down into distinct categories. Expert judgment is used to assign scores to each category based on its relative importance or contribution to seismic vulnerability.

This multi-level structure (Figure 1) allows for a detailed and granular assessment of pipeline components and their susceptibility to seismic hazards.

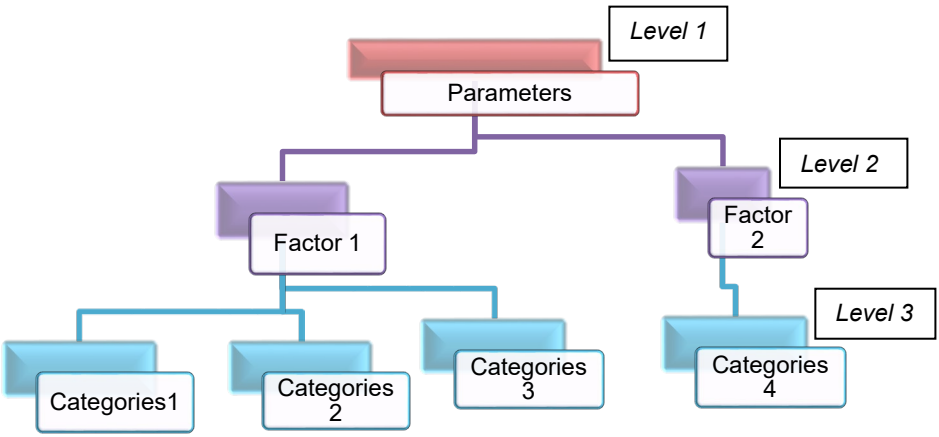


Figure 1 – The used multi-level structure

Weight determination using AHP

The AHP method is applied to assign weights to each parameter and factor, based on pairwise comparisons using Saaty's scale. These weights indicate the relative importance of each element within the decision-making process in contributing to the overall vulnerability. While the categories themselves are not directly included in the pairwise comparison matrices, they are scored using expert judgement to quantify their impact within each factor.

Summary of weights and scores

Table 2 presents the full hierarchical structure, including parameters, factors, categories, and their respective weights and scores. These values form the foundation for the Vulnerability Index calculation for water pipelines.

Table 2 – Hierarchical structure and weights for water pipeline vulnerability assessment

Parameters	Weight	Factor	Weight	Category	Score
Structural	0.571	Materials	0.75	Asbestos Cement	60
				Cast Iron	50
				Ductile Iron	40
				Steel	30
				Galvanized Steel	20
				Polyvinyl chloride (PVC)	10
				Polyethylene HDPE	0
		Diameters	0.25	φ < 75 mm	50
				75 mm <φ<150 mm	40
				150 mm <φ<250 mm	30
				250 mm <φ<450 mm	20
				450 mm < φ <1000 mm	10
				φ > 1000 mm	0
Ground	0.143	Soil Type	0.75	Alluvium: very soft soil S1	40
				Dilluvium: soft soil S2	30
				Medium Soil S3	20
				Medium Rocky Soil S4	10
				Hard Rock Soil S5	0
		Slide	0.25	No slippage	0
				Medium Slippage	10
				Significant Slippage	30
Seismic Hazard	0.286	Intensity	0.539	MMI<8	10
				8≤MMI<9	20
				9≤MMI<10	30
				10≤MMI<11	40
				11≤MMI	50
		Liquefaction	0.163	0≤LP*<5	0
				5≤LP<15	10
				15≤LP	30
		Fault Cross	0.294	No intersection	0
				One intersection	10
				Multiple intersections	30

**LP stands for liquefaction potential (according to the Iwasaki method)*

Analytical expression of the vulnerability index

The overall Vulnerability Index (VI) for each pipeline segment is calculated using the following expression:

$$VI = \sum_{i=1}^{3} W_i \left(\sum_{j=1}^{2\ or\ 3} W_{ij} \left(\sum_{k=1}^{3\ or\ 5\ or\ 6\ or\ 7} C_{ijk} W_{ij} \right) \right) \quad (1)$$

Where:

Wi is the weight of the ith parameter,

Wij is the weight of the jth factor under parameter i,

Cijk is the score assigned to the kth category under factor j.

Classification of vulnerability levels

Based on expert feedback and seismic risk considerations, the following classification system is proposed for interpreting the computed VI values.

Table 3 – Seismic vulnerability classification for water pipelines

VI	Vulnerability Level	Interpretation	Color Code
0 < VI< 25	Low	Low risk of damage	Green
25 ≤ VI < 35	Medium	Moderate risk; replacement recommended	Orange
35 ≤ VI < 50	High	High risk; urgent replacement required	Red

Interpretation:

Green - Low-risk segments; no immediate action is necessary;

Orange - Moderate-risk segments; replacement is advised in the medium term;

Red - High-risk segments; urgent replacement or reinforcement is recommended.

Seismic vulnerability of the sewer network

The methodology originally designed to evaluate the seismic vulnerability of the drinking water distribution network has been extended to the sewer (wastewater) system. Given the structural and operational differences between these two systems, specific factors relevant to

sewer pipelines have been incorporated within the same AHP-based framework.

Identification of relevant factors and AHP structure

Similar to the water supply analysis, the AHP methodology is structured into three levels for the wastewater network:

Level 1 – Parameters: The three primary parameters are structural, geotechnical (ground-related), and seismic hazard conditions;

Level 2 – Factors: Each parameter comprises specific factors tailored to sewer infrastructure, such as wastewater chemical composition and slope;

Level 3 – Categories: For each factor, categories are defined and scored using expert judgment to reflect their contribution to seismic vulnerability.

Identified Factors:

A. Structural Parameter:
   1. Pipe material,
   2. Pipe diameter,
   3. Chemical nature of the wastewater.

B. Ground Parameter:
   1. Soil type,
   2. Landslide risk,
   3. Slope.

C. Seismic Hazard Parameter:
   1. Seismic intensity,
   2. Fault crossings,
   3. Liquefaction potential.

These factors are evaluated within the AHP framework to quantify their relative influence on seismic vulnerability.

Weight assignment using AHP

The AHP method is employed to determine the weights of each parameter and factor. Expert-based pairwise comparisons are conducted to ensure the prioritization reflects real-world significance and local context. Table 4 summarizes the derived weights for the parameters, factors, and categories.

Table 4 – AHP weights for seismic vulnerability assessment of sewer pipelines

Parameters	Weight	Factor	Weight	Category	Score
Structural	0.685	Materials	0.633	Asbestos	50
				Sand stone	40
				Cast Iron	30
				Reinforced concrete	20
				Polyvinyl chloride (PVC)	10
				Polyethylene HDPE	0
				PRV	0
		Diameters	0.261	D < 300 mm	20
				300 ≤ D ≤ 600 mm	10
				D > 600 mm	0
		Chemical nature of the water	0.106	PH<7 (acid)	20
				PH>7 (basic)	10
Ground	0.093	Soil type	0.707	Alluvium: very soft soil S1	40
				Dilluvium: soft soil S2	30
				Medium Soil S3	20
				Medium Rocky Soil S4	10
				Hard Rock Soil S5	0
		Slide	0.201	No slippage	0
				Moderate Slippage	10
				Significant Slippage	30
		Slope	0.092	1%< p ≤ 3%	20
				3% < p ≤ 5%	10
				p >5%	0
Seismic Hazard	0.221	Intensity	0.724	MMI<8	10
				8≤MMI<9	20
				9≤MMI<10	30
				10≤MMI<11	40
				11≤MMI	50
		Cross with fault	0.083	No intersection	0
				One intersection	10
				Multiple intersections	30
		Liquefaction	0.193	0≤LP*<5	0
				5≤LP<15	10
				15≤LP	30

**LP stands for liquefaction potential (according to the Iwasaki method)*

Analytical expression of the Vulnerability Index (VI)

The Vulnerability Index for sewer pipelines is calculated using the same formula as for water pipelines:

$$VI = \sum_{i=1}^{3} W_i \left(\sum_{j=1}^{3} W_{ij} \left(\sum_{k=1}^{2\ or\ 3\ or\ 5\ or\ 7} C_{ijk} W_{ij} \right) \right) \quad (2)$$

Where:

W_i is the weight of the parameter,
W_{ij} is the weight of the corresponding factor,
C_{ijk} is the score of the category.

Vulnerability classification for sewer pipelines

A classification system is established to interpret the calculated VI values for sewer pipelines. This system enables decision-makers to identify priority areas for intervention

Table 5 – Seismic vulnerability classification for sewer pipelines

VI	Vulnerability Level	Interpretation	Color Code
0 < VI< 15	Low	Minor risk; no immediate action required	Green
15 ≤ VI < 25	Medium	Moderate risk; monitoring recommended	Orange
25 ≤ VI < 40	High	High risk; reinforcement or replacement needed	Red

This classification mirrors that used for water pipelines and supports consistent risk communication and management strategies across both network types.

Case studies and results

To demonstrate the applicability of the proposed methodology, two case studies on the water supply and wastewater networks of Blida, Algeria were conducted. These case studies illustrate how the AHP-based Vulnerability Index (VI) approach can be used to assess seismic risk and guide infrastructure management decisions.

Case study: water supply network of Blida

The water distribution system of Blida extends over approximately 94 km and includes pipelines made of various materials such as cast iron, asbestos cement, steel, PVC, and HDPE. The pipe diameters range from 50 mm to 800 mm.

This network is situated in a seismically active area, directly influenced by the Soumaa–Bouinan fault, a 30 km-long fault capable of generating earthquakes with a maximum magnitude of 6.8 ± 0.28 (according to CRAAG studies). This corresponds to an intensity of IX < MMI < X on the Modified Mercalli Intensity (MMI) scale (CRAAG, 2005). Liquefaction potential across the study area was assessed based on criteria from reference (Bahi & Bensaibi, 2012).

A previous study of the same network was conducted using an empirical approach (Halfaya, 2013). The results of that empirical evaluation were compared to those obtained using the AHP-based analytical method described in this paper.

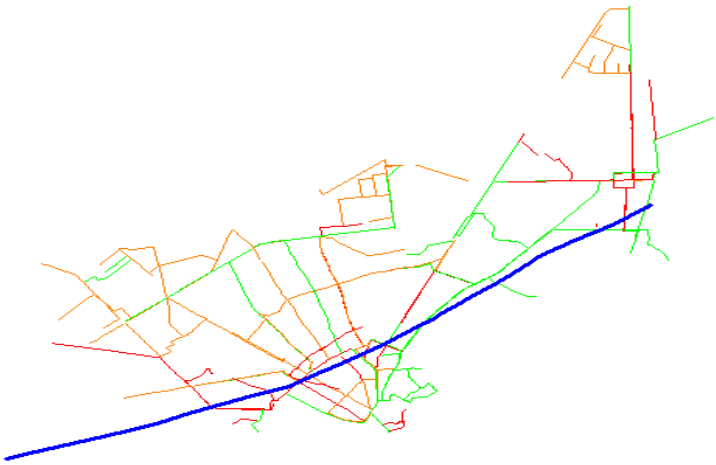


Figure 2 – GIS-based seismic vulnerability map of the water network

The comparison reveals discrepancies between the two approaches, with the AHP-based method providing more nuanced, data-driven classification based on localized geological and infrastructural factors.

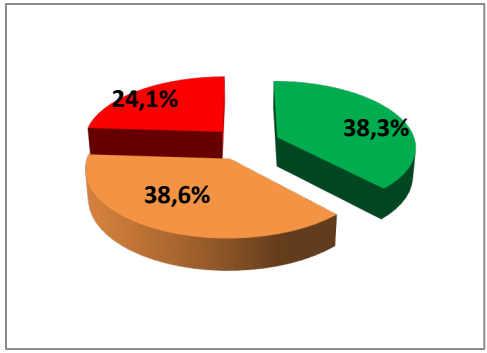


Figure 3 – Distribution of pipeline vulnerability classes (empirical method)

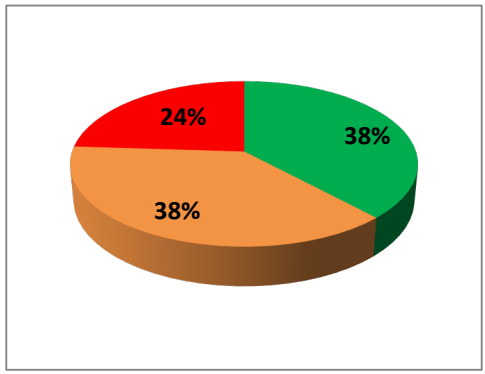


Figure 4 – Distribution of pipeline vulnerability classes (analytical method)

Case studies: sewer network of Blida

Two sets of case studies were carried out to evaluate seismic risk within the wastewater pipeline network using the developed methodology.

Reinforced concrete pipes

This analysis focused on two reinforced concrete (RC) sewer pipes of different diameters: 300 mm and 1000 mm. The conditions for each pipe segment were evaluated based on the factors and categories defined in the AHP hierarchy.

Table 6 – Seismic vulnerability results for reinforced concrete sewer pipes

Materials	RC	
Diameters Φ (mm)	300	1000

Chemical nature of the wastewater	Basic	
Type de sol	S1	
Liquefaction	0≤ PL≤5	
Side	No slippage	
Slope	3% < p ≤ 5%	
Intensity	MMI ≤ 8	
Cross with Fault	1 intersection	
Vulnerability Index (VI)	15.6	13.82
Classification		

These results suggest that both pipes fall within the low to moderate vulnerability range, with diameter playing a significant role in risk differentiation.

Newly installed pipelines (2022)

This study assessed several sewer pipelines recently installed across multiple localities in Blida. The following assumptions were applied:

Chemical Nature of Wastewater: Basic
Ground Type: Soil S1
No Landslide Risk
Seismic Intensity: IX < MMI < X (USGS)
No Liquefaction Risk

Table 7 - Seismic vulnerability assessment of sewer pipelines in Blida (2022 installations)

Localities	Materials	Diameters	Slope (for 1000)	Number of intersections with fault	VI	Classification
Bougara	RC	1000	4	1	17.2	
Larbaa	PVC	300	5	0	14.5	
Bougara	PVC	500	6	1	14.6	
O.Yaich	PEHD	400	6	1	10.3	
Chréa	PEHD	300	6	0	10.1	
Larbaa	PEHD	300	6	0	10.1	
Bouarfa	PEHD	500	6	0	10.1	
O.E.Alleug	RC	1200	5	0	17	
Bouarfa	RC	800	6	0	17	

Analysis

The results confirm that reinforced concrete (RC) pipes consistently present higher vulnerability indices compared to PVC and HDPE alternatives. This aligns with established knowledge regarding material brittleness and seismic performance. Nevertheless, RC pipes continue to be used in certain locations—likely due to cost, local availability, or legacy infrastructure constraints.

Conclusion

This study proposes a systematic methodology for evaluating seismic risk in underground water supply and wastewater networks, by integrating the Analytic Hierarchy Process (AHP) with a structured Vulnerability Index (VI) framework. The method incorporates a wide range of parameters—spanning geological, geotechnical, and structural characteristics—including soil type, liquefaction potential, pipeline material, diameter, burial depth, and age. These parameters are assigned relative weights based on expert evaluations through the AHP method.

The methodology was applied to the city of Blida, Algeria—an urban area characterized by high seismic activity and diverse subsurface conditions. By leveraging GIS tools and field data, a seismic vulnerability map was generated to identify critical segments of the water and sewer networks. The findings facilitate strategic planning, allowing decision-makers to prioritize maintenance, reinforcement, or replacement of vulnerable pipelines.

The results demonstrate the practical value of the AHP-based approach in bridging the gap between engineering data and operational decision-making. The methodology offers several advantages: adaptability to various urban contexts, transparency in weighting and scoring, and the ability to incorporate both expert knowledge and field-based observations. It is particularly well-suited for use in developing countries, where infrastructure vulnerabilities are significant and technical data may be scarce.

Beyond civilian infrastructure, the proposed methodology holds significant potential for military applications. Military bases, forward operating posts, and command facilities frequently depend on buried pipeline systems to maintain essential services such as potable water, sanitation, and cooling systems. In seismically active regions or post-conflict reconstruction zones, ensuring the continuity and resilience of such lifeline infrastructure is a strategic priority. The AHP-based

framework can assist military engineers and planners in identifying critical vulnerabilities, supporting logistics continuity, and enhancing the resilience of mission-critical installations.

Future work

Further enhancements could include integrating probabilistic seismic hazard models, incorporating real-time monitoring data (e.g., ground motion sensors), and refining the AHP weighting process using machine learning algorithms. Additionally, the inclusion of socioeconomic and strategic impact indicators—such as population exposure, service disruption costs, and recovery priorities—would broaden the scope and utility of the methodology, ultimately contributing to more resilient and sustainable infrastructure systems in both civilian and military contexts.

References

Adafer, S., Bensaibi, M. 2017. Seismic vulnerability classification of roads. Energy Procedia, Vol.139, pp. 624-630.

Ansal, A., Kurtuluş, A., & Tönük, G. 2008. Damage to Water and Sewage Pipelines in Adapazari During 1999 Kocaeli, Turkey Earthquake . *International Conference on Case Histories in Geotechnical Engineering*. 5.

ATC 25. 1991. Seismic Vulnerability and Impact of Distribution of Lifelines in the Conterminous United States.

ATC 25-1.1991. Seismic Vulnerability and Impact of Disruption of Lifelines in the Conterminous United States ATC-25, Redwood City, CA 25-1.

Bahi, F.Z., Bensaibi, M. 2012. Liquefaction index method : Algerian cases studies ». *Proceedings of the 5th Asian-Pacific Symposium on Structural Reliability and its Applications, Sustainable Civil Infrastructures, Singapore, Singapore.*

Ballantyne, D.2010. Seismic vulnerability assessment and design of pipelines. *Journal American Water Works Association*, Volume102, Issue5. https://doi.org/10.1002/j.1551-8833.2010.tb10111.x

Baris, A., Spacagna, R.L., Paolella, L., et al. 2021. Liquefaction fragility of sewer pipes derived from the case study of Urayasu (Japan) . *Bull Earthquake Eng* 19, 3963–3986. https://doi.org/10.1007/s10518-020-00957-2

Bata, M.H., Carriveau, R., & Ting, D.SK. 2022. Urban water supply systems' resilience under earthquake scenario. *Scientific Reports* 12, 20555. https://doi.org/10.1038/s41598-022-23126-8

Bernasconi, M., Choirat, C., & Seri, R.2010. The Analytic Hierarchy Process and the Theory of Measurement . *Management Science* Vol. 56, No. 4, pp. 699–711. https://doi.org/10.1287/mnsc.1090.1123

Bhushan, N., Rai, K.2004. Strategic Decision Making: Applying the Analytic Hierarchy Process. *Springer, Berlin*, 9, 11-21. https://doi.org/10.1007/b97668

Boskabadi, A., Rosenberger J. M., & Shahandashti, M. 2020. A two-stage stochastic programming approach for enhancing seismic resilience of water pipe networks. *In Proc., of the 2020 IISE Annual Conf*., 495–500. Peachtree Corners, GA: Institute of Industrial and Systems Engineers.

Braun, M., Piller O., Deuerlein J., Mortazavi I., & Iollo A. 2020. Uncertainty quantification of water age in water supply systems by use of spectral propagation. *J.Hydroinf.* 22 (1): 111–120. https://doi.org/10.2166/hydro.2019.017

CRAAG. 2005. Étude géologique, géophysique et géotechnique des piémonts Est et Ouest de la ville de Blida. (Centre de Recherche en Astronomie, Astrophysique et Géophysique), Rapport.

Christodoulou, S. E., & Fragiadakis M. 2015. Vulnerability assessment of water distribution networks considering performance data .*J.Infrastruct.Syst.* 21(2):014040. https://doi.org/10.1061/(ASCE)IS.1943-555X.0000224.

Farahmandfar, Z., Piratla, K., & Andrus, R. D.2016. Resilience evaluation of water supply networks against seismic hazards . *Journal of Pipeline Systems Engineering and Practice*, 04016014. https://doi.org/10.1061/(ASCE)PS.1949-1204.0000251

FEMA. 1997. Earthquake loss estimation methodology HAZUS technical volumes. NIBS Document number 5201. National Institute of Building Sciences.

FEMA. 2000. Estimating earthquake losses with HAZUS. Federal Emergency Management Agency.

Germoso, C., Gonzalez, O., & Chinesta, F.2021. Seismic vulnerability assessment of buried pipelines: A 3D parametric study. *Soil Dynamics and EarthquakeEngineering*Volume143.https://doi.org/10.1016/j.soildyn.2021.106627

Giovinazzi, S., Black, J. R., Milke, M., Esposito, S., Brooks, K. A., Craigie, E. K. and Liu,M. 2015. Identifying Seismic Vulnerability Factors for Wastewater Pipelines after theCanterbury (NZ) Earthquake Sequence 2010-2011. (ASCE), *Pipelines Conference* 2015,23-26 , Baltimore (MD), USA. https://doi.org/10.1061/9780784479360.029

Halfaya, F.Z. 2013. Evaluation des courbes de vulnérabilité sismique d'un réseau de conduites enterrées. Thèse de Doctorat, Ecole Normale Supérieure de CACHAN, France.

Halfaya, F.Z., Bensaibi, & M., Davenne, L. 2017. Seismic vulnerability assessment of water supply network. *International Conference on Advances in Sustainable Construction Materials & Civil Engineering Systems (ASCMCES-17)*, Sharjah, United Arab Emirates.

Halfaya, F.Z., Bensaibi, M.2024. Seismic vulnerability assessment of buried water supply and sanitation pipelines using the analytic hierarchy process: a methodology and application, *Studies in Engineering and Exact Sciences*, ISSN: 2764-0981, Curitiba, v.5, n.1, p. 585-602. https://doi.org/10.54021/seesv5n1-033

Hou, B., Huang, J., Miao, H., Zhao, X., Wu, S. 2023. Seismic resilience evaluation of water distribution systems considering hydraulic and water quality

performance. *International Journal of Disaster Risk Reduction*,Volume 93. https://doi.org/10.1016/j.ijdrr.2023.103756

Kerpelis P., Golfinopoulos S.K., & Alexakis D. 2021. A Proposed Theoretical Approach for the Estimation of Seismic Structural Vulnerability of Wastewater Treatment Plants. *Sustainability*, 13(9), 4835. https://doi.org/10.3390/su13094835

Maruyama, Y., Kimishima K., & Yamazaki F. 2011. Damage assessment of buried pipes due to the 2007 Niigata Chuetsu-Oki earthquake in Japan. *J. Earthquake Tsunami* 5 (1): 57–70. https://doi.org/ 10.1142/S179343111100098X

Matsuhashi, M., Tsushima, I., Fukatani, W., Yokota T. 2014. Damage to sewage systems caused by the Great East Japan Earthquake, and governmental policy . *Soils and Foundations*, Volume 54, Issue 4, Pages 902-909.

Omkarprasad, S.V., and Sushil, K.2006. Analytic hierarchy process: An overview of applications. *European Journal of Operational Research,* vol. 169, issue 1, 1-29. https://doi.org/ 10.1016/j.ejor.2004.04.028

O'Rourke,M., & Deyoe, E.2004. Seismic Damage to Segmented Buried Pipe. *Earthquake Spectra*, 20:4: 1167. https://doi.org/10.1193/1.1808143

O'Rourke, M.2009. Wave Propagation Damage to Continuous Pipe . *Proc. Technical Council on Lifeline Earthquake Engineering*. Lifeline Earthquake Engineering in a Multihazard Environment, Oakland, California. https://doi.org/10.1061/41050(357)76

OYO Corporation. (1999). RADIUS methodology; IDNDR.

Rahimi A., Rezaii M.2021. Seismic Performance Evaluation of Buried Sewage Collection Pipelines . *Shock and Vibration*, vol., Article ID 6669505, 12 pages. https://doi.org/10.1155/2021/6669505

RISK-UE. 2003. Geo-ter, Vulnerability assessment of lifelines and essential facilities (WP06): methodological handbook potable water utility system Appendix11:water pipes, report n GTR-RSK 0101-152av7.

Roy, A., Pudasaini, B., & Shahandashti, M. 2021. Seismic Vulnerability Assessment of Water Pipe Networks under Network Uncertainties. In *Pipelines* (pp. 171–179).

Roy, A., Shahandashti, M., & Rosenberger, J. M. 2022. Effects of Network Uncertainty on Seismic Vulnerability Assessment of Water Pipe Networks . *Journal of Pipeline Systems Engineering and Practice*, 13(3), 04022016. https://doi.org/10.1061/(ASCE)PS.1949-1204.0000652

Roy A., Rosenberger J.M., & Shahandashti M. 2023. Impact of Water Network Uncertainties on Seismic Rehabilitation Decision-Making for Water Pipelines . *Pipelines.* https://doi.org/10.1061/9780784485019.039

Saaty, R.W.1987. The analytic hierarchy process-what it is and how it is used. *Mat/d Modelling*. Vol. 9, No. 3-5, pp. 161-176, USA.
https://doi.org/10.1016/0270-0255(87)90473-8

Sharveen, S., Roy, A., & Shahandashti, M. 2022. Risk-Averse Proactive Seismic Rehabilitation Decision-Making for Water Distribution Systems. *In Pipelines* (pp. 81–90).

Tucker, M.S. 2010. Performance of ductile-iron pipe in earthquake/seismic zones. *Journal American Water Works Association*, Volume 102, Issue 5. https://doi.org/10.1002/j.1551-8833.2010.tb10112.x

Indeks seizmičke ranjivosti kritične urbane vodovodne i kanalizacione infrastrukture zasnovan na metodi AHP

Fatma Zohra Halfaya[a], **autor za prepisku**, *Mahmoud* Bensaibi[b]
[a] University of Blida 1, Civil Department, People's Democratic Republic of Algeria
[b] Infrastructure Studies Control and Assistance Group, GEICA, People's Democratic Republic of Algeria

OBLAST: građevinarstvo
KATEGORIJA (TIP) ČLANKA: originalni naučni rad

Sažetak:

Uvod/cilj: Ovo istraživanje razvija sistematsku metodologiju za procenu seizmičke ranjivosti podzemnih vodovodnih i kanalizacionih mreža. Cilj je integracija geoloških, geotehničkih i strukturnih parametara u jedinstveni okvir za odlučivanje koji omogućava upravnicima infrastrukture da identifikuju i prioritizuju ranjive segmente u regionima sklonim zemljotresima.

Metode: Metodologija kombinuje pristup Indeksa ranjivosti (eng. VI) sa metodom Analitičkog hijerarhijskog procesa (AHP) kako bi se dodelile relativne težine faktorima kao što su materijal cevi, prečnik, starost, dubina ukopa, tip tla, potencijal za likvefakciju, seizmička jačina i ukrštanje sa rasedima. Težine su određene na osnovu stručnog mišljenja i uporednih parova. Alati geografskog informacionog sistema (GIS) i terenska ispitivanja podržavaju prostornu analizu. Pristup je primenjen na grad Blida, Alžir, koji odlikuje visoki seizmički rizik i raznoliki tipovi tla.

Rezultati: Pristup Indeksa ranjivosti koji se zasniva na AHP metodi proizveo je detaljne mape ranjivosti vodovodnih i kanalizacionih mreža, klasifikujući segmente cevi na niske, srednje i visoke nivoe ranjivosti. Ovaj metod je pokazao veću preciznost i kontekstualnu relevantnost u poređenju sa empirijskim procenama, otkrivajući lomljivost materijala, prečnik i geotehničke uslove kao ključne determinante.

Zaključak: Okvir Indeksa ranjivosti i AHP metode pruža robustan, prilagodljiv i transparentan instrument za procenu seizmičkog rizika po vitalnu infrastrukturu. Njegova primena se proteže na civilni i vojni sektor, podržavajući strateško planiranje, ciljane mere ublažavanja rizika i unapređenje otpornosti kritičnih podzemnih cevovoda u seizmički aktivnim regionima.

Ključne reči: analitički hijerarhijski proces (AHP), indeks ranjivosti, mreža vodosnabdevanja, kanalizaciona mreža, seizmički rizik, GIS.

Paper received on: 5 September 2025.
Manuscript corrections submitted on: 23 November 2025.
Paper accepted for publishing on: 11 December 2025.

© 2026 The Authors. Published by Vojnotehnički glasnik / Military Technical Courier (www.vtg.mod.gov.rs). This article is an open access article distributed under the terms and conditions of the Creative Commons Attribution license (http://creativecommons.org/licenses/by/4.0/rs/).



Performance of self-compacting repair mortar including metakaolin and glass fibers

Boukhelkhal Aboubakeur[a], *Djoudi* Amina[b], *Hadj* Aissa Yacine[c], *Benguit* Amar[d], *Cherifi* Rima Hibat Errahmane[e]

[a] University of Laghouat, Research Laboratory of Civil Engineering, Laghouat, People's Democratic Republic of Algeria
e-mail: a.boukhelkhal@lagh-univ.dz, **corresponding author**,
ORCID iD: https://orcid.org/0000-0002-6742-6925

[b] University of Laghouat, Research Laboratory of Civil Engineering, Laghouat, People's Democratic Republic of Algeria
e-mail: a.djoudi@lagh-univ.dz,
ORCID iD: https://orcid.org/0009-0009-8893-2171

[c] University of Laghouat, Research Laboratory of Civil Engineering, Laghouat, People's Democratic Republic of Algeria
e-mail: y.hadjaissa@lagh-univ.dz,
ORCID iD: https://orcid.org/0009-0008-6588-1749

[d] University of Laghouat, Laboratory of Structure Rehabilitation and Materials, Laghouat, People's Democratic Republic of Algeria
e-mail: a.benguit@lagh-univ.dz,
ORCID iD: https://orcid.org/0000-0003-3906-355

[e] University of Djelfa, Applied Automation and Industrial Diagnostic Laboratory, Djelfa, People's Democratic Republic of Algeria
e-mail: rima.cherifi@univ-djelfa.dz,
ORCID iD: https://orcid.org/0009-0001-9222-5762

https://doi.org/10.5937/vojtehg74-61431

FIELD: materials
ARTICLE TYPE: original scientific paper

Abstract:

Introduction*: Self compacting mortar is known as a highly fluid mortar that can flow and fill all spaces under its own weight without vibration or compaction. This experimental work aims to produce a self-compacting mortar (SCM) that can be used to repair damaged structural concrete by replacing a proportion of ordinary Portland cement with metakaolin (MK) and adding glass fibers (GF).*

Methods: Mixtures including various percentages of MK and GF were prepared and tested. All mixtures were tested in the fresh state to assess fluidity and viscosity through mini-slump flow and mini V-funnel flow time

Acknowledgment: This research was sponsored by the General Directorate for Scientific Research and Technological Development (DGRSDT) of the Algerian Minister of Higher Education and Scientific Research.

tests, respectively. Physical and mechanical properties of all mixtures were measured, such as compressive strength, flexural strength and water absorption. In order to check the performance of prepared SCM in structural repair two experiments were conducted on damaged reinforced concrete beam and cylindrical specimens.

Results: The results showed that the addition of GF and MK needs an increase in SP dosage to reduce their negative effect on the fluidity and the viscosity of SCM mixtures. The use of MK up to 10% of cement as replacement resulted in a compressive strength gain of 11 MPa at 28 days and 13 MPa at 56 days. Similar behavior was observed in the mixture containing 0.4% of GF and 10% of MK. Adding GF with 0.2, 0.4, and 0.6% led to flexural strength gains of 4, 6, and 15%, respectively. Water absorption was reduced by 29% when 15% of MK was incorporated. Using MK improves the bond between the repair mortar and the concrete substrate.

Conclusion: Following a rigorous analysis of the obtained results, it can be concluded that MK and GF can be used to improve mechanical properties and reduce water absorption of SCM mixtures. The mixture including 0.4% of GF and 10% of MK exhibited the best performance and was considered more suitable for repairing damaged SCC beams.

Key words: self-compacting mortar, metakaolin, glass fibers, strength, absorption, reparation.

Introduction

The service life of concrete building can be affected by numerous actions from physical, mechanical, and chemical origins. Under such conditions, concrete structures exhibit many typical types of damage, such as cracks, spalling, and reduction of flexural stiffness and bearing capacity. To ensure adequate behavior in service of concrete structures, damaged concrete structures should be repaired. The choice of repair materials is very difficult, it is affected by many factors such as cost, damaged element and parent material, method of repair and density of reinforcement bars. In concrete structural applications, repair materials should have similar characteristics to the parent concrete in terms of dimensional stability, chemical and transport properties (Hassan et al., 2001). In general, repair material should have good workability with higher dimensional stability and low permeability. Self-compacting mortar is a highly fluid mortar that can flow and put in place without vibration. This material is very useful for overhead repairs, especially to facilitate the placement of mortar in congested zones such as thin repairs with closely spaced reinforcing bars (Lacombe et al., 1999). SCM including mineral additions and fibers can

develop superior performance. The use of mineral additions was confirmed to be very useful in improving the workability, stability, mechanical, and durability characteristics of SCC and SCM (Boukhelkhal & Kenai, 2022; Barluenga et al., 2015; Hammat et al., 2021; Sharma & Khan, 2021; Boukhelkhal et al., 2022, Benguit et al., 2024). MK is a calcined clay that has been thermically treated to obtain a highly reactive pozzolanic material. Adding MK to mortars and concretes offers many technical and environmental advantages. It was reported that the partial substitution of cement by MK reduces the carbon dioxide emitted into the atmosphere, the unit cost of concrete, and the energy required for its production (Kavitha et al., 2015, 2016). The same authors reported that the use of 10% of MK was more suitable to produce SCC with good fresh and hardened properties. According to Siddique et al. (2026), the incorporation of MK in high strength concrete significantly improves its mechanical and durability performance, particularly at the cement replacement level of 10–15 %. Kavitha et al. (2016) stated that inclusion of MK decreases the permeability and ingress of chloride ions into the concrete due to the refined pore structure of the concrete. Ouldkhaoua et al. (2023) reported that the use of calcined kaolinite clay (CK) consumed a significant part of the SP dosage and decreased SCM fluidity. The mixture made with 15% CK exhibited lower fluidity, with a reduction of 3%.

The introduction of fibers in the concrete matrix opens new possibilities in civil and structural engineering. Numerous authors stated that adding fibers improves the tensile strength, flexural strength, dynamic properties, crack resistance, and ductility of concrete (Mohammadi et al., 2008; Manoharan and Anandan, 2014). Many types of fibers are available, includig steel, polymer, rubber, glass, polypropylene and vegetable fibers. Vedhasakthi and Chithra (2023) studied the incorporation of basalt fibers (BF) in a volume range of 0.1% to 0.5% to improve SCC properties such as compressive, split-tensile, flexural, residual, and impact strength properties. The research findings revealed that compressive strength and split-tensile strength increased at 0.3% volume fraction of BF, whereas the flexural strength, residual strength, and impact strength increased at 0.4% volume fraction of BF. Güneyisi et al. (2019) conducted an experimental laboratory study to investigate the fresh and rheological characteristics of glass fiber reinforced self-compacting concrete containing nanosilica. They observed that an elevation of the nanosilica (NS) content from 0% to 4% and the glass fiber (GF) volume fraction from 0% to 1.5% resulted in a rise in both the slump flow and V-funnel flow times. The Herschel-Bulkley model was used to characterize the rheological behavior of fresh glass fiber reinforced mortar. The results showed that the shear-thickening

intensity increased with the increase of glass fiber volume fraction for the cement-fly while the addition of glass fiber resulted in the rheological behavior of cement-silica fume binary mortar changing from shear-thickening to shear-thinning response (Jiao et al. 2019). Rosas et al. (2025) have concluded that mineral wool (MW) has primarily been studied as a supplementary cementitious material (SCM) due to its pozzolanic activity and capacity to densify the microstructure, while glass fiber (GF) has been used as reinforcement to enhance tensile and flexural strength. It is recommended to limit the proportion of fibers in concrete to prevent mixing difficulties, which cause poor compaction, non-uniform repartition of fibers, and an increase in voids volume (Sukontasukkul et al., 2018; Wan & Takahashi, 2016). Zhang et al. (a 2024) have demonstrated that incorporating waste glass fiber improves its axial compressive strength, with an improvement of 2.2∼15.3 %. Scanning electron microscopy (SEM) techniques were applied to explore the influence mechanism of waste glass fibers on glass fiber-reinforced self-compacting recycled concrete (RGF-SCRC). The results showed that after adding an appropriate content of waste glass fiber, the porosity and the number of large pores decreased. It was also noticed that specimens with the 7.5 kg/m3 alkali-resistant glass fiber content showed the best mechanical properties (Zhang et al., b 2024).

This study aims to produce a repair mortar with high fluidity, which includes mineral additions and fibers, that can be successfully used to repair damaged structural concrete elements. To achieve this goal, MK was incorporated as a partial replacement of cement at substitution ratios of 5, 10, and 15%, while glass fibers were added with different percentages (0.2, 0.4 and 0.6%). The objective of this research was to determine the mixtures that achieve self-compacting requirements and offer acceptable physical and mechanical properties.

Materials and experimental program

Materials

The cement used in this work was CEMI 42.5. Metakaolin was used as a partial replacement of cement. It was obtained by thermal treatment of kaolin clay for 3 hours at 850 °C (Said-Mansour et al., 2011). Table 1 presents the physical characteristics and chemical composition of cement and metakaolin. The results of this table indicate that MK consists predominantly of alumina (33%) and silica (49.3%). The results of laser distribution analysis (Figure 1) on cement and metakaolin showed that MK is finer than cement. It was noted that the proportion of particles of a finer

size is higher in MK, with about 50% of particles finer than 4 µm, while 50% of cement particles are finer than 13.7 µm. The curve of particle size destruction of sand was also plotted in Figure 1. It can be clearly seen that sand has continuous particle size destruction.

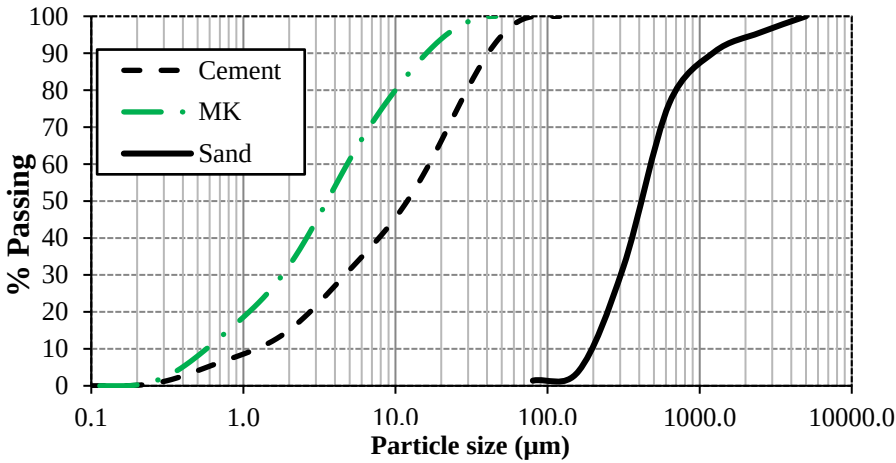


Figure 1 - Particle size distribution of sand, ordinary cement and metakaolin

Table 1 - Chemical and physical properties of cement and metakaolin

Element		OPC	MK
SiO_2 (%)		18.83	49.30
CaO (%)		61.54	0.08
MgO (%)		1.27	0.40
Al_2O_3 (%)		4.20	33.00
Fe_2O_3 (%)		5.31	2.37
SO_3 (%)		1.96	-
K_2O (%)		0.49	2.93
T_iO_2 (%)		0.20	0.24
Na_2O (%)		0.21	0.09
P_2O_5 (%)		0.29	-
Loss on ignition (%) (%)		5.70	10.5
Specific density		3.11	2.45
Blaine fineness (cm^2/g)		3300	8500
Fineness characteristics	d_{10} (µm)	1.4	0.7
	d_{50} (µm)	13.7	4
	d_{90} (µm)	46.7	18.3

Figure 2 shows the results of SEM analysis of cement and MK. As can be observed, metakaolin has finer and less angular particles shape compared to those of cement. This confirmed the results of Figure 1. A kind of locally commercial glass fiber with a density of 0.91 g/cm^3 and a length of 1.50 ± 0.25 cm (Figure 3) was used in this study.

River sand was used as fine aggregates in all self-compacting mortar mixes. It has 5 mm maximum aggregate size, specific gravity of 2.47 and absorption coefficient of 1.16%. Superplasticizer (SP) type polycarboxylates based High-Range Water Reducers (HRWR) was employed to reach desired fluidity. The superplasticizer's density, pH and solid particle concentration are 1.07 g/cm^3, 8 and 30%, respectively. Potable water was used for mixing of mixtures constituents and curing of the specimens.

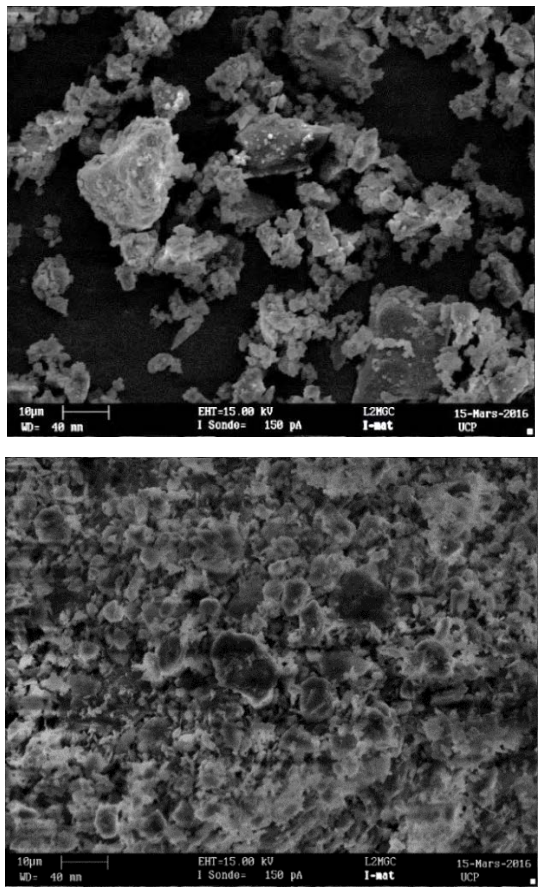


Figure 2 - Particle shape of: (a) ordinary cement and (b) metakaolin



Figure 3 - Glass fibers with a length of 1.50 ± 0.25 cm

Mix proportion design

A total of eight mixtures were prepared and tested. One was a control mix, three contained different ratios of metakaolin (5, 10, and 15%), three others including glass fibers at 0.2, 0.4, and 0.6%, and one mixture contained a combination of metakaolin (10%) and glass fibers (0.4%). The composition of the SCM reference mix is determined based on Okamura and Ozawa (1995) mix design method, in which the sand/mortar ratio (S/M), total content of binder, and water-binder ratio (w/b) were kept constant at 0.5, 693 kg/m3 and 0.4, respectively. To provide the desired fluidity, SP was used with a dosage of 1.1% of the binder in the control mix, while in mixtures incorporating MK and GF, the dosage of SP was varied to satisfy the required fluidity (slump flow diameter ranged between 27.5 and 33.5 cm, and flow time between 2 and 10 s). The proportions of the SCM mixtures are given in Table 2.

Table 2 - Mix proportions of SCM mixes for 1 m^3

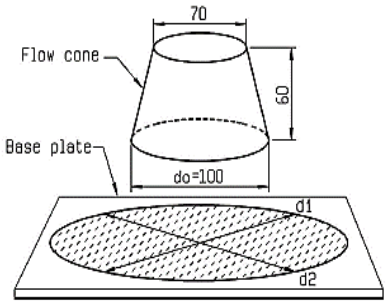
Mixes	w/b	Constituents						
		Cement (kg)	Metakaolin (kg)	Glass fibers (kg)	Sand (kg)	Water (kg)	SP (%)	SP (kg)
100C	0.4	692.6	-	0	1300	278.8	1.10	7.59
5MK		658.0	34.6	0			1.15	7.94
10MK		623.4	69.2	0			1.30	8.98
15MK		588.7	103.9	0			1.45	10.01
0.2GF		692.6	-	1.38			1.15	7.94
0.4GF		692.6	-	2.76			1.35	9.32
0.6GF		692.6	-	4.14			1.60	11.05
10MK+0.4GF		623.4	69.2	2.76			1.60	11.05

Note: 5MK→ 5% of metakaolin and 95% of ordinary Portland cement

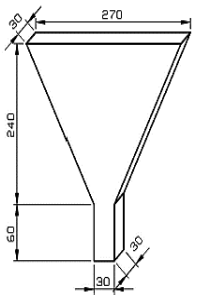
Test procedure

Fresh mortar tests

According to the EFNARC standard (EFNARC, 2002), mini slump flow and mini v-funnel tests are two main tests that allow the assessment of the fluidity, filling ability, and stability of fresh self-compacting mortar. In the first test, the final slump flow diameter of the mortar was determined. Slump flow diameters ranging from 27.5 and 33.5 cm are recommended to obtain slump flow values in the range of 55-85 cm for SCC (Safiuddin, 2008; Jin & Domone, 2002). In the second test, the mini v-funnel was filled completely with mortar and the bottom outlet was opened, allowing to the mortar to flow out (Figure 4.b). The v-funnel flow time Tv was measured. During these tests, it is possible to assess the risk of segregation or bleeding through visual control.



(a)



(b)

Figure 4 - Schematization of SCM tests, (a) mini-slump flow test, (b) mini v-funnel test (Jooste, 2006)

Hardened mortar tests

From each mortar mixture, prismatic specimens with dimensions of 40×40×160 mm^3 in size were prepared and stored in water until the age of testing. According to the European Standard EN 196-1 (EN 196-1, 2016), three specimens from each mixture were used to evaluate flexural strength at 28 days and compressive strength at 28 and 56 days. Water absorption was measured at 28 days. The microstructures of each mixture's specimens were examined by scanning electron microscopy (SEM).

In order to check the performance of the designed mortars as repair materials, two experiments were conducted. In the first test, small beams of reinforced SCC were made (50x10x10 cm), and then deformed in the tension part. After 28 days, repair mortars that included GF and MK were added, as it can be seen in Figure 5. For the second test (slant shear test), cylindrical samples with a diameter of 10 cm and a height of 20 cm of SCC were prepared with an inclined surface (Figure 6). After a water-curing period of 28 days, the repair mortars that included only MK were applied without any compaction. This test, which puts the bond interface into a combined state of compression and shear, is adopted in BS6319: Part 4 (British Standard Institute, 1984). The mix-design of repair mortars is already given in Table 2. All specimens were cured in conditioning chamber (T=20 °C, RH > 90%) and then tested at 28 days after repair.

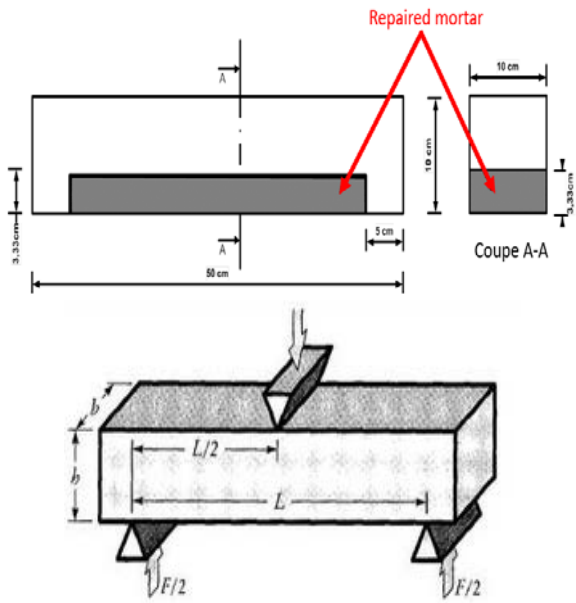


Figure 5 - Preparation of beam specimens for the 3P flexural strength test

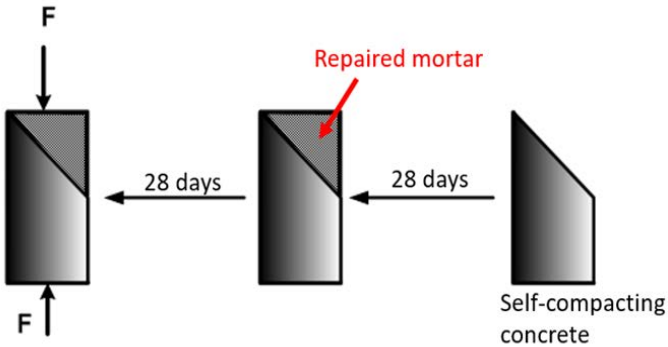


Figure 6 - Preparation of cylindrical specimens for the slant shear strength test

Results and discussion

Properties of fresh mortar

The effect of MK as a partial cement replacement and GF at different percentages on the workability of self-compacting mortar was investigated based on two fresh mortar tests, namely, slump flow and V-funnel. Figures 7 and 8 present the obtained results. It is important to note that for equitable comparison, differences between the slump flow values and between the flow time values were minimized using varied dosages of superplasticizer, as shown in Table 2. The values are within the recommended values of EFNARC of 27–33 cm for slump flow and 2–10 s for flow time, except for the 0.6GF mixture. From Figure 7, it can be observed that the slump flow values decreased as the MK and GF content increased. This decrease varied between 0.25 cm and 1.25 cm between the reference mortar and mortars with 5 and 15% MK, respectively. It can be seen from Figure 8 that the flow time increased with the increase of MK replacement rates. For example, when the %MK increased from 5% to 15%, the flow time increased from about 37 to 49%. The decrease in slump flow in mortar including GF was more pronounced. Increasing GF content from 0.2 to 0.6 decreased the slump flow by 2.5 cm to 4 cm. The results of Figure 8 indicated a significant increase in the V-funnel flow time with the addition of GF. Adding GF resulted in an important increase in the V-funnel flow time (40 to 98%). It should be observed that mixtures named 0.4GF and 10MK+0.4GF reached values superior to 10 s. V-funnel flow time is a good indicator of viscosity, so its increase means an increase in viscosity and vice versa. Visual control showed that all designed SCM mixtures have good homogeneity and stability (Figure 9).

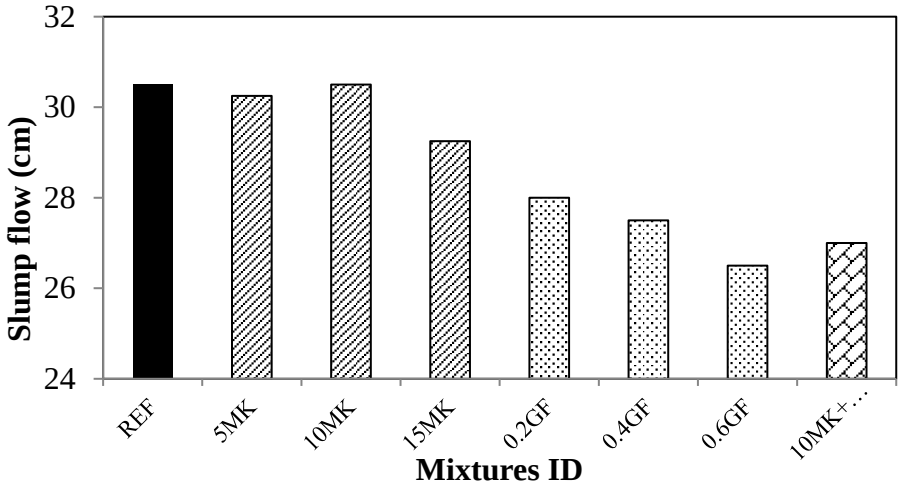


Figure 7 - Variation of slump flow for different SCM mixtures

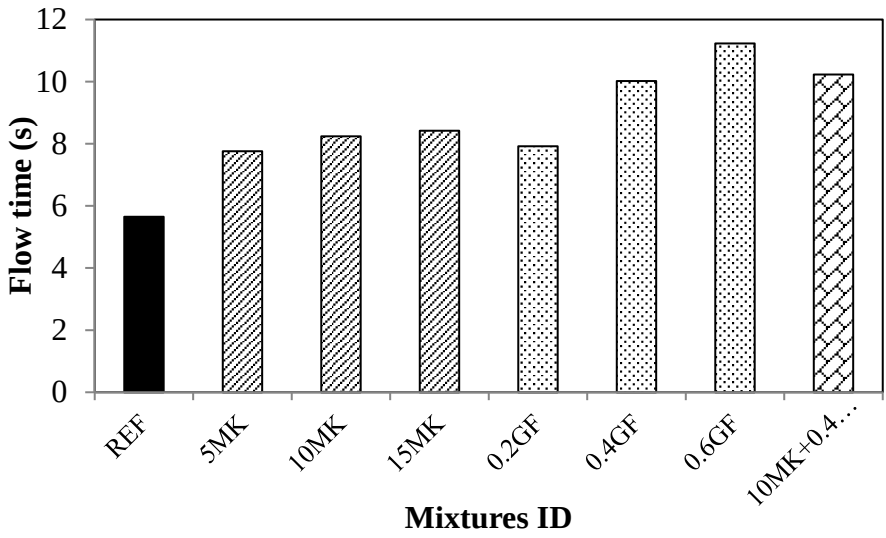
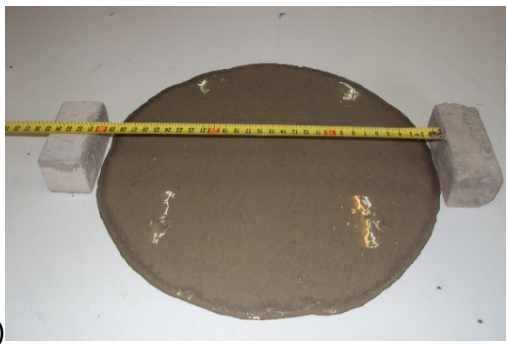


Figure 8 - Variation of flow time for different SCM mixtures

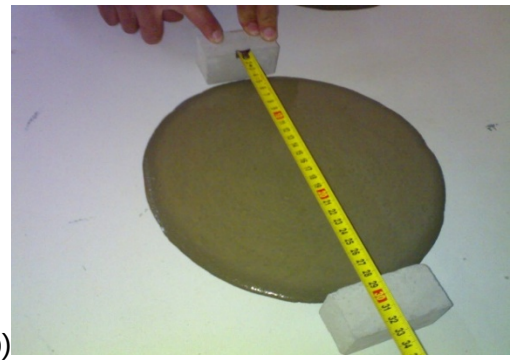
Similar results for the impacts of MK and GF on the fresh properties of mortars and concretes were reported in the literature (Yu et al., 2022; Güneyisi et al., 2019; Zhang et al., b 2024). Some authors pointed out that the fine MK powder with higher specific area adsorbed more water, and therefore, it significantly reduced the fluidity and systematically increased the viscosity of concrete at the mixing stage when the ratios of water to cementing material kept constant (Qin et al., 2019; Hammat et al., 2021).

The decrease in V-funnel flow time with the addition of GF is attributed to the following two reasons: on the one hand, a layer of slurry will be wrapped around the surface of the glass fibers, resulting in less slurry wrapping around the aggregates and reducing the lubrication effect of the slurry on the aggregates; on the other hand, the accumulation of glass fiber forms a framework in concrete, which increases the internal friction force that the cement slurry needs to overcome and limits the movement of aggregates (Zhang et al., b 2024).

(a)



(b)



(c)

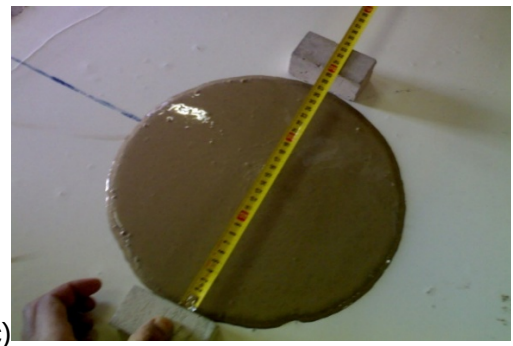


Figure 9 - Slump flow of the SCM mixtures: (a) 100C, (b) 15MK, (c) 0.2GF

Properties of hardened mortar

Compressive strength

Figure 10 shows the evolution of compressive strength of the developed SCM mixtures at 28 and 56 days. The reported values of compressive strength are the average of three specimens prepared for each mixture. The values of 28-day compressive strength varied between 24.6 and 35.4 MPa. The introduction of MK in SCM mixtures significantly increased the compressive strength, with an optimum at 10%. The mixture including 10MK and 0.4GF showed also superior 28-day compressive strength in comparison to the control mix. It was observed that adding GF had no effect on compressive strength. Similar results were observed for 56-day compressive strength. It was noted that the 28-day compressive strength for mixtures made with MK is 22-39% more than that of the corresponding plain cement mixture. At 56 days, this reached 32-49%. This may be attributed to the pozzolanic reaction of MK which ocurred after 28 days. In fact, MK is an ultra-fine pozzolana and its superior performance could be attributed to the filling effect, where the MK particles fill the space between cement particles and also to the pozzolanic reaction between silica from MK and portlandite (calcium hydroxide C-H) from hydrated cement, which generates secondary calcium silica hydrate (C-S-H). This resulted in a more refined pore structure and denser cement matrix.

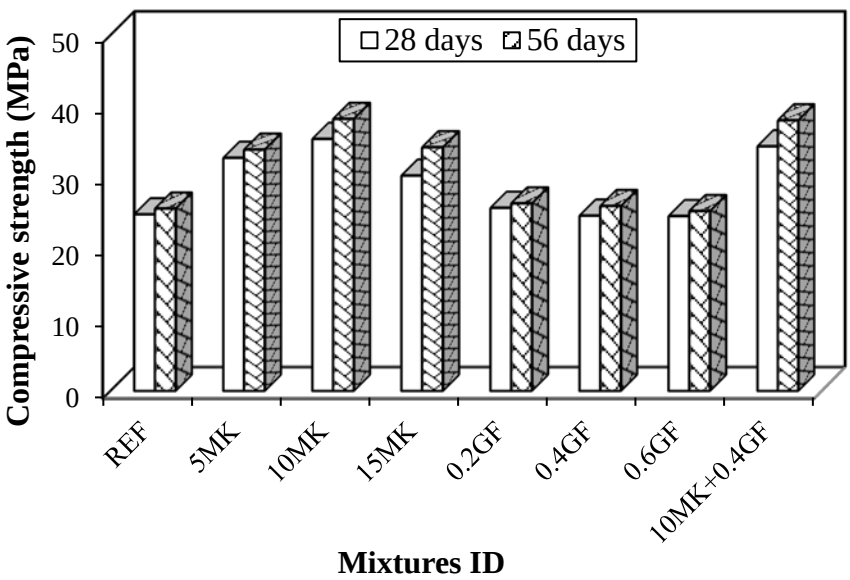


Figure 10 - Effects of MK and GF on compressive strength of SCM mixtures

Flexural strength

Figure 11 shows the evolution of the 28-day flexural strength of the developed SCM mixtures. Compared to the mixture with plain cement, it appears that the introduction of MK and GF increased the flexural strength and as the amount of GF increased, the flexural strength increased. For example, the use of 0.2, 0.4 and 0.6% of GF led to flexural strength superior to that of the mixture without fibers by 4, 6 and 15%, respectively. For MK mixtures, similar trends were observed to those of compressive strength with an optimum of 10%. The combined use of MK and GF (10MK+0.4GF) showed the highest flexural strength. The introduction of fine powder reduces the interconnectivity of the pore system and enhances the interfacial transition zone and, consequently, the flexural strength increased. The improvement of flexural strength when GF was added may be due to the bridging effect of GF between cracks during the loading process. A higher fiber content forms a denser fiber network, thereby increasing the possibility of effective bridging and improving the bearing capacity of SCM mixtures. However, excessive fiber content leads to fiber conglobation, which reduces flexural performance (Zhang et al., b 2024).

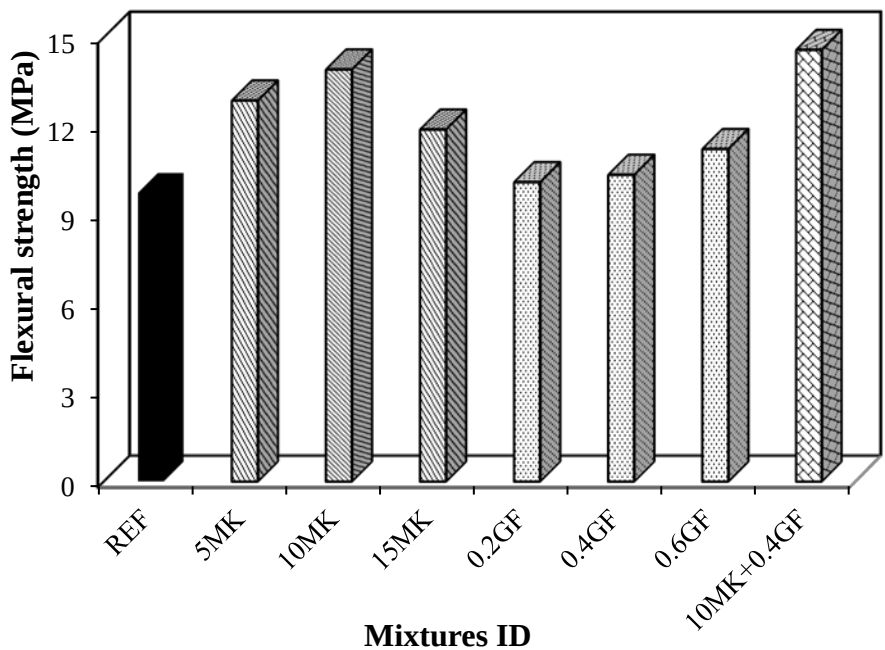


Figure 11 - Effects of MK and GF on 28 days- flexural strength of SCM mixtures

Water absorption

The water absorption of the developed SCM mixtures was evaluated by measuring the water absorbed after complete immersion for 72 h (Figure 12). A lower durability is expected for a concrete material with a higher water absorption. The water absorption values of GF mortars were slightly lower than those of the corresponding reference mix. For MK mixtures, water absorption decreased by 2, 14 and 29% for substitution levels of 5, 10 and 15%, respectively. The mixture including both MK and GF (10MK+0.4GF) showed a water absorption value of 5%, which is lower than that of the plain cement mortar by about 13%. The reduction in water absorption with increasing MK content may be due to the formation of supplementary calcium silicate hydrates (C-S-H), which contributes to clogging the pore system, and results in a decrease in total porosity and hence leads to the concrete with a denser cement microstructure. According to Figure 1, MK has finer particle size than cement. This improves the grading curve of the binder's particles and makes the cement matrix denser.

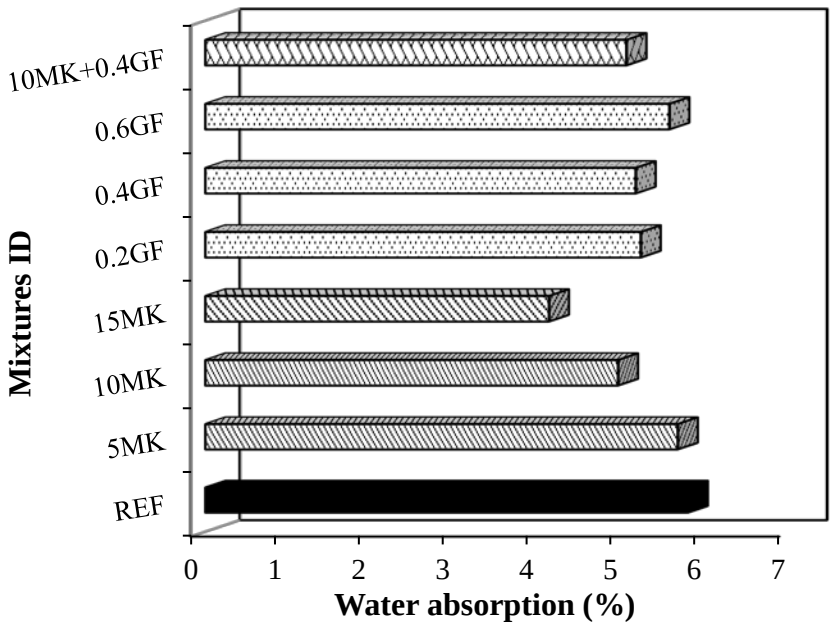
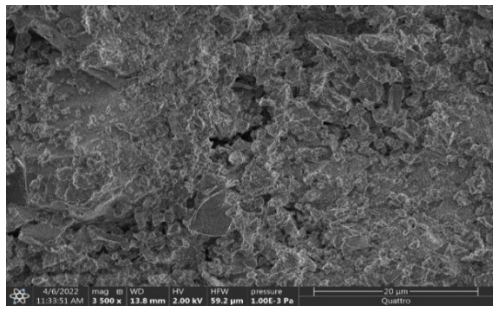


Figure 12 - Effects of MK and GF on the water absorption of SCM mixtures

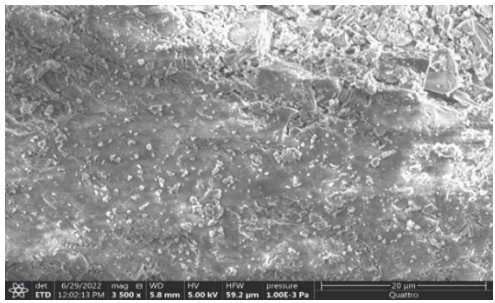
Microstructure examination:

SEM images for some selected SCM specimens are depicted in Figure 13. The mixture without MK and GF showed some voids and micro-pores in the sample (Figure13a). There is also the absence of dense C-S-H and a bond between particles. The introduction of MK resulted in a more uniform and refined structure (Figure13b) as compared to the mixture with only cement (Figure13a). Figure 13c shows better cohesion and a bond between GF and the blended cement matrix. With the addition of MK, the particle size of the binder is improved and the SCM structure becomes more homogeneous and dense.

(a)



(b)



(c)

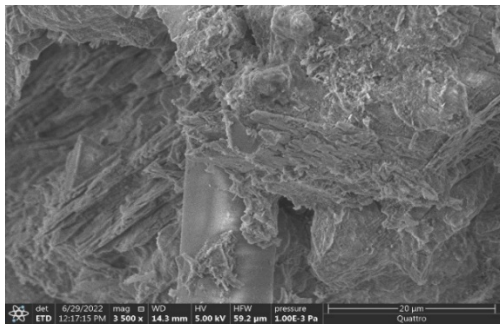


Figure 13 - SEM images of (a) plain cement SCM, (b) MK cement SCM and (c) SCM with GF and MK

Slant shear strength

Figure 14 depicts the variation in the slant shear strength of concrete repaired by mortars including cement and MK. Slant shear strength values varied from 25 to 31 MPa. Mixtures with MK replacements of 5%, 10% and 15% developed slant shear strengths of 25.66, 28.73 and 31.43 MPa, these values are higher by about 4%, 16% and 27% in comparison to the control mixture, respectively. These results showed beneficial effects of MK on improving the bond between repair mortar and the SCC substrate. In fact, the presence of MK in SCM resulted in enhancing cement matrix microstructure, which may be due to the physical effect, providing therefore a filling of pores and micropores. The advantage effect of MK may also attributed to the pozzolanic reaction (chemical effect) which is effective in reducing the average size of pores and segmenting large pores.

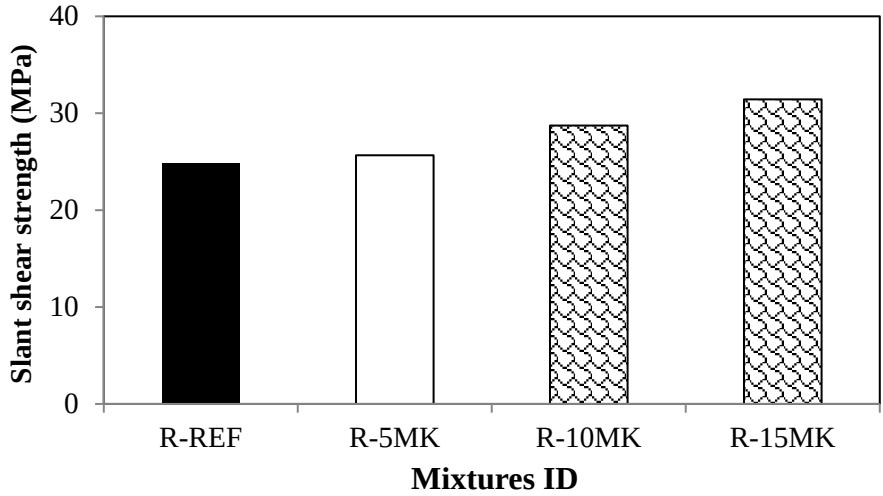


Figure 14 - Evolution of slant shear strength for the SCC cylindrical specimens repaired by different mortar compositions

Figure 15 presents the failure modes of some SCM specimens under slant shear force. The failure mode can reflect the bond performance. According to Feng et al. (2024), the substrate failure mode indicates excellent bond performance, indicating that the interfacial bond strength exceeds the concrete substrate strength, and the interface failure indicates a weak bond performance that the interfacial bond strength is weaker than that of the concrete substrate. Cracks appeared in concrete substrates and repair materials. The failure modes of repair specimens are a combination

of failure in the SCC substrate and repair mortars, which indicates relatively better interfacial bond properties.



Figure 15 - Evolution of flexural strength for the beam repaired by different mortar compositions

Flexural strength

Figure 16 illustrates the flexural strength of SCC beams repaired by mortars including various proportions of GF and MK. Flexural strength values ranged from 10.54 to 11.62 MPa. It was observed that increasing GF content increased the flexural strength. The increase in flexural strength is 3, 4 and 10% for GF content of 0.2, 0.4 and 0.6%, respectively. The combined use of MK and GF (10MK+0.4GF) showed approximately similar performance to that of the mixture including 0.6% of GF. Jasiczak and Mikołajczak (2003) stated that the presence of fibers in the internal structure of the concrete bridges cracks and allows the concrete elements to deform plastically. Moreover, the use of fibers contributes to the reduction of stress concentration at the crack's end, which, if the fibers

were absent, would accelerate the propagation of the cracks and reduce the flexural strength. MK contributes to improving flexural strength. This may be explained by (i): the physical effect, in which MK particles fill the gaps between cement particles and (ii) the physico-chemical effect, in which pozzolanic reaction takes place between silicon dioxide from MK with calcium hydroxide and water to form new calcium silicate hydrate. This results in a more refined pore structure and a denser cement matrix (Al-Akhras 2006; Boukhelkhal et al., 2019).

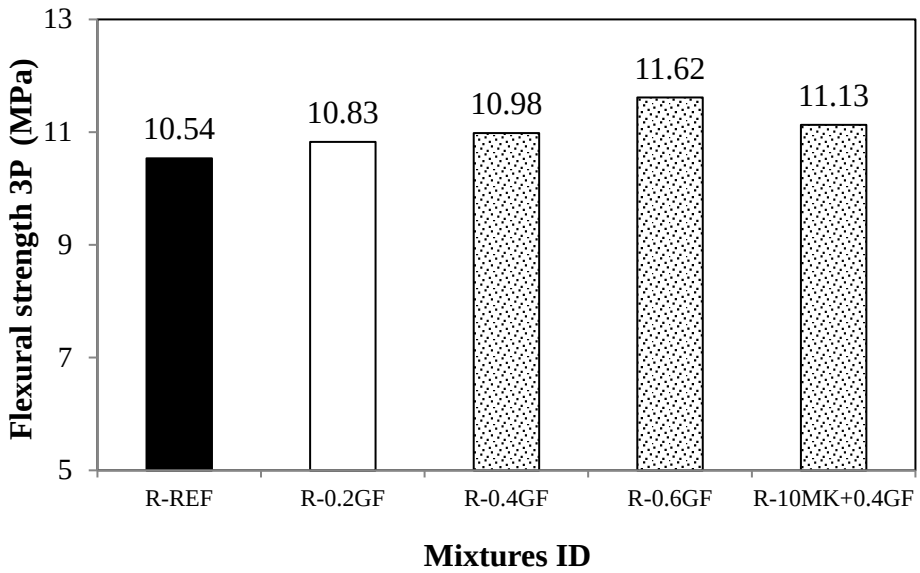


Figure 16 - Evolution of flexural strength for the beam repaired by different mortar compositions

Conclusion

The elaboration of self-compacting repair mortar incorporating metakaolin and glass fibers offers a promising solution for addressing environmental concerns in the construction industry. By utilizing industrial new powder and enhancing the properties of repair mortar, this approach enhances construction practices and the long-term durability of structures. Based on the findings, the following conclusions could be drawn:

- The use of metakaolin requires a higher dosage of superplasticizer in order to achieve self-compatibility of all mortars.
- Adding glass fibers significantly affected the fluidity and viscosity of the mortar, so it should not exceed a percentage of 0.6%.

- Replacing proportions of cement with metakaolin resulted in improved compressive and flexural strengths and reduced water absorption with an optimum of 10%.
- Flexural strength slightly increased with increasing GF content.
- When the amount of MK is increased from 5 to 15%, the slant shear strength increased by 26 to 31%, respectively. This means that MK had beneficial effects in improving the bond between repair mortars and concrete substrate.
- Specimens' beam repaired by GF and MK showed superior performance to those repaired by cement mortar alone.

Regarding all conducted tests, it can be stated that the mixture including the combination of 0.4% of GF and 10% of MK is the best since it has acceptable fresh properties combined with superior mechanical properties as compared to the other mixtures.

References

Al-Akhras, N. 2006. Durability of metakaolin concrete to sulfate attack. *Cement and Concrete Research*, 36, pp. 1727–1734. Available at: https://doi.org/10.1016/j.cemconres.2006.03.026

Barluenga, G., Palomar, I., Puentes, J. 2015. Hardened properties and microstructure of SCC with mineral additions. *Construction and Building Materials*, 94, pp. 728-736. Available at: https://doi.org/10.1016/j.conbuildmat.2015.07.072.

Benguit, A., Boukhelkhal, A., Azzouz, L. 2024. Durability of self-compacting mortar based on composite binder under external chemical attacks. *Cement Wapno Beton*, 29(1), pp. 71-81. Available at: https://doi.org/10.32047/CWB.2024.29.1.5

Boukhelkhal, A., Azzouz, L., Kenai, S., Kadri, E.H., Benabed, B. 2019. Combined effects of mineral additions and curing conditions on strength and durability of self-compacting mortars exposed to aggressive solutions in the natural hot-dry climate in North African desert region. *Construction and Building Materials*, 197, pp. 307-318. Available at: https://doi.org/10.1016/j.conbuildmat.2018.11.233

Boukhelkhal, A., Hamdaoui, A., Sebguig, B. 2022. Some engineering properties of sustainable self-compacting mortar made with ceramic and glass powders. *Építőanyag: Journal of Silicate Based and Composite Materials,* 74(1), pp. 21-26. Available at: https://doi.org/10.14382/epitoanyag-jsbcm.2022.4

Boukhelkhal, A., Kenai, S. 2022. Assessment of fluidity retention, mechanical strength and cost production of blended cement self-compacting concrete using the concept of a performance index. *Frattura ed Integrità Strutturale,* 16(60), pp. 89–101. Available at: https://doi.org/10.3221/IGF-ESIS.60.07

British Standard Institute. 1984. Testing of Resin Composites for Use in Construction, BS 6319, Part 4: Method for Measurement of Bond strength Slant Shear Method.

EFNARC. 2002. Specification and Guidelines for Self-compacting Concrete. Norfolk, UK, Februry.

EN 196-3. 2016. Methods of testing cement-Part 1: Determination of strength.

Feng., S, Xiao., H, Li., H. 2022. Comparative studies of the effect of ultrahigh-performance concrete and normal concrete as repair materials on interfacial bond properties and microstructure. *Engineering Structures,* 222. Available at: https://doi.org/10.1016/j.engstruct.2020.111122

Güneyisi, E., Atewi, Y.R., Hasan, M.F. 2019. Fresh and rheological properties of glass fiber reinforced self-compacting concrete with nanosilica and fly ash blended. *Construction and Building Materials*, 211, pp. 349-362. Available at: https://doi.org/10.1016/j.conbuildmat.2019.03.087

Hammat, S., Menadi, B., Kenai, S., Thomas, C., Kirgiz, M.S., De Sousa Galdino A.G. 2021. The effect of content and fineness of natural pozzolana on the rheological, mechanical, and durability properties of self-compacting mortar. *Journal of Building Engineering,* 44. Available at: https://doi.org/10.1016/j.jobe.2021.103276

Hassan, K.E., Brooks, J.J., Al-Alawi, L. 2001. Compatibility of repair mortars with concrete in a hot-dry environment. *Cement and Concrete Composites*, 23(1), pp. 93-101. Available at: https://doi.org/10.1016/S0958-9465(00)00073-1

Jasiczak, J., Mikołajczak, P. 2003. Technologia betonu modyfikowanego domieszkami I dodatkami – przegla¸d tendencji krajowych i zagranicznych. Oficyna Wydawnicza Politechniki Poznan´ skiej, Poznan´ (in Polish).

Jiao, D., Shi, C., Yuan, Q., Zhu, D., De Schutter, G. 2019. Effects of rotational shearing on rheological behavior of fresh mortar with short glass fiber. *Construction and Building Materials*, 203, pp. 314-321. Available at: https://doi.org/10.1016/j.conbuildmat.2019.01.133

Jin, I., Domone, P. 2002. Relationships between the fresh properties of SCC and its mortar component. In: Shah SP, Daczko JA, Lingscheit JN, editors. Proceedings of the first North American conference on the design and use of self-consolidating concrete, Chicago, USA.

Jooste, J.P. 2006. approaches to mix design and measurement of workability for self-compacting concrete, A dissertation of Master of Science in Engineering, University of the Witwatersrand, Johannesburg, pp.187.

Kavitha, O.R., Shanthi, V.M., Prince Arulraj, G., Sivakumar, P. 2015. Fresh micro-and macrolevel studies of metakaolin blended self-compacting concrete. *Applied Clay Science*, 114, pp. 370–374. Available at: https://doi.org/10.1016/j.clay.2015.06.024

Kavitha, O.R., Shanthi, V.M., Prince Arulraj, G., Sivakumar, V.R. 2016. Microstructural studies on eco-friendly and durable self-compacting concrete blended with Metakaolin. *Applied Clay Science*, 124, pp. 143–149. Available at: https://doi.org/10.1016/j.clay.2016.02.011

Lacombe, P., Beauprd, D., Pouliot, N. 1999. Rheology and bonding characteristics of self-leveling concrete as a repair material. *Materials and Structure*s, 32, pp. 593-600. Available at: https://doi.org/10.1007/BF02480494

Manoharan., S.V, Anandan, S. 2014. Steel Fibre Reinforcing Characteristics on the Size Reduction of Fly Ash Based Concrete. *Advances in Civil Engineering*. Available at: https://doi.org/10.1155/2014/217473

Mohammadi, Y., Singh, S.P., Kaushik, S.K. 2008. Properties of steel fibrous concrete containing mixed fibres in fresh and hardened state. *Construction and Building Materials*, 22, pp. 956–965. Available at: https://doi.org/10.1016/j.conbuildmat.2006.12.004

Okamura, H., Ozawa, K. 1995. Mix-design for self-compacting concrete. Concrete Library of Japan Society of Civil Engineers, 25, pp. 107-120.

Ouldkhaoua, Y., Laidani, Z., Sahraoui, M., Benabed, B., Canpolat, O., Abousnina, R. 2023. Performance evaluation of self-compacting repair mortar containing calcined kaolinite clay and waste glass. Available at: http://dx.doi.org/10.2139/ssrn.4615236

Qin., Z, Zhou., S, Ma., C, Long., G, Xie., Y, Chen., B. 2019. Roles of metakaolin in magnesium phosphate cement: Effect of the replacement ratio of magnesia by metakaolin with different particle sizes. *Construction and Building Materials,* 227. Available at: https://doi.org/10.1016/j.conbuildmat.2019.116675

Rosas, M.H., Carvalho, V.R., Rocha, J.H.A., Peixoto, R.A.F., Defáveri, K.C.S. 2025. Low-carbon cement-based composites reinforced with mineral wool and glass fibers: a concise bibliometric analysis and systematic review. *Journal of Building Engineering,* 111. Available at: https://doi.org/10.1016/j.jobe.2025.113501

Safiuddin, M. 2008. Development of self-consolidating high performance concrete incorporating rice husk ash. Ph.D. thesis, Ontario University, Canada.

Said-Mansour, M., Kadri, E.H., Kenai, S., Ghrici, M., Bennaceur, R. 2011. Influence of calcined kaolin on mortar properties. *Construction and Building Materials*, 25 (5), pp. 2275-2282. Available at: https://doi.org/10.1016/j.conbuildmat.2010.11.017

Sharma, R., Khan, R.A. 2021. Sulfate resistance of self compacting concrete incorporating copper slag as fine aggregates with mineral admixtures. *Construction and Building Materials*, 287. Available at: https://doi.org/10.1016/j.conbuildmat.2021.122985

Siddique, R., Sidhu, A.S., Klemczak, B. 2026. High strength concrete and the impact of metakaolin on its mechanical, durability and microstructural characteristics – A review. *Journal of Building Engineering*, 118. Available at: https://doi.org/10.1016/j.jobe.2025.114925

Sukontasukkul, P., Pongsopha, P., Chindaprasirt, P., Songpiriyakij, S. 2018. Flexural performance and toughness of hybrid steel and polypropylene fibre reinforced geopolymer. *Construction and Building Materials,* 161, pp. 37-44. Available at: https://doi.org/10.1016/j.conbuildmat.2017.11.122

Vedhasakthi, K, Chithra, R. 2023. Strength attributes and microstructural characterization of basalt fibre incorporated self-compacting concrete. *Journal of Building Engineering,* 78. Available at: https://doi.org/10.1016/j.jobe.2023.107592

Wan, Y., Takahashi, J. 2016. Tensile and compressive properties of chopped carbon fiber tapes reinforced thermoplastics with different fiber lengths and molding pressures. *Composite Part A,* 87, pp. 271–281. Available at: https://doi.org/10.1016/j.compositesa.2016.05.005

Yu, Z., Zhang., T, Deng., Y. 2022. The micro-facial characteristics and mechanical behavior of metakaolin and steel fibers modified concrete at high fluidity. *Case Studies in Construction Materials,* 16. Available at: https://doi.org/10.1016/j.cscm.2022.e01019

Zhang, F., Lu, Z., Wang, D. b 2024. Working and mechanical properties of waste glass fiber reinforced self-compacting recycled concrete. *Construction and Building Materials*, 439. Available at: https://doi.org/10.1016/j.conbuildmat.2024.137172

Zhang, F., Zheng, R., Liao, G., Wang, D., Lu, Z., Meng, H., Lu, Z. a 2024. Axial compressive and long-term shrinkage behaviors of self-compacting recycled concrete reinforced with recycled glass fiber. *Construction and Building Materials*, 455, pp. 139-158. Available at: https://doi.org/10.1016/j.conbuildmat.2024.139158

Performanse samozbijajućeg maltera za reparaciju sa metakaolinom i staklenim vlaknima

Boukhelkhal Aboubakeur[a], **autor za prepisku**, *Djoudi* Amina[a], *Hadj* Aissa Yacine[a], *Benguit* Amar[b], *Cherifi* Rima Hibat Errahmane[c]

[a] University of Laghouat, Research Laboratory of Civil Engineering, Laghouat, People's Democratic Republic of Algeria

[b] University of Laghouat, Laboratory of Structure Rehabilitation and Materials, Laghouat, People's Democratic Republic of Algeria

[c] University of Djelfa, Applied Automation and Industrial Diagnostic Laboratory, Djelfa, People's Democratic Republic of Algeria

OBLAST: materijali
KATEGORIJA (TIP) ČLANKA: originalni naučni rad

Sažetak:

Uvod/cilj: Samozbijajući malter je poznat kao malter visoke fluidnosti koji može da teče i popuni sve prostore pod sopstvenom težinom, bez vibriranja ili zbijanja. Cilj ovog eksperimentalnog istraživanja je razvoj samozbijajućeg maltera koji se može koristiti za sanaciju oštećenog konstrukcijskog betona zamenom određenog udela običnog portland cementa metakaolinom i dodatkom staklenih vlakana.

Metode: Pripremljene su i ispitane mešavine sa različitim procentima metakaolina i staklenih vlakana. Sve mešavine su ispitane u svežem stanju radi procene fluidnosti i viskoznosti ispitivanjem rasprostiranja testom mini-slump i vremena proticanja kroz mini V-levak. Izmerena su fizička i mehanička svojstva svih mešavina, kao što su čvrstoća pri pritisku, čvrstoća pri savijanju i upijanje vode. Kako bi se proverile performanse pripremljenog samougrađujućeg maltera u konstrukcijskoj sanaciji, sprovedena su dva eksperimenta na oštećenoj armiranobetonskoj gredi i cilindričnim uzorcima.

Rezultati: Rezultati su pokazali da dodatak staklenih vlakana i metakaolina zahteva povećanje doze superplastifikatora kako bi se smanjio njihov negativan uticaj na fluidnost i viskoznost mešavina. Upotreba metakaolina do 10% kao zamene za cement povećala je čvrstoću pri pritisku od 11 MPa nakon 28 dana i 13 MPa nakon 56 dana. Slično ponašanje uočeno je kod mešavine koja je sadržala 0,4% staklenih vlakana i 10% metakaolina. Dodavanje staklenih vlakana u količinama od 0,2, 0,4 i 0,6% dovelo je do povećanja čvrstoće pri savijanju od 4, 6 i 15%. Upijanje vode smanjeno je za 29% kada je ugrađeno 15% metakaolina. Upotreba metakaolina poboljšava vezu između reparaturnog maltera i betonske podloge.

Zaključak: Na osnovu detaljne analize dobijenih rezultata, može se zaključiti da se metakaolin i staklena vlakna mogu koristiti za poboljšanje mehaničkih svojstava i smanjenje upijanja vode mešavina samougrađujućeg maltera. Mešavina koja je sadržala 0,4% staklenih vlakana i 10% metakaolina

pokazala je najbolje performanse i ocenjena je kao pogodnija za sanaciju oštećenih greda od samozbijajućeg betona.

Ključne reči: samozbijajući malter, metakaolin, staklena vlakna, čvrstoća, upijanje, reparacija.

Paper received on: 8 June 2025.
Manuscript corrections submitted on: 21 January 2026.
Paper accepted for publishing on: 18 February 2026.

© 2026 The Authors. Published by Vojnotehnički glasnik / Military Technical Courier (www.vtg.mod.gov.rs).This article is an open access article distributed under the terms and conditions of the Creative Commons Attribution license (http://creativecommons.org/licenses/by/4.0/rs/



Treatment and improvement of clay soils by adding waste rubber in arid regions

Mohammed Fatehi[a], *Benamar* Balegh[b], *Hamid* Sellaf[c], *Adda* Hadj Mostefa[d], *Mohamed Elamine* Dahamnie[e], *Lyacine* Bennacer[f]

[a] University of Ahmed Draia, Adrar, Department of Civil Engineering, Adrar, People's Democratic Republic of Algeria + Sustainable Development and Information Technology Laboratory, Adrar, People's Democratic Republic of Algeria
e-mail: fathi.moha@univ-adrar.edu.dz,
ORCID iD: https://orcid.org/0009-0003-7488-4566

[b] University of Ahmed Draia, Adrar, Department of Civil Engineering, Adrar, People's Democratic Republic of Algeria + Civil Engineering and Environmental Laboratory, Sidi Bel Abbes, People's Democratic Republic of Algeria
e-mail: ben.balegh@univ-adrar.edu.dz, **corresponding author**,
ORCID iD: https://orcid.org/0000-0002-8529-7063

[c] University of Saida, Department of Civil Engineering and Hydraulic, Saida, People's Democratic Republic of Algeria + Structures, Materials, and Hydraulics Engineering Laboratory (LISMH), Saida, People's Democratic Republic of Algeria
e-mail: hamid.sellaf@univ-saida.dz,
ORCID iD: https://orcid.org/0009-0006-3943-3024

[d] University of Relizane, Department of Civil Engineering and Public Works, Innovative Materials and Renewable Energies Laboratory, Relizane, People's Democratic Republic of Algeria
e-mail:addahadjmostefa@yahoo.fr,
ORCID iD: https://orcid.org/0009-0004-0086-9280

[e] University Oran 1 - Ahmed Ben Bella, Condensed Matter Science Laboratory(LSMC), Oran 1, People's Democratic Republic of Algeria
e-mail: dahamnimohamedelamine@gmail.com,
ORCID iD: https://orcid.org/0000-0001-5920-1198

[f] University of Ahmed Draia, Adrar, Department of Civil Engineering, Adrar, People's Democratic Republic of Algeria
e-mail: lyacine.bennacer@univ-adrar.edu.dz
ORCID iD: https://orcid.org/0000-0002-8547-6811

https://doi.org/10.5937/vojtehg74-62203

FIELD: materials, civil engineering
ARTICLE TYPE: original scientific paper

Abstract:

Introduction/purpose: This study examines the effect of waste rubber granules on the geotechnical properties of clay soils in arid regions. The

ACKNOWLEDGMENT: This work was supported by Sustainable Development and Information Technology Laboratory, Adrar, Algeria.

findings are of practical relevance to construction, foundation engineering, and environmental sustainability, as the incorporation of recycled rubber can enhance soil performance while mitigating ecological impacts.

Methods: To evaluate this potential, a series of laboratory experiments was conducted on clay samples blended with varying proportions of waste rubber granules (0%, 5%, 10%, 15%, 20%, and 25%). The mixture samples were prepared in arid area conditions. To ensure a more uniform distribution of particles in the mixtures, the selected samples with varying compositions were subjected to a hydraulic device.

Results: The results demonstrate a clear trend of decreasing liquid limit, swell potential, and swelling pressure as the rubber granules content increases. The cohesion improves with the incorporation of rubber granules. The stress–strain curves obtained from unconfined compressive strength (UCS) tests indicated that the addition of rubber granules enhanced the UCS of the soil.

Conclusion: These results emphasize the positive impact of waste rubber granules in enhancing the mechanical properties of the specimens. The incorporation of rubber granules significantly alters the physical structure of clay soil and helps mitigate both swelling potential and compaction. The pressure, recompression indices, and unconfined compressive strength (UCS) of the samples rise proportionally with the increase in rubber content, contrary to the fact that cohesion decreases as the proportion of waste tire rubber increases.

Key words: clay, waste rubber, swelling behavior, compressibility, compressive strength, arid region.

Introduction

In Algeria, arid zones account for almost 95% of the national territory, with around 80% classified as hyper-arid (Halitim, 1988). Many regions have reported problems associated with soil swelling, prompting extensive research on this phenomenon (Hadji et al., 2014). Several stabilization techniques have been investigated and applied, leading to a notable reduction in the swelling potential of problematic soils. The swelling–shrinkage phenomenon generally occurs in arid regions, where extended droughts are interrupted by short periods of rainfall, and it is also prevalent in Mediterranean climates.

In most cases, buildings cannot withstand these soil movements without sustaining damage, leading to the formation of cracks that may reach several centimeters in width, distorting doors and windows, detaching adjacent buildings from each other, and even breaking buried pipes. These disorders can also affect exterior landscaping (Xu et al., 2022).

Additionally, used tyres are inconvenient and harmful. By size, age, wear, and face shape, they comprise a diverse population. The primary materials of the waste tires are steel, silicon, carbon dioxide, and synthetic rubber. Every year, Algeria produces more than 26,000 tons of trash tires (Trouzine et al., 2012). Landfills are the places where used tires can be disposed of. In the field of civil engineering, various methods exist for recycling tires for use as decorative features and retaining walls (Sellaf et al., 2018; Hajoui et al., 2024; Raj et al., 2024; Shukla et al., 2024).

Balegh et al. (2024) investigated the mixing of two types of tire shavings with compressive soil. Their findings showed that the fluidity limit, swelling time, and swelling potential gradually decreased as the proportion of rubber particles in the samples increased. This reduction is particularly notable in soils with medium swelling potential, as the high compressibility of rubber particles leads to a marked increase in both compaction and decompression indices with rising rubber particle content. Moreover, investigating the effect of waste rubber on geotechnical and mechanical performance of clay can play a significant role in geotechnical projects (Akbarimehr et al., 2021).

This research focused on the effect of rubber granules on the behavior of clay soil in the regions. It proposes a method for improving these local materials, including clay soil, by adding rubber granules for use in building projects. In this study, Atterberg limit, swelling consolidation, load discharge, Compression and recompression index, direct shear, and unconfined compression strength tests were combined to investigate the behavior of clay soils mixed with waste rubber granules.

Experimental study

The soil and rubber granules

The physical characteristics of a clay soil from the desert area of the south-western Algerian province of Adrar were examined. In accordance with AFNOR-approved standard procedures, this soil underwent several laboratory tests to ascertain its physical characteristics (NF P 94-068; NF P 94-057; NF 94-056; NF P 94-054; and NF P 94-051). The clay soil utilized in the experiment is depicted in Figure 1.

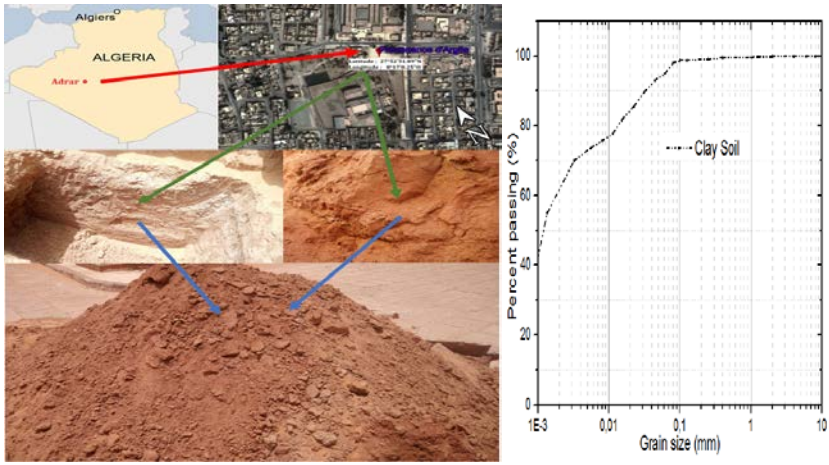


Figure 1 – Grainsize distributions for clay soil

Table 1 summarizes the geotechnical properties of the clay soil, providing a detailed description of its main characteristics. The soil is distinguished by a relatively high liquid limit (40%) and a plasticity index of 20%, with a specific gravity (Gs) of 2.45. Based on the Unified Soil Classification System (USCS), the soil is categorized as high-plasticity clay (CH). Additionally, the chemical composition of the clay was determined using wavelength-dispersive X-ray spectroscopy, in accordance with the NF EN 1744-1 standard, and the results are presented in Table 2.

Table 1 – Properties of the clay soil

Properties	Properties	Units	Clay soil
Consistency limits : NF: 94051	Liquid limit,	[%]	40
	Plastic limit,	[%]	20
	Plasticity index,	[%]	20
Specific weight NF: P 94-054	Specific weight		2.45
Grains sizes analysis NF: P 94-057	Sand,	[%]	10
	Silt,	[%]	31.33
	Clay,	[%]	58.67
	Maximum dry density	g/cm^3	1.92
Compaction NF P 94-093	Volume of blue VB	(cm^3)	20.5
	Specific surface SST	(m^2/g)	430.5

Table 2 – Chemical composition of clay

Component	Clay
SiO2 ,[%]	60.65
Al2O3 ,[%]	19.35
Fe2O3 ,[%]	0.95
CaO ,[%]	5.05
MgO ,[%]	0.30
NaOH ,[%]	0.30
Cl ,[%]	1.40
SiO3 ,[%]	1.5
P.F2 ,[%]	9.5

Rubber fibers can be obtained from used tires through the process of grinding the rubber with a friction machine. Then the rubber crumbs resulting from the process are collected and sifted through a two-mm sieve. Tire rubber is composed of a complex mixture of elastomers, mainly styrene-butadiene, polyisoprene, and polybutadiene. In addition to these polymers, tires contain several key additives, including stearic acid (1.2%), zinc oxide (1.9%), and extension oil (1.9%), as well as a significant proportion of carbon black (31.0%) (Balegh et al., 2023; Sellaf et al., 2022). In Figure 2, a rubber granules sample from a used tire is illustrated.



Figure 2 – Clay soil and rubber granules

Mixture design

Preparation of clay soil-rubber content mixtures

Because temperature can influence the properties of rubber, the water content of the samples was measured after they were dried at 35 ± 5 °C. Based on relevant studies on rubber-reinforced clays, the proportions of rubber commonly investigated are 1%, 2%, 3%, 4%, and 5% of the total weight of the reinforced samples (Akbulut et al., 2007). In all the referenced studies, fibres and either lime or cement were mixed with soils. Bekhiti et al. (2020) investigated mixtures made with dune sand, in which rubber powder and lime were used as partial replacements. To examine the effect of these additives, rubber content was incorporated at proportions ranging from 8% to 20% in increments of 4%, while lime was added at levels between 2% and 5% in increments of 1%. All percentages were calculated relative to the dry weight of the mixture. Since the fibers tended to clump together, considerable effort and time were required to achieve a uniform distribution within the mixtures.

The rubber mixture, composed of 0, 5, 10, 15, 20, and 25% rubber granules of the sample weight, was prepared after the clay and arid area samples have been prepared and oven-dried at 105 degrees Celsius.

To ensure a more uniform distribution of particles in the mixtures, selected samples with varying compositions were subjected to a hydraulic device that applied an additional load of approximately 1 kPa. The samples were then covered with plastic sheets to reduce water loss.

Experimental results and discussion

Consistency limits

Atterberg limit tests were carried out in accordance with the AFNOR NF P 94-051 standard to determine the consistency limits of the clay soils and their mixtures.

Liquid limit

Figure 3 presents the influence of rubber content on the consistency limits of clay and its mixtures. The results indicate a steady decline in the liquid limit as the proportion of rubber increases. However, the rate of reduction remains relatively consistent across all mixtures, varying between 3% and 5%.

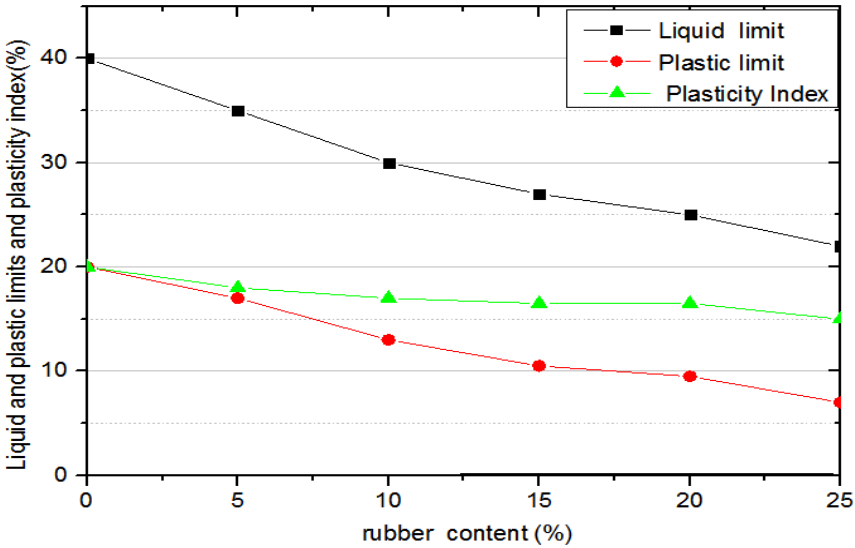


Figure 3 – Effect of rubber content on the consistency limits of clay soil

Plastic limit

For clay soils, the plasticity limit of samples incorporating 5% rubber granules shows an initial decrease, followed by a gradual increase, with only minor reductions ranging from 1% to 2%. The variations observed in the consistency limits of these mixtures can be explained by factors such as the type of mixture (Bell, 1993), cation exchange capacity, and the relative proportion of clay minerals present (Schmitz et al., 2004). Notably, Cetin et al. (2006) found that in clay soils with superficial cohesion, the plasticity limit initially remains nearly constant, then decreases slightly, before stabilizing once more. These trends align with the behavior typically observed in fine-grained cohesive soils of medium plasticity (Cetin et al., 2006).

Swell-consolidation tests

Consolidation and swelling tests were performed on all compacted samples in accordance with the AFNOR XP 94-91 standard. The composite specimens, prepared following the specified procedure, were evaluated using a standard oedometer. The initial void ratio (E) differed from one sample to another. Each specimen was assembled in five layers, each 4 mm thick, and carefully compacted within the oedometer cell.

For the second sample, the additional cost was set at 0.2 times lower than that of the first sample. After reaching the final height (ΔH), the specimen was subjected to further vertical loading until the initial void ratio (e) was restored. The swelling potential (S%) and swelling pressure (Ps) were then determined for both the natural soil and its mixtures. The swelling potential is defined as the ratio of the increase in sample thickness during immersion (ΔH) to its original thickness (H).

Swell potential

Figure 4 illustrates the evolution of swelling potential (S%) over time for clay soil samples stabilized with varying proportions of waste rubber granules (0, 5, 10, 15, 20, and 25% by weight). The results indicate that untreated clay soil reaches a swelling potential of 4.25% after 26 days, whereas soil reinforced with 5% rubber exhibits a swelling potential of 4.05% after 28 days. For the reinforced samples, the ultimate swelling potential decreases progressively with increasing rubber content, with stabilization occurring over a similar period for the 5% mixture and within shorter durations for mixtures containing 10%, 15%, and 25% rubber.

All samples were prepared with a water content of 20%, while the rubber itself is capable of absorbing up to 4% of its weight. Consequently, the initial water-to-clay ratios were approximately 0.12, 0.25, 0.37, 0.50, and 0.62 for mixtures containing 0%, 5%, 10%, 15%, and 25% scrap tire rubber, respectively. These variations in water-to-clay ratio may explain the reduced time required to reach maximum heave.

Swelling pressure

Figures 4 and 5 present the swelling pressure values of the studied specimens. The swelling pressure (ps) decreases with increasing waste rubber granules content. For soil A, the swelling pressure of the untreated soil was 75 kPa. For the composite samples containing 10%, 15%, 20%, and 25% rubber, the values decreased to 71 kPa, 65 kPa, 48 kPa, and 38 kPa, respectively.

Several researchers, including Du et al. (2020), Hu et al. (2019), and Odriozola and Aguilar (2005), have concluded that the physicochemical nature of expansive soils is highly complex, controlling the swelling process, swelling behavior, and soil-water interaction mechanisms.

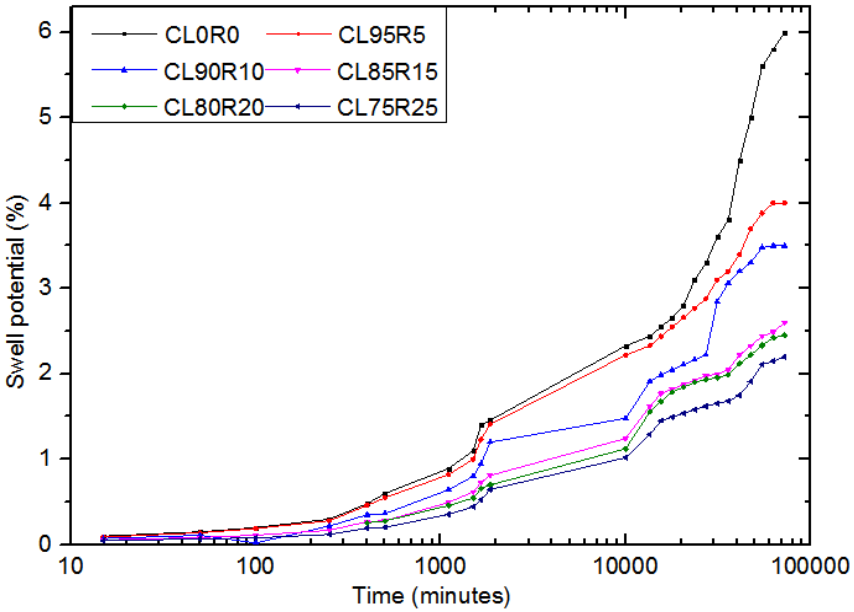


Figure 4 – Effect of the rubber content on the swell potential of clay soil

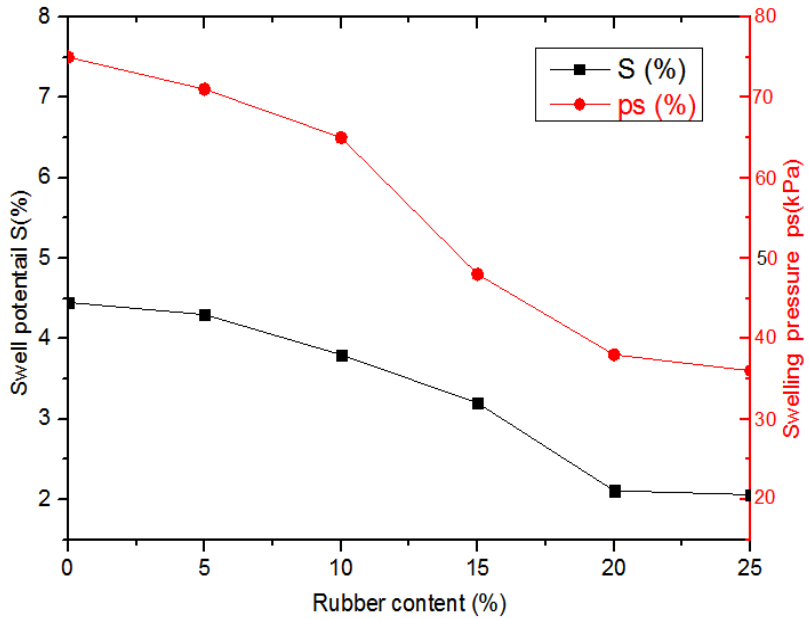


Figure 5 – Effect of the rubber content on swell potential and swelling pressure of clay soil

Loading–unloading tests

The mechanical behavior of clay soils was assessed by analyzing the compression index (Cc) and the recompression index (Cr) for mixtures containing different proportions of waste rubber granules, in accordance with the AFNOR XP P 94-090-1 standard.

Compression index

The pressure coefficient "Cc" is the slope of the linear portion of the pressure void ratio curve. Figure 6 shows the difference in compressive modulus as a function of the rubber content.

The minimum value of the coefficient of compression "Cc" varies from 0.22 for the sample clay soil composed of 0% rubber content, in contrast to the maximum value of 0.44 for the sample clay soil composed of 25% rubber content. The values of the compression coefficient "Cc" of the samples increase with the increase in the rubber content from 20 to 35%, as this gave results for coefficients of "Cc" ranging from 0.24 to 0.31, 0.38, 0.42 to 0.44.

Recompression index

The recompression index (swelling) is the indicator resulting from the release of loads or the removal of pressure. It is a measure used to study the compression and recompression of soils, particularly those with exceptionally high compressibility. In this study, we refer to it as the Cr factor.

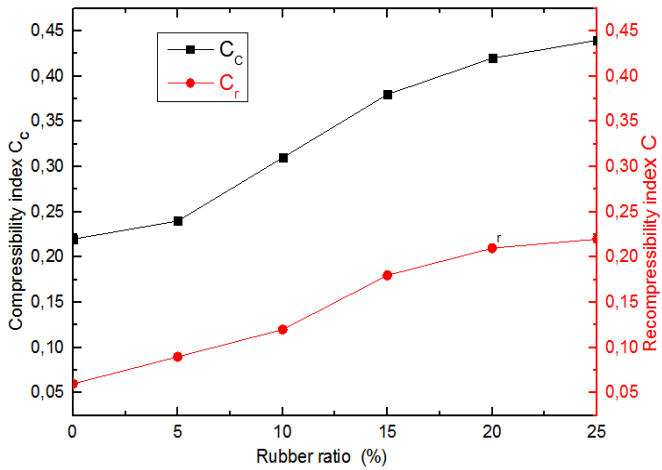


Figure 6 – Effect of the rubber content on compression and recompression indices of clay soil

The curves shown in Figure 6 illustrate the relationship between the Cr factor of compression and the rubber content. In general, Cr factor values are around five times lower than the Cc factor (Bardet, 1997). For all samples tested, Cr factor values are around 3 or 3.5 times lower than the Cc modulus values, and increase with increasing rubber content. Cr factor values range from 0.06 to 0.22. Cr factor values for samples supported with rubber increased from 30% to 42%. Previous studies have shown a relationship between the physical properties of expansive soil (liquid limit and initial void ratio) and the Cr recompression factor (Kordnaeij et al., 2015).

Direct Shear Tests (DST)

To assess the soil's shear properties, direct shear tests (DST) were conducted in the laboratory, including the determination of the point of elasticity and cohesion (C), as well as the soil's angle of internal friction (Ø). These properties were examined under various soil humidity and dry bulk density conditions, in accordance with French standard NF P 94-071-1.

All soil samples containing varying proportions of rubber were subjected to these tests. The specimens were prepared in accordance with the procedure outlined in paragraph two to ensure homogeneous mixing. The shear test results are illustrated in Figures 7 and 8.

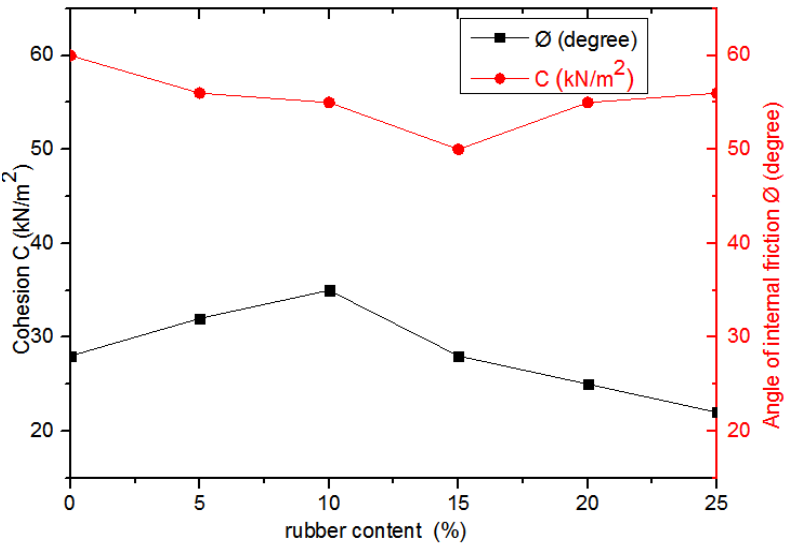


Figure 7 – Effect of rubber content on cohesion and angle of internal friction of the clay soil

The data show that cohesion improves with the incorporation of rubber granules, reaching maximum value in samples containing 10% rubber with 90% clay, after which it decreased as the rubber content increased. This indicates an optimal mixture composition of the mixture (90% clay and 10% rubber). The influence of material shape on elastic modulus and shear strength is well documented. Due to the variable contact surface of rubber grains depending on the shape of the material, elastic modulus and shear strength, like other factors, are naturally influenced by shape. Similar observations regarding the influence of shape on the modulus of elasticity and shear strength have been reported in previous studies, notably by Islami et al. (2024) and Haq et al. (2024). The internal friction angle exhibits irregular variations depending on the amount of tire rubber granules (TRP) added.

These observations from Figure 7 indicate that the cohesion values and friction angle do not exhibit direct proportionality to the quantity of clay soil added to the mixtures. This lack of direct proportionality suggests that there is an anomaly or non-linear behavior in the relationship between rubber content and these shear properties.

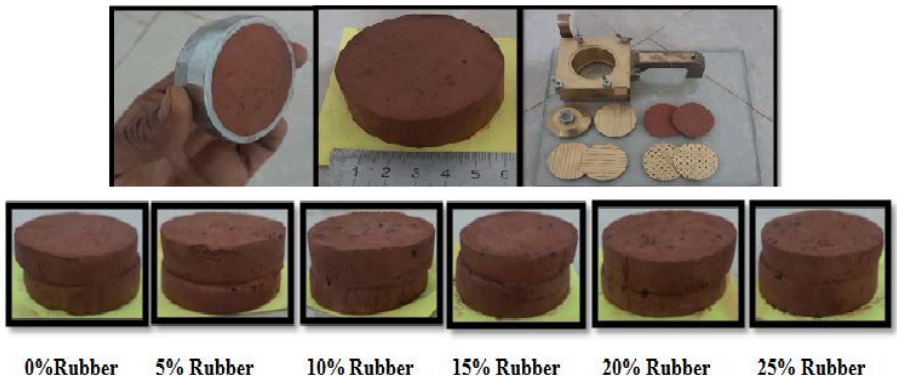


Figure 8 – Clay samples with different rubber content

Unconfined compression strength

Compressive strength tests were conducted in an open environment on soil samples containing varying amounts of rubber. Each test was performed on three cylindrical specimens with dimensions of 80 mm in diameter and 160 mm in height. After their initial weight was recorded, the specimens were placed in sealed bags and stored in the laboratory at a controlled temperature of 22 ± 2 °C for 28 days. They were then subjected to static loading in the OPM using a double press at a constant speed of 1.14 mm/min.

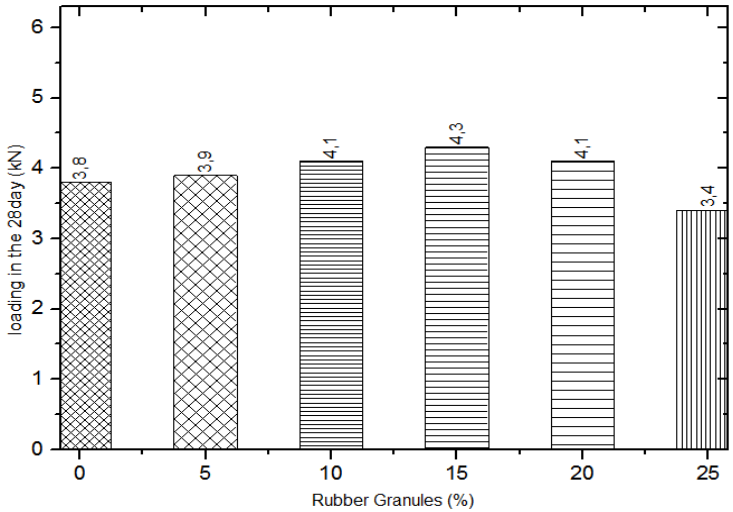


Figure 9 – Effect of rubber content on the UCS of mixtures

The results presented in Figures 9 and 10 illustrate the effect of rubber content on unconfined compressive strength (UCS) after 28 days. A distinct upward trend is observed, with UCS values increasing as the proportion of rubber granules rises. In particular, incorporating 5% to 15% rubber into clay soil samples enhances UCS by approximately 4% to 5%. These outcomes are in good agreement with the findings by Rouaiguia et al. (2020).

After adding 20 to 25 percent rubber content, the compressive strength index decreases by approximately 4 to 5 percent, which can be attributed to the inconsistent composition or mixture of the samples, as well as the lack of interaction and harmony between the rubber particles and the clay soil particles.

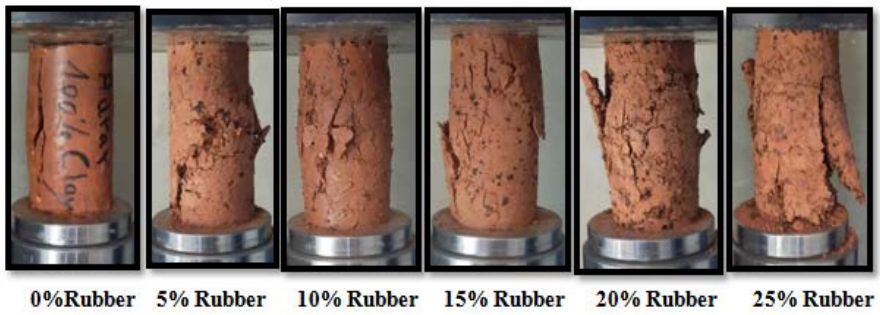


Figure 10 – Compression test on cylindrical specimens (50x100 mm^2) of mixtures of clay and rubber content after 28 days

Conclusion

In this work, we conducted an experimental study to stabilize clay soils by adding waste rubber granules in varying percentages. The primary objective of this research was to qualitatively assess the reduction of swelling potential in clay soils with distinct swelling characteristics through the addition of waste rubber granules, using a controlled laboratory experimental setup. Waste rubber granules are a non-biodegradable material; however, when blended with soil and buried, they become shielded from major degrading factors such as light and heat. Based on this study, the following conclusions and recommendations can be drawn:

- The incorporation of rubber granules significantly alters the physical structure of clay soil, as reflected in the notable changes observed in its liquid limit and plastic limit.
- Incorporating rubber granules into expansive clay samples helps mitigate both swelling potential and compaction.
- This behavior can be explained by the substitution of expansive clay with rubber granules, combined with the resistance of rubber particles to swelling when in contact with clay minerals.
- The pressure and recompression indices rise proportionally with the increase in rubber content.

Shear test results indicate that cohesion decreases as the proportion of waste tire rubber increases, whereas the internal friction angle shows a fluctuating trend.

- The unconfined compressive strength (UCS) of the samples increased progressively with higher rubber granules content.
- The deformation values also rose with increasing rubber granules content, which can be attributed to the non-homogeneous nature of the mixture.

References

AFNOR French Standardisation Association. 1991. NF P94-054: Soils: Reconnaissance and testing - Determination of the density of solid particles in soils - Water pycnometer method [online]. Available at: https://www.boutique.afnor.org/fr-fr/norme/nf-p94054/sols-reconnaissance-et-essais-determination-de-la-masse-volumique-des-parti/fa020767/11077 [Accessed: 16October 2025].

AFNOR French Standardisation Association. 1992. NF P94-057: Soils: Reconnaissance and testing - Soil particle size analysis - Sedimentation method [online]. Available at: https://www.boutique.afnor.org/fr-fr/norme/nf-p94057/sols-reconnaissance-et-essais-analyse-granulometrique-des-sols-methode-par-/fa020768/11074 [Accessed: 16 October 2025].

AFNOR French Standardisation Association. 1993. NF P94-051: Soils: Reconnaissance and testing - Determination of Atterberg limits - Cup liquidity limit - Roller plasticity limit [online]. Available at: https://www.boutique.afnor.org/fr-fr/norme/nf-p94051/sols-reconnaissance-et-essais-determination-des-limites-datterberg-limite-d/fa020765/11080 [Accessed: 16 October 2025].

AFNOR French Standardisation Association. 1995. XP P 94-091, Soils: investigations and testing, Odometer swelling test. Determination of deformations by loading several test specimens [online]. Available at: https://www.boutique.afnor.org/fr-fr/norme/xp-p94091/sols-reconnaissance-et-essais-essai-de-gonflement-a-loedometre-determinatio/fa042150/11053 [Accessed: 16 October 2025].

AFNOR French Standardisation Association. 1996. NF P94-056: Soils: investigations and testing - Particle size analysis - Dry sieving method after washing [online]. Available at: https://www.boutique.afnor.org/fr-fr/norme/nf-p94056/sols-reconnaissance-et-essais-analyse-granulometrique-methode-par-tamisage-/fa026936/11075 [Accessed: 16 October 2025].

AFNOR French Standardisation Association. 1997. XP P 94-090-1: Soils: investigations and tests, Oedometer test, Part 1: Compressibility test on quasi-saturated fine materials with stepwise loading [online]. Available at: https://www.boutique.afnor.org/fr-fr/norme/xp-p940901/sols-reconnaissance-et-essais-essai-oedometrique-partie-1-essai-de-compress/fa047092/11054 [Accessed: 16 October 2025].

AFNOR French Standardisation Association. 1998a. NF EN 1744-1: Tests to determine the chemical properties of aggregates - Part 1: Chemical analysis [online]. Available at: https://www.boutique.afnor.org/fr-fr/norme/nf-en-17441/essais-pour-determiner-les-proprietes-chimiques-des-granulats-partie-1-anal/fa039721/62422 [Accessed: 16 October 2025].

AFNOR French Standardisation Association. 1998b. NF P94-068: Soils: investigation and testing - Measurement of the methylene blue adsorption capacity of a soil or rock material - Determination of the methylene blue value of a soil or rock material by the spot test [online]. Available at:

https://www.boutique.afnor.org/fr-fr/norme/nf-p94068/sols-reconnaissance-et-essais-mesure-de-la-capacite-dadsorption-de-bleu-de-/fa043689/394 [Accessed: 16 October 2025].

Akbarimehr, D., Eslami, A., Aflaki, E. & al.2021. Investigating the effect of waste rubber in granular form on strength behavior of Tehran clay. *Arabian Journal of Geosciences*, 14(1831). Available at: https://doi.org/10.1007/s12517-021-08188-8

Akbulut, S., Arasan, S. & Kalkan, E. 2007. Modification of clayey soils using scrap tire rubber and synthetic fibres. *Applied Clay Science*, 38(1-2), pp.23–32.Available at: https://doi.org/10.1016/j.clay.2007.02.001.

Balegh, B. & Sellaf, H. 2022. Treatment of Leachate of Landfills Using Filters of Ceramic Waste and Scrap Rubber Waste. *Water, Air, & Soil Pollution,*233(526). Available at: https://doi.org/10.1007/s11270-022-06004-x.

Balegh, B., Sellaf, H., Hadj Mostefa, A. & Mahmoudi, N. 2024. Evaluating the Impact of Rubber Particles on the Swelling Potential and Pressure of Tizi Soil in an Area Located in North Western Algeria. Jordan Journal of Earth & Environmental Sciences, 15(3), pp.208. Available at: https://jjees.hu.edu.jo/files/Vol15/No3/jjees_Vol_15_No_3_P8.Pdf

Bardet, J.P. 1997. *Experimental Soil Mechanics*. NJ, USA: Prentice Hall, Upper Saddle River. ISBN: 9780133749359.

Bekhiti, M., Ghrieb, A. & Rebih, Z. 2020. Valorisation of Dune Sand Treated with Lime and Scrap Tyre Rubber Powder as a Road Foundation Material. Journal of Materials and Engineering Structures “JMES”, 7(3), pp.487-500. Available at: https://revue.ummto.dz/index.php/JMES/article/view/2235/pdf

Bell, F. 1993. *Engineering treatment of soils*. London, UK:CRC Press. ISBN: 9780429176784.

Cetin, H., Fener, M. & Gunaydin, O. 2006. Geotechnical properties of tire-cohesive clayey soil mixtures as fill material. *Engineering Geology*, 88(1-2), pp.110 – 120. Available at: https://doi.org/10.1016/j.enggeo.2006.09.002.

Du, J.& al. 2020. Revealing expansion mechanism of cement-stabilized expansive soil with different interlayer cations through molecular dynamics simulations, *The Journal of Physical Chemistry C*, 124(27). Available at: https://doi.org/10.1021/acs.jpcc.0c03376.

Hajoui, G., Manssouri, I., Manssouri, T. & al. 2024. Characterization of rubber-clay composites as recycled waste lightweight construction materials. *Innovative Infrastructure Solutions*,9(304). Available at: https://doi.org/10.1007/s41062-024-01619-x.

Halitim, A.1988. Soils of the arid regions of Algeria.PhDThesis. Algeria: OPU. Algies.

Hadji, R., Limani, Y., Boumazbeur, A., Demdoum, A., Zighmi, K., Zahri, F.& Chouabi, A. 2014. Climate change and its influence on shrinkage–swelling clays susceptibility in a semi-arid zone: a case study of Souk Ahras municipality, NE-Algeria. *Desalination and Water Treatment*, 52(10–12), pp. 2057-2072. Available at: https://doi.org/10.1080/19443994.2013.812989

Raj, R., Yadav, B. & Kumar, S. 2024. Utilization of recycled rubber crumbs and tile powder as additives to enhance clayey soil performance. *Discover Materials,*4(71). Available at: https://doi.org/10.1007/s43939-024-00146-x.

Rouaiguia, A. & El Aal, AKA. 2020. Enhancement of the Geotechnical Properties of Soils Using Marble and Lime Powders, Guelma City, Algeria. *Geotechnical and Geological Engineering*, 38, pp.5649–5665. Available at: https://doi.org/10.1007/s10706-020-01368-5.

Sellaf, H. &Balegh, B. 2023.An Experimental Study on the Effect of Rubber Waste Powder on the Strength Parameters of Tuff and Bentonite Soils Treated with Cement.*Engineering,Technology & Applied Science Research*, 13(2), pp.10322-10327. Available at: https://doi.org/10.48084/etasr.5580.

Sellaf, H., Balegh, B. &Bekhiti, M. 2022. The Assessment and Treatment of Dredged Sediments and Limestone Tuff Using Waste Ceramic with Low-Cement.*Advanced Engineering Forum*, 48, pp.45–58. Available at: https://doi.org/10.4028/p-2j4d93.

Sellaf, H., Balegh, B. & Hadj Mostefa, A. 2024. Exploring the Influence of Plastic Powder Incorporation on Geotechnical Properties of Expansive Soil Stabilized with Granite Powder for Building Applications. *International Journal of Engineering Research in Africa*, 68,pp.85-97. Available at: https://doi.org/10.4028/p-k5beQX.

Sellaf, H., Trouzine, H. &Asroun, A. 2018. Assessment of the performance of sediments and scrap rubber layers to filter the leachate of landfills, *International Journal of Engineering Research in Africa*,35, pp.162-174. Available at: https://doi.org/10.4028/www.scientific.net/JERA.35.162.

Schmitz, R.M., Schreoder, C. & Charlier, R. 2004.Chemo-mechanical interactions in clay: a correlation between clay mineralogy and Atterberg limits. *Applied Clay Science*, 26(1–4),pp.351–358.Available at: https://doi.org/10.1016/j.clay.2003.12.015.

Shukla, A., Kumar, R. & Jaiswal, A. 2024. Influence of Incorporating Waste Rubber Crumbs on Shear Parameters of Recycled and Natural Materials. *National Academy Science Letters*, 48, pp.475–478. Available at: https://doi.org/10.1007/s40009-024-01508-y.

Sudhakar, S., Duraisekaran, E. & DilliVignesh, G. 2021. Performance Evaluation of Quarry Dust Treated Expansive Clay for Road Foundations, *Iranian Journal of Science and Technology, Transactions of Civil Engineering*, 45,pp.2637–2649. Available at: https://doi.org/10.1007/s40996-021-00645-4.

Trouzine, H.,Bekhiti, M. &Asroun, A. 2012. Effects of Scrap Tire Rubber Fibre on Swelling Behaviour of Two Clayey Soils in Algeria. *geosynthetics international*,19(2),pp.124-132.Available at: https://doi.org/10.1680/gein.2012.19.2.124.

Türköz, M., Savaş, H. & Tasci, G. 2018. The effect of silica fume and lime on geotechnical properties of a clay soil showing both swelling and dispersive features, *Arabian Journal of Geosciences*, 11(735). Available at: https://doi.org/10.1007/s12517-018-4045-x.

Xu, J.J., Tang, C.S., Cheng, Q. *&al. 2022.* Investigation on desiccation cracking behavior of clayey soils with a perspective of fracture mechanics: a review. *Jjournal of Soils Sediments,22,*pp.859–888. Available at: https://doi.org/10.1007/s11368-021-03082-y

Zhao, L., Jiang, H. & Li, J. 2020. Pore-scale evaluation on the mechanism of water sensitivity for sandstones containing non-swelling clays, *Arabian Journal of Geosciences*, 13(54). Available at: https://doi.org/10.1007/s12517-019-5023-7.

Eslami, A., Akbarimehr,D., Rahai A., Karakouzian,M. 2024.Investigation of constitutive properties of high plasticity clay soils mixed with crushed rubber tire waste, Heliyon, 10(5), e26655, Available at: https://doi.org/10.1016/j.heliyon.2024.e26655

Haq,M., Khan, MA., Ali, S., Ali, K., Yusuf,M., Kamyab, H., Irshad,K.2024. Enhancing clayey soil performance with lime and waste rubber tyre powder: Mechanical, microstructural, and statistical analysis Environmental Research,256(1), 119217, Available at: https://doi.org/10.1016/j.envres.2024.119217

Tretiranje i poboljšavanje glinovitih tla dodavanjem otpadne gume u sušnim područjima

Mohammed Fatehi[a], *Benamar* Balegh[b], **autor za prepisku**, *Hamid* Sellaf[c], *Adda* Hadj Mostefa[d], *Mohamed Elamine* Dahamnie[e], *Lyacine* Bennacer[f]

[a] University of Ahmed Draia, Adrar, Department of Civil Engineering, Adrar, People's Democratic Republic of Algeria +
Sustainable Development and Information Technology Laboratory, Adrar, People's Democratic Republic of Algeria

[b] University of Ahmed Draia, Adrar, Department of Civil Engineering, Adrar, People's Democratic Republic of Algeria +
Civil Engineering and Environmental Laboratory, Sidi Bel Abbes, People's Democratic Republic of Algeria

[c] University of Saida, Department of Civil Engineering and Hydraulic, Saida, People's Democratic Republic of Algeria +
Structures, Materials, and Hydraulics Engineering Laboratory (LISMH), Saida, People's Democratic Republic of Algeria

[d] University of Relizane, Department of Civil Engineering and Public Works, Innovative Materials and Renewable Energies Laboratory, Relizane, People's Democratic Republic of Algeria

[e] University Oran 1 - Ahmed Ben Bella, Condensed Matter Science Laboratory(LSMC), Oran 1, People's Democratic Republic of Algeria,

[f] University of Ahmed Draia, Adrar, Department of Civil Engineering, Adrar, People's Democratic Republic of Algeria

OBLAST: materijali, građevinarstvo
KATEGORIJA (TIP) ČLANKA: originalni naučni rad

Sažetak:

Uvod/cilj: Ovaj rad ispituje uticaj otpadnih gumenih granula na geotehnička svojstva glinovitog tla u sušnim područjima. Rezultati su od praktičnog značaja za građevinarstvo, geotehničko inženjerstvo i održivost životne sredine, budući da dodavanje reciklirane gume može poboljšati svojstva zemljišta i istovremeno ublažiti uticaj na životnu sredinu.

Metode: U cilju procene ovog potencijala sproveden je niz laboratorijskih ispitivanja na uzorcima gline sa različitim udelima otpadnih gumenih granula (0%, 5%, 10%, 15%, 20% i 25%). Mešani uzorci pripremljeni su u uslovima sušnog područja. Kako bi čestice u smešama bile ravnomernije raspoređene, odabrani uzorci različitog sastava podvrgnuti su delovanju hidrauličkog uređaja.

Rezultati: Rezultati pokazuju jasan trend smanjenja granice tečenja, potencijala bubrenja i pritiska bubrenja sa povećanjem sadržaja gumenih granula. Kohezija se povećava dodatkom gumenih granula. Krive napon–deformacija dobijene ispitivanjima jednoaksijalne čvrstoće pri pritisku pokazale su da dodavanje gumenih granula povećava jednoaksijalnu čvrstoću tla pri pritisku.

Zaključak: Ovi rezultati naglašavaju pozitivan uticaj otpadnih gumenih granula na poboljšanje mehaničkih svojstava uzoraka. Ugradnja gumenih granula značajno menja fizičku strukturu glinovitog zemljišta i doprinosi smanjenju potencijala bubrenja i zbijanja. Pritisak, indeksi rekompresije i jednoaksijalna čvrstoća pri pritisku uzoraka povećavaju se proporcionalno sa povećanjem sadržaja gume, nasuprot činjenici da se kohezija smanjuje povećavanjem udela otpadne gume iz pneumatika.

Ključne reči: glina, otpadna guma, ponašanje pri bubrenju, stišljivost, čvrstoća pri pritisku, sušno područje.

Paper received on: 16 October 2025.
Manuscript corrections submitted on: 25 November 2025.
Paper accepted for publishing on: 23 January 2026.

© 2026 The Authors. Published by Vojnotehnički glasnik / Military Technical Courier (www.vtg.mod.gov.rs). This article is an open access article distributed under the terms and conditions of the Creative Commons Attribution license (http://creativecommons.org/licenses/by/4.0/rs/).

Properties of modified bitumen based on SBS-polymers of various topologies

Dmitrii Y. Nebratenko[a], *Linfan* Wang[b]

[a] Russian University of Transport, Institute of Roads, Construction and Structures, Department of Highways, Airfields, Base and Foundations + D.I. Mendeleev Russian University of Chemical Technology, Department of Chemistry and Technology of High Molecular Weight Compounds Moscow, Russian Federation
e-mail: nebratenko@mail.ru, **corresponding author**,
ORCID iD: https://orcid.org/0000-0002-3607-8876

[b] Bauman Moscow State Technical University, Moscow, Russian Federation
e-mail: 1602978339@qq.com,
ORCID iD: https://orcid.org/0009-0007-8423-8428

https://doi.org/10.5937/vojtehg74-62332

FIELD: materials and chemical technology
ARTICLE TYPE: original scientific paper

Abstract:

Introduction/purpose: It is obvious that the use of traditional petroleum road bitumen (residual or semi-blown) is unable to provide the required interval between repairs of road surfaces. Therefore, the use of modified bitumen, called polymer bitumen binders (PmB), is increasingly being envisaged in design solutions. The fundamental difference between ordinary bitumen and PmB is that the latter contains polymers of a specific nature, styrene–butadiene thermoelastoplasts (SBS polymers), which create an elastic spatial mesh inside the binder, providing the binders with low-temperature crack resistance and increased elastic recovery. At the same time, the process of using such binders and polymer asphalt concrete mixtures based on them does not undergo fundamental technological changes.

Methods: Two types of bitumen were used as binders: semi-blown petroleum road bitumen BND 50/70 and polymer-modified binder PmB 60. Various polymer modifiers were introduced into their composition: thermoelastoplast class polymers consisting of styrene and butadiene monomers. A feature of these polymers is their different spatial structure, and topology, while maintaining the styrene butadiene 30/70 ratio. The studies were carried out under standard modes and temperatures, specified by the requirements of the national standard GOST R 52056-2003 «Polymer-bitumen road binders based on styrene-butadiene-styrene block copolymers. Technical specifications».

Results: The replacement of the type of road binder used from viscous bitumen (BND) to viscoelastic binder (PmB) is a factor that undoubtedly improves the operational parameters of the pavement, including, in

particular, resistance to permanent viscoplastic deformation (rutting) and critical low-temperature stresses (formation of temperature cracks).

Conclusion: The use of linear grades of SBS polymers, including grades produced in Russia (primarily with 1.2-addition in the side polymer chain), is advisable when correcting the properties of viscous petroleum road bitumen. For bitumen-polymer compositions based on other bitumen and bitumen-containing petroleum products, when the required polymer content which exceeds the standards for road binders, radial grades with a branched structure of the main polymer chain are more effective.

Key words: petroleum road bitumen, polymer-modified bitumen binders (PmB), styrene-butadiene thermoelastoplast of various topologies.

Introduction

The general characteristics and behaviors of asphalt concrete pavements during destruction are largely explained by the behavior of the bitumen binder used in the production of asphalt mixtures. Alternating transport loads and cyclical temperature fluctuations of asphalt concrete pavements lead to the appearance of mixed tensile and shear deformations in them (Kalgin et al., 2014; Bratchun et al., 2018). At subzero temperatures, traditional road bitumen behaves mainly as a low-plastic and even brittle phase. At elevated temperatures, ordinary bitumen is unable to provide the required level of shear stability of road surfaces and to counteract the occurrence of both rutting and plastic deformation (Zhevanov et al., 2023; Shepitko et al. 2018; Kretov et al. 2008). At the same time, the continuous aging process of organic binders can significantly affect the overall strength and bearing capacity of road coverings and asphalt concrete mixtures. Therefore, various options for regulating both the initial technical properties of binders and their operational characteristics are often considered in road materials science (Tyukilina et al., 2008; Kiselev et al., 2005, Piskunov et al.; 2021).

One of the most common methods of polymer modification of bitumen is the use of synthetic high-molecular compounds. Polymers can provide bitumen with such important qualities as resistance to fracture (elasticity) at low temperatures, elasticity at high temperatures, longer fatigue life and increased moisture resistance (Nebratenko et al., 2022).

At the same time, it is generally recognized that SBS polymers have a sufficiently high degree of compatibility with oxidized bitumen, and also give binders increased tensile strength. They have the ability to increase the flexibility and elasticity of bitumen binders and ensure the efficient operation of polymer asphalt concrete at low temperatures (Rudensky et al., 2009; Gokhman, 2017).

The polymer blocks that make up the SBS copolymer behave differently when placed in bitumen at temperatures above 100-120°C. However, it is precisely this difference that ensures such an effective modification of the properties of a typical bitumen binder.

Polystyrene agglomerates consisting of polystyrene blocks of different polymer macromolecules and being the physical nodes of the thermoplastic mesh, when heated to temperature above 100°C, first turn into a viscous-plastic, and then into a viscous state. The polymer agglomerates decrease, and when mixed in a dispersion medium, this favors a uniform distribution of the thermoelastic components throughout the volume of the bitumen binder.

At the same time, the polybutadiene chains of SBS polymers swell, absorbing the maltene components of bitumen, and, as a result of Brownian thermal motion, repeatedly overlap with each other and with the spatial structures of asphaltenes, providing a physical mesh of meshes. This, subsequently, prevents the uncontrolled runoff of the binder from the surface of stone materials and helps to increase the range of transportation of polymer asphalt concrete mixtures.

After lowering the temperature of the bitumen polymer system under consideration to values close to the point of curing (yield point) of polystyrene, solid polystyrene domains are formed in the system again. However, this time, their location in the polymer grid may not coincide with the previous location, and the number of polybutadiene chains captured by them. The latter, due to their large length, explained by the significant molecular weight of polybutadiene units, which exceeds the same indicator of polystyrene blocks by more than 3 times, are able to carry several polystyrene formations of various sizes. The number and size of polystyrene agglomerates and their location in the volume of bitumen binder are determined, among other things, by the radial or linear structure of styrene butadiene thermoelastoplast, and so far, have not been studied in detail.

Correction of the composition and structure of road bitumen when mixed with SBS polymers improves their elastic-strength properties. Their softening temperature increases, which has a positive effect under the operating conditions of polymer asphalt concrete at elevated temperatures. A decrease in the penetration of polymer-containing compositions and an increase in viscosity over the operating temperature range slightly change the conditions of their processing; however, this can be adjusted by varying the component composition (dilution/dilution) of the initial bitumen binder. The implementation of this approach is possible by introducing plasticizers or softeners into the binder (which are not true

solvents for SBS polymers), since a specific feature of styrene-butadiene thermoelastoplast is the presence of two peak values of the solubility parameter characterizing polystyrene and polybutadiene blocks of the polymer chain (this is confirmed by the effectiveness of the use of industrial oil, consisting of a mixture of two and more diverse standard base oil of petroleum origin, in the composition of PmB). These changes in binder parameters significantly improve the performance properties of polymer asphalt concrete mixtures and polymer asphalt concrete based on them.

The traditional amount of styrene butadiene thermoelastoplast (SBS polymers) used to modify bitumen binders ranges from 3 to 5%, and even for cast asphalt concrete it does not exceed 8-10%. When mixed with bitumen, the SBS polymers form various structures and phase systems depending on the quantitative content and structure of SBS polymers, as well as on the group composition of the initial binder (Urcheva et al., 2013).

Materials and methods

This study was conducted in order to further study the effect of the structure of the polymer modifier directly on the properties of bitumen binders. During the study, petroleum bitumen road viscous grades BND 50/70 were used as the initial bitumen binder, which meet the requirements of GOST 33133-2014 and were produced at one of the refineries in the Volga Federal District (Table 1).

Table 1 – Indicators of the initial bitumen binders

№	Technical parameters	Requirements of GOST 33133-2014 for the BND 50/70	Actual values for the brand BND 50/70
1	Penetration, 0.1 mm, at 25 ºC	51-70	63
2	Penetration, 0.1 mm, at ºC	3,5	6,8
3	Extensibility, cm, at 25 ºC	60	78
4	Extensibility, cm, at 0 ºC	3,5	4,3
5	Softening point (ring and ball), ºC	51	52
6	Fraass breaking point, ºC	– 16	– 22
7	Flash point, ºC	230	306
8	Change in the mass of the sample after aging, %	±0,6	0,5

It is known that styrene butadiene thermoelastoplasts of various types and structures are used in the modification of the vast majority of petroleum bitumen in Russia (in 98% of cases) and in most countries of the world (in 75% of cases) (Guidance Manual, 2024). In this study,

samples of commercial batches of styrene butadiene thermoelastoplast of Russian production with linear and radial structures were used as a modifier. The physical characteristics of the above grades of styrene butadiene thermoelastoplast are presented in Table 2.

Table 2 – Technical parameters of SBS polymers used in this study

№	Technical parameters	SBS L 30 01 K	DST L 30 01 (SR)	SBS R 30 00 A
1	Kinematic viscosity of 5.23% solution in toluene at 25ºC, cSt	24 ± 5	12 ± 5	20-30
2	Melt flow rate at 150°C	0-1	0-1	0-1
3	Conditional tensile strength, MPa	≥ 13	≥ 14,7	≥ 8
4	Tensile stress at 300 % elongation, MPa	≥ 2,5	≥ 2,7	≥ 2
5	Relative elongation, %	≥ 650	≥ 700	≥ 550
6	The contents of the 1.2 links, %	9-13	35 - 42	10-18
7	Shore A hardness, units	72±5	72±5	80±5
8	Melting point, ºC	≥ 200	≥ 200	≥ 210
9	Flash point, ºC	232	232	232

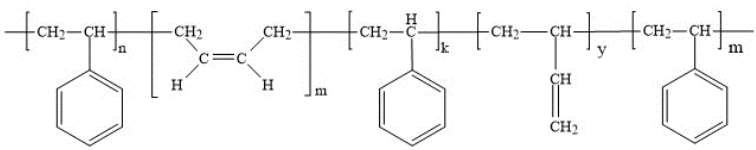
The thermoelastoplast of linear structure SBS L 30 01 K, industrially produced at “Voronezhsintezkauchuk JSC”, was chosen as the first polymer modifier (Figure 1, item 1). It is a product of the block copolymerization of styrene and butadiene in a solution of hydrocarbons in the presence of an organolithium catalyst. In its initial state, it is characterized by sufficiently high strength (about 13-15 MPa) and elongation (more than 750%). The product can contain up to 10 wt. % of di-block components in its composition.

The second modifier used was thermoelastoplast high-vinyl butadiene-styrene DST L 30 01 (SR) (Figure 1, items 2 and 3, cis- and trans-configurations). It is powdered with calcium stearate and stabilized with non-darkening antioxidants.

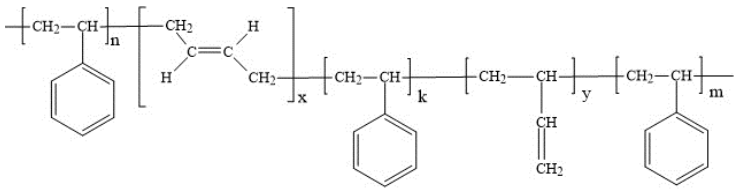
As the third alternative to the previous two, styrene butadiene thermoelastoplast of the radial structure, SBS R 30 00 A, was used. It is essentially a product of styrene and butadiene block polymerization in a hydrocarbon solution in the presence of an alkyl lithium catalyst. SBS R 30 00 A is dusted with amorphous silica (Figure 1, item 4).

$$\left\{ C_4H_9\left[-CH_2-\underset{\displaystyle C_6H_5}{\underset{|}{CH}}- \right]_n\left[-C_4H_6- \right]_m \right\}_2 Si\,(C_6H_5)_2$$

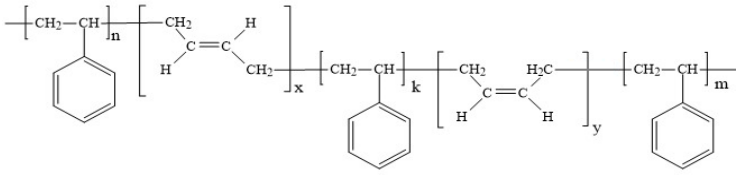
1)



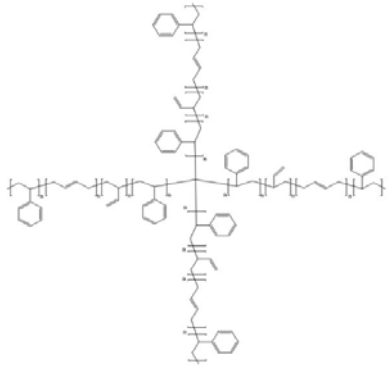
2)



3)



4)



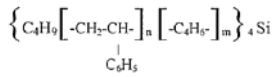


Figure 1 – The chemical formula / structure of macromolecules of styrene-butadiene thermoelastoplast: 1) linear SBS L 30-01 K; 2) cis- and high-vinyl DST L 30 01 (SR); 3) trans- and high-vinyl DST L 30 01 (SR); 4) radial SBS R 30-00A

Macromolecules of styrene-butadiene thermoelastoplast, composed of styrene and butadiene monomer units combined into rather long blocks,

have a specific structure and properties. According to the theory of the structure of dispersed systems, butadiene blocks are a dispersion medium (about 70 wt. %). They are quite long and have the necessary elasticity to ensure the mobility of the elements of the dispersed phase in it.

The latter (about 30 wt. %) are polystyrene domains chemically bonded to butadiene blocks. It is the block structure that explains the unique ability of SBS polymers to be evenly distributed over the entire volume of bitumen after melting at temperatures above 100°C (for example, in the production of PMB or the manufacture of asphalt mixtures). After lowering the temperature of the system under consideration below 100°C (for example, during compaction and subsequent operation of roads), polystyrene blocks again become centers of rigidity, blocking the free movement of polybutadiene chains. At the same time, the polybutadiene units retain segmental mobility, which ensures an elastic recovery of 85-95% for the PmB, significantly exceeding the requirement of ≥80% specified in GOST R 52056-2003 (the indicator is measured at 25°C). In this respect, traditional semi-blown bitumen is characterized only by plasticity, but it has absolutely no real elasticity in the presence of significant plasticity.

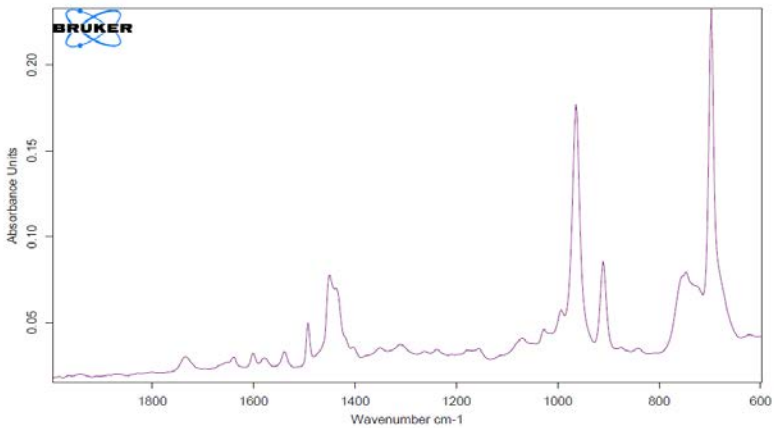


Figure 2 – IR spectrum of styrene butadiene thermoelastoplast

It is extremely difficult to distinguish brands of SBS polymers of different structures, but with the same molecular weight, based solely on the available physical and mechanical parameters. For identification, the IR spectrometry method is most often used, which makes it possible to determine the presence by absorption bands, the quantitative content of

certain structural and functional groups, and hence the compounds themselves, by absorption intensity.

In particular, the absorption of spectral bands at frequencies of 910 and 966 cm-1 makes it possible to detect an increase in the content of 1,2- or 1,4-vinyl groups in polybutadiene (fluctuations =C–H) (Rozhkov et al., 2024). Due to the greater mobility of the double-bonded group in the side chain, its more active interaction with bitumen components is possible, and in particular, with asphaltene agglomerates (which is typical for the brand DST L 30 01 (SR)). The typical IR spectrum of the SBS polymer is shown in Figure 2.

Due to the different aggregate state of the PmB components, it is necessary to use devices with a high shear force and an active cutting part when mixing. During this study, high-speed laboratory dispersers IKA ULTRATURRAX of the T18 and T25 digital brands were used, differing in the amount of torque on the rotor shaft. According to traditional technology, the initial bitumen in the heated state is first homogenized, and, if necessary, a plasticizer, usually of petroleum origin, is introduced into its composition. Then, with a low stirring intensity (about 300-500 rpm), polymer granules are portioned onto the bitumen surface. Over a short period of time, the solid granules are wetted and immersed in the binder volume. Further, during 15-20 minutes at high mixing intensity (about 3000-5000 revolutions per minute), the process of intensive mechanical grinding of agglomerates of SBS polymers located in bitumen occurs as they pass through the cutting unit of the dispersant. This leads to both an increase in the number of particles and an increase in their specific surface area, limiting the stage of physical interaction with the binder components. In this case, the crushed polymer particles are evenly distributed over the entire available volume of bitumen binder. This is important to ensure the formation, during the subsequent swelling of the polymer in the maltene phase of the bitumen binder, of a uniform interpenetrating elastomeric network of styrene-butadiene thermoelastoplast throughout the binder volume. The swelling process of SBS polymer macromolecules takes at least 3 hours, and its intensification is facilitated by mixing the system with a paddle mixer with a frequency of 300-500 revolutions per minute at temperatures of the order of 130-140°C. These temperatures ensure relatively low viscosity values of the bitumen binder, but do not cause its intense peroxidation or oxidation of SBS polymers by double bonds. This stage is called "aging" because during it the binder acquires a stable level of technical properties due to the physical modification of bitumen during the following physical processes: penetration of the plasticizer into the

space between the polymer macromolecules, as well as direct swelling of styrene-butadiene thermoelastoplast blocks in oils.

The quantitative indicators of the obtained mixed compositions were evaluated in accordance with the requirements of current national standards. In particular, extensibility is determined in accordance with the interstate standard GOST 33138-2014 Public roads. Petroleum road bitumen is viscous. A method for determining extensibility" in which a sample of the bitumen binder under test is stretched in a ductilometer at a constant speed of 5.00 ± 0.25 cm/min until a given elongation (at least 100 mm) or rupture is obtained at a temperature of 25 ± 0.5°C and/or 0 ± 0.5°C.

The elasticity of the SBS polymer-modified bitumen binder is determined immediately after testing the tensile strength of the samples, by estimating, after a given time, a decrease in the length of the halves of the ruptured polymer bitumen thread and calculating the elasticity index.

This simple and convenient standardized approach makes it possible to evaluate the effect of each type of polymer modifier on the ability to elastically restore the initial length of the binder sample and to evaluate the ability of the final asphalt concrete coating to prevent the formation of ruts, its fatigue crack resistance and a number of other performance indicators. The practical experience that most representatives of road materials science who deal with the polymer modification of bitumen binders already have today makes it possible to clearly indicate the absence (Figure 3, left) or presence (Figure 3, right) of elastomeric components in the composition of binders from the appearance of samples after testing on a ductilometer with a high degree of reliability.



Figure 3 – Physical manifestation of orientation effects during stretching of different types of binders (at 0°C): traditional bitumen (right), polymer bitumen binder (left)

Results and discussion

Summary data on the effect of the topology of SBS polymers on the physico-technical properties of polymer-bitumen binders based on SBS polymers of various compositions and structures are illustrated in Table 3. BND 50/70 was used as the starting bitumen; the role of the plasticizer was played by base oil SN-400 (a product of rectification of residual oil

rungs – raw materials for compounding during the manufacture of various grades of commercial industrial oil) in the amount of 5.3 wt. %.

Table 3 – Indicators of polymer-bitumen binders based on SBS polymers of various structures

№	Technical parameters	The actual values for PmB 60 based on		
		SBS L 30 01 K	DST L 30 01 (SR)	SBS R 30 00 A
1	Penetration, 0.1 mm, at 25^{0}C	65	66	67
2	Penetration, 0.1 mm, at 0^{0}C	28	31	26
3	Extensibility, cm, at 25^{0}C	70	70	98
4	Extensibility, cm, at 0^{0}C	4,0	4,0	4,8
5	Softening point (ring and ball), 0^{0}C	52	53	56
6	Fraass breaking point, 0^{0}C	– 22	– 23	– 20
7	Elasticity at 25^{0}C, %	93	95	88
8	Elasticity at 0^{0}C, %	25	35	20

A general analysis of the change in binder properties with the content of SBS polymer confirms that both linear and radial grades of SBS polymers affect the properties of bitumen. However, it was found that at low concentrations (up to 2.5-2.8%), the influence of linear grades is most noticeable, and for radial grades, the threshold values are concentrations of 3.5-4%. In the case of an increase in the content of SBS polymer in the binder to 8-10%, the effect of radial polymers is noticeably higher than that of linear polymers. This, in particular, explains the widespread use of radial grades for the modification of roofing bitumen, the content of SBS polymers in which, according to customer requirements, can exceed 12-15% (Lyusova et al., 2010; Akimov et al., 2018).

These effects are most pronounced in the case of modification of petroleum bitumen with the lowest initial penetration. Their rigid asphaltene structure is unable to provide recovery within any appreciable limits (Figure 4); however, with the introduction of even a small amount of linear SBS polymers, the mixed composition begins to show elasticity.

Using the residual amounts of low molecular weight components in BND 50/70 bitumen, SBS polymers swell and increase in volume, imparting elastic properties to the resulting mixed composition. In the event of a further increase in polymer concentration, two scenarios are possible. With the parallel introduction of petroleum maltene fractions with the polymer, it is possible to successfully continue swelling, increase the cross-link density of the resulting interpenetrating polymer network, and maintain the elastic-strength properties of the binder at the required level.

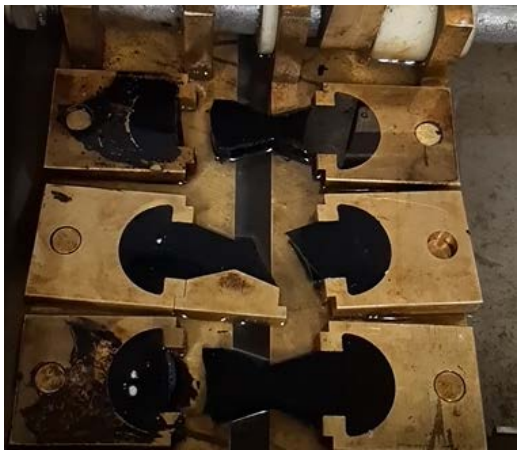


Figure 4 – Brittle fracture of BND 50/70 samples during tensile testing (at 0°C)

However, when exclusively dry SBS polymers enter the bitumen volume, the component composition of the binder is depleted due to a decrease in the content of mobile low-molecular-weight hydrocarbons in bitumen absorbed by the surface layers of polymer granules. Ultimately, this leads to embrittlement of asphalt concrete produced on the basis of such binders.

Conclusion

The active introduction of polymer-bitumen binders into the daily practice of the road construction industry requires a revision of the methods for assessing the presence of polymer modifiers (SBS polymers) in the binder in the required amount, available primarily in trivial field laboratory conditions.

The replacement of the type of binder used from viscous (BND) to viscoelastic (PmB) is a factor that certainly improves the operational parameters of the pavement, including, in particular, resistance to permanent viscoplastic deformation (rutting) and critical low-temperature stresses (formation of temperature cracks).

It has been shown that, regardless of the type of the initial binder, the first changes in quality characteristics are recorded already when the SBS-polymer content is up to 3.0 wt. %. Physically, this is most evident with a high degree of elongation of the sample and its subsequent elastic contraction.

The use of domestic linear grades of SBS-polymers, including fairly new grades, is advisable in the case of adjusting the properties of road

binders - semi–blown bitumen, petroleum road viscous. For bitumen-polymer compositions based on other types of bitumen and bitumen-containing petroleum products, in which the required polymer content exceeds the standards of road binders, radial grades with a branched structure of the main polymer chain behave more effectively.

The approach considered in this study to determining the presence of SBS-polymers in binders can certainly be used for an objective instrumental assessment of the composition of polymer-bitumen binders in the field, which is extremely important in the context of the transition to work with regionally oriented requirements for road binders.

References

Kalgin, Yu.I., Strokin A.S., Tyukov E.B. 2014. Promising technologies for the construction and repair of road surfaces: textbook. Manual. Voronezh GASU. *Voronezh*, 226. [online]. Available at: https://cchgeu.ru/upload/iblock/fbc/14j6qfkc5biceryc19u4uzw8vhfc1ne0/UP-Perspektivnye-tekhnologii.pdf [Accessed: 17 June 2026].

Bratchun, V.I., Bespalov V.L. 2018. On the expediency of complex modification of asphalt road concrete. *Construction and man-made safety*, 11(63), pp.47-55. [online]. Available at: https://www.google.com/url?sa=t&rct=j&q=&esrc=s&source=web&cd=&ved=2ahUKEwiCm4juq4yPAxVDExAIHSkgBQEQFnoECB0QAQ&url=https%3A%2F%2Fcyberleninka.ru%2Farticle%2Fn%2Fo-tselesoobraznosti-kompleksnoy-modifikatsii-dorozhnyh-asfaltobetonov.pdf&usg=AOvVaw0yDnghmsXUaNiWq4uXDxsk&opi=89978449 [Accessed: 17 June 2026].

Zhevanov V., Bratchun V., Postoenko V. 2023. Increasing the fatigue life of asphalt concrete by complex modification of their structure. *Proceeding of the Donbas National Academy of Civil Engineering and Architecture*, 4(162), pp.70-75. [online]. Available at: https://www.google.com/url?sa=t&rct=j&q=&esrc=s&source=web&cd=&cad=rja&uact=8&ved=2ahUKEwjH96bvrYyPAxXELBAIHV8sA3UQFnoECBsQAQ&url=https%3A%2F%2Fdonnasa.ru%2Fpublish_house%2Fjournals%2Fvestnik%2F2023%2F2023-4(162)%2Fst_13_zhevanov_bratchun_postoenko.pdf&usg=AOvVaw1-dnC4qwjJeZIQPxRv_o-T&opi=89978449 [Accessed: 17 June 2026].

Shepitko, T.V., Lutsky S.Y., Artyushenko I.A. 2018. Intensive technology for construction of a roadbed in the permafrost zone. *World of Transport and Transportation*, 16(1), pp.58–64. Available at: https://doi.org/10.30932/1992-3252-2018-16-1-6

Kretov V. A., Gladkikh A. S. 2008. Improving the durability of “semi-rigid” travel clothes. *Science and technology in the road industry,* 4, pp.30-32. [online]. Available at: https://lib.madi.ru/nitdo/ [Accessed: 17 June 2026].

Tyukilina, P.M., Gureev A.A. 2008. Patterns of influence of plasticizer composition on elasticity and cohesive strength of polymer-bitumen binders. *Oil refining and petrochemical industry*, 2, pp.12–16. Available at: https://www.elibrary.ru/item.asp?id=32613974 [Accessed: 17 June 2026].

Kiselev, V.P. 2005. Joint use of secondary products of the timber chemical industry with the material resources of other industries by components of organomineral mixtures. *Bulletin of Orenburg State University*. 10, pp.126-129. [online]. Available at: https://cyberleninka.ru/article/n/sovmestnoe-ispolzovanie-vtorichnyh-produktov-lesohimicheskoy-otrasli-s-materialnymi-resursami-drugih-proizvodstv-komponentami [Accessed: 17 June 2026].

Piskunov, I.V., Harpaev, A.V., Bashkirtseva, N.Yu., and Rozhkov, 2021. The main trends in the production and use of bitumen materials. Oil refining and petrochemistry. *Scientific and technical achievements and best practices*, 11, pp.3-16. [online]. Available at: https://www.npnh.ru/2021/11-2021/ [Accessed: 17 June 2026].

Nebratenko, D.Yu., Boksha M.Yu., Isakov A.M. Influence of SBS polymers of various structure on the properties of semi-blown bitumen binders. Roads and Bridges. 21. pp.5-16. (2022). Available at: https://doi.org/10.7409/rabdim.022.001

Rudensky, A.V., Kalgin Yu. I. 2009. Asphalt concrete road coverings on modified bitumen: textbook. stipend. *Voronezh*, 143 [online]. Available at: https://search.rsl.ru/ru/record/01004406011?ysclid=mecltn3czl648592488 [Accessed: 17 June 2026].

Gokhman L. M. 2017. Substantiation of regulatory requirements for polymer asphalt concrete according to GOST 9128-2013. *The herald of HADU.* 79, pp.22-27. [online]. Available at: https://cyberleninka.ru/article/n/obosnovanie-normativnyh-trebovaniy-k-polimerasfaltobetonu-po-gost-9128-2013. [Accessed: 17 June 2026].

Urcheva, Yu.A., Syroezhko A.M., Maidanova N.V., Vasiliev V.V. 2013. Choice of polymer for preparation, polymer-bitumen binder with improved quality indicators. *Izvestiya SPbGTI (TU),* 19(45), pp.12-16. [online]. Available at: https://cyberleninka.ru/article/n/vybor-polimera-dlya-prigotovleniya-polimerno-bitumnogo-vyazhuschego-s-uluchshennymi-pokazatelyami-kachestva. [Accessed: 17 June 2026].

Butadiene Product Stewardship Guidance Manual. 2024. American Chemistry Council. USA. 63 [online]. Available at: https://www.google.com/url?sa=t&rct=j&q=&esrc=s&source=web&cd=&cad=rja&uact=8&ved=2ahUKEwjH6ZqKv4yPAxXgDRAIHWpcDP4QFnoECBUQAQ&url=https%3A%2F%2Fwww.americanchemistry.com%2Fcontent%2Fdownload%2F5364%2Ffile%2FButadiene-Product-Stewardship-Guidance-Manual.pdf&usg=AOvVaw1tDou0K6-WdPnDKrm5Bbax&opi=89978449 [Accessed: 17 June 2026].

Rozhkov, I.M., Kharpaev A.V., Nebratenko D.Yu., Kretov V.A. 2024. The ABCD method for determining the low-temperature properties of ordinary and modified binders. *SibADI Bulletin.* 21. 2(96), pp.324-340. Available at: https://doi.org/10.26518/2071-7296-2024-21-2-324-340.

Lyusova L.R., Yevtushenko V.A., Starkova E.S., Igoshin Yu.G. 2010. Resin modification of adhesives based on styrene-butadiene thermoelastoplast. *Industrial production and use of elastomers*. 2, pp.24-26. [online]. Available at: https://www.elibrary.ru/query_results.aspn [Accessed: 17 June 2026].

Akimov S. F., Akimova E. Sh. 2018. Assessment of the technical and economic efficiency of the installation of soft roofing on a flat roof. *Economics of construction and environmental management,* 4 (69), pp.5-16. [online]. Available at: https://cyberleninka.ru/article/n/otsenka-tehniko-ekonomicheskoy-effektivnosti-ustroystva-myagkogo-krovelnogo-pokrytiya-na-ploskoy-kryshe [Accessed: 17 June 2026].

Svojstva modifikovanog bitumena na bazi SBS-polimera različitih topologija

Dmitrii Y. Nebratenko[a], **autor za prepisku**, *Linfan* Wang[b]

[a] Russian University of Transport, Institute of Roads, Construction and Structures, Department of Highways, Airfields, Base and Foundations + D.I. Mendeleev Russian University of Chemical Technology, Department of Chemistry and Technology of high molecular weight compounds Moscow, Russian Federation

[b] Bauman Moscow State Technical University, Moscow, Russian Federation

OBLAST: materijali i hemijske tehnologije
KATEGORIJA (TIP) ČLANKA: originalni naučni rad

Sažetak:

Uvod/cilj: Evidentno je da upotreba tradicionalnog naftnog putnog bitumena (rezidualnog ili poluduvačkog) ne može da obezbedi potreban interval između sanacija kolovoznih površina. Zbog toga se u projektnim rešenjima sve više predviđa upotreba modifikovanog bitumena, odnosno polimernih bitumenskih veziva. Osnovna razlika između običnog bitumena i polimernih bitumenskih veziva ogleda se u tome što polimerna bitumenska veziva sadrže polimere specifične prirode, stiren-butadien termoplastične elastomere (SBS-polimere), koji unutar veziva stvaraju elastičnu prostornu mrežu, čime pružaju otpornost na pojavu pukotina pri niskim temperaturama i povećanu elastičnu obnovu. Istovremeno, postupak primene ovih veziva i polimernih asfaltnih betonskih mešavina na njihovoj osnovi ne trpi suštinske tehnološke promene.

Metode: Dve vrste bitumena su korišćene kao veziva: poluduvački naftni putni bitumen BND 50/70 i polimerom modifikovano vezivo PmB 60. U njihov sastav dodati su različiti polimerni modifikatori: termoplastični elastomeri koji pripadaju klasi polimera sastavljenih od monomera stirena i butadiena. Ove polimere odlikuje različita prostorna struktura, odnosno topologija, uz zadržavanje odnosa stirena i butadiena 30/70. Ispitivanja su sprovedena u standardnim uslovima i na standardnim temperaturama

definisanim zahtevima nacionalnog standarda GOST R 52056-2003 „Polimer-bitumenska putna veziva na bazi blok-kopolimera stiren-butadien-stirena. Tehnički uslovi".

Rezultati: Zamena korišćenog putnog veziva, odnosno prelazak sa viskoznog bitumena na viskoelastično vezivo, predstavlja faktor koji nesumnjivo poboljšava eksploatacione karakteristike kolovozne konstrukcije, uključujući, pre svega, otpornost na trajne viskoplastične deformacije (kolotražine) i kritična naprezanja pri niskim temperaturama (nastanak temperaturnih pukotina).

Zaključak: Upotreba linearnih tipova SBS-polimera, uključujući i tipove proizvedene u Rusiji (pre svega one sa 1,2-pripojem u bočnom polimernom lancu), preporučljiva je pri korekciji svojstava viskoznog naftnog putnog bitumena. Kod bitumensko-polimernih sastava na bazi drugih vrsta bitumena i naftnih proizvoda koji sadrže bitumen, kada je potreban sadržaj polimera koji je veći od standardima propisanog sadržaja za putna veziva, efikasniji su radijalni tipovi sa razgranatom strukturom glavnog polimernog lanca.

Ključne reči: naftni putni bitumen, polimerom modifikovana bitumenska veziva (eng. PmB), stiren-butadien termoplastični elastomeri različitih topologija.

Paper received on: 22 October 2025.
Manuscript corrections submitted on: 11 November 2025.
Paper accepted for publishing on: 23 December 2025.

© 2026 The Authors. Published by Vojnotehnički glasnik / Military Technical Courier (www.vtg.mod.gov.rs). This article is an open access article distributed under the terms and conditions of the Creative Commons Attribution license (http://creativecommons.org/licenses/by/4.0/rs/).

Comparative analysis of the traditional and modern taper tap manufacturing processes

Dejan Bajić[a], *Slavica* Prvulović[b], *Eleonora* Desnica[c], *Mića* Đurđev[d], *Ljiljana* Radovanović[e], *Branislava* Radišić[f]

Univeristy of Novi Sad, "Mihajlo Pupin" Technical Faculty, Zrenjanin, Republic of Serbia

[a] e-mail: dejan.bajic@tfzr.rs, **corresponding author**,
ORCID ID: https://orcid.org/0000-0001-7435-9604

[b] e-mail: slavica.prvulovic@tfzr.rs,
ORCID ID: https://orcid.org/0000-0001-6353-7145

[c] e-mail: eleonora.desnica@tfzr.rs,
ORCID ID: https://orcid.org/0000-0003-2816-3584

[d] e-mail: mica.djurdjev@tfzr.rs,
ORCID ID: https://orcid.org/0000-0002-1825-2754

[e] e-mail: ljiljana.radovanovic@tfzr.rs,
ORCID ID: https://orcid.org/0000-0002-5234-4820

[f] e-mail: branislava.radisic@tfzr.rs,
ORCID ID: https://orcid.org/0009-0007-3664-2012

https://doi.org/10.5937/vojtehg74-60426

FIELD: mechanical engineering
ARTICLE TYPE: research paper

Abstract:

Introduction/purpose: This paper presents a comparative analysis of traditional and modern manufacturing processes used for producing a taper tap – a fishing tool commonly used during well workover operations. The goal of this research is to examine differences in production time and efficiency between traditional machining (conventional lathe and milling machine) and modern, CNC-based manufacturing, based on the hypothesis that modern techniques offer superior time efficiency.

Methods: The study involved the experimental manufacturing of a taper tap using both the traditional approach (conventional lathe and milling machine) and a CNC machine. Time was measured for all key stages, including production preparation (process sheet creation (traditional method) or 3D modeling and programming (modern method)), machine operating time, and active machining. Fusion 360 software was used for CAD/CAM modeling and CNC programming. Time was recorded using a stopwatch and machine-generated data.

Results: The results show that while the modern process required 37 minutes more for production preparation, it significantly reduced machine operating time by 41.5 minutes and active machining time by 1 hour and 19.3 minutes compared to the traditional method. In total, the CNC-based

approach is faster for the entire manufacturing process of a taper tap in a serial production scenario.

Conclusion: The research confirms that the modern manufacturing process provides clear advantages in terms of time efficiency. Despite the longer preparation time, its overall productivity in repetitive production justifies its implementation. Nevertheless, traditional methods retain relevance in cases requiring manual adjustments or rapid single interventions.

Key words: machining, traditional, modern, CNC, time-efficiency, petroleum industry, machining time.

Introduction

Today's advanced manufacturing conditions impose an accelerated work pace in the industry, making time optimization a crucial factor across all production sectors (Ghafoorpoor Yazdi et al., 2018). In practice, these are very complex requirements, involving the consideration of multiple factors and resulting in multiple local optimal solutions (Zhang, 2025). Integrating modern technologies into both the preparation for production the and manufacturing processes of a component is a key step toward achieving greater time efficiency, which enhances economic efficiency as well (Dunarea de Jos University of Galati, Industrial Engineering Department 800201, Romania et al., 2017; Subramanian et al., 2019; Tönissen et al., 2015). The goal is to maintain, or even improve, the high quality of the final product while optimizing production time through the use of advanced technologies (Puška and Stojanović, 2024; Simić et al., 2023).

This paper presents a detailed analysis of the time required for the complete preparation and manufacturing process of a taper tap (a tool that is commonly used during workover in the petroleum industry) using two approaches: the traditional method (on a conventional lathe and milling machine) and a CNC machine. Additionally, the paper examines the factors that may influence the duration of the production process, such as CNC programming complexity, the interaction between the machine and operators, the expertise and experience of programmers and operators, the need for manual interventions during the manufacturing process, and other related aspects.

This study also aims to provide insights from both technical and technological perspectives into the similarities and differences between traditional and modern manufacturing methods for the same component. Furthermore, it seeks to recommend the most efficient production process in terms of the optimal choice of methods, time, and quality of manufacturing.

Methodology

Research problem

The main problem addressed by this research is the divided opinions among experts regarding the manufacturing of individual components. These opinions are divided regarding the time required for production preparation and the time needed for the actual manufacturing of the component.

Research subject

The subject of this research is the comparison of traditional and modern manufacturing methods for a taper tap from the perspective of time efficiency.

Research objective

The objective of this research is to identify and quantify the differences in the time required to perform the same manufacturing process using traditional and modern methods.

Research task

The research aims to determine which of the two manufacturing processes gives better results in terms of time efficiency. Additionally, the task is to present the advantages and disadvantages of each process relative to the other.

Research hypothesis

Compared to the traditional method, the modern manufacturing process of a taper tap provides an advantage in terms of time efficiency.

Research methods, techniques, and instruments

For the preparation of the manufacturing process and the generation of ISO G-code, a licensed version of Fusion 360 software was used. The manufacturing process was carried out on the Haas ST-40 CNC machine, a PA-30 Potisje Ada conventional lathe, and a GUK-1P Prvomajska milling machine. Additionally, a stopwatch was used to quantify the time spent during the preparation for manufacturing and machining processes.

Downtimes in the petroleum industry

During operations such as drilling and cementation of a well, well completion, workover, or well maintenance, certain delays and interruptions during the ongoing operation may occur (Boldrin et al., 2023; Elgibaly, 2019). A delay represents both a temporal and economic loss for the company performing the work (Aoudia et al., 2008; Maleki et al., 2023). Although modern machine learning and AI tools aim to predict and minimize downtimes (Chuka Anthony Arinze et al., 2024), in practice, most of the oil and gas wells experience a downtime at some point during their construction or completion that requires intervention (Al-Subaiei et al., 2021). To fix the problem, i.e., restoring the well to its previous (operational) state, it is necessary to use special equipment (Lei et al., 2020; Vasić, 2013). Various tools specifically designed for removing stuck equipment from the well can be used during the process (Vasić, 2013), one of which is a taper tap fishing tool.

Downtimes may occur due to various circumstances:

- Pipe breakage,
- Jamming of well equipment components,
- Presence of foreign objects in the well (residual logging equipment, wireline, cables, an object that has fallen into the borehole etc.).

The following section discusses the types of downtimes that can be resolved using a taper tap fishing tool.

Taper tap

If a breakage of drill pipes occurs, which most commonly happens at the pipe joints, the drill pipe line is interrupted, leading to rig downtime (Albdiry and Almensory, 2016). If the other diameter of a drill pipe is slightly smaller than the wellbore diameter, it is impossible to use a fishing tool that engages on the outside surface of a tube or a stuck tool, such as an overshot; so a fishing tool that engages with the internal diameter (such as taper tap) has to be employed to retrieve the broken equipment from the well (Martinović & Moslavac, 2011; Vasić, 2013).

The taper tap (Figure 1) is one of the oldest and simplest tools used for catching equipment stuck in the wellbore. Internal fishing refers to an operation in which the fishing tool is lowered into the well and engages the broken tool or pipe by its inner diameter. The body of the taper tap can vary in diameter, length, thread type, chip groove presence, etc. (Liakh et al., 2021; Martinović and Moslavac, 2011; Vasić, 2013).



Figure 1 - A cross-section of a taper tap (https://runinall.com/fishing-tools/5215-taper-tap.html, n.d.)

Traditional and modern methods - comparison

The traditional method

The three main time parameters relevant to this study are:

- Time for preparing the process sheet,
- Machine operating time and
- Machining time.

To eliminate any potential ambiguities and uncertainties that may occur during the manufacturing process and thereby enhance time efficiency, the development of a high-quality process sheet requires a certain amount of time. In addition to active machining time, the process of manufacturing also requires machine operating time (workpiece centering, tool approach, tool change, workpiece repositioning, transitioning to another machine, etc.).

A stopwatch was used to measure the time required for manufacturing the taper tap. The time required for preparing the process sheet was recorded, along with the active machining time and the machine operating time.

Process sheet creation time

The process sheet was created based on the workshop drawing provided by the client. Before beginning the preparation of the process

sheet, it is necessary to review the drawing. Each process sheet can be created in multiple ways; however, its quality is determined by its precision, clarity, and the minimal number of operations required. Precision and clarity reduce the time needed for interpreting the process sheet, while minimizing the number of operations directly impacts the manufacturing time of the component. The time required for preparing the process sheet largely depends on the expertise of the engineer responsible for its creation. The time spent on creating the process sheet was 2 h 8 min.

Machine operating time

Considering that the time required for machine operating depends on the operator's skill, the most accurate research results will be obtained by taking the average time in minutes for each operation listed in Table 1.

Table 1 - Number of individual operations and machine operating time per operation

Operation	Number of repetitions of operations	Measured operation time	Average operation time	Total average operation time
Tool preparing	1	11 min 49 s	12 min	12 min
First centering of the workpiece	1	4 min 49 s	5 min	5 min
Setting the operating mode of the machine	11	14 s - 22 s	0,3 min	3.3 min
Tool approach to the workpiece and tool retract stroke	63	8 s - 21 s	0,4 min	25,2 min
Tool change	15	46 s - 1 min 20 s	1 min	15 min
Workpiece rotation and recentering	2	52 s - 1 min 12 s	1 min	2 min
Machine changeover (positioning the workpiece in the milling machine)	1	2 min 49 s	3 min	3 min
Total average duration of all operations				1 h 5.5 min

Considering the total time required for performing individual operations, the total average duration of all operations amounts to 65.5 minutes, i.e., 1 hour and 5.5 minutes.

Active machining time

The active machining time is defined as the period during which material is removed from the workpiece. The time consumption during these operations mainly depends on the machining parameters applied during the process and only to a small extent on the operator's skill.

Table 2 - Number of individual operations and machining time per operation

Operation	Number of repetitions of operation	Measured operation time	Total average operation time
Facing	2	16 s	32 s
Spot drilling	2	14 s	28 s
Drilling a smaller diameter	2	10 min 15 s	20 min 30 s
Drilling a bigger diameter	1	5 min 51 s	5 min 51 s
Chamfering	5	2 s	10 s
Rough turning - external	1	33 min 45 s	33 min 45 s
Finish turning - external	1	7 min 34 s	7 min 34 s
Rough turning - internal	1	9 min 1 s	9 min 1 s
Finish turning - internal	1	4 min 45 s	4 min 45 s
Thread cutting on a cone - external	1	22 min 4 s	22 min 4 s
Thread cutting on a cone - internal	1	11 min 24 s	11 min 24 s
Thread cutting for guider	1	12 min 24 s	12 min 24 s
Chip groove milling	4	1 min 58 s	7 min 52 s
Total duration of all operations			2 h 16.3 min

By summing the machining time per operation, the total duration of all operations amounts to 2 hours, 16 minutes, and 20 seconds.

The total time required to manufacture the taper tap using the traditional method is 5 hours, 29.8 minutes.

The modern method

The three main time parameters relevant to this study are:

- Time needed for 3D modeling in the software Fusion 360,
- Machine operating time, and
- Machining time.

Before starting work in the software, it is essential to review the workshop drawing provided by the client. 3D modeling and CNC machine programming of the Haas ST-40 CNC machine were performed using Fusion 360 software. The duration of work in the software is a relative factor, as it depends on the engineer's expertise and familiarity with the software environment. The efficiency of modeling relies on the user's proficiency with the software interface, whereas the efficiency of programming, in addition to software knowledge, also requires an understanding of tool properties, machining parameters, and machine performance. The total time spent on modeling the taper tap and programming the CNC machine was 2 hours and 43 minutes.

Machine operating time

Unlike the traditional manufacturing method, which requires continuous machine servicing, the modern manufacturing approach significantly reduces the time spent on physical interaction with the machine. The CNC machine used in this study does not require any operator intervention during the material removal process.
Table 3 presents the CNC machine servicing operations along with the measured, average, and total operating times.

It is important to emphasize that CNC machine operating time depends on the operator's expertise and efficiency, as in traditional manufacturing. Therefore, the precisely measured operating time cannot be considered a universal reference; instead, the average servicing time must be determined from the recorded values.

The number of machine servicing operations in modern manufacturing is lower than in traditional machining. This is a direct result of the high level of process automation. In CNC machining, the total average duration of all operations for manufacturing the taper tap was 24 minutes.

To determine the active machining time, using a stopwatch is not necessary. Upon completion of the programming process, the software automatically calculates and sums the time required for each operation during the technological process. The software calculated that the time

required to manufacture the taper tap on the CNC machine is 56 minutes and 54 seconds, approximately 57 minutes (Figure 2).

Table 3 - Number of individual operations and machine operating time per operation

Operation	Number of repetitions of operations	Measured operation time	Average operation time	Total average operation time
Tool preparation and tool mounting on the turret	1	17 min 2 s	17 min	17 min
Workpiece setup	1	1 min 53 s	2 min	2 min
Workpiece rotation	1	1 min 2 s	1 min	1 min
Steady rest setup	1	1 min 49 s	2 min	2 min
Steady rest removal	1	46 s	1 min	1 min
Tailstock setup	1	49 s	1 min	1 min
Total average duration of all operations				24 min

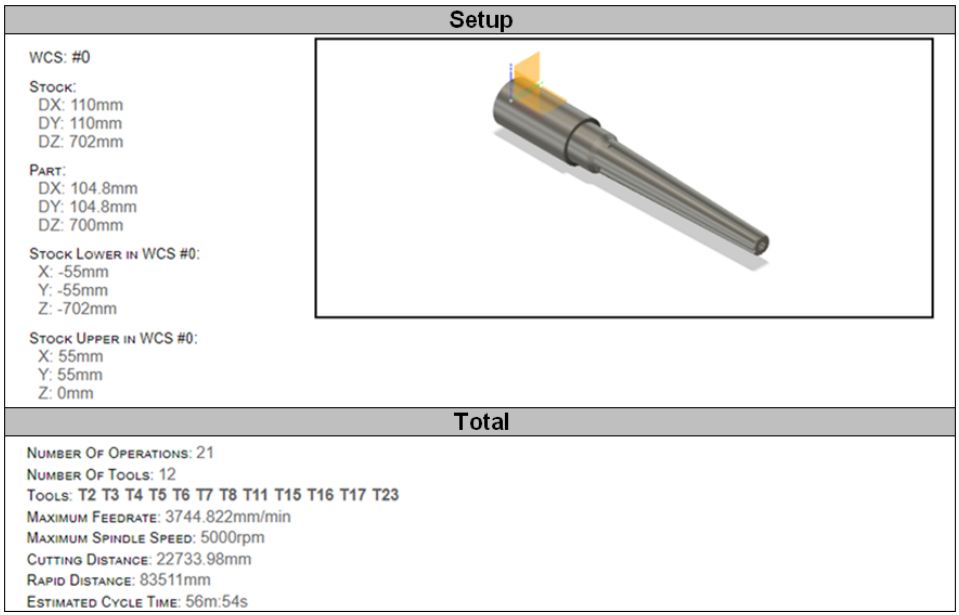


Figure 2 - Basic data on the machining operations on the CNC machine, as well as the duration of all operations calculated by the Fusion 360 software

The total time required to manufacture the taper tap using the modern method is 4 hours and 6 minutes.

Discussion

The two manufacturing methods used the same tools during the manufacturing process, while the primary difference is the order of operations. The order of operations in each method is adapted to the machining conditions in such a way that the manufacturing time of the given part is minimized (the fewer interruptions in the process due to workpiece positioning, the less time is needed for machine operating).

The next aspect to discuss is the time spent on preparation for the machining process: in traditional manufacturing, this involves creating the process sheet, while in modern manufacturing, it involves 3D modeling and CNC machine programming. Research has shown that preparation time for modern manufacturing is 37 minutes longer than the time required to create the process sheet for traditional machining.

Machine operating time for manufacturing the taper tap using the modern method is 41.5 minutes shorter than the machine operating time for the same element using the traditional method, which is a significant difference. This segment highlights the advantage of automated machining, as many operations that need to be performed manually on a conventional lathe or milling machine (such as a cutting tool approach to the workpiece) are performed quickly and more precisely by guiding the cutting tool via computer control.

The last factor considered in this study, which affects the overall duration of the manufacturing process, is the active machining time. Analyzing the results obtained, it is evident that, in terms of time efficiency, modern manufacturing has an advantage over traditional methods by 1 hour and 19.3 minutes (approximately 1 hour and 20 minutes).

These results directly indicate that, if serial production were to be implemented, manufacturing using the modern method would save 2 hours and 0.8 minutes (approximately 2 hours) for each subsequent element compared to traditional manufacturing. The research conducted in this paper confirms the initial hypothesis that the modern process of manufacturing the taper tap offers a time efficiency advantage over traditional methods.

Conclusion

The analysis of the conducted research clearly shows that the modern manufacturing method has numerous advantages over the traditional method. Although the modern manufacturing method requires more time for preparation, it should be considered that the preparation needs to be done only once for each manufacturing method. This directly indicates that

in the long run, when multiple identical parts need to be produced, the modern manufacturing method is more time-efficient.

Even though machining time is shorter on CNC machines compared to conventional lathes and milling machines, the traditional manufacturing method still plays a very important role in modern production, especially when quick manual adjustments are required on a workpiece, for which 3D modeling and CNC programming would take a lot of time. This directly indicates that the traditional manufacturing method still plays a key role in the manufacturing industry, despite the advantages provided by modern technologies.

References

Afteni, C. & Frumuşanu, G. 2017. A Review on Optimization of Manufacturing Process Performance. *International Journal of Modeling and Optimization*, 7(3), pp. 139–144. Available at: https://doi.org/10.7763/IJMO.2017.V7.573

Albdiry, M.T. & Almensory, M.F. 2016. Failure analysis of drillstring in petroleum industry: A review. *Engineering Failure Analysis*, 65, pp. 74–85. Available at: https://doi.org/10.1016/j.engfailanal.2016.03.014

Al-Subaiei, W., Al-Herz, E., Al-Marri, W., Al-Otaibi, R., Ashyan, H. & Jaber, H. 2021. Industry 4.0 Smart Predictive Maintenance in the Oil Industry to Enable Near-Zero Downtime in Operations. In: 11th Annual International Conference on Industrial Engineering and Operations Management, Singapore, pp. 7067–7077, 7–11. mart. Available at: https://doi.org/10.46254/AN11.20211234

Aoudia, M., Belmokhtar, O. & Zwingelstein, G. 2008. Economic impact of maintenance management ineffectiveness of an oil and gas company. *Journal of Quality in Maintenance Engineering*, 14, pp. 237–261. Available at: https://doi.org/10.1108/13552510810899454

Arinze, C.A., Izionworu, V.O., Isong, D., Daudu, C.D. & Adefemi, A. 2024. Predictive maintenance in oil and gas facilities, leveraging AI for asset integrity management. *International Journal of Frontiers in Engineering and Technology Research*, 6(1), pp. 16–26. Available at: https://doi.org/10.53294/ijfetr.2024.6.1.0026

Boldrin, R., Martinez, R., Nunes, M., Ayusso, A. & Vivas, V. 2023. Successful Customized Thru-Tubing Plug & Abandonment from a Light Well Intervention Vessel as an Alternative to Heavy Workover Operations to Reduce Time and Cost – A Case Study from Brazil. In: ADIPEC, Abu Dhabi, UAE, paper SPE-216746-MS, 2–5. oktobar. Available at: https://doi.org/10.2118/216746-MS

Elgibaly, A. 2019. Well control during drilling and workover operations. *Journal of Petroleum and Mining Engineering*, 21(2), pp. 104–120. Available at: https://doi.org/10.21608/jpme.2020.79316

Ghafoorpoor Yazdi, P., Azizi, A. & Hashemipour, M. 2018. An Empirical Investigation of the Relationship between Overall Equipment Efficiency (OEE) and Manufacturing Sustainability in Industry 4.0 with Time Study Approach. *Sustainability*, 10(9), 3031. Available at: https://doi.org/10.3390/su10093031

Lei, Q., Li, Y., Li, T., Li, H., Guan, B., Bi, G., Wang, J., Weng, D., Huang, S. & Han, W. 2020. Technical status and development direction of workover operation of PetroChina. *Petroleum Exploration and Development*, 47(1), pp. 161–170. Available at: https://doi.org/10.1016/S1876-3804(20)60015-5

Liakh, M., Yatsyshyn, T., Gavryliv, S., Gavryliv, Y., Shkitsa, L., Monkova, K., Monka, P.P. & Liakh, V.-D. 2021. Environmentally-efficient approaches to oil and gas producing sites. E3S Web of Conferences, 280, 09002. Available at: https://doi.org/10.1051/e3sconf/202128009002

Maleki, M.H., Zare Bahnamiri, M.J., Ghotbi Vayeghan, B., Adeli, O.A. & Hasankhani, F. 2023. Identifying and Prioritizing Risks Related with Time Delays in Oil and Gas Projects. *Petroleum Business Review,* 7(3), pp. 89–110. Available at: https://doi.org/10.22050/pbr.2023.325756.1249

Martinović, D. & Moslavac, B. 2011. Opremanje i održavanje bušotina. Zagreb, Croatia: Rudarsko-geološko-naftni fakultet Sveučilišta u Zagrebu.

Subramanian, G., Patil, B.T. & Kokate, M. 2019. Review of Modern Technologies in Manufacturing Sector. In: 2019 International Conference on Advances in Computing, Communication and Control (ICAC3), Mumbai, India, pp. 1–6. Available at: https://doi.org/10.1109/ICAC347590.2019.9036835

Taper Tap [online]. Available at: https://runinall.com/fishing-tools/5215-taper-tap.html [Accessed: 29 March 2025].

Tönissen, S., Rey, J. & Klocke, F. 2015. Economic efficiency of manufacturing technology integration. *Journal of Manufacturing Systems*, 37, pp. 173–181. Available at: https://doi.org/10.1016/j.jmsy.2015.07.003

Vasić, M. 2013. Alati za instrumentaciju. Serbia: NIS Naftagas.

Uporedna analiza tradicionalnog i savremenog tehnološkog postupka izrade instrumentacionog trna

Dejan Bajić, **autor za prepisku**, *Slavica* Prvulović, *Eleonora* Desnica, *Mića* Đurđev, *Ljiljana* Radovanović, *Branislava* Radišić

Univerzitet u Novom Sadu, Tehnički fakultet „Mihajlo Pupin", Zrenjanin, Republika Srbija

OBLAST: mašinstvo
KATEGORIJA (TIP) ČLANKA: originalni naučni rad

Sažetak:

Uvod/cilj: Ovaj rad predstavlja komparativnu analizu tradicionalnog i modernog načina izrade instrumentacionog trna - alata koji se koristi u procesu instrumentacije u naftnim bušotinama tokom remontnih radova. Cilj ovog istraživanja je da ispita razlike u pogledu vremenske efikasnosti između tradicionalnog načina obrade (univerzalni strug i glodalica) i

modernog (obrada na CNC mašini), polazeći od hipoteze da savremene tehnike izrade pružaju veću vremensku efikasnost.

Metode: Ovo istraživanje bazirano je na eksperimentalnoj praktičnoj izradi instrumentacionog trna na dva načina: tradicionalni i moderni. Izmereno je potrebno vreme za izvršenje svake ključne operacije koja je sprovedena prilikom izrade instrumentacionog trna, uključujući pripremu izrade (kreiranje tehnološke liste (kod tradicionalnog načina izrade) ili 3D modelovanje i programiranje u softveru (kod morednog načina izrade)), vremena opsluživanja mašine, kao i vremena aktivne obrade (skidanja strugotine). Za potrebe 3D modelovanja i programiranja CNC mašine, korišćen je softver Fjužn 360. Vreme je mereno štopericom, te evidentirano, dok je jedan deo vremenskog parametra pridobijen iz samog softvera (pocenjeno vreme izrade na moderan način koje pruža softver).

Rezultati: Rezultati pokazuju da iako je moderan način izrade zahtevao 37 minuta više za radove koji obuhvataju pripremu proizvodnje, on ipak ima prednost u odnosu na tradicionalan metod u drugim segmentima. Vreme opsluživanja mašine je kod modernog metoda skraćeno za 41,5 minuta, dok je vreme skidanja strugotine kraće za 1 sat i 19,3 minuta u poređenju sa tradicionalnim metodom. Generalno gledano, moderan način izrade pruža znatno veću vremensku efikasnost prilikom proizvodnje instrumentacionog trna u slučaju masovne proizvodnje.

Zaključak: Istraživanje je potvrdilo polaznu hipotezu da moderan način izrade pruža veću vremensku efikasnost u poređenju sa tradicionalnim načinom izrade. Uprkos dužem procesu pripreme izrade, prilikom masovne proizvodnje moderan način je daleko efikasniji od tradicionalnog u domenu vremenske efikasnosti. Ipak, tradicionalna metoda i dalje može imati ključnu ulogu u proizvodnji pojedinačnih elemenata ili brzih manuelnih prepravki.

Ključne reči: mašinska obrada, tradicionalno, moderno, CNC, vremenska efikasnost, naftna industrija, vreme izrade.

Paper received on: 26 July 2025.
Manuscript corrections submitted on: 8 September 2025.
Paper accepted for publishing on: 21 November 2025.

© 2026 The Authors. Published by Vojnotehnički glasnik / Military Technical Courier (www.vtg.mod.gov.rs).This article is an open access article distributed under the terms and conditions of the Creative Commons Attribution license (http://creativecommons.org/licenses/by/4.0/rs/)

CALL FOR PAPERS AND ARTICLE FORMATTING INSTRUCTIONS

The instructions to authors about the article preparation for publication in *Military Technical Courier* are based on the Regulations on categorization and ranking of scientific journals of the Ministry of Education, Science and Technological Development of the Republic of Serbia (Official Gazette of the Republic of Serbia, No 159/20). This Regulations aims at improving the quality of national journals and raising the level of their compliance with the international system of scientific information exchange.

Military Technical Courier / Vojnotehnički glasnik (www.vtg.mod.gov.rs/index-e.html, ISSN 0042-8469 – print issue, e-ISSN 2217-4753 – online, UDC 623+355/359, DOI: 10.5937/VojnotehnickiGlasnik; https://doi.org/10.5937/VojnotehnickiGlasnik), is a peer-reviewed scientific journal.

The owners of the journal are the Ministry of Defence of the Republic of Serbia and the Serbian Armed Forces. The publisher and financier of *Military Technical Courier* is the University of Defence in Belgrade (Military Academy).

The program of the journal is based on the annual classification of journals performed by a relevant Ministry as well as on its indexing in international indexing databases.

The journal covers scientific and professional fields within the educational-scientific field of **Natural-Mathematical Sciences**, as well as within the educational-scientific field of **Technical-Technological Sciences**, and especially the field of **defense sciences and technologies**. It publishes theoretical and practical achievements leading to professional development of all members of Serbian, regional and international academic communities as well as members of the military and ministries of defence in particular. It publishes papers with balanced coverage of analytical, experimental, and applied research as well as numerical simulations from various disciplines. The material published is of high quality and relevance, written in a manner that makes it accessible to a wider readership. The journal welcomes papers reporting original theoretical and/or practice-oriented research as well as extended versions of already published conference papers. Manuscripts for publication are selected through a double-blind peer-review process to validate their originality, relevance, and readability. This being so, the objective is not only to keep the quality of published papers high but also to provide a timely, thorough, and balanced review process.

The editorial policy of *Military Technical Courier* is based on the COPE Core Practices, common COPE, DOAJ, OASPA and WAME Principles of Transparency and Best Practice in Scholarly Publishing as well as on the best accepted practices in scientific publishing. Military Technical Courier has been a COPE (Committee on Publication Ethics) member since 2nd May 2018 and a member of OASPA (Open Access Scholarly Publishers Association) since 27th November 2015.

The Ministry of Science, Technological Development and Innovation of the Republic of Serbia classified *Military Technical Courier* for the year 2025, on December, 2025:

- **on the list of periodicals for computer sciences,**
  category: reputed national journal **(M51)**,
- **on the list of periodicals for electronics, telecommunications and IT,**
  category: reputed national journal **(M51)**,
- **on the list of periodicals for mechanical engineering,**
  category: reputed national journal **(M51)**,
- **on the list of periodicals for materials and chemical technology,**
  category: national journal of international importance **(M24)**.

The approved lists of national periodicals for the year 2025 can be viewed on the website of *Military Technical Courier*, page *Journal categorization*.

More detailed information can be found on the website of the Ministry of Education, Science and Technological Development of the Republic of Serbia.

The information on the categorization can be also found on the website of KOBSON (Consortium of Libraries of Serbia for Unified Acquisition).

The periodical is categorized in compliance with the Regulations on categorization and ranking of scientific journals of the Ministry of Education, Science and Technological Development of the Republic of Serbia (Official Gazette of the Republic of Serbia, No 159/20). More detailed information can be found on the website of the Ministry of Education, Science and Technological Development.

The journal is in the Serbian Citation Index – SCIndex (data base of national scientific journals), in the Scientific Information System Redalyc, and in the Russian Index of Science Citation/Российский индекс научного цитирования (RINC/РИНЦ) and is constantly monitored depending on the impact within the bases themselves. More detailed information can be viewed on the website of *Military Technical Courier*, page *Journal indexing*.

Military Technical Courier, in terms of its content, offers the possibility of open access (DIAMOND OPEN ACCESS) and applies the Creative Commons Attribution (CC BY) licence on copyright. The copyright details can be found on the *Copyright notice and Self-archiving policy* page of the journal's website.

Manuscripts are submitted online, through the electronic editing system ASSISTANT, developed by the Center for Evaluation in Education and Science – CEON.

The access and the registration are through *Military Technical Courier* site http://www.vtg.mod.gov.rs/index-e.html, on the page *ASSISTANT* or the page *SCINDEKS* or directly through the link (aseestant.ceon.rs/index.php/vtg).

The detailed instructions about the registration for the service are on the website http://www.vtg.mod.gov.rs/index-e.html, on the page *Instructions for ASSISTANT*.

All authors submitting a manuscript for publishing in *Military Technical Courier* should register for an ORCID ID following the instructions on the web page *Registration for an ORCID identifier*.

Military Technical Courier publishes articles in English, using Arial and a font size of 11pt with Single Spacing.

The procedures of article preparation, writing and editing should be in accordance with the *Publication ethics statement* (http://www.vtg.mod.gov.rs/publication-ethics-statement.html).

The article should contain an abstract with keywords, introduction (motivation for the work), body (adequate overview of the representative work in the field, a clear statement of the novelty in the presented research, suitable theoretical background, one or more examples to demonstrate and discuss the presented ideas), conclusion, and references (without heading and subheading enumeration). The article length should not normally exceed 16 pages of the A4 paper format with single spacing, up to a maximum of 24 pages with references and supplementary material included.

The article should be formatted following the instructions in the Article Form which can be downloaded from website page *Article form*.

Title

The title should be informative. It is in both Journal's and author's best interest to use terms suitable for indexing and word search. If there are no such terms in the title, the author is strongly advised to add a subtitle.

Letterhead title

The letterhead title is given at a top of each page for easier identification of article copies in an electronic form in particular. It contains the author's surname and first name initial (for multiple authors add "et al"), article title, journal title and collation (year, volume, issue, first and last page). The journal and article titles can be given in a shortened form.

Author's name

Full name(s) of author(s) should be used. It is advisable to give the middle initial. Names are given in their original form (with diacritic signs if in Serbian).

Author's affiliation

The full official name and seat of the author's affiliation is given, possibly with the name of the institution where the research was carried out. For organizations with complex structures, give the whole hierarchy (for example, University of Defence in Belgrade, Military Academy, Department for Military Electronic Systems). At least one organization in the hierarchy must be a legal entity. When some of multiple authors have the same affiliation, it must be clearly stated, by special signs or in other way, which department exactly they are affiliated with. The affiliation follows the author's name. The function and title are not given.

Contact details

The postal addresses or the e-mail addresses of the authors are given in the first page.

Type of articles

Classification of articles is a duty of the editorial staff and is of special importance. Referees and the members of the editorial staff, or section editors, can propose a category, but the editor-in-chief has the sole responsibility for their classification.

Military Technical Courier publishes scientific articles.

Scientific articles:

– Original scientific papers (giving the previously unpublished results of the author's own research based on scientific methods);

– Review papers (giving an original, detailed and critical view of a research problem or an area to which the author has made a contribution demonstrated by self-citation);

– Short communications or Preliminary communications (original scientific full papers but shorter or of a preliminary character);

– Scientific commentaries or discussions (discussions on a particular scientific topic, based exclusively on scientific argumentation) and opinion pieces.

Exceptionally, in particular areas, a scientific paper in the Journal can be in a form of a monograph or a critical edition of scientific data (historical, archival, lexicographic, bibliographic, data survey, etc.) which were unknown or hardly accessible for scientific research.

Papers classified as scientific must have at least two positive reviews.

If the journal contains non-scientific contributions as well, the section with scientific papers should be clearly denoted in the first part of the Journal.

Short communications are usually 4-7 pages long, research articles and case studies 10-14 pages, while reviews can be longer. Page number limits are not strict and, with

appropriate reasoning, submitted manuscripts can also be longer or shorter. If extended versions of previously published conference papers are submitted, Editors will check if sufficient new material has been added to meet the journal standards and to qualify such manuscripts for the review process. The added material must not have been previously published. New results are desired but not necessarily required; however, submissions should contain expansions of key ideas, examples, elaborations, etc. of conference papers.

Language

The language of the article should be English. The grammar and style of the article should be of good quality. The systematized text should be without abbreviations (except standard ones). All measurements must be in SI units. The sequence of formulae is denoted in Arabic numerals in parentheses on the right-hand side.

Abstract and summary

An abstract is a concise informative presentation of the article content for fast and accurate evaluation of its relevance. It contains the terms often used for indexing and article search. A 100- to 250-word abstract has the following parts: introduction/purpose of the research, methods, results and conclusion.

Keywords

Keywords are terms or phrases showing adequately the article content for indexing and search purposes. They should be allocated having in mind widely accepted international sources (index, dictionary or thesaurus), such as the Web of Science keyword list for science in general. The higher their usage frequency is, the better. Up to 10 keywords immediately follow the abstract and the summary, in respective languages. For this purpose, the ASSISTANT system uses a special tool KWASS for the automatic extraction of key words from disciplinary thesauruses/dictionaries by choice and the routine for their selection, i.e. acceptance or rejection by author and/or editor.

Article acceptance date

The date of the reception of the article, the dates of submitted corrections in the manuscript (optional) and the date when the Editorial Board accepted the article for publication are all given in a chronological order at the end of the article.

Acknowledgements

The name and the number of the project or programme within which the article was realised is given in a separate note at the bottom of the first page together with the name of the institution which financially supported the project or programme.

Article preliminary version

If an article preliminary version has appeared previously at a meeting in a form of an oral presentation (under the same or similar title), this should be stated in a separate note at the bottom of the first page. An article published previously cannot be published in *Military Technical Courier* even under a similar title or in a changed form.

Tables and illustrations

All the captions should be in the original language as well as in English, together with the texts in illustrations if possible. Tables are typed in the same style as the text and are denoted by Arabic numerals at the top. Photographs and drawings, placed

appropriately in the text, should be clear, precise and suitable for reproduction. Drawings should be created in Word or Corel.

For figures and graphs, proper data plot is recommended i.e. using a data analysis program such as Excel, Matlab, Origin, SigmaPlot, etc. It is not recommended to use a screen capture of a data acquisition program as a figure or a graph.

Citation in the text

Citation in the text must be uniform. *Military Technical Courier* applies the Harvard Referencing System given in the Harvard Style Manual. When citing sources within your paper, i.e. for in-text references of the works listed at the end of the paper, place the year of publication of the work in parentheses and optionally the number of the page(s) after the author's name, e.g. (Petrovic, 2012, pp.10-12). A detailed guide on citing, with examples, can be found on *Military Technical Courier* website on the page *Instructions for Harvard Style Manual*. In-text citations should follow its guidelines. For checking in-text citations, the ASSISTANT system uses a special tool CiteMatcher to find out quotes left out within papers and in reference lists.

Footnotes

Footnotes are given at the bottom of the page with the text they refer to. They can contain less relevant details, additional explanations or used sources (e.g. scientific material, manuals). They cannot replace the cited literature.

Reference list (Literature)

The cited literature encompasses bibliographic sources such as articles and monographs and is given in a separate section in a form of a reference list. References are not translated to the language of the article.

In compiling the reference list and bibliography, *Military Technical Courier* applies the Harvard System – Harvard Style Manual. All bibliography items should be listed alphabetically by author's name, without numeration. A detailed guide for listing references, with examples, can be found on *Military Technical Courier* website on the page *Instructions for Harvard Style Manual*. Reference lists at the end of papers should follow its guidelines. In journal evaluation systems, non-standard, insufficient or inconsequent citation is considered to be a sufficient cause for denying the scientific status to a journal.

Authorship Statement

The Authorship statement, submitted together with the paper, states authors' individual contributions to the creation of the paper. In this statement, the authors also confirm that they followed the guidelines given in *Call for papers* and *Publication ethics and malpractice statement of the journal*.

All articles are peer reviewed.

The list of referees of *Military Technical Courier* can be viewed at website page *List of referees*. The article review process is described on the *Peer Review Process* page of the website.

Editorial Team

Address of the Editorial Office:
Vojnotehnički glasnik / Military Technical Courier
Veljka Lukića Kurjaka 33
11042 Belgrade, Republic of Serbia
e-mail: vojnotehnicki.glasnik@mod.gov.rs,
tel.: +381 11 3603 260

POZIV I UPUTSTVO AUTORIMA O NAČINU PRIPREME ČLANKA

Uputstvo autorima o načinu pripreme članka za objavljivanje u *Vojnotehničkom glasniku* urađeno je na osnovu Pravilnika o kategorizaciji i rangiranju naučnih časopisa Ministarstva prosvete, nauke i tehnološkog razvoja Republike Srbije („Službeni glasnik RS“, broj 159/20). Primena ovog Pravilnika prvenstveno služi unapređenju kvaliteta domaćih časopisa i njihovog potpunijeg uključivanja u međunarodni sistem razmene naučnih informacija.

Vojnotehnički glasnik / Military Technical Courier (www.vtg.mod.gov.rs, ISSN 0042-8469 – štampano izdanje, e-ISSN 2217-4753 – online, UDC 623+355/359, DOI: 10.5937/VojnotehnickiGlasnik; https://doi.org/10.5937/VojnotehnickiGlasnik), jeste recenzirani naučni časopis.

Vlasnici časopisa su Ministarstvo odbrane Republike Srbije i Vojska Srbije. Izdavač i finansijer časopisa je Univerzitet odbrane u Beogradu (Vojna akademija).

Programska orijentacija časopisa zasniva se na godišnjoj kategorizaciji časopisa, koju vrši nadležno državno ministarstvo u određenim oblastima, kao i na njegovom indeksiranju u međunarodnim indeksnim bazama.

Časopis obuhvata naučne, odnosno stručne oblasti u okviru obrazovno-naučnog polja **prirodno-matematičkih nauka**, kao i u okviru obrazovno-naučnog polja **tehničko-tehnoloških nauka**, a naročito oblasti **odbrambenih nauka i tehnologija**. Objavljuje teorijska i praktična dostignuća koja doprinose usavršavanju svih pripadnika srpske, regionalne i međunarodne akademske zajednice, a posebno pripadnika vojski i ministarstava odbrane. Publikuje radove sa uravnoteženim izveštavanjem o analitičkim, eksperimentalnim i primenjenim istraživanjima, kao i numeričkim simulacijama, obuhvatajući različite discipline. Objavljeni materijali su visokog kvaliteta i relevantnosti, napisani na način koji ih čini dostupnim širokoj čitalačkoj publici. Svi radovi koji izveštavaju o originalnim teorijskim i/ili praktično orijentisanim istraživanjima ili proširenim verzijama već objavljenih radova sa konferencija su dobrodošli. Radovi za objavljivanje odabiru se dvostruko slepim postupkom recenzije kako bi se osigurala originalnost, relevantnost i čitljivost. Pritom cilj nije samo da se kvalitet objavljenih radova održi visokim već i da se obezbedi pravovremeni, temeljni i uravnoteženi postupak recenzije.

Uređivačka politika *Vojnotehničkog glasnika zasniva* se na preporukama Odbora za etičnost u izdavaštvu (COPE Core Practices) i zajedničkim principima transparentnosti i najbolje prakse u izdavaštvu COPE, DOAJ, OASPA i WAME, kao i na najboljim prihvaćenim praksama u naučnom izdavaštvu. Vojnotehnički glasnik je član COPE (Committee on Publication Ethics) od 2. maja 2018. godine i član OASPA (Open Access Scholarly Publishers Association) od od 27. novembra 2015. godine.

Ministarstvo nauke, tehnološkog razvoja i inovacija Republike Srbije utvrdilo je decembra 2025. godine kategorizaciju Vojnotehničkog glasnika, za 2025. godinu:

- **na listi časopisa za računarske nauke:**
  kategorija vrhunski časopis nacionalnog značaja **(M51),**
- **na listi časopisa za elektroniku, telekomunikacije i informacione tehnologije:**
  kategorija vrhunski časopis nacionalnog značaja (**M51),**
- **na listi časopisa za mašinstvo:**
  kategorija vrhunski časopis nacionalnog značaja **(M51),**
- **na listi časopisa za materijale i hemijske tehnologije:**
  kategorija nacionalni časopis međunarodnog značaja (**M24).**

Usvojene liste domaćih časopisa za 2025. godinu mogu se videti na sajtu *Vojnotehničkog glasnika*, stranica *Kategorizacija časopisa*.

Detaljnije informacije mogu se pronaći i na sajtu Ministarstva prosvete, nauke i tehnološkog razvoja Republike Srbije.

Podaci o kategorizaciji mogu se pratiti i na sajtu KOBSON-a (Konzorcijum biblioteka Srbije za objedinjenu nabavku).

Kategorizacija časopisa izvršena je prema Pravilniku o kategorizaciji i rangiranju naučnih časopisa Ministarstva prosvete, nauke i tehnološkog razvoja Republike Srbije („Službeni glasnik RS", broj 159/20).

Časopis se prati u kontekstu Srpskog citatnog indeksa – SCindeks (baza podataka domaćih naučnih časopisa), Naučno-informacionog sistema Redalyc i Ruskog indeksa naučnog citiranja (RINC). Podvrgnut je stalnom vrednovanju (monitoringu) u zavisnosti od uticajnosti (impakta) u samim bazama. Detalji o indeksiranju mogu se videti na sajtu *Vojnotehničkog glasnika*, stranica *Indeksiranje časopisa*.

Vojnotehnički glasnik, u pogledu svog sadržaja, pruža mogućnost otvorenog pristupa (DIAMOND OPEN ACCESS) i primenjuje Creative Commons (CC BY) odredbe o autorskim pravima. Detalji o autorskim pravima mogu se videti na sajtu časopisa, stranica *Autorska prava i politika samoarhiviranja*.

Radovi se predaju putem onlajn sistema za elektronsko uređivanje ASISTENT, koji je razvio Centar za evaluaciju u obrazovanju i nauci (CEON).

Приступ и регистрација за сервис врше се на сајту www.vtg.mod.gov.rs, преко странице *АСИСТЕНТ* или *СЦИНДЕКС*, односно директно на линку aseestant.ceon.rs/index.php/vtg.

Detaljno uputstvo o registraciji i prijavi za servis nalazi se na sajtu www.vtg.mod.gov.rs, stranica *Uputstvo za ASISTENT*.

Potrebno je da se svi autori koji podnose rukopis za objavljivanje u *Vojnotehničkom glasniku* registruju u registar ORCID (Open Researcher and Contributor ID), prema uputstvu na stranici sajta *Registracija za dobijanje ORCID identifikacione šifre*.

Vojnotehnički glasnik objavljuje članke na engleskom jeziku (arial, veličina slova 11 pt, prored Single).

Postupak pripreme, pisanja i uređivanja članka treba da bude u saglasnosti sa *Izjavom o etičkom postupanju* (http://www.vtg.mod.gov.rs/izjava-o-etickom-postupanju.html).

Članak treba da sadrži sažetak sa ključnim rečima, uvod (motivaciju za rad), razradu (adekvatan pregled reprezentativnosti rada u njegovoj oblasti, jasnu izjavu o novini u predstavljenom istraživanju, odgovarajuću teorijsku pozadinu, jedan ili više primera za demonstriranje i diskusiju o predstavljenim idejama), zaključak i literaturu (bez numeracije naslova i podnaslova). Obim članka treba da bude do jednog autorskog tabaka (16 stranica formata A4 sa proredom Single), a najviše 24 stranice.

Članak treba da bude napisan na obrascu za pisanje članka, koji se u elektronskoj formi može preuzeti sa sajta na stranici *Obrazac za pisanje članka*.

Naslov

Naslov treba da odražava temu članka. U interesu je časopisa i autora da se koriste reči prikladne za indeksiranje i pretraživanje. Ako takvih reči nema u naslovu, poželjno je da se pridoda i podnaslov.

Tekući naslov

Tekući naslov se ispisuje sa strane svake stranice članka radi lakše identifikacije, posebno kopija članaka u elektronskom obliku. Sadrži prezime i inicijal imena autora (ako autora ima više, preostali se označavaju sa „et al." ili „i dr."), naslove rada i časopisa i

kolaciju (godina, volumen, sveska, početna i završna stranica). Naslovi časopisa i članka mogu se dati u skraćenom obliku.

Ime autora

Navodi se puno ime i prezime (svih) autora. Veoma je poželjno da se navedu i srednja slova autora. Imena i prezimena domaćih autora uvek se ispisuju u originalnom obliku (sa srpskim dijakritičkim znakovima), nezavisno od jezika na kojem je napisan rad.

Naziv ustanove autora (afilijacija)

Navodi se pun (zvanični) naziv i sedište ustanove u kojoj je autor zaposlen, a eventualno i naziv ustanove u kojoj je autor obavio istraživanje. U složenim organizacijama navodi se ukupna hijerarhija (npr. Univerzitet odbrane u Beogradu, Vojna akademija, Katedra prirodno-matematičkih nauka). Bar jedna organizacija u hijerarhiji mora biti pravno lice. Ako autora ima više, a neki potiču iz iste ustanove, mora se, posebnim oznakama ili na drugi način, naznačiti iz koje od navedenih ustanova potiče svaki od navedenih autora. Afilijacija se ispisuje neposredno nakon imena autora. Funkcija i zvanje autora se ne navode.

Kontakt podaci

Adresa ili e-adresa svih autora daje se pored imena i prezimena autora.

Kategorija (tip) članka

Kategorizacija članaka obaveza je uredništva i od posebne je važnosti. Kategoriju članka mogu predlagati recenzenti i članovi uredništva, odnosno urednici rubrika, ali odgovornost za kategorizaciju snosi isključivo glavni urednik.

Vojnotehnički glasnik objavljuje naučne članke.

Naučni članak je:

– originalan naučni rad (rad u kojem se iznose prethodno neobjavljeni rezultati sopstvenih istraživanja naučnim metodom);

– pregledni rad (rad koji sadrži originalan, detaljan i kritički prikaz istraživačkog problema ili područja u kojem je autor ostvario određeni doprinos, vidljiv na osnovu autocitata);

– kratko ili prethodno saopštenje (originalni naučni rad punog formata, ali manjeg obima ili preliminarnog karaktera);

– naučna kritika, odnosno polemika (rasprava na određenu naučnu temu, zasnovana isključivo na naučnoj argumentaciji) i osvrti.

Izuzetno, u nekim oblastima, naučni rad u časopisu može imati oblik monografske studije, kao i kritičkog izdanja naučne građe (istorijsko-arhivske, leksikografske, bibliografske, pregleda podataka i sl.), dotad nepoznate ili nedovoljno pristupačne za naučna istraživanja.

Radovi klasifikovani kao naučni moraju imati bar dve pozitivne recenzije.

Ako se u časopisu objavljuju i prilozi vannaučnog karaktera, naučni članci treba da budu grupisani i jasno izdvojeni u prvom delu sveske.

Poželjno je da obim kratkih saopštenja bude 4 do 7 stranica, naučnih članaka i studija slučaja 10 do 14 stranica, dok pregledni radovi mogu biti i duži. Broj stranica nije strogo ograničen i, uz odgovarajuće obrazloženje, prijavljeni članci takođe mogu biti duži ili kraći.

Ako su radovi koji su prethodno objavljeni na konferenciji prošireni, urednici će proveriti da li je dodato dovoljno novog materijala koji ispunjava standarde časopisa i kvalifikuje podnesak za postupak recenzije. Dodati materijal ne sme biti prethodno objavljen. Novi rezultati nisu nužno potrebni, ali su poželjni. Međutim, podnesak treba da sadrži proširene

ključne ideje, primere, razrade, itd., koji su prethodno bili sadržani u podnesku sa konferencije.

Jezik rada

Jezik rada treba da bude engleski.

Tekst mora biti jezički i stilski doteran, sistematizovan, bez skraćenica (osim standardnih). Sve fizičke veličine moraju biti izražene u Međunarodnom sistemu mernih jedinica – SI. Redosled obrazaca (formula) označava se rednim brojevima, sa desne strane u okruglim zagradama.

Sažetak

Sažetak jeste kratak informativan prikaz sadržaja članka koji čitaocu omogućava da brzo i tačno oceni njegovu relevantnost. U interesu je uredništava i autora da sažetak sadrži termine koji se često koriste za indeksiranje i pretragu članaka. Sastavni delovi sažetka su uvod/cilj istraživanja, metodi, rezultati i zaključak. Sažetak treba da ima od 100 do 250 reči i treba da se nalazi između zaglavlja (naslov, imena autora i dr.) i ključnih reči, nakon kojih sledi tekst članka.

Ključne reči

Ključne reči su termini ili fraze koje adekvatno predstavljaju sadržaj članka za potrebe indeksiranja i pretraživanja. Treba ih dodeljivati oslanjajući se na neki međunarodni izvor (popis, rečnik ili tezaurus) koji je najšire prihvaćen ili unutar date naučne oblasti. Za npr. nauku uopšte, to je lista ključnih reči Web of Science. Broj ključnih reči ne može biti veći od 10, a u interesu je uredništva i autora da učestalost njihove upotrebe bude što veća. U članku se pišu neposredno nakon sažetka.

Sistem ASISTENT u tu svrhu koristi specijalnu alatku KWASS: automatsko ekstrahovanje ključnih reči iz disciplinarnih tezaurusa/rečnika po izboru i rutine za njihov odabir, tj. prihvatanje odnosno odbacivanje od strane autora i/ili urednika.

Datum prihvatanja članka

Datum kada je uredništvo primilo članak, datum kada je uredništvo konačno prihvatilo članak za objavljivanje, kao i datumi kada su u međuvremenu dostavljene eventualne ispravke rukopisa navode se hronološkim redosledom, na stalnom mestu, po pravilu na kraju članka.

Zahvalnica

Naziv i broj projekta, odnosno naziv programa u okviru kojeg je članak nastao, kao i naziv institucije koja je finansirala projekat ili program, navodi se u posebnoj napomeni na stalnom mestu, po pravilu pri dnu prve strane članka.

Prethodne verzije rada

Ako je članak u prethodnoj verziji bio izložen na skupu u vidu usmenog saopštenja (pod istim ili sličnim naslovom), podatak o tome treba da bude naveden u posebnoj napomeni, po pravilu pri dnu prve strane članka. Rad koji je već objavljen u nekom časopisu ne može se objaviti u *Vojnotehničkom glasniku* (preštampati), ni pod sličnim naslovom i izmenjenom obliku.

Tabelarni i grafički prikazi

Poželjno je da naslovi svih prikaza, a po mogućstvu i tekstualni sadržaj, budu dati dvojezično, na jeziku rada i na engleskom jeziku.

Tabele se pišu na isti način kao i tekst, a označavaju se rednim brojevima sa gornje strane. Fotografije i crteži treba da budu jasni, pregledni i pogodni za reprodukciju. Crteže treba raditi u programu word ili corel. Fotografije i crteže treba postaviti na željeno mesto u tekstu.

Za slike i grafikone ne sme se koristiti snimak sa ekrana računara programa za prikupljanje podataka. U samom tekstu članka preporučuje se upotreba slika i grafikona neposredno iz programa za analizu podataka (kao što su Excel, Matlab, Origin, SigmaPlot i drugi).

Navođenje (citiranje) u tekstu

Način pozivanja na izvore u okviru članka mora biti jednoobrazan.

Vojnotehnički glasnik za referenciranje (citiranje i navođenje literature) primenjuje Harvardski sistem referenci, odnosno Harvardski priručnik za stil (Harvard Referencing System, Harvard Style Manual). U samom tekstu, u običnim zagradama, na mestu na kojem se vrši pozivanje, odnosno citiranje literature nabrojane na kraju članka, obavezno u običnoj zagradi napisati prezime citiranog autora, godinu izdanja publikacije iz koje citirate i, eventualno, broj stranica. Npr. (Petrović, 2012, pp.10–12).

Detaljno uputstvo o načinu citiranja, sa primerima, dato je na stranici sajta *Uputstvo za Harvardski priručnik za stil*. Potrebno je da se pozivanje na literaturu u tekstu uradi u skladu sa pomenutim uputstvom.

Sistem ASISTENT u svrhu kontrole navođenja (citiranja) u tekstu koristi specijalnu alatku CiteMatcher: otkrivanje izostavljenih citata u tekstu rada i u popisu referenci.

Napomene (fusnote)

Napomene se daju pri dnu strane na kojoj se nalazi tekst na koji se odnose. Mogu sadržati manje važne detalje, dopunska objašnjenja, naznake o korišćenim izvorima (na primer, naučnoj građi, priručnicima), ali ne mogu biti zamena za citiranu literaturu.

Lista referenci (literatura)

Citirana literatura obuhvata, po pravilu, bibliografske izvore (članke, monografije i sl.) i daje se isključivo u zasebnom odeljku članka, u vidu liste referenci. Reference se ne prevode na jezik rada i nabrajaju se u posebnom odeljku na kraju članka.

Vojnotehnički glasnik, kao način ispisa literature, primenjuje Harvardski sistem referenci, odnosno Harvardski priručnik za stil (Harvard Referencing System, Harvard Style Manual).

Literatura se obavezno piše na latiničnom pismu i nabraja po abecednom redosledu, navodeći najpre prezimena autora, bez numeracije.

Detaljno uputstvo o načinu popisa referenci, sa primerima, dato je na stranici sajta *Uputstvo za Harvardski priručnik za stil.* Potrebno je da se popis literature na kraju članka uradi u skladu sa pomenutim uputstvom..

Nestandardno, nepotpuno ili nedosledno navođenje literature u sistemima vrednovanja časopisa smatra se dovoljnim razlogom za osporavanje naučnog statusa časopisa.

Sistem ASISTENT u svrhu kontrole pravilnog ispisa liste referenci koristi specijalnu alatku RefFormatter: kontrola oblikovanja referenci u skladu sa Harvardskim priručnikom za stil.

Izjava o autorstvu

Pored članka dostavlja se Izjava o autorstvu u kojoj autori navode svoj pojedinačni doprinos u izradi članka. Takođe, u toj izjavi potvrđuju da su članak uradili u skladu sa Pozivom i uputstvom autorima i Izjavom o etičkom postupanju časopisa.

Svi radovi podležu stručnoj recenziji.

Spisak recenzenata *Vojnotehničkog glasnika* može se videti na stranici sajta *Spisak recenzenata*. Proces recenziranja objašnjen je na stranici sajta *Recenzentski postupak*.

Uredništvo

Adresa redakcije:
Vojnotehnički glasnik
Veljka Lukića Kurjaka 33
11042 Beograd
e-mail: vojnotehnicki.glasnik@mod.gov.rs
telefon: 011/3603-260

Graphic design editor
Marija Marić, e-mail: marija.maric@mod.gov.rs

Proofreading, English language editing and translation
Maja Hristić, e-mail: maja.hristic@hotmail.com

CIP – Cataloguing in the publication
National Library of Serbia, Belgrade

623+355/359

VOJNOTEHNIČKI glasnik : naučni časopis Ministarstva odbrane i Vojske Srbije = Military Technical Courier : Scientific Journal of the Ministry of Defence and Serbian Armed Forces / glavni i odgovorni urednik Dragan Trifković. - God. 1, br. 1 (1953)- . - Beograd : Univerzitet odbrane u Beogradu, Vojna akademija, 1953- (Beograd : Vojna štamparija). - 23 cm

Tromesečno. - Glavni stvarni naslov od br. 1 (2026) Military Technical Courier. - Tekst na engl. jeziku. -
Drugo izdanje na drugom medijumu:
Vojnotehnički glasnik (Online) = ISSN 2217-4753
ISSN 0042-8469 = Војнотехнички гласник
COBISS.SR-ID 4423938

Price: 600.00 RSD

Printed in 100 copies

According to the Opinion of the Ministry of Science and Technological Development No. 413-00-1201/2001-01 of 12 September 2001, *Military Technical Courier* is a publication of special interest for science.

UDC: National Library of Serbia, Belgrade

Address: Vojnotehnički glasnik/Military Technical Courier,
Veljka Lukića Kurjaka 33, 11042 Belgrade, Republic of Serbia

https://www.scopus.com/sourceid/21101207440
http://www.vtg.mod.gov.rs/index-e.html
http://aseestant.ceon.rs/index.php/vtg/issue/current
http://scindeks.nb.rs/journaldetails.aspx?issn=0042-8469
https://www.redalyc.org/revista.oa?id=6617
http://elibrary.ru/title_about.asp?id=53280
https://doaj.org/toc/2217-4753

Military Technical Courier has entered into an electronic licensing agreement with EBSCO Publishing. The full text of *Military Technical Courier* can be found in EBSCO Publishing databases.

e-mail: vojnotehnicki.glasnik@mod.gov.rs, X: @MilTechCourier
Subscription to print edition: e-mail: vojnotehnicki.glasnik@mod.gov.rs;

The journal is published quarterly.

The first printed issue of the *Military Technical Courier* was published on 1 January 1953.
The first electronic edition of the *Military Technical Courier* was published online on 1 January 2011.

Printed by Vojna štamparija, Belgrade, Ratka Resanovica 1,
e-mail: vojna.stamparija@mod.gov.rs

Likovno-grafički urednik
Marija Marić, e-mail: marija.maric@mod.gov.rs

Prevodilac i lektor za engleski jezik
Maja Hristić, e-mail: maja.hristic@hotmail.com

CIP – Katalogizacija u publikaciji
Narodna biblioteka Srbije, Beograd

6623+355/359

VOJNOTEHNIČKI glasnik : naučni časopis Ministarstva odbrane i Vojske Srbije = Military Technical Courier : Scientific Journal of the Ministry of Defence and Serbian Armed Forces / glavni i odgovorni urednik Dragan Trifković. - God. 1, br. 1 (1953)- . - Beograd : Univerzitet odbrane u Beogradu, Vojna akademija, 1953- (Beograd : Vojna štamparija). - 23 cm

Tromesečno. - Glavni stvarni naslov od br. 1 (2026)
Military Technical Courier. - Tekst na engl. jeziku. -
Drugo izdanje na drugom medijumu:
Vojnotehnički glasnik (Online) = ISSN 2217-4753
ISSN 0042-8469 = Војнотехнички гласник
COBISS.SR-ID 4423938

Cena: 600,00 dinara

Tiraž: 100 primeraka

Na osnovu mišljenja Ministarstva za nauku, tehnologiju i razvoj Republike Srbije, broj 413-00-1201/2001-01 od 12. 9. 2001. godine, časopis „Vojnotehnički glasnik" je publikacija od posebnog interesa za nauku.

UDK: Narodna biblioteka Srbije, Beograd

Adresa redakcije: Vojnotehnički glasnik,
Veljka Lukića Kurjaka 33,11042 Beograd

https://www.scopus.com/sourceid/21101207440
http://www.vtg.mod.gov.rs
http://aseestant.ceon.rs/index.php/vtg/issue/current
http://scindeks.nb.rs/journaldetails.aspx?issn=0042-8469
https://www.redalyc.org/revista.oa?id=6617
http://elibrary.ru/title_about.asp?id=53280
https://doaj.org/toc/2217-4753

Vojnotehnički glasnik je licenciran kod EBSCO Publishing-a.

Kompletan tekst *Vojnotehničkog glasnika* dostupan je u bazama podataka EBSCO Publishing-a.

e-mail: vojnotehnicki.glasnik@mod.gov.rs; X: @MilTechCourier

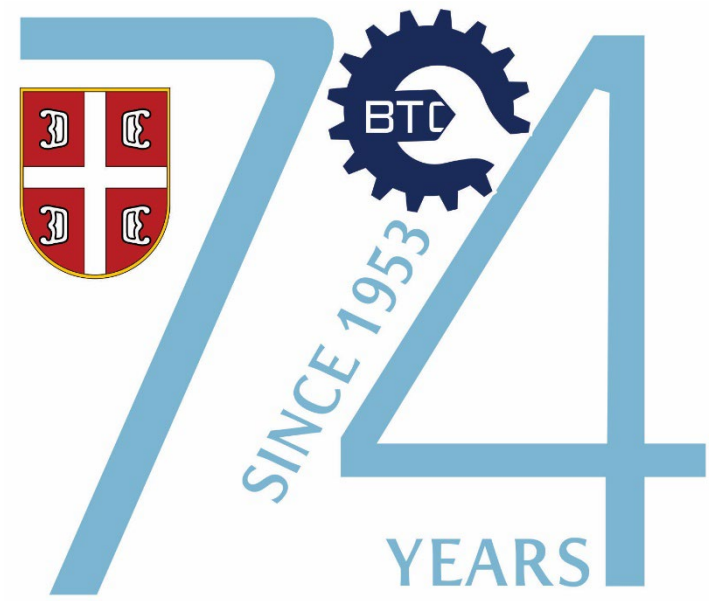
Pretplata na štampano izdanje: e-mail: vojnotehnicki.glasnik@mod.gov.rs;

Časopis izlazi tromesečno.

Prvi štampani broj Vojnotehničkog glasnika objavljen je 1.1.1953. godine.

Prvo elektronsko izdanje Vojnotehničkog glasnika na Internetu objavljeno je 1.1.2011. godine

Štampa: Vojna štamparija, Beograd, Ratka Resanovica 1,
e-mail: vojna.stamparija@mod.gov.rs


BTC
SINCE 1953
74
YEARS


VTC
OD 1953.
74
GODINA

ISSN 0042-8469
e-ISSN 2217-4753
UDC 623 + 355/359

SCIENTIFIC JOURNAL OF THE MINISTRY OF DEFENCE AND SERBIAN ARMED FORCES

MILITARY TECHNICAL COURIER

VOLUME 74 • NUMBER 4 • OKTOBER – DECEMBRE 2026.

NAUČNI ČASOPIS MINISTARSTVA ODBRANE I VOJSKE SRBIJE

VOJNOTEHNIČKI GLASNIK

VOLUMEN 74 • BROJ 4 • OKTOBAR – DECEMBAR 2026.

www.vtg.mod.gov.rs
COBISS.SR-ID 4423938
DOI: 10.5937/VojnotehnickiGlasnik